Aus dem International Max Planck Research School on Biomimetic Systems Potsdam-Golm/ Institut für Chemie Potsdam-Golm

Composite materials made of chitosan and nanosized apatite; Preparation and physicochemical characterization

Dissertation

Zur Erlangung des akademischen Grades
Doktor der Naturwissenschaften
(Dr. rer. nat.)
in der Wissenschaftsdisziplin Naturstoffchemie

eingereicht bei der
Mathematisch-Naturwissenschaftlichen Fakultät
der Universität Potsdam

von
Viorel Marin Rusu
Geboren in Bistrita
Rumänien

Potsdam, im September 2004

Gutachter:

Prof. Dr. Martin G. Peter

Prof. Dr. Julian Vincent

Prof. Dr. Peter Fratzl

Abstract

Taking inspiration from nature, where composite materials made of a polymer matrix and inorganic fillers are often found, e.g. bone, shell of crustaceans, shell of eggs, etc., the feasibility on making composite materials containing chitosan and nanosized hydroxyapatite were investigated.

A new preparation approach based on a co-precipitation method has been developed. The developed method is flexible allowing that different types of composites to be obtained. The formation of hydroxyapatite in the chitosan matrix was carried out from soluble salts as precursors at moderate pH of 10-11 for 24h. In its earlier stage of formation, the composite occurs as hydrogel as suspended in aqueous alkaline solution and it can be collected either by filtration or centrifugation techniques. Since the composite hydrogel exhibits a strong alkaline reaction, several washing steps were required to reach the neutral pH. In order to get solid composites various drying procedures including freeze-drying technique, air-drying at room temperature and at moderate temperatures, between 50^{o}C and 100^{o}C were used. Physicochemical studies showed that the composites exhibit different properties with respect to their structure and composition. *IR* and Raman spectroscopy probed the presence of both chitosan and hydroxyapatite in the composites. Hydroxyapatite as dispersed in the chitosan matrix was found to be in the nanosize range (15-50 nm) and occurs in a bimodal distribution with respect to its crystallite length. Two types of distribution domains of hydroxyapatite crystallites in the composite matrix such as cluster-like (200-400 nm) and scattered-like domains were identified by the transmission electron microscopy (*TEM*) and by confocal scanning laser microscopy (*CSLM*) measurements. Relaxation *NMR* experiments on composite hydrogels showed the presence of two types of water sites in their gel networks, such as free and bound water. Mechanical tests, such as three points bending and compressive tests showed that the mechanical properties of composites are one order of magnitude less than those of compact bone but comparable to those of porous bone. The enzymatic degradation rates of composites showed slow degradation processes. The yields of degradation were estimated to be less than 10% by loss of mass, after incubation with lysozyme (100,000 U/mg), for a period of 50 days. Since the composite materials were found biocompatible by the *'in vivo'* tests, the simple mode of their fabrication and their properties recommend them as potential candidates for the non-load bearing bone substitute materials.

Keywords: *chitosan, hydroxyapatite, hydrogels, composite biomaterials, nanoparticles, bimodal distribution, bone substitute materials;*

Zusammenfassung

Inspiriert von Natur, bei der Kompositmaterialien aus Polymermatrices und anorganischen Füllstoffen z.B. in Knochen, Krustentieren und Eierschalen vorzufinden sind, wurde die Herstellungsmöglichkeit von Kompositmaterial aus Chitosan und Hydroxyapatitdispersionen untersucht.

Basierend auf einem Kopräzipitationsverfahren wurde eine neue Herstellungsmethode entwickelt, die als flexibler Zugang zu einem Spektrum von Komposittypen führt. Die Herstellung von Hydroxyapatit in einer Chitosanmatrix erfolgt über die löslichen Komponenten $CaCl_2$ und NaH_2PO_4 und Einstellung des pH auf 10-11 über 24 h. In den frühen Phasen der Kompositbildung entsteht ein in der wässrigen alkalischen Lösung suspendiertes Hydrogel, das durch Filtration und Zentrifugation isoliert werden kann. Über mehrere Waschschritte wird das alkalische Hydrogel neutralisiert. Um feste Kompositmaterialien zu erhalten, werden Gefriertrocknung, Lufttrocknung bei Raumtemperatur oder Lufttrocknung bei höheren Temperaturen bis 50-100°C eingesetzt, was einen weiteren Einfluss auf die Struktur und die physikochemischen Eigenschaften hat. IR und Ramanspektroskopie klären das Vorhandensein von Chitosan und Hydroxyapatit im Kompositmaterial. Hydroxyapatit ist als Nanopartikel der Größe von 15-50 nm in bimodaler Verteilung in der Chitosanmatrix dispergiert, und in durch Transmissionselektronenmikroskopie (TEM) und Konfokaler Laserscanmikroskopie (CSLM) nachweisbaren 200-400 nm großen Clustern assembliert. NMR-Relaxationsmessungen an Hydrogelkompositmaterial decken die Existenz zweier Klassen vorkommenden Wassers im Netzwerk auf, gebundenes und freies Wasser. Mechanische Tests wie die Dreipunktbiegung und Kompressionstests zeigen, dass die mechanische Festigkeit etwa eine Größenordnung unter der von massivem Knochen liegt, der Festigkeit von porösem Knochen aber gleichkommt. Enzymatische Abbauraten des Kompostimaterials sind als langsam einzuschätzen. Eine 50-tägige Einwirkzeit von Lysozym führte zu einem Abbau von 10 % der Kompositmasse.

Die sich durch *in vivo* Tests herausstellende Biokompatibilität, die einfachen Herstellungsmöglichkeiten und die physikochemischen Eigenschaften empfehlen dieses Material als vielversprechenden Kandidaten für Knochenersatzmaterial in mäßig belasteten Bereichen.

Stichworte: *Chitosan, Hydroxyapatit, Nanopartikel, Hydrogel, Kompositmaterial, bimodale Verteilung, Biomaterial, Knochenersatz*

Die vorliegende Arbeit wurde in der Zeit zwischen Januar 2001 und Dezember 2003 im Rahmen der Max Plank International Research Scool am Institut für Chemie der Universität Potsdam in Golm unter der Leitung von Prof. Dr. Martin G. Peter durchgeführt.

Herrn Prof. Dr. Martin G. Peter danke ich für die Überlassung des interessanten Themas, sein stetes Interesse an dieser Arbeit und für seine Diskussionsbereitschaft und Hilfestellung.

''*Self-assembled materials in the 21st century may represent building blocks comparable to those of alloys, plastics, and semiconductors in the 20th century*''

W. M. Tolles
Materials challenges for the next century
(MRS Bulletin October 2000)

''*Any intelligent fool can make things bigger, more complex, and more violent. It takes a touch of genius and a lot of courage to move in opposite direction*''

Albert Einstein (1879-1955)

List of Abbreviations

ACP	Amorphous calcium phosphate
ADC	Analog-to-digital converter
BCPs	Biphasic calcium phosphate
BMPs	Bone morphogenetic proteins
BET	Brunauer, Emmet, Teller (*BET* surface area)
CPMG	Carr-Purcell-Meiboom-Gill, a *NMR* pulse sequence
CDHAp	Calcium deficient hydroxyapatite
CPs	Calcium phosphates salts
CSLM	Confocal scanning laser microscopy
DA	Degree of acetylation
DBM	Demineralised Bone Matrix
DCPA	Dicalcium phosphate anhydrous
DCPD	Dicalcium phosphate dihydrate
DD	Degree of deacetylation
EDS	Energy disperse X-ray spectroscopy
F_A	Mol fraction of N-Acetylglucosamine residues
FID	Free induction decay
GPC	Gel permeation chromatography
GlcN	Glucosamine
GlcNAc	N-Acetylglucosamine
HAp	Hydroxyapatite
HDPE	High dense polyethylene
IR	Infrared
MALSD	Multiple angle light scattering detector
MALDI-TOF	Matrix assisted laser desorption ionisation –time of flight
MCPA	Monocalcium phosphate anhydrous
Max	Maximum
Min	Minimum
Mod.	Modulus
no. exp.	Number of experiments
NMR	Nuclear magnetic resonance
NCCPs	Noncrystalline calcium phosphates
OCP	Octacalcium phosphate
OM	Optical microscopy
OxHAp	Oxyapatite
PE	Polyethylene
PLA	Polylactide
PHE	Polyhydroxyesters
PS	Polysulphone
SEM	Scanning electron microscopy
S_c	Shrinking coefficient
S.D.	Standard deviation
TEM	Transmission electron microscopy
α-TCP	α - tricalcium phosphate
β-TCP	β - tricalcium phosphate
TGA	Thermogravimetric analysis
TTCP	Tetracalcium phosphate
UV-VIS	Ultraviolet visible
XRD	X-ray diffraction
YD	Yield of degradation
Yld. Str.	Yield at stress
v	Volume
wt	Weight

Table of Contents

1 Introduction

The development of new biomaterials for different engineering applications has been focused recently on the design of the so called bio-inspired or biomimetic materials. Substantial research is being carried out at present in this field, due to its large application area. Examples of highly ordered, structured materials that are made from different constituents are ubiquitous in nature. Wood, shells of marine molluscs, exoskeleton of insects, dentine and bone are few examples of highly complex materials produced in nature. A common facet of natural materials is that they contain different components in a very well organized defined structure over several length scale levels[1]. Thus, both the composition and the structure are responsible for the micro- and macroscopic properties. The fabrication of new biomaterials using biomimetic approaches gives the possibility to control the architecture (the structure) and the chemistry (the composition) of developed biomaterials. These types of biomaterials actually, should give very specific cellular responses that lead to the formation of new tissue mediated by biomolecular recognition signals. For example, the composites used as bone replacement materials should permit the attachment of osteoblast cells due to some apatite or/ and carbonate apatite layers but do not allow the attachment of blood cells[2, 3]. The notion of bio-inspiration, is using biological concepts, solutions, mechanisms, functions and design features which are abstracted as starting points for the new approaches of producing synthetic materials with high ordered structures and very specific properties[4]. The aim is not to try reproducing a particular biological function or structure, but to use such knowledge as a source of guiding principles and ideas. The tissue-engineering application is a research area that deals with the design, development and production of biomaterials that can be implanted inside of the body as artificial organs or/and to help in healing processes of a wounded organ. Many of these tissue-engineering applications use polymer composite materials. In order to fabricate artificial biomaterials, the main idea[5] in biomimetic and/or biologically inspired approaches is to produce nanocrystallites of inorganic biological compounds dispersed in the polymer matrices.

The natural polymers[6, 7, 8] or their derivatives, are increasingly used as an alternative to synthetic polymers because of their biodegradability and biological activity. Based on the above considerations, this project proposes the development, production and characterization of new composite materials, containing chitosan as the polymer matrix. Chitosan is the main derivative of chitin, a natural abundant biopolymer being a biodegradable and environmentally friendly material. The decreasing costs of chitosan, associated with its properties, make it very attractive for various applications.

2 Aim of the Project

2.1 Statement of Hypotheses

Biomaterials containing calcium phosphates, *CPs*, ceramics and particularly those based on hydroxyapatite, *HAp,* exhibit excellent biological activities[9]. Unfortunately, beside this excellent bioactivity some problems are raised in using the *CPs* bioceramics for biomedical purposes. They present a slower resorption rate *in vivo* compared to the rate of new bone formation. The crystalline features[9] of *CPs* bioceramics are the cause of the slow rate of resorption. The brittleness due to their crystallinity is an additional problem. One solution to increase the resorption rate '*in vivo'* of *CPs* bioceramics is to decrease their particle size and hence their degree of crystallinity. The use of only nanoparticles of *CPs* to fabricate biomaterials raises mechanical problems; these materials become very brittle[10]. The solution might be the incorporation of *CPs* nanoparticles in polymer matrices as composite biomaterials. It is expected that the mechanical properties of the composite to combine the stiffness of polymers with the hardness of *CPs* fillers.

Composite materials composed of a polymer matrix and inorganic fillers such as bone, dentine (collagen and apatite), shell of crustaceans (chitin, proteins and calcium carbonate), shell of eggs (glycoproteins and calcium carbonate) having either role of protection, mechanical support or cutting are just some examples from nature. Taking inspiration from natural materials, we try to mimic such composite biomaterials using chitosan as the polymeric matrix and *HAp* as the inorganic phase. The idea to use chitosan is supported by several factors such as it is biocompatible, biodegradable, bioactive by its biodegradation oligomers. Moreover, it can be easy obtained from chitin. Chitosan in solid form shows strong polymeric chain interactions through the hydrogen bonds while in acidic solution abundant positive charges along the chain are formed. In solution, chitosan exhibits different conformations[11] with respect to solution parameters (pH, ionic strength, temperature, etc). Both chitosan and *HAp* are soluble in acidic media, but insoluble in neutral and alkaline media. Based on these considerations, the possibility to co-precipitate a composite material either in neutral or basic media is feasible. Due to the high charge density of chitosan in solution, a strong interaction with the precursory salts of *HAp* is expected to take place. Our interest is to see how stepwise co-precipitation method can be established in order to control the entire precipitation process. At present, only a few approaches to obtain *chitosan/CPs* composite materials are described in literature, being based either on mixing, co-precipitation methods or employing the mineralization of chitosan in solid forms (especially as membranes or scaffolds) in simulated body fluids[12], *SBF*. Yamaguchi *et al.*[13] have developed one step co-

precipitation method that lead to *chitosan/HAp* composites. In this approach the pH of the system jumps from 1÷2 instantaneously to 13÷14 (pH of calcium hydroxide aqueous suspension). Consequently, the formed composite has probably a heterogeneous structure. The mixing approaches[14, 15] are based on the mixing of a chitosan solution with different *CPs* fillers followed by their co-precipitation as composite. Our belief is that a stepwise co-precipitation method might achieve a higher degree of structural organization in the composite compared to the methods discussed above. The possibility to produce different types of composites, such as *chitosan*/*brushite* and/or *chitosan/ACPs* can be reached via this approach. Also, of interest is the production of *chitosan/HAp* composites containing several bioactive cations at trace levels (μg/g composite). The idea is supported that some cations are frequently involved in biological enzymatic processes, particularly in bone formation, and therefore might improve the bioactivity of the composite materials. Cations such as Zn^{2+}, Cu^{2+} and Mn^{2+} are considered to be complexed to chitosan before the co-precipitation of composites. Mn^{2+} is the cofactor[16] for a group of glucosyl-transpherases enzymes involved in mucopolysaccharide synthesis and implicitly in the new bone formation. A diminished level of Zn^{2+} in body from the normal limits affects the growth rate of young organisms, inducing a decreased bone mineralization[17] processes. In many studies about the role of mineral traces in osteoporosis, Saltman *et al.* [18] have showed that Cu^{2+}, Mn^{2+} and Zn^{2+} have an important role in mineralization processes of bone. Strause *et al.*[19] have proposed treatments with *CPs* and minerals for remineralization of bone accompanied with some other biologically active substances, in principal hormones and bone morphogenic proteins, *BMPs*.

2.2 Targets of the project

The goals of the project consist of two main points as presented below.

- *The development of a stepwise co-precipitation method in order to obtain composite materials containing chitosan or/and chitosan derivatives and bioactive calcium phosphate compounds, CPs, (mainly HAp) for bone repair purposes.*

- *Physicochemical characterizations of composites with respect to their composition, structure, and properties will be achieved. Various analytical methods and techniques such as thermo-gravimetric analysis, TGA, FT-IR spectroscopy, Raman spectroscopy, NMR spectroscopy, optical microscopy, OM, scanning electron microscopy, SEM, transmission electron microscopy, TEM, confocal scanning laser microscopy, CSLM, XRD, partial enzymatic degradation tests, mechanical tests, will be involved. A wide range of analytical methods must be employed to investigate the composite samples since each of these methods has its own limitations and therefore it is necessary to combine all results to obtain a comprehensive view.*

3 Literature Review

In this section , the practical and theoretical aspects of the following points are discussed.

i) *chitin and chitosan production, properties and some application area;*
ii) *biologically relevant CPs compounds;*
iii) *bone structure and properties as a reference for providing the qualitative and quantitative prameters for the fabrication of bone replacement materials;*
iv) *economical aspects about the ortopaedic market;*
v) *bone grafts and composite materials as bone substitute materials, present status;*

3.1 Chitin and Chitosan

Polysaccharides[20] are natural polymers consisting of a large number of monosaccharide residues linked together. In the case of polysaccharides that contain a substantial proportion of amino sugar residues, the term glycosaminoglycans or aminoglycans is often used. It is not possible to attribute one distinct molecular weight for polysaccharides, since they are polydisperse. Therefore, they are characterized by an average molecular weight. The number of monosaccharide units (residues) in a polysaccharide is termed the degree of polymerization*, DP*. Polysaccharides occur in an enormous structural diversity[21] as they are produced by a great variety of species, including microbes, algae, fungi, plants and animals. The most well known polysaccharides are cellulose, chitin, chitosan, starch and glycogen.

3.1.1 Occurrence, structure and properties

Chitin is an abundant[22] biopolymer on earth and like cellulose, is a renewable material. Chitin occurs most abundantly in the shells of crustaceans, which are the main source of production, but also in insect exoskeletons, in fungi, in yeasts, etc. However, on industrial scale, chitosan is primarily produced from the processing of chitin. Neither chitin nor chitosan[23] are homopolymers since both of them are composed of the same monomers, *N*-acetyl-2-amino-2-deoxy-D-glucopyranose and 2-amino-2-deoxy-D-glucopyranose units, which are linked through β-D (1→4) glycosidic bonds. In chitin, the predominant units are *N*-acetyl-2-amino-2-deoxy-D-glucopyranose while chitosan has a greater content of 2-amino-2-deoxy-D-glucopyranose units. Both chitin and chitosan are linear co-polymers. The criterion proposed to distinguish between chitin and chitosan refers to their solubility in acidic aqueous solutions. Chitosan is soluble in dilute acidic aqueous solution (except aqueous sulphuric acid solutions), while chitin is not[24]. The chemical structure of chitin and chitosan compared to some natural related polysaccharides are shown in *Figure 3.1.1*. These polysaccharides

contain β-D (1→4) glycosidic bonds, except hyaluronic acid, which contains β-D (1→3) and β-D (1→4) glycosidic bond.

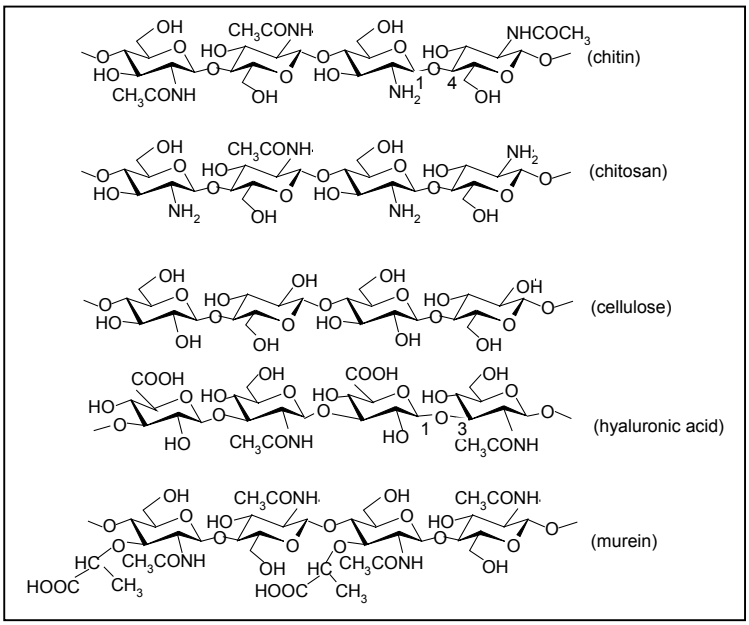

Figure 3.1.1 Chemical structure of chitin and chitosan compared to those of structurally similar type of polymers such cellulose and murein and to a non-similar polymer, hyaluronic acid.

Chitin occurs in three forms[25], denominated *α, β,* and *γ*- chitin. *α*-Chitin, obtained from the shells of crustaceans, shows a compact structure and exhibits the orthorhombic crystalline form with the polymer chains arranged anti-parallel. *β*-Chitin, obtained from squid pens, is monoclinic with the polymer chains arranged parallel. γ- Chitin combines the structural features of the first two types of chitin, having two pairs of chains in a parallel orientation that oppose each other. In aqueous acidic solution, chitosan can adopt several conformations[26, 27], such as sphere-like, random coil or rod-like structures. The properties of chitin and chitosan include polycation formation, the ability to form films and the potential to chelate metal ions. Both chitin and chitosan can be functionalized and transformed into derivatives[28]. Chitin is more hydrophobic[28] than chitosan due to its higher content of acetylated amino groups. Chitin is insoluble in water and in most common organic solvents. However, in certain conditions, a water-soluble form of chitin can be obtained. Chitin is soluble in highly halogenated organic solvents, as well as in certain solvent systems that contain dimethylacetamide with lithium chloride[29]. The deacetylation of chitin[30] can be performed either in heterogeneous or in homogenous conditions using highly concentrated alkaline solutions. Chitosan, the deacetylated product of chitin, is soluble[31] in dilute aqueous acidic solutions (acetic, hydrochloric, citric, malic, formic acids). Chitosan becomes a

polycation in aqueous acidic solutions and it forms polyelectrolyte complexes with polyanions[32]. Chitosan derivatives are easily obtained. A few types of derivatives are exemplified. Hydroxyalkyl chitosans[33] are obtained in reactions of chitosan with epoxides. As a function of reaction conditions, the functionalization might take place either at the amino groups or at hydroxyl groups, giving N-hydroxyalkyl- or O-hydroxyalkyl chitosan derivatives, respectively. Quaternary chitosan ammonium salts[34] can be produced following either the substitution or the addition reaction routes. Chitosan permits the typical reactions of amines, of which *N*-acylation and the Schiff reaction are the most important ones[35].

3.1.2 Methods of preparation of chitin and chitosan

Recently, different procedures for the preparation of chitin and chitosan have been proposed and developed[36]. Each of them is adapted to the raw materials source that is used. In natural form, chitin occurs as a complex composite material (with $CaCO_3$ and associated with proteins, carotenoids, etc). One attractive approach to produce chitin from crustacean shells is a biotechnological method using lactic acidic fermentation[37]. The classical procedure to manufacture chitin[38] requires three main steps as deproteinization, demineralization and decoloration. Chitosan is obtained from chitin through *N*-deacetylation reaction[39]. The amide bond from acetylated amine residues along the chitin chain is difficult to hydrolyze by comparison with other carbonyl-containing groups (e.g. esters). Consequently, this process is carried out at temperatures higher than 70°C (in many approaches the temperature is about 100°C) using concentrated aqueous alkali solutions (NaOH or KOH) at concentrations of 40-50% (wt/wt). Chitosan properties depend on a number of process parameters[36], such as concentration of alkali, mass ratio between the solid base and chitin, deacetylation reaction time, type of chitin used as a raw material, particle size of chitin, method of deacetylation and reaction atmosphere.

3.1.3 Physicochemical characterization of chitosan

Since chitin and chitosan are not monodisperse, an average of molecular weight as well as of the degree of deacetylation*, DD,* are measured[40, 41, 42]. It should be mentioned that, besides *DD*, there are other ways to express the ratio between *GlcN* and *GlcNAc* residues from the polymer structure such as the degree of acetylation, *DA*, and the mol fraction of *N*-acetylglucosamine units, F_A. The structural parameter expressed either as *DD, DA* or F_A has a strong effect on chitosan properties; therefore its determination is imperative. In order to

determine the *DD*, multiple approaches, including *UV-VIS* spectroscopy, first derivative of *UV* spectrometry[43], ^{1}H-*NMR* spectroscopy[44], ^{13}C solid state *NMR*[45], *IR* spectroscopy[46] methods, have been utilized and reported in the literature.

In the case of the molecular weight of chitosan the number-average, the weight-average or the viscosity- average molecular weight (M_n, M_w and M_v, respectively) are used. For random polymer distributions, the average molecular weight increases in the following order $M_n < M_v < M_w$. The polydispersity index is given by the ratio M_w/M_n[47]. The average molecular weight of chitosan using viscometry, a simple and a rapid method, can be easily determined. Unfortunately, this method does not provide the absolute values of molecular weight. In order to obtain the molecular weight distribution, gel permeation chromatography[42], *GPC*, coupled with a multiple-angle light scattering detector, *MALSD*, must be performed.

3.1.4 Applications of chitosan and chitosan derivatives

Chitosan and its derivatives are applied in fields like cosmetics[48], in wastewater treatment[49], to produce fibers[50] and films[51], for different purposes in surgery[52], or in the food industry[53]. A number of degradable polymers including chitosan as a natural polymer are used for drug-delivery purposes[54-57]. In order to fabricate biomaterials for bone tissue repair purposes, Muzzarelli *et al.* have studied chitosan derivatives such as imidasolchitosan[58], *N*, *N* –dicarboxymethylchitosan[59] and 6-oxychitin[60]. The *in vivo* and *in vitro* studies have demonstrated the osteoinductive and osteogenetic capacity of chitosan derivatives. Klokkevold *et al.*[61] have evaluated *in vitro* effect of chitosan on osteoblast differentiation as well as on bone formation. The results of these experiments suggested that chitosan promotes the differentiation of osteoprogenitor cells and facilitates the formation of new bone.

3.2 Calcium Phosphates (*CPs*), biologically relevant compounds

3.2.1 Occurrence, types and properties

Calcium phosphates, *CPs,* are the most important inorganic constituents of biological hard tissues[62]. They are present in bone, teeth, dentine and cartilage mainly as hydroxyapatite, *HAp*. Besides *HAp*, other *CPs* like carbonated apatite, *CHAp*, octacalcium phosphate, *OCP* amorphous calcium phosphate, *ACPs*, and dicalcium phosphate dihydrate, *DCPD*, have been identified in biological tissues. These compounds have shown to support osteoblastic adhesion and proliferation[9]**.** *CPs* based biomaterials made of the combination and processing

of these materials are brittle. For this reason, these materials are used primarily as fillers and/or as coating materials. The proposed mechanism of *CPs* integration into bone tissue is through an initial process of dissolution and resorption, followed by a subsequent precipitation of a carbonate-substituted calcium deficient biological apatite[63].

Table 3.2.1 Summary of the natural occurrence of CPs compounds in living tissues[63].

MINERAL	FORMULA	ORGANISM	LOCATION	FUNCTION
Hydroxyapatite	$Ca_{10}(PO_4)_6(OH)_2$	Vertebrates	Bone	Endoskeleton
		Mammals	Teeth	Cutting/grinding
		Fish	Scales	Protection
Octacalcium phosphate	$Ca_8H_2(PO_4)_6$	Vertebrates	Bone/teeth	Precursor phase
Amorphous Calcium phosphate; **variable**		Chitons	Teeth	Precursor phase
		Gastropods	Gizzard plates	Crushing
		Bivalves	Gills	Ion store
		Mammals	Mitochondria	Ion store
		Mammals	Milk	Ion store

The occurrence of *CPs* biominerals in living tissues is shown in *Table 3.2.1*. *CPs* compounds can be broadly classified into two categories according to the fabrication method[64]. The first group contains *CPs* obtained by sintering method in the $CaO\text{-}P_2O_5\text{-}H_2O$ system at temperatures ranging from 500°C up to 1500°C. The second category can be obtained through precipitation from saturated solution at room temperature.

CPs family includes the following compounds[64].

- ***Monocalcium phosphate anhydrous***, *MCPA*, Ca $(H_2PO_4)_2$, is a highly soluble and acidic *CPs*. Due to its strongly acidic properties, it is incompatible with and nonexistent in an '*in vivo'* environment (pH 7-7.4).
- ***Dicalcium phosphate anhydrous***, $CaHPO_4$, and ***dicalcium phosphate dihydrate, (brushite),*** $CaHPO_4{\cdot}2H_2O$, (*DCPA, DCPD*). Both are biocompatible, biodegradable, and osteoconductive materials. *DCPD* is a metastable compound found in fracture calculus and considered a precursor of *HAp* in bone formation.
- ***α-*** and ***β-Tricalcium phosphate***, *α-TCP, β-TCP*, $Ca_3(PO_4)_2$, the two types have the same formula, but different crystallographic structures, with *α-TCP* more degradable than *β-TCP*. Both are widely used as bone substitutes as powders, granules, or blocks.
- ***Octacalcium phosphate***, *OCP*, $Ca_8H_2(PO_4)_6{\cdot}5H_2O$, is a metastable precursor of *HAp* in teeth and bones.
- ***Hydroxyapatite***, *HAp*, $Ca_{10}(PO_4)_6$ $(OH)_2$, is an osteoconductive material, which is the most stable *CPs* at moderately acidic, neutral and basic pH. It is found in bone, dentine and teeth.
- ***Biphasic calcium phosphate***, *BCPs*, is a mixture of *HAp* and *β-TCP*, which makes it more soluble compared to the pure *HAp*.
- ***Tetracalcium phosphate***, *TTCP*, $Ca_4(PO_4)_2O$, is the most basic and soluble *CPs* below pH 5. *TTCP* is biocompatible, but poorly biodegradable.
- ***Oxyapatite,*** *OxHAp*, $Ca_{10}(PO_4)_6O$, is a decomposition product of *HAp*.
- ***Calcium-deficient hydroxyapatite***, *CDHAp*, $Ca_{10\text{-}x}(HPO_4)_x(PO_4)_{6\text{-}x}(OH)_{2\text{-}x}$, is similar to bone mineral but lacking the ionic substitutions. *CDHAp* is a poorly crystalline material

with a Ca/P ratio varying between 1.5 and 1.67; it is the main product of many *CPs* based cements.

- ***Amorphous calcium phosphate***, *ACP*, has various compositions, being especially *'in vivo'* involved in the biochemical transformations of *CPs* phases towards *HAp*.

Some relevant properties of *CPs* compounds are comprises in *Table A-I-1* from *Appendix A-I.*

3.2.2 Solubility diagrams of *CPs*. Thermodynamic driving force

The precipitation of a mineral from its aqueous solution occurs when the solution becomes supersaturated with that compound at a particular pH. Dissolution of a compound takes place when the surrounding aqueous environment is unsaturated with respect to that compound[65]. The driving forces that control the dissolution and precipitation reactions are related to the levels of super- or sub-saturation defined with regard to the thermodynamic solubility constants[66]. The equilibrium reaction for a simple system, *AX*, can be represented by

$$AX\ (s) \leftrightarrow A^{n+} + X^{n-}\ (aq), \qquad (\textbf{3.2.2-1})$$

where (s) indicates solid and (aq) aqueous states, respectively. A variation in Gibbs free enthalpy, ΔG, in the system described in *Equation 3.2.2-1* is given by

$$\frac{\Delta G}{RT} = \frac{\mu^0_{A,aq} + \mu^0_{X,aq} - \mu_{AX,s}}{RT} + \ln I_P^{AX}, \qquad (\textbf{3.2.2-2})$$

where μ^0 is the standard molar Gibbs free enthalpy (so called standard chemical potential), $\mu_{AX,s}$ is the Gibbs free enthalpy of the solid compound *AX*, *R* is the ideal gas constant, *T* is the absolute temperature, and I_p^{AX} is the ionic activity product of compound *AX*.

The ionic activity product is calculated by

$$I_p^{AX} = \left(A^{n+}\right)\left(X^{n-}\right), \qquad (\textbf{3.2.2-3})$$

where (A^{n+}) and (X^{n-}) are molar concentrations of cation and anion, respectively.

In the state of equilibrium $\Delta G=0$; *Equation 3.2.2-2* becomes

$$\frac{\mu^0_{A,aq} + \mu^0_{X,aq} - \mu_{AX,s}}{RT} = -\ln I_P^{AX} = \ln K_{sp}^{AX}. \qquad (\textbf{3.2.2-4})$$

The last term of the above relationship contains the solubility product, K_{sp}^{AX}, of the compound *AX.* Based on this consideration, *Equation 3.2.2-2* can be rewritten as follows,

$$\frac{\Delta G}{RT} = \ln \frac{I_p^{AX}}{K_{sp}^{AX}} = \ln S, \qquad (\textbf{3.2.2-5})$$

where S is the thermodynamic saturation level. With respect to the parameter *S*, the evolution of the system can be discussed. When *S* is less than unity, the solution is sub-saturated and *ΔG* is negative. The result is that the driving forces favor the product on the right side of the *Equation 3.2.2-1*, and the solid is dissolved. If *S* exceeds unity, the solution will be super-saturated and *ΔG* is positive. The driving force will move to the left (according to *Equation 3.2.2-1*) and the solid compound, *AX*, is precipitated[67]. These basic concepts are useful in understanding the solubility properties of *CPs* compounds in aqueous systems as a function of pH. The solubility diagrams in a ternary system of ***$Ca(OH)_2$-H_3PO_4-H_2O*** at 37°C, in a graphical representation of log [Ca^{2+}] against pH are presented in *Figure 3.2.1*. The concentration of [Ca^{2+}] is expressed in mol/L. A common feature of these isotherms is that they show a negative slope in acidic, neutral and moderately basic (up to 10) pH ranges. Above pH 10, all compounds exhibit positive slopes. At a given pH value, a *CPs* salt, whose isotherm lies below the others is relatively less soluble[68] (thermodynamically more stable). Based on these considerations some useful conclusions can be deduced. *HAp* is the least soluble over a wide range of pH[69]. When the pH is decreased below 4.2, *DCP* becomes the least soluble *CPs* compound. At physiological pH of 7.04, the solubility of various *CPs* is in the following order ***TTCP>α-TCP>DCPD>DCP>OCP>β-TCP>HAp***[70] .

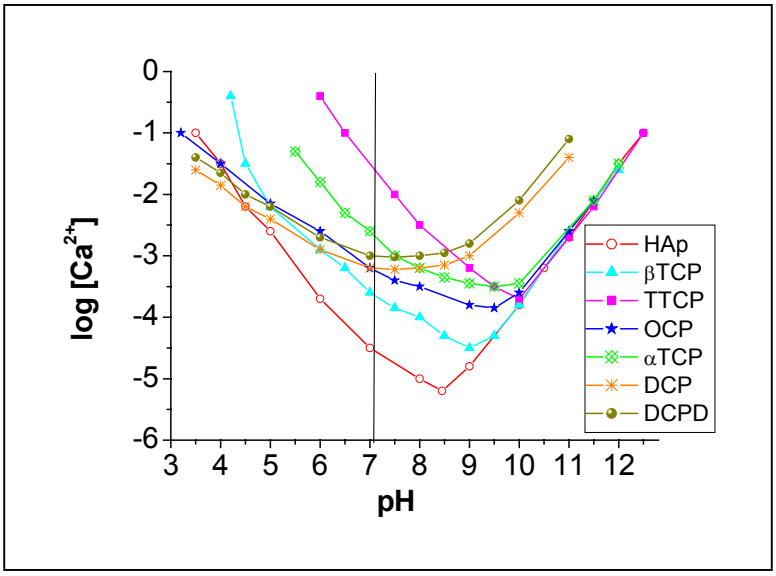

Figure 3.2.1 Solubility isotherms of CPs compounds in equilibrium with the their ions in solution at 37°C, in a representation of log [Ca^{2+}] against pH. Concentration of [Ca^{2+}] is expressed in mol/L. The vertical line shows the physiological pH.

3.3 Bone as natural biocomposite

As natural composite, bone exhibits a complex organization[71] with an anisotropic structure. Of a particular interest, is continuous remodeling. Being permanently colonized by both osteoblasts and osteoclast cells, bone should be considered and treated as a living tissue. The design and fabrication of bone substitute materials requires knowledge of physical, chemical, biochemical and mechanical properties of bone tissues, because they provide quantitative parameters necessary for the fabrication of bone replacement implants.

3.3.1 Structure of bone

The term ''bone'' refers to a family of materials, which are built up of mineralized collagen fibrils. Bone as a material is difficult to analyze due to its high level of organization (over several length scales). Chemically speaking, the main constituents of bone are collagen (about 20%), calcium phosphates phases, mainly *HAp* 70% and water 10%. The remaining 1% consists of other organic materials such as proteins, polysaccharides and lipids[72]. The organic matrix not only gives bone its toughness but also contains the osteoinductive and growth factors necessary for continual bone growth and repair. When the mineral component of bone is removed, the organic matrix and osteoinductive factors can be isolated[73]. From demineralised bone, bone morphogenic proteins, *BMP*, can also be isolated. The structure of bone can be seen in *Figure 3.3.1*.

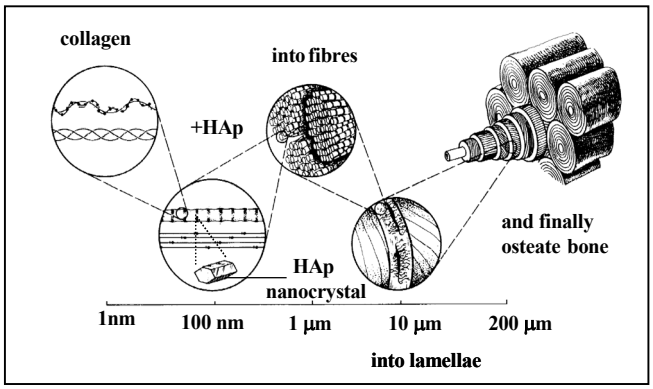

Figure 3.3.1 Hierarchy of bone [71]

Collagen is the polymer matrix organized in the form of a triple helix at the smallest stage, then in micro-fibers on a more macroscopic scale. The diameter of collagen fibers varies from 0.05 μm up to 2 μm. The *HAp* crystallites in a plate-like shape are packed along the polymer chains, being deposited in a parallel orientation and having a laterally shifted

position with respect to the previous row. Normally, *HAp* crystallites are 20-40 nm long, 20 nm wide, and 1.5-5 nm thick[74].

3.3.2 Natural formation of bone

Bone is the habitat of four different cell types[73]; osteoprogenitor cells, osteoblasts, osteocytes, and osteoclasts. Osteoprogenitor cells are the mesenchymal stem cells for bone. They remain in small numbers in fully formed bone and differentiate to form osteoblasts. Osteoblasts are the cells responsible for the production of new bone matrix during osteogenesis. Osteocytes are mature bone cells that make up the majority of cells in bone. Osteoclasts are responsible for bone resorption, the process of breaking down old bone matrix. Osteoblasts and osteoclasts work in balance, resorbing and forming bone simultaneously, to maintain healthy bone tissue. Bone tissue is continuously remodeled. Osteogenesis is the process by which new bone matrix is formed.

Mature bone occurs in two forms: compact or cortical (dense) and cancellous (spongy). Compact bone is highly vascularized and so, housed within every central canal is at least one blood vessel. Osteons adapt to the mechanical functions of bone by elongating along lines of stress and increasing the strength of bone along these lines. Spongy bone, found in the interior of compact bone, contains neither osteons nor blood vessels. It shows low density and an open and interconnected porous structure. It is developed in regions of low stress.

3.3.3 Mechanical properties of bone

The anisotropic structure means directionality. This directionality results from the fact that bone has evolved to be both tough and stiff. There are two opposing properties which are optimized in bone structure. Bone is both viscoelastic and semi -brittle. The load region profiles are a function of the strain rate as shown in *Figure 3.3.2*. At high strain rate, the compact bone behaves like a brittle ceramic. Conversely, at low strain rate, the response of bone shows great toughness (the area below the load curve), mostly due to its hierarchical structure that stops cracks deflection after a minimal propagation[75, 76]. The main toughening mechanism seems to be the formation of micro-cracks, which appear in the plastic region of the stress-strain curve. The mechanical properties of bone depend on a lot of parameters[76, 77, 78], such as the type of bone, compact or cancellous, density, moisture, mode of applied load, direction of applied load, type of bone.

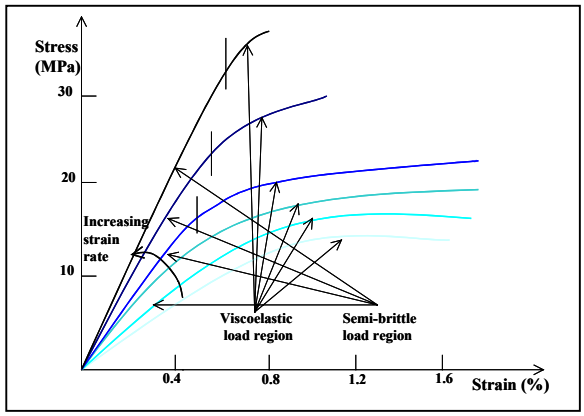

Figure 3.3.2 Load deflection curves for human compact bone according to Park[77].

The mechanical performance of human bone is summarized in *Table 3.3.1*.

Table 3.3.1 Summary of mechanical properties of human bone.

	Compact bone Test direction related to bone axis (to the long axis) Parallel	Normal (perpendicular)	Cancellous bone	Reference
Compressive strength (MPa)	130-224	133	5-10	[76, 77]
Tensile Strength (MPa)	124-174	50	-	[76,77]
Young's modulus (GPa)	17-20	11.5	0.05-0.1	[75-79]

3.4 Bone grafting materials

Due to a variety of diseases and injuries or a lack of stress, loading response in bones can be skewed. Bone can regenerate by repairing defects up to a certain size and can form new tissue. If the defect is too large, a surgeon has to intervene and fill up the defect with suitable materials[80]. The mechanical stability of bone is thereby affected, potentially leading to subsequent fracture. There are several possibilities of correcting bone defects by grafting[81]. The biochemistry of bone grafts and bone substitutes is treated from an understanding of bone formation processes of osteogenesis, osteoinduction and osteoconduction.

i) ***Graft Osteogenesis****- The cellular elements within a donor graft survive transplantation and synthesize new bone at the recipient site.*

ii) ***Graft Osteoinduction****- New bone is realized through the active recruitment of host mesenchymal stem cells from the surrounding tissue, which differentiate into bone-forming osteoblasts. This process is facilitated by the presence of growth factors within the graft; principally bone morphogenetic proteins*[82] *(BMPs).*

iii) ***Graft Osteoconduction****- Both blood vessel incursion and new bone formation into a defined structure is facilitated.*

All bone grafting (as bone based materials) and as well as the artificial bone-graft-substitute materials are so far characterized through these processes. Besides them, there are some

others, for example the biodegradation rate of the graft. The materials used in bone grafting can be broadly divided into autografts, allografts, xenografts, synthetic bone substitutes and combinations of these.

3.4.1 Autograft

Autogenous bone[83], which is taken preferably from the iliac crest of the patient, has the best biological properties to fill up the defects of bone. However, the additional operation at the iliac crest causes, in up to 20% of the cases, undesirable side effects like pain, haematomas and infections at the operation site. Unfortunately, the amount of autograft is limited and, consequently, some other sources of bone grafts must be involved.

3.4.2 Allograft

Allograft is a bone piece from a human donor[84], available from the bone bank of the hospital or bought from a commercial supplier. Allografts can be processed in various ways for long-term preservation. Freezing and freeze-drying reduce the immunoresponse. Unfortunately, after these operations the mechanical strength is decreased. Allogenic bone does not possess the desirable biological properties of autogenous bone and additionally, it introduces the risk of transmission of diseases. Autogenous grafting has been shown to be superior to allografting in many cases with respect to the remodeling and bone healing time.

3.4.3 Animal bone/Xenograft

The use of xenogenic transplants[85, 86] (mostly untreated animal bone) has the main disadvantage of strong immunological reactions of the human recipient towards the transplant due to its foreign proteins, besides the risk of the transmission of pathogens.

3.4.4 Orthopedic market

The declaration of the next 10 years as the international Bone and Joint Decade[87], 2000-2010, has as impact a strong investment in orthopedic materials research area. Thus, in the near future new competitive biomaterials are expected to come onto the market.

3 Literature Review

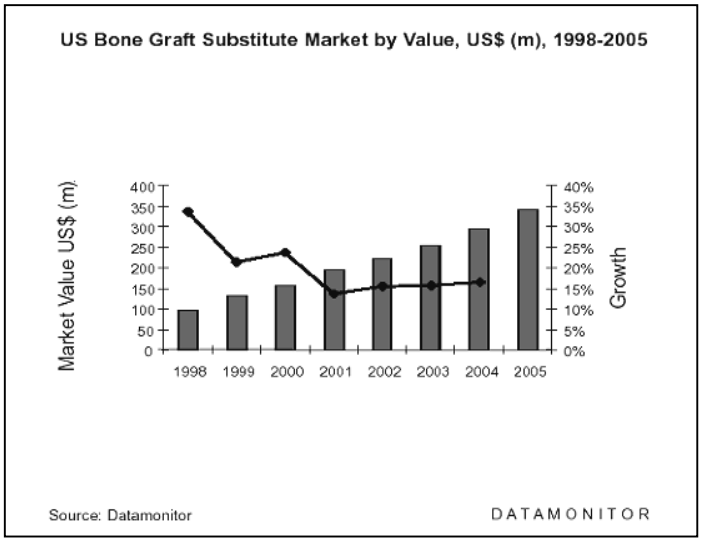

Figure 3.4.1 Evolution in time for the US Bone graft substitute Market since 1998, with some previsions until 2005.

European bone-graft procedures are currently dominated by autografts and allografts. Synthetic bone-graft substitutes currently account for only 10% of such procedures, but their market share may rise dramatically, according to a report published by Datamonitor -London. According to Datamonitor's[87], synthetic bone-graft substitutes could attain an average annual growth rate of 42% and capture US$ 73.8 M value in the European market by 2003.

In US and Japan, the situation is different from the European Union. The US bone graft substitutes market[88] grew by 23.5% in 2001, reaching a market value of $194 M. The market is forecasted to attain a value of $342 M in 2005 presenting an increase of 76.4% since 2001, as shown in *Figure 3.4.1*. The allografts are not more than one-third from the total sales volume during recent years[89], (*Figure 3.4.2*). A sketch of the global orthopaedic market sector since 1999 is shown, alongside predictions (*Figure 3.4.3*). The proportions between different types of required implants are also represented. The top three places are occupied by knee, hip, and spinal implants. Trauma devices occupy the fourth place. Consequently, many companies develop new bone graft substitute products and improve the existing products.

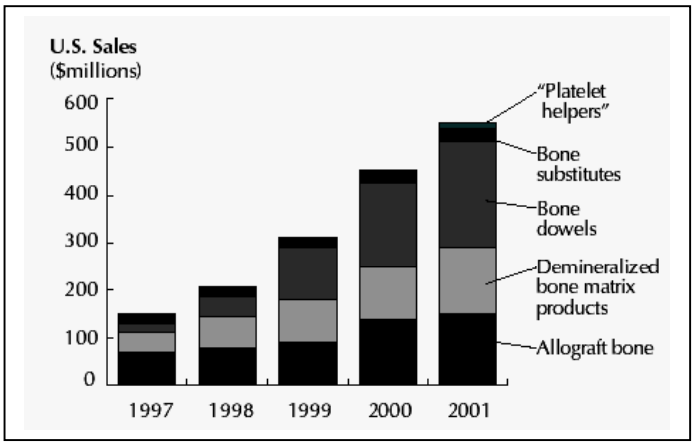

Figure 3.4.2 US sales for different orthopaedic materials during a period of five years, starting from 1997.

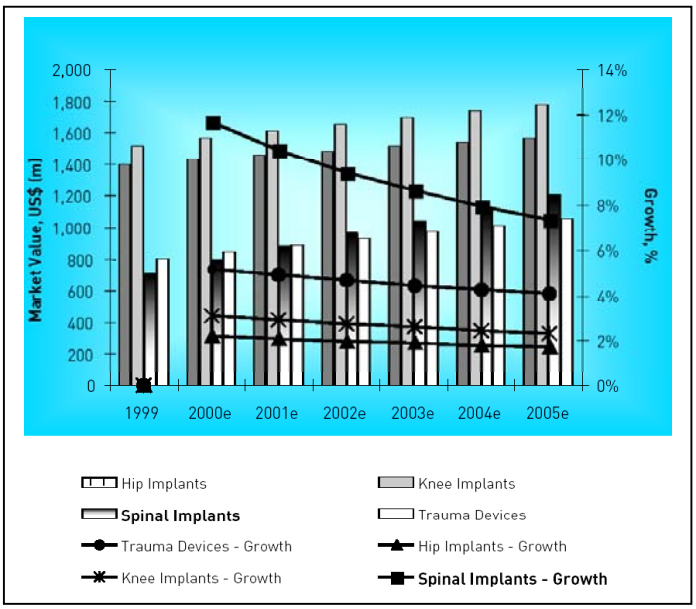

Figure 3.4.3 Global Orthopedic Market[87] Value by Report, US$ (m) and growth, %, 1999-2005.

Market growth is expected to be driven by the incorporation of innovative technologies (such as bone morphogenic proteins and other growth factors) into novel and existing bone graft substitute products.

3.5 Artificial bone substitute materials

Artificial bone substitute material[86] is defined as a biomaterial not contained in, or derived from, the body. After implantation, these materials substitute for structural elements, tissues and their functions or parts of their functions in the body. The main requirements of these materials are the following.

- *To have a positive influence on the amount and quality of newly formed bone.*
- *To shorten the period of bone formation and healing process.*
- *To develop an implant with improved mechanical load bearing properties.*

The ideal bone substitute must be biocompatible, bioresorbable, osteoconductive, osteoinductive, structurally similar to bone, easy to use and cheap. Substitutes are variable in their composition, their mechanisms of action and their claims of action.

3.5.1 Bioactive ceramics

The use of synthetic compounds that are similar to bone apatite[90] is advantageous for replacing the hard tissue. Hence, there has been a sustained interest over the last 20 years in hydroxyapatite (*HAp*, $Ca_{10}(PO_4)_6(OH)_2$), which resembles bone apatite and is a bioactive bioceramic. *HAp* possesses excellent biocompatibility and is osteoconductive. Another attractive member of the calcium phosphate family, for medical applications, is *TCP*, $Ca_3(PO_4)_2$, which plays an important role as a bioresorbable bioceramic. *TCP* has been used for bone repair in the form of ceramic blocks, granules or calcium phosphate cements. Both *HAp* and *TCP* are brittle and thus, cannot be used as load-bearing implants in the human body.

3.5.2 Composite materials

A composite material consists of two or more mechanically distinct phases (metallic, ceramic, or polymeric) which are separated by interface(s)[91]. Due to their unique features, composite materials consisting of ceramic/polymer, ceramic/ceramic and glass/ceramic are considered most desirable. A composite is designed to have a combination of the best characteristics of each of the component materials. The classification of engineering composite materials is based on the matrix materials (metals, ceramics, and polymers) or on the reinforcement dimensions/shapes (particles, whiskers/short fibers, and continuous fibers).

Classification:

i) Using the material matrix as the basis for their classification[91, 92], there are three types of composites;

- Polymer matrix composites, e.g., *PE/HAp*, chitosan*/HAp*, collagen/*HAp*, etc.
- Metal matrix composites, e.g., Ti / *HAp*, Ti–6Al–4V / *HAp*;
- Ceramic and glass matrix composites, e.g., ceramic or glass based materials.

ii) Using the bioactivity of composites as the basis for their classification[93, 94], there are also three types of composites that can be denominated as follows.

- Bioinert composites, e.g., carbon/carbon fibers.
- Bioactive composites, e.g., stainless steel/Bioglasss, *HAp/HDPE*, etc.
- Bioresorbable composites, e.g., *TCP/PLA*.

3.5.2.1 Ceramic/ceramic and ceramic/glass composites

In order to improve their mechanical properties, such as hardness and fracture toughness, ceramic/ceramic composite materials have been designed and synthesized. *HAp*-reinforced zirconia composites have been studied[95] for their biocompatibility and mechanical properties. Coated porous *HAp* with *β-TCP* has also been reported in the literature[70]. The presence of *TCP* in a *HAp* material increases its biodegradability. Glass-reinforced *HAp* composites[96] with improved flexural bending strength compared to the unmodified *HAp* have been obtained by sintering using P_2O_5 glasses as sintering aid[97].

3.5.2.2 Ceramic/metal composites

The rationale of ceramic/metal biocomposites for implant applications was to combine the excellent mechanical properties of metals with the good biological properties of *CPs* coatings[98]. Ti, Ti-alloys, stainless steel and cobalt chromium alloys are used as metallic substrates. Two methods of coating are currently implemented: plasma spraying and precipitation from saturated solutions. The coating from supersaturated solutions of calcium phosphates does not achieve a strong interfaces between metal and ceramic but allows coating of internal surfaces that are difficult to reach with plasma spraying methods. The thickness of the *HAp* coatings is on the range of 40-200 μm. The coatings must be thick enough to counter the resorbability of *HAp*, which is about 15-30 μm per year[99].

3.5.2.3 Ceramic (*HAp, TCP, ACPs*)/polymer composites

The blending of a polymer with a mineral to give a "*composite*" material[100], which combines the toughness and flexibility of the polymer with the strength and hardness of the mineral filler, has its beginnings in nature. The advantage of such composites was believed to be the enhancement of the osteogenic potential, given by the calcium phosphate compounds and by the binder characteristic of the polymer matrix in inhibiting the migration of calcium compounds[101].

a) HAp/Polyethylene composites, PE,

Since 1980, Bonfield *et al.*[102, 103] have developed *HAp/PE* such composites for bone replacement purposes. In order to obtain *HAp/PE* composites, three main technologies were developed.

i) Hydrostatic extrusion
ii) Fiber drawing

iii) Fiber compaction

With increasing the *HAp* content, both Young's modulus and bioactivity of composites increase while the ductility decreases. *HAp/PE* composites exhibit brittle/ductile transition when the *HAp* volume content exceeds 40-45%. Their Young's modulus is in the range of 1-8 GPa. Unfortunately, they are bioactive only through the apatite phase and are not biodegradable. Moreover, the presence of the hydrophobic polyethylene decreases the ability to bind to bone surfaces.

b) HAp/Poly-α-hydroxyesters, PHE,

- Polylactide*, PLLA,* reinforced ceramic composites

A ceramic/polymer composite with polylactide[104, 105], *PLLA*, as polymer phase has been obtained. *PLLA* polymer matrix was found to be biodegradable. The method of production is based on the mixing of *HAp* powder with the monomer (lactic acid) before poly-condensation. Another approach[106, 107] employs solvent casting in which the *PLA* is dissolved prior mixing with *HAp* particles. The aim of this approach is to improve the adhesion forces between polymer matrix and fillers. These composites range between 5 and 12 GPa for the Young's modulus and between 10 and 30 MPa for the tensile strength. Unfortunately, there are several reports concerning the toxicity of the biodegradation products of these composite materials. The developed acidic products change the local pH value into the implant site leading to inflammation processes.

- *Polyglycolide (polyhydroxyacetic acid) reinforced ceramic composites*

Schwarz *et al.*[108] have produced a composite material that mimics the porous structure of bone, as displayed in *Figure 3.5.1*. Sodium chloride was used as porogenous agent.

c) HAp/Polysulfone, PSU,

PSU as biomedical polymer can be used to produce bone substitute materials[109, 110]. *PSU* is an amorphous polymer that is biodegradable, which possesses high specific strength and modulus.

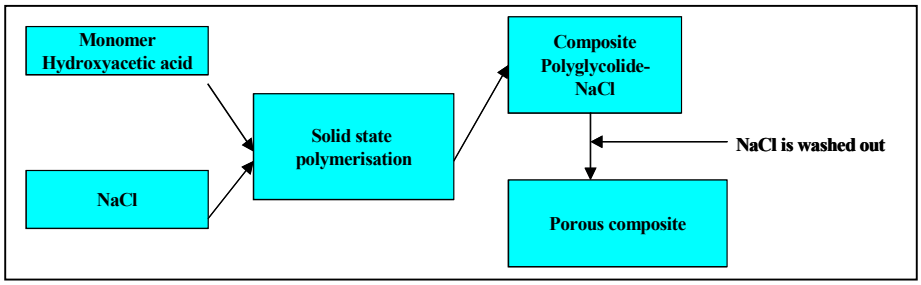

Figure 3.5.1 Sketch of the preparation of a polyglycolide based composite according to Schwartz[108] approach.

To develop bioactive composites for load bearing prostheses, *PSU* may be a better choice for the composite matrix than *PE*. *PSU* can provide a higher level of mechanical properties for composites. Another advantage is that these composites are biodegradable compared to those based on *PE*, which are bioactive but not biodegradable.

d) HAp/Collagen composites

HAp/collagen composite materials are promising candidates for bone replacement purposes because of their resemblance to bone from bioactivity and biodegradability point of view. These composites are similar to natural bone with respect to chemical composition, but they do not show such a complex hierarchical organization as bone. Actually, the key is to produce materials having different organization levels, which can induce specific properties. There are several approaches reported in the literature concerning the *Hap*/collagen production. One method is by mixing *HAp* powder with a collagen solution and hardened by *UV* irradiation[111] or high pressure of about 200 MPa for several days[112]. Another approach deals with the precipitation of *HAp* as nanocrystallites onto collagen fibers[113]. Du *et al.*[114] have reported a simple method to produce *CPs*/collagen composites. By adjusting the reaction conditions and the ratio of components, they prepared several types of *CPs*/collagen composites, such as noncrystalline calcium phosphates, *NCCPs*/collagen, poor crystalline calcium phosphates, *PCCPs*/collagen and *TTCP*/collagen composites. The mechanical properties[115] of these types of composites are still very poor and ranged from 2 to 6.5 MPa for compressive strength and up to 2 GPa for the Young's modulus. *HAp*/collagen nanocomposite was produced by Kikuchi *et al.*[116], using a co-precipitation method, as shown in *Figure 3.5.2*. In spite of their poor mechanical properties, these composites show high osteoconduction and therefore are very promising materials for bone tissue engineering.

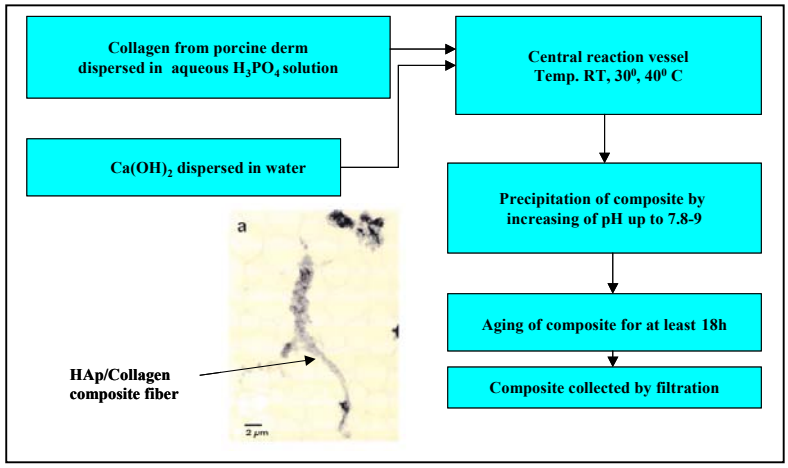

Figure 3.5.2 Sketch of the preparation of a HAp/collagen composite using a co-precipitation method, according to Kikuchi[116]. In the left part, a composite fibre is shown.

The research of this variety of composites is still in an early stage of development.

e) CPs/Gelatine composites

Yaylaoglu *et al.*[117] have developed a *CPs*/gelatine composite implant that mimic the structure and function of bone for filling voids in bone while releasing bioactive compounds like drugs and growth hormone into the implant site to assist in healing. This approach is shown in *Figure 3.5.3*.

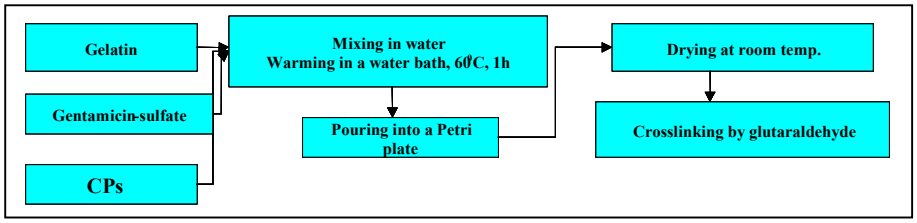

Figure 3.5.3 Sketch of the preparation of a composite containing CPs and gelatine according to Yaylaoglu[117] approach.

f) HAp/Chitin composites

Gea *et al.*[118] have prepared *HAp*/chitin composite materials having *HAp* in a range of 25%, 50% and 75% wt% fractions.

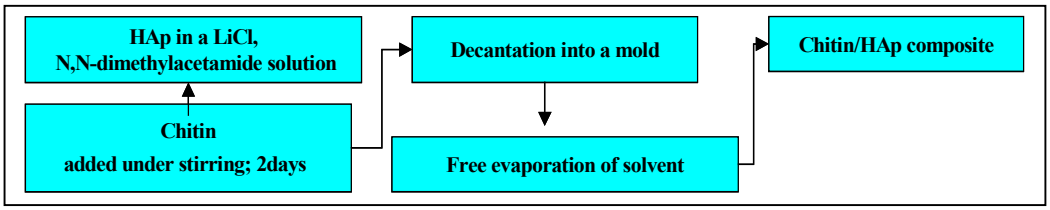

Figure 3.5.4 Sketch of the preparation of a HAp/chitin composite, according to Gea[118] approach.

The *HAp* was incorporated in chitin solutions and air- and freeze-dried. A modified procedure described by Khorb *et al.* [119, 120] was used. The *HAp*/chitin composites were exposed to cell cultures and implanted into the intra-musculature of a rat model. *HAp*/chitin materials were found to be non-cytotoxic and degradable *in vivo*.

g) HAp/Chitosan composites

- *Porous CPs/ nested chitosan sponges*

The procedure for the fabrication of this type of composite was developed by Zhang *et al.* [121]. It was designed to be used for load bearing bone implants. The approach is presented in *Figure 3.5.5*. The macroporous *CPs* bioceramics (as a mixture between *HAp* and *TCP*), with the pore diameters ranging from 300 μm to 600 μm, were prepared using a porogen burnout technique. Chitosan sponges were formed inside the bioceramic pores first

by introducing the chitosan solution into the pores of bioceramic, followed by freeze-drying when porous chitosan scaffolds inside the large pores were obtained.

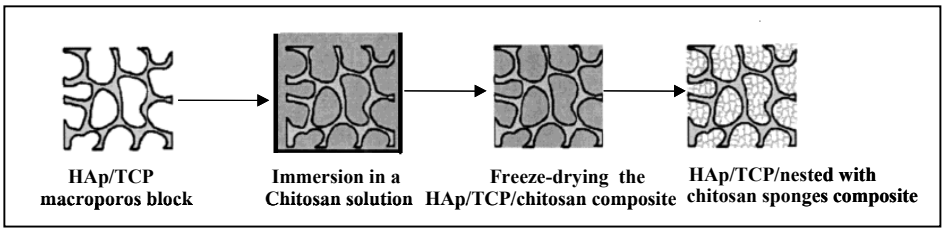

Figure 3.5.5 Simplified sketch of the preparation of a porous CPs/ nested chitosan sponges composite, according to Zhang [121] approach.

•*Chitosan-bound hydroxyapatite as bone-filling paste*

The approach is based on a sol/gel phase transition[122]. Chitosan was dissolved in an aqueous malic acid solution, and a chitosan film was formed by mixing the sol with *HAp* powder, followed by neutralization with sodium polyphosphate.

• *CPs, Invert glass/chitosan composites*

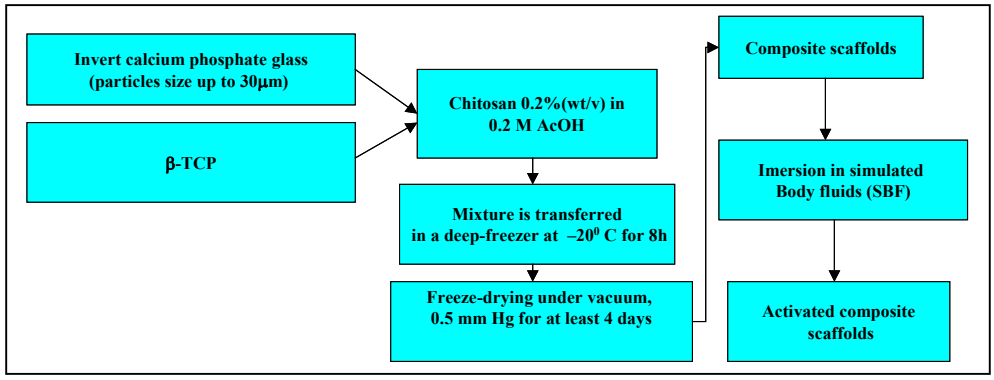

Figure 3.5.6 Sketch of the preparation of a CPs invert glass/ chitosan composite by a mixing method developed by Zhang[123].

Zhang *et al.*[123] have developed a macroporous *chitosan*/*CPs* composite scaffold for tissue engineering by using a mixing method, as shown in *Figure 3.5.6*.

The chemical composition of the invert calcium phosphate glass is 57 % CaO, 28 % P_2O_5, 12.0% TiO_2, and 3.0 % Na_2O. Scaffold materials were found to be biocompatible, biodegradable and osteoconductive allowing to the osteoblast cells to attach and to migrate through the porous structure of the composite.

•*HAp/chitosan nanocomposites*

Yamaguchi *et al.*[124] have prepared *HAp*/*chitosan* nanocomposites by co-precipitation. Briefly, an aqueous chitosan solution of 3 wt% was prepared by dissolving chitosan powder in 1 wt% acetic acid aqueous solution. Then, the chitosan solution was added to an H_3PO_4

solution 8.5 wt%. The ratio of chitosan to H_3PO_4 was adjusted for the final *chitosan/HAp* composition to range from 20/80 wt% to 80/20 wt%. The obtained chitosan/H_3PO_4 solution was added (drop-wise) to a Ca $(OH)_2$ suspension of 0.5 molar with vigorous stirring. The composite was formed in an alkaline media in time.

Ito *et al.*[125] have prepared *chitosan/HAp* membranes; their physical properties and effects *'in vivo'* have been evaluated. A *chitosan*/*HAp* weight ratio of 11:4 was found to give the most appropriate optimal performance of the membrane with respect to shrinkage, tensile properties, hardness, calcium ion release, morphology and adequate *in vivo* performance.

Sunny *et al.*[126] have reported the preparation of *chitosan/HAp* microspheres as potential bone and periodontal filling materials. The *HAp* powder was mixed with a chitosan solution followed by paraffin oil, hexane and a surfactant and the microsphere production process commenced. Subsequently, glutaraldehyde was added to crosslink chitosan, yielding spherical particles ranging from 125 to 1000 μm.

Lee *et al.*[127] have proposed *chitosan/TCP* sponges as tissue engineering scaffolds for bone formation by three- dimensional osteoblast culture.

Viala *et al.*[128, 129] have studied the effect of chitosan on *OCP* crystal growth. Chitosan has a strong effect on *CPs* crystallization. The crystal growth mechanism in the absence and the presence of ions as well as in the presence of organic molecules was studied. They have prepared a *chitosan*/*HAp* composite by mixing the *HAp* powder with a chitosan solution, followed by their precipitation.

A focused review was published by C. Muzzarelli and R.A.A. Muzarelli[130] in which an overview on natural and artificial chitin and chitosan based composite materials is presented.

Summary

The information reviewed in the section of Literature Review is giving the state of the art in chitosan, *CPs*, bone and bone substitute materials. The state of knowlege was used on one side to develop a preparation approach of nanocomposites made of chitosan and *HAp* and on the other side to characterize them, in order to be tested as candidates for bone substitute materials.

4 Materials and Methods

4.1 Materials

4.1.1 Chitin and chitosan samples

a) Krill chitin flakes from *Polymar GmbH;* Bremerhaven*,* a demineralized and deproteinized chitin sample.
M_v = 1,000,000; *DD* = 51.47%, *Ash content* =1.9%

b) Krill chitosan samples; were prepared in our laboratory through the deacetylation of Krill chitin flakes *(a).*

i) Two times deacetylated chitosan*;* M_v=320,000±5% (by viscosimetry); *DD* = 75±3% (by ^{1}H-*NMR*)
ii) Three times deacetylated chitosan*; Mv* = 270,000±5% (by viscosimetry); *DD* = 95±3% (by ^{1}H-*NMR*)

c) Crab chitosan samples purchased from *Sigma Company*

i) *Lot no.91K1265*; M_v = 550,000 ±5% (by viscosimetry) *DD* = 80±3% (by ^{1}H-*NMR*)
ii) *Lot no. 114F-014;* M_v = 510,000 ±5% (by viscosimetry) *DD* = 84±3% (by ^{1}H-*NMR*)

d) Insect chitosan

Prepared by Marcin Struszcyk (August 2000), M_v = 396,000 (by viscosimetry); *DD* = 66.2% (by potentiometric titration)

e) Shrimp chitosan **(**north Atlantic shrimp, *Pandalus borealis*)
delivered by Primex, Iceland.
Batch # TM1238, M_v = 305,000 ± 5%
DD = 87% (by colloidal titration); *DD* = 91% (by ^{1}H-*NMR*)
Ash content = 0.3%

4.1.2 Chemicals

i) Acetic acid glacial *(Acros Organics)*, purity >99%
ii) Sodium hydroxide *(Merck)*, purity 98%
iii) $CuSO_4$ anhydrous *(Sigma)*, purity 99%
iv) $MnCl_2 \bullet 4H_2O$ *(Fluka),* purity 99%
v) $Zn(NO_3)_2 \bullet 2\ H_2O$ *(Sigma)*, purity 99%
vi) $CaCl_2$ dried and $CaCl_2 \bullet 2H_2O$ *(Riedel-deHaën)*, purity 99%
vii) NaH_2PO_4 *(Merck)*, purity 99%
viii) NaCl *(Merck),* purity 99%
ix) $MgSO_4$ *(Riedel- deHaën)*, purity 99.5%
x) $MgCl_2$ *(Merck)*, purity 99%
xi) $NaHCO_3$ *(Roth)*, purity 99%
xii) D_2O, DCl, D_3CCOOD *(Merck)*, purity 99.8%
xiii) Lysozyme from egg white *(Merck)*, 100,000 U/mg

4 Materials and Methods

4.2 Analytical methods

4.2.1 *FT-IR* spectroscopy

A brief description of the principle of *FT-IR* spectroscopy [131] is given in *Appendix A-II.*

Sample preparation

The chitosan and composite samples were dispersed in KBr pellet and analysed. The concentration of samples was in the range of 0.5-2 wt%. Due to the strong *IR* adsorption of water, which can cover the interesting bands of the sample, the samples must not contain water over a certain limit. Consequently, the chitosan and the composite samples were dried in the oven at temperatures between 60° and 80° C for 12-24 h.

Data analysis

All *IR* spectra of samples, were corrected with respect to the KBr background spectrum.

Determination of DD by IR spectroscopy

In order to determine the *DD* or the *DA* (which can also be expressed as F_A) of chitosan samples, several combinations of bands have been tried[132]. The *DD* can be determined taking into consideration either the amide I band (1655 cm^{-1}) or the amide II band (1575-1590 cm^{-1}) compared to various reference bands. Very often, the bands in the range of 2870-2877 cm^{-1} and 3440 cm^{-1} are taken as reference bands. An important issue of *IR* spectroscopic method is to draw the baseline in order to calculate its absorbance.

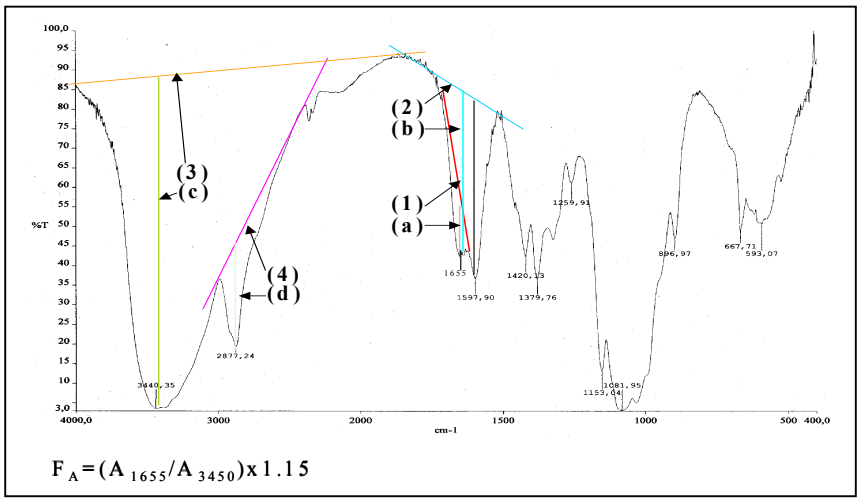

Figure 4.2.1-1 IR spectrum of chitosan (crab chitosan; Lot no. 91K1265, Sigma). In the spectrum, the baselines for the interest bands such as 3440, 2877, 1655 and 1597 cm^{-1} are presented. The peak baselines are shown by digits while the peak intensities are shown by small letters.

The *DD* of chitosan samples used in this project was determined according to the Muzzarelli's approach[43]. The absorbance of the first amide band (1655 cm^{-1} was calculated

considering the baseline drawn as (*1-a*). The band from 3450 cm^{-1}, with the baseline drawn as (*3-c*) as reference band (*Figure 4.2.1-1*), was used.

Identification of components in composite samples by IR spectroscopy

Since the *IR* spectra encrypt structural information about the components, the composite samples with different combination ratios between chitosan and *HAp* were analyzed. The task is to identify the characteristic group frequencies of chitosan and *HAp* and to emphasize the band shift.

4.2.2 Raman spectroscopy

A description of Raman spectroscopy principles[133, 134] is given in *Appendix A-III.*

Sample preparation

Since the solid samples of chitosan and composites do not require any additional preparation steps, they were directly analysed by Raman spectroscopy.

Data analysis

The samples were analysed by Raman spectroscopy as complementary to the *IR* spectroscopy, with respect to their characteristic group frequencies[135, 136, 137] given by the sample components. In order to identify the composite components, the chemical band shifts were studied and on the other side, the structural changes resulted during drying processes of composites were probed. The bands shifts according to the literature data[138], were assigned. The results are discussed in *Section 5.7.*

4.2.3 Microscopic techniques

Some constructive details and the general considerations about the microscope techniques[139] are treated in *Appendix A-IV.*

Sample preparation

OM- The composite samples were analyzed as soft hydrogel on a microscopic glass slide without any additional preparation.

SEM - Electrically conductive samples are required. In order to make the samples electrically conductive, the solid composites, either as freeze-dried and or air-dried samples were covered by a thin layer of gold.

TEM- The samples such as air-dried compact composites and soft composite hydrogel as formed after the co-precipitation were prepared as follows.

i) From solid compact composite, the *TEM* samples as thin sections using an ultramicrotome apparatus were prepared. The samples slides were then fixed on a microscopic grid.

ii) The composite hydrogels were analyzed as sample replicas. The procedure consists of freeze-drying the hydrogel with liquid nitrogen, followed by

covering the frozen sample with a paraffin layer. The sample replica was obtained by releasing the hydrogel in acidic media.

CSLM-The composite samples as thin sections of with the thickness 0.5 –1 mm were analyzed in water environment.

Evaluation of particle size distribution

The analysing procedure[140] requires taking an area domain from a microscopic image, and counting the total number of particles by using *Equation 4.2.3-1,*

$$N_t = \sum_i N_i \qquad \textbf{(4.2.3-1)}$$

where N_t expresses the total number of particles while N_i is the number of fraction '*i'*, with the same features, either for the particle length or for the width. The percentage of each population with the same characteristics was calculated according to *Equation 4.2.3-2.*

$$FN(\%) = \frac{N_i}{\sum_i N_i} \times 100 \qquad \textbf{(4.2.3-2)}$$

FN represents the fraction number, expressed as percentage (%). The particle size[141, 142] can be measured using the scale bar. The calculation of crystallite size (length and the width) was performed according to *Equation 4.2.3-3.*

$$[S_i]_{l,w} = \frac{\langle i \rangle_{l,w} \times \langle SB \rangle}{L_{SB}} \qquad \textbf{(4.2.3-3)}$$

where: $[S_i]_{l,w}$ is the size of fraction, *i,* either the length, *l*, or the width, *w*, given in *nm*;
$\langle i \rangle_{l,w}$ is the length of crystallite measured by a ruler, given in *mm;*
$\langle SB \rangle$ is the scale bar, given in *nm;*
L_{SB} is the length of scale bar, as measured in *mm;*

4.2.4 *NMR* spectroscopy

A brief description of *NMR* spectroscopy [143, 144] is given in *Appendix A-V.*

a) Determination of the DD by ^{1}H-NMR

Work up procedure

The method is based on the procedure developed by Varum *et al*[44]. Briefly, a chitosan sample of about 100 mg was suspended in 10 mL of 0.07 *M* HCl at room temperature with stirring overnight. A small amount of $NaNO_2$ in solid form, between 9-10 mg, was added to the stirring solution and left to react for 4 hours. Chitosan was hydrolysed under conditions described above. The solution was dried by lyophilisation. Water was exchanged three times with D_2O, each time lyophilising the sample between exchanging operations. At the end, for the *NMR* measurements, the samples were dissolved in 1.5 mL of D_2O with DCl, at pD of 5-5.5 and in order to get a clear solution the samples were filtered using filter papers. The proton spectra of samples were recorded on a Bruker system; 300 MHz *NMR* spectrometer, at room temperature with 32 scans with a pulse interval of 3 s.

I_a-I_e are the integral intensities of different types of protons (*Figure 4.2.4-1*).

DA was calculated according to *Equation 4.2.4-1*.

$$DA = 7\,(I_b + I_e) / [\,4\,(I_a + I_c + I_d) + I_b + I_e] \cdot 100, \qquad \textbf{(4.2.4-1)}$$

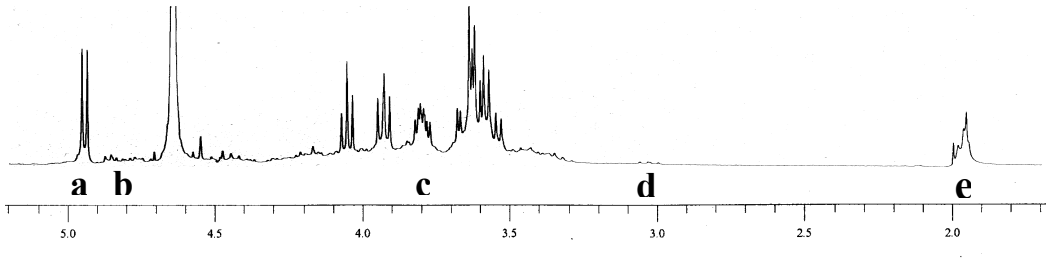

Figure 4.2.4-1 ^{1}H-NMR spectra of a chitosan sample. The signals of the proton are labeled as are shown in the figure. The assignments of proton signals are the following,

a *- amino protons*
b *- anomeric protons*
c-d *- protons from the sugar ring*
e *- protons of CH_3 group from the N-acetyl residues.*

b) NMR relaxation experiments

One of the methods to investigate the amount of bound water and its dynamics consists of a treatment of the magnetization decay of protons or deuterons given by the *CPMG* (Carr-Purcell-Meiboom-Gill) pulse sequence by a bi-exponential analysis[145]. From *NMR* relaxation experiments, two relaxation times T_1 and T_2 can be measured. T_1, (spin-lattice relaxation time) is mostly characteristic for the fast dynamics, while the T_2, (spin-spin relaxation time) characterizes the slow dynamics**.** The *NMR* solvent relaxation behavior can be understood as a rapid exchange between the constrained solvent molecules, bound at an interface (with a short relaxation time, T_{2b}) and free solvent molecules from the bulk (with a long relaxation time, T_{2f}). It is more convenient to express the results in terms of relaxation rate, *R*, which is defined as,

$$R = 1/T \qquad \textbf{(4.2.4-2)}$$

where: R is relaxation rate in $1/s$ (Hz)
T is relaxation time in seconds (s).

When two exchange sites[146] *A* and *B* are considered in the fast exchange regime, the relaxation rates of molecules in these sites are averaged and measured by the fractions f_A and f_B with respect to the corresponding site *A* and *B,* respectively,

$$R_{2obs} = f_a\, R_{2a} + f_b\, R_{2b} \qquad \textbf{(4.2.4-3)}$$

where: R_{2obs} is the transverse relaxation rate
R_{2a} and R_{2b} are the fast and slow relaxation rates corresponding to these two sites
f_a and f_b are the fractions of solvent molecules referred to *A* and *B* sites.

$$f_a + f_b = 1 \qquad \textbf{(4.2.4-4)}$$

To facilitate the evaluation of the relaxation rate in a complex system, the specific relaxation rate, R_{2sp}, normalised on free solvent (free water or other composed system; i.e. D_2O in water, etc) was introduced, being defined as[147],

$$R_{2sp}=R_2/R^{\circ}_2-1 \qquad \textbf{(4.2.4-5)}$$

The R_{2sp} monitors the relative change of the relaxation rate due either to the increase of the fraction of water molecules or to the water system interactions.

Sample preparation

Materials

A powdered sample of a composite hydrogel (50:50 wt%) was obtained by freeze-drying. The composite was prepared using a crab chitosan (*Lot no. 114F-014*, *Sigma*).

D_2O *(Merck)*, concentration in D_2O of 99.9%;

$CaCl_2 \bullet 2H_2O$ *(Riedel de Haën)*, purity of 99%;

H_2O-ultrapure, was prepared in a *Purlab Plus UV/UF System*, which ensures a water conductivity of 0.055μS/cm. The specific resistance was higher than 18MΩ/cm.

Work up procedure

A stock solution of 10% D_2O in ultrapure water as solvent for the *NMR* experiments was used. 1.93 g of freeze-dried composite sample with initial moisture content of 17 wt% was dispersed in 20 mL of *NMR* solvent. The final concentration was 80 mg/mL. In order to reach a complete re-hydration of composite, the sample was allowed to uptake water for 96 h at room temperature (ca. 22°C) A series of six samples containing dispersed composites (concentration of 80 mg/mL) with different $CaCl_2$ amounts were prepared. A series of $CaCl_2$ solutions in the *NMR* solvent with different concentrations such 0.4, 2, 5, 12, 22, 55 wt% as a *NMR* reference samples were used.

4.2.5 Electrophoretic mobility measurements

Some theoretical and practical considerations about electrokinetic phenomena[148-152] are discussed in *Appendix A-VI.*

Data analysis

By applying the Photon Correlation Spectroscopy, the velocity of charged particles in the electrical field is measured. An interference pattern arises due to the intersection of two laser fascicles. The movement of particles within this pattern leads to a correlation time of the dispersed light. Since the particles' transport rates were evaluated, the zeta potential values and the particle size distributions can be determined using *Equation A-4.2.5-3*, as discussed in *Appendix A-VI*. The zeta potential values and the average particle size were obtained using Malvern dedicated Software. The main parts of a Zeta-Sizer apparatus such as laser system, optics, measuring cell, and data block analysis are shown in *Figure 4.2.5-1*.

4 Materials and Methods

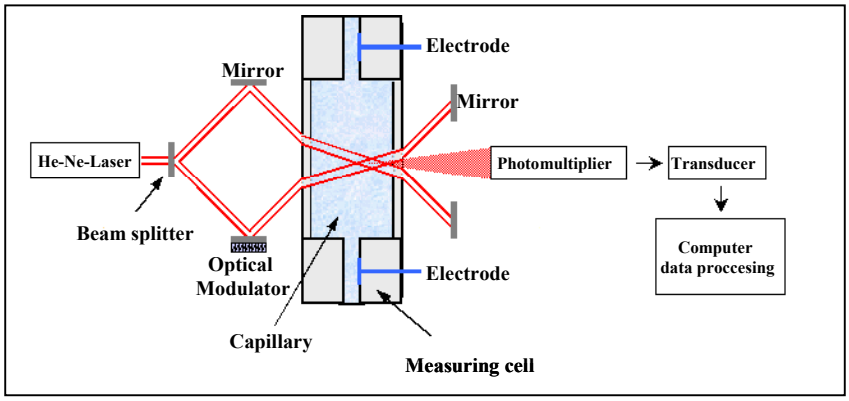

Figure 4.2.5-1 Sketch of a Zeta –Sizer apparatus.

Sample preparation for zeta measurements

Materials

The composite samples in a solid freeze-dried form with different ratio between components such as *chitosan/HAp* 50:50 wt%, *chitosan/HAp* 60:40 wt%, *chitosan/HAp* 30:70 wt%, *chitosan/HAp* 15:85 wt% and *HAp* dispersed in aqueous solutions were measured. The composite samples used in these experiments were prepared using a crab chitosan (*Lot no. 91K1265, Sigma*).

H_2O-ultrapure was prepared in a *Purlab Plus UV/UF System.*

$CaCl_2 \bullet 2H_2O$ (Riedel- deHaën), purity 99%

Acetic acid glacial *(Across Organics)*, purity 99%

Sodium hydroxide *(Merck)*, purity 99%

Sodium chloride *(Merck)*, purity 99%

Hydroxyapatite prepared in the laboratory, from $CaCl_2$ and NaH_2PO_4 in aqueous media[69].

Work up procedure

The composites and *HAp* samples, depending on the type of experiment either in ultrapure water or in aqueous solutions at different pH and ionic strength were dispersed. These aspects are discussed in *Section 5.5*. The concentrations of the dispersed composite samples ranged between 10 and 25 mg/mL. Before ζ-potential measurements, the samples were sonicated for 10 min. The ζ-potential was determined by electrophoresis using a Malvern system.

Sample preparations for particle size measurements

First, all samples were filtered through a 0.8 μm (pore size) cellulose membrane. Four types of samples obtained according to the following procedures, were analysed.

Work up procedure

i) The composite hydrogel sample 50:50 wt% was dispersed in bidistilled water and sonicated for 10 min.

ii) The apatite particles were released from the composite hydrogel by combustion of the chitosan matrix in a furnace at 800°C. Then, by sonication for 10 min the apatite particles were dispersed. The particle concentrations ranged between 5 and 10 mg/mL (in bidistilled water).

iii) The apatite particles were released from the composite hydrogel by dissolution of the chitosan matrix in acidic media. The first method used HCl (1M) and the second one acetic acid (1M). After the acidic treatments, the samples were sonicated then, filtered and finally, the particle size distribution was determined. A Malvern system was used.

4.2.6 Determination of the average molecular weight by viscometry

a) Mark- Houwink-Sakurada equation

A sketch of the most commonly used instrument for measuring the viscosity [153] of polymer solutions is shown in *Figure 4.2.6-1*. As illustrated in the sketch regarding the solution behaviour that is passing through the measuring capillary, some regions must be considered. Viscosity measurements on dilute polymer solutions are used to estimate rapidly the average molecular weight of polymers. The viscosity of the polymer solution, η, at polymer concentration, c, and the solvent viscosity, η_0, are related to the relative viscosity, η_{rel}, the reduced viscosity, η_{red}, the inherent viscosity, η_{inh}, and the intrinsic viscosity, $[\eta]$, through the following equations, given as *4.2.6-1- 4.2.6-4*.

$$\eta_{rel} = \eta/\eta_0 = t/t_0 \qquad \textbf{(4.2.6-1)}$$

$$\eta_{red} = (\eta_{rel}-1)/c \qquad \textbf{(4.2.6-2)}$$

$$\eta_{inh} = (\ln \eta_{rel})/c \qquad \textbf{(4.2.6-3)}$$

$$[\eta] = \lim_{c\to 0} \eta_{red} = \lim_{c\to 0} \eta_{inh} \qquad \textbf{(4.2.6-4)}$$

Practically, the flow time of the polymer solutions *(t)* is compared to the flow time of the solvent *(t_0)*. The relative viscosity is obtained according to *Equation 4.2.6-1*. The power law relation between intrinsic viscosity and the average molecular weights of polymers is expressed according to *Equation 4.2.6-5,*

$$[\eta] = KM^a \qquad \textbf{(4.2.6-5)}$$

which is known as Mark-Houwink-Sakurada equation. The constants, K and a, are tabulated for many natural and synthetic polymers. The averages of the molecular weight are determined by summing the weight fraction w_i of species M_i over all values.

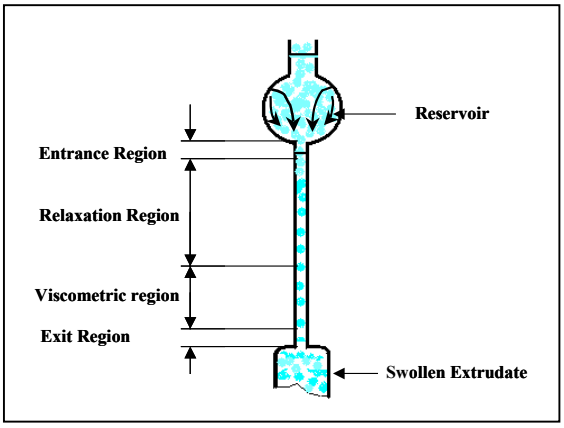

Figure 4.2.6-1 Sketch of a capillary viscometer. The flowing regions are illustrated.

In regard to the number-, weight-, *z*-averages and viscosity molecular weight averages, they are calculated as follows,

$$M_n = 1/\sum_{i=1}(w_i / M_i) \qquad \textbf{(4.2.6-6)}$$

$$M_w = \sum_{i=1} M_i / w_i \qquad \textbf{(4.2.6-7)}$$

$$M_z = \left(\sum_{i=1} M_i^2 w_i\right) \Big/ \left(\sum_{i=1} M_i w_i\right) \qquad \textbf{(4.2.6-8)}$$

$$M_v = \left(\sum_{i=1} M_i^a w_i\right)^{1/a} \qquad \textbf{(4.2.6-9)}$$

The ratio between the weight and the number averages, M_w/M_n, is known as the polydispersity index.

b) Determination of the average molecular weight of chitosan by viscometry

This viscometric method was used to determine the average molecular weight of chitosan samples due to its rapidity and simplicity.

Work up procedure

A chitosan stock solution with a concentration of 0.1-0.2 % wt/v (dissolved in the solvents used for viscometric measurements) was prepared. The stock solution was allowed to dissolve at room temperature under a slow stirring. The dissolution time must not be prolonged too much due to the depolymerisation of chitosan. Depolymerization takes place during dissolution, affecting the viscosity average molecular weight results. After its dissolution, usually 3-4 h, the chitosan stock solution was filtered under vacuum, by using either 0.45 μm cellulose membrane or a sintered glass funnel. The chitosan insoluble fractions were evaluated by weighing the filter membrane or the sintered glass funnel before and after filtration of the chitosan solution. Later, the filter membrane or the sintered glass funnel was dried in the oven at 100°-105°C until constant weight. By difference, the insoluble fractions together with the impurities were determined. Then, the chitosan concentration must be corrected with respect to the moisture content as well as to its insoluble fraction. A series of at least five chitosan solutions were prepared from a chitosan stock solution with concentrations ranging from 0.01 to 0.1 g/dL.

The determination of the sample viscosity was carried out by comparing the flow times through a capillary tube, t_i, for a set of sample solutions to the corresponding flowing time, t_0, of the system of solvents. From the graphical representation of the reduced viscosity against the concentration of chitosan solutions, the limiting value of the reduced viscosity (by extrapolation of η for polymer concentration zero, $[\eta]_{c=0}$), was determined. In order to determine the viscosity average molecular weight of chitosan samples, two systems of solvents as described below were used.

i) *0.2 M acetic acid, 0.1 M sodium chloride and 4 M urea; (M_V in the range from 113,000 to 500,000) using literature values for $K=8.93 \times 10^{-4}$ (dLg^{-1}) and $a=0.71$*[154].

ii) *0.1M acetic acid and 0.2 M sodium chloride (M_v in the range from 90,000 to 1,140,000) using literature values for $K=1.81 \times 10^{-5}$ (dLg^{-1}) and $a=0.93$*[22].

Since over a defined range of molecular weights K and a are constants independent of polymer molecular weight, the viscosity average molecular weight of chitosan samples, was calculated using *Equation 4.2.6-5.*

4.2.7 Thermogravimetric analysis (*TGA*)

A short description of this technique[155] is given in *Appendix A-VII.*

Sample preparation

Certain amounts (between 46,20 mg and 90,20 mg) of *chitosan/HAp* 50:50 wt% composite samples, prepared from krill chitosan (*2K2X*) were analyzed.

4.2.8 X-ray analysis

A description of this technique[156] in given in *Appendix A-VIII.*

a) Determination of crystallites size

XRD is sensitive to the crystallite size[157] and the relationship, which gives the crystallite size, L, is the Scherrer law *(Equation 4.2.8-1).*

$$L = \frac{K\lambda}{\beta_m \cos\theta} \qquad \textbf{(4.2.8-1)}$$

where: L is the crystallite size
λ is the wavelength of X-ray radiation
β_m is the band width at the half of the maximum intensity
K is a constant referred to the crystallite shape and is approximately equal to unity.
θ is the diffraction angle (degree)

However, the data obtained by X-ray diffraction needs refinement since not only the crystal shape and size but also the lattice strain influences peak broadening[158, 159]. The lattice strain is measured as a change in the *3d*-spacing for a strained sample compared to the same

lattice, unstrained. For more details, see *Appendix A-VIII.* The broadening of (002) reflection peak, β, fitted by a Gaussian function**,** which is experimentally measured in its squared form as a squared sum function of two main contributions is expressed, according to *Equation 4.2.8-2,*

$$\beta^2 = \beta^{*2} + \beta_{inst}^2 \qquad \textbf{(4.2.8-2)}$$

where β* represents the crystallite size contribution to the peak broadening while the β_{inst} is the instrumental broadening contribution. Consequently, the average crystallite size contribution is obtained using the *Equation 4.2.8-3.*

$$\beta^* = \sqrt{\beta^2 - \beta_{inst}^2} \qquad \textbf{(4.2.8-3)}$$

Besides these two contributions, there is an additional quantum induced by the lattice strain which comes with its own contribution to the global effect of peak broadening. As compared to the size broadening effect which depends on $1/cos\theta$, the lattice strain contribution follows a $tan\theta$ function. For the purposes of this project, the strain lattice contribution was neglected. The instrumental broadening contribution on a muscovite monocrystal was determined by using different detector slits with a *Ni* filter at 2θ=26.8^o and using a measuring step of 0.01^o. Its contribution was evaluated at β_{inst}=0.062 (degree-2θ).

All measured line widths were then corrected with respect to the instrumental broadening contribution by using the *Equation 4.2.8-3*.

b) Evaluation of crystalinity degree

The crystallinity degree noted with X_c, was introduced[160] in order to make distinction between different apatite samples, see *Appendix A-VIII.* This was defined as the corresponding fraction of crystalline apatite phase in the volume of powdered sample. For low crystallinity samples, the peaks between (112) and (300) reflections are strongly affected. Since X_c is sensitive to the average crystallite size, an empirical relation between X_c and the β_{002} was deduced (*Equation 4.2.8-4*),

$$\beta_{002} \times \sqrt[3]{X_c} = K_A \qquad \textbf{(4.2.8-4)}$$

where: X_c is the crystallinity degree
β_{002} is the width of peak at the half high, of (002) reflection peak expressed in (°)
K_A is a constant set at 0.24.

The conversion of β_{002} (rad) in β_{002} (°) using *Equation 4.2.8- 5* is obtained.

$$\beta_{002}(rad) = \beta_{002}(^\circ) \times \pi / 180 \qquad \textbf{(4.2.8-5)}$$

The crystallinity of composite samples was determined using the *Equation 4.2.8-4*.

Sample preparation

i) Composites with different proportions of chitosan and *HAp* as follows 80:20 wt%, 50:50 wt%, 30:70 wt%, 15:85 wt%, 0:100 wt%, were analyzed.
They were prepared using shrimp chitosan (*TM 1238*, *Primex*). The samples were powdered by freeze-drying.

ii) The formation of *HAp* in the chitosan matrix was monitored during its formation for a composite sample with the ratio between chitosan and *HAp* of 30:70 wt%.

4.2.9 Applied mechanics

Strength and deformation

Strength and deformation measurements[161, 162] yield important parameters such as Young's modulus, yield point, ultimate strain, elastic strain, plastic strain, and stress to failure.

As shown in *Figure 4.2.9-1,* different materials behave differently under deformation. The stress-strain curves are a function of material composition and structure.

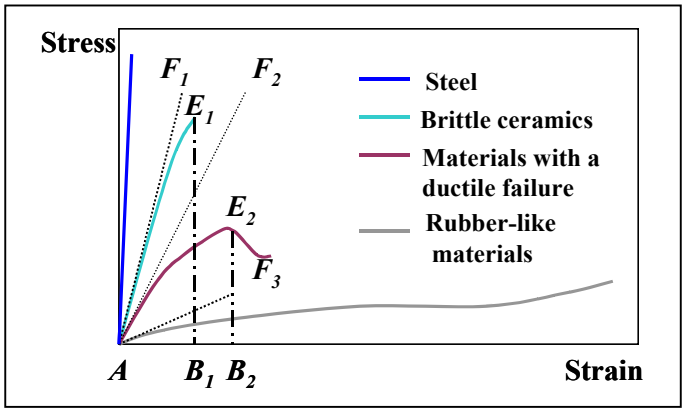

Figure 4.2.9-1 Stress-strain curves for various types of materials.

AF_1, AF_2 and AF_3 are the tangents drawn to the first linear part of the stress-strain curves. The tangents are important since they give the bending and compressive Young's modulus values. The maximum stress values shown as E_1 and E_2 lead to the ultimate strain values figured as B_1, B_2, as seen in *Figure 4.2.9-1*.The ultimate bending strength, σ_b, the bending and the compressive Young's modulus values, $E_{b,c}$, were calculated according to *Equations 4.2.9-1* and *4.2.9-2,*

$$\sigma_b = \frac{2F_{\max}L}{A} \qquad \textbf{(4.2.9-1)}$$

$$E_{b,c} = \frac{L}{A}\frac{\Delta F}{\Delta l} \qquad \textbf{(4.2.9-2)}$$

where *Fmax* is the maximum load (N), *L* is the support (sample holder) span (mm), *A* is the transverse section of the specimen (mm^2), $\frac{\Delta F}{\Delta l}$ is the gradient of the linear domain of load-displacement curve (N/mm).

Three points bending test

This test and is very convenient and easy to perform. The sketch of the machine is shown in *Figure 4.2.9-2*. The load cell is moved until the tip touches the specimen. Then, it loads the sample by pressing it in the middle. Since the ends of the sample are fixed in two points, the specimen begins bending. The response to deformation is recorded as load deformation curve.

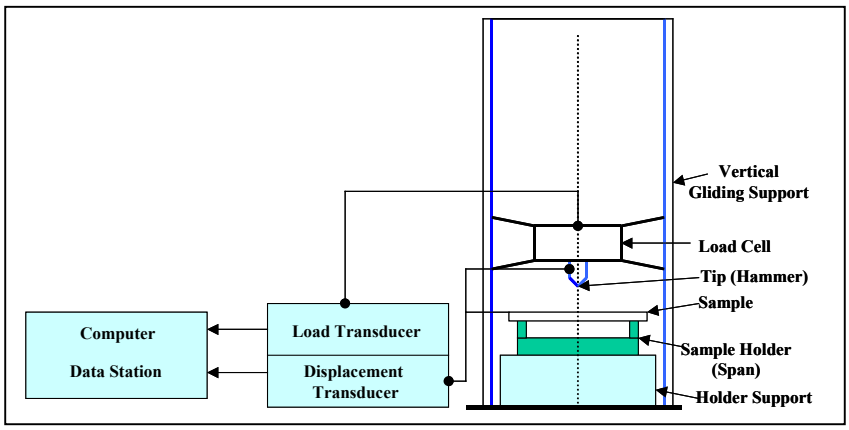

Figure 4.2.9-2 Sketch of a mechanical test apparatus.

Sample preparation

Rectangular specimens with different compositions were analysed both dry and wet, by three point bending tests as well as in compression mode. The descriptions of samples are given in *Section 5.9*. The samples were rectangular ca. 3-5 mm x 3-5 mm x 20-25 mm.

4.2.10 Drying and swelling of composites under controlled conditions

Many models have been proposed to explain the formation of association gel networks[163] by independent interactions between the chain segments. Some models are important for theoretical and practical approaches[164]. Brief descriptions of some important gel models are presented in *Appendix A-IX.*

a) Determination of shrinking coefficients of disk shaped composite samples

The composite hydrogel samples were disk shaped. They were left to dry under controlled conditions (humidity of about 45-50 % and temperature of 23-25^{0}C). The shrinking coefficients, as the ratio between the final volumes (V_f) to the initial ones (V_i) were calculated, according to *Equation 4.2.10-1.*

$$S_c = \frac{V_f}{V_i} \qquad \textbf{(4.2.10-1)}$$

b) Determination of the swelling capacity of composites

The samples were kept in a flask containing bidistilled water at pH 7 and left to swell until equilibrium. The process can be followed by various parameters such as mass, volume or sample diameter. The process is time dependent being described by *Equation 4.2.10-2,*

$$SC_t = \frac{cp_t - cp_{t_0}}{cp_{t_0}} \qquad \textbf{(4.2.10-2)}$$

where: SC_t is the swelling capacity at a certain swelling time *t,*
cp_t, cp_{to} are control parameters measured in the swelling experiments at different times as compared to its initial value, measured at t_o.

c) Determination of swelling cooperative diffusion coefficients of composites

The swelling kinetics of composites in bidistilled water as disk shaped samples can be followed as a function of time. By measuring the sample diameter using an electronic digital calliper and a magnifying glass (10X Bima), the increase of sample diameter, Δd (as a result of swelling) was determined. From swelling experiments, using Li-Tanaka's approach[165], the swelling diffusion coefficients of composite samples were evaluated. Samples with different compositions in bidistilled water at pH 7 were swollen. The diameters, d_i, were measured at different times. The maximum diameter, d_∞, defines the equilibrium swelling state. By plotting the increase of sample diameter normalised to initial diameter, $\Delta d/d_0$, against the swelling time, swelling kinetics curves were obtained. In order to evaluate the swelling diffusion coefficients, according to *Equation A-4.2.10-7* (*Appendix A-IX*), the term $''\ln\left(\frac{d_\infty - d_t}{d_\infty - d_0}\right)''$ as a function of swelling time was plotted. The slopes and the intercepts (to OY axis) of the graphs give the structural parameters of the hydrogel network. Since all the

structural parameters were determined, the swelling diffusion coefficients, D_c, can be calculated[165, 166], using *Equation 4.2.10-3,*

$$D_c = \frac{3a_\infty^2}{\tau_1 \alpha_1^2} \qquad \textbf{(4.2.10-3)}$$

where: a_∞ is half of the thickness of the disk at the maximum swelling capacity
α_1 is a function of R and implicitly of B_1 and can be evaluated as was described by Tanaka's gel model for the disk shaped samples.
τ_1 is the relaxation time, as discussed in *Appendix A-IX.*

4.2.11 Partial enzymatic degradation of composites

Enzymatic degradation[167, 168] experiments were performed on solid composite samples. They were previously swollen in *SBF* at pH 7.04 for 48 h in order to reach swelling equilibrium. The initial weight of the solid composites ranged from 0.2000 g to ca. 0.40000 g. They were weighed to an accuracy of ±0.0002 g using a *Sartorius* analytical balance. The composite samples were incubated in Eppendorph tubes of 2 mL with 1.5 mL of lysozyme solution (1.0 mg/mL in *SBF* corresponding to 100,000 U activity/mg). Enzymatic degradation was carried out at 37^o C in a thermostated water bath for 50 days. In order to measure the yield of degradation, the weight loss of samples was monitored. At different intervals, between 1 and 5 days, the samples were weighed. The sample was left on filter paper for about 2 minutes. Then the sample was weighed. Since a fluctuation of mass of ±0.0004 g was observed, the mean value was considered. The yield of degradation, *YD,* was calculated by the weight decay of sample normalized on its initial weight using *Equation 4.2.11-1,*

$$YD = \frac{m_i - m_t}{m_i} = \frac{\Delta m_{it}}{m_i} \qquad \textbf{(4.2.11-1)}$$

where m_i and m_t are the sample masses at initial time and at time t, respectively. As a control sample (blank), a composite sample 50:50 wt% was incubated in *SBF* at 37^{o}C without enzyme. No degradation phenomena were observed after 50 days. The *YD* plotted against time gives the degradation curve. From the curve slope the degradation rate can be determined. The pH during the degradation period was monitored with a sensitive pH paper (Macharey-Nagel). In order to determine the degradation products (chitosan oligomers), at the end of the degradation experiments the supernatant solutions were freeze-dried. The amount of freeze-dried samples between 2 and 5 mg was dispersed in 50 μL of a mixture of water and methanol 1:1 (v/v). The samples were analyzed by *MALDI-TOF* mass spectroscopy.

4.2.12 Determination of moisture content *(W_{cont})*

Different amounts of chitosan, between 0.10-0.30 g were weighed with an accuracy of ± 0.0002, in dry vials of known mass. The samples were placed in the oven at ~110ºC and allowed to dry for 24-48 h (until constant weight). The water content was calculated according to following equation,

$$W_{cont.}(\%) = \frac{\Delta m}{m_i} x100 \qquad \textit{(4.2.12-1)}$$

where: Δm is the difference between the initial mass and the final one
m_i represents the initial mass of the sample.

4.2.13 Determination of ash content *(A_c)*

The ash content of chitosan sample was gravimetrically determined. A chitosan sample of about 25-30 mg was pyrolyzed in furnace at 800°C for 12 h. The ash content A_c was calculated according to the following equation,

$$A_c = \frac{m_i}{m_0} x100(\%) \qquad \textit{(4.2.13-1)}$$

where: m_1 is the weight of pyrolyzed sample residue
m_0 is the weight of initial chitosan sample

4.3 Preparative methods

4.3.1 Preparation of chitosan by heterogeneous deacetylation of chitin

Work up procedure

In a three necks round flask of 5L volume, 78-80 g of chitin (krill chitin), and 2.5 L of 50 % wt/wt aqueous sodium hydroxide solution were added. Under an argon atmosphere and using a mechanical stirring, the temperature was brought between 97 and 105°C (controlled by a temperature controller with an inner thermometer). The reaction was allowed to proceed between 1 and 2 h. The chitosan suspension was filtered through a cotton filter using a Büchner funnel and washed with bidistilled water until the neutral pH (free of alkali). The colourless chitosan material was washed three times with 200 mL MeOH and one time with 200 mL ethylic ether. Then, the chitosan sample was left to dry in the oven at 60°C. The recovered amount was between 64 and 66 g, which corresponds to a yield of 80-82 %. In order to obtain chitosan with a high *DD*, the reaction must be repeated several times.

4.3.2 Procedure of regeneration of chitosan

Depending on the source, chitosan requires purification before using it as raw material in the composite preparation. In order to isolate exclusively the soluble chitosan fractions it was precipitated from solution by adding an alkaline solution. The procedure consists of preparation of a chitosan solution in 1% aqueous acetic acid. In order to avoid problems in the filtration task, the chitosan concentration must not exceed 0.5 wt%. The dissolution of citosan was achieved by simple shaking or under a gentle stirring (at low stirring rate) for a few hours (3-4h). The prolongation of dissolution time is not recommended because of depolymerization of the chitosan. The solution was filtered to remove the particulate impurities and the insoluble polymer fractions. The filtration was performed under vacuum, first using a filter paper and then using a cellulose membrane (0.45μm). After filtration, a clear solution was obtained. In the next step, chitosan was precipitated with an aqueous dilute solution of sodium hydroxide or ammonia. Chitosan sample in hydrogel form, semi-solid was washed with distilled water until free of alkali (neutral pH), then lyophilised. The recovery yield was between 80 % and 95 %, depending on the type of chitosan.

4.3.3 Preparation of composites containing chitosan and *HAp*

The preparation of composite was achieved by a co-precipitation method developed in our working group. This method entails the generation of a dilute solution of chitosan (0.1-0.5 wt%) in 1 v% acetic acid, followed by the addition of aqueous solutions of calcium chloride and sodium dihydrogen phosphate. A dilute solution of sodium hydroxide was slowly added to the stirring solution, bringing the pH to a value above 10 and initiating the formation of *HAp*. Then, the suspension was stirred for 24 hours to allow the complete formation of the composite constituents. By varying the initial concentrations of chitosan and of inorganic salts, composites with various combination ratios were obtained. The composite in a hydrogel form was collected by filtration and washed until free of alkali (neutral pH). By drying the composite hydrogel, either at room temperature or at elevated temperature (below 100^{o}C), a solid ceramic-like composite was obtained. By freeze-drying the composite hydrogel, solid powdered composite was obtained.

5 Experimental Results and Discussions

5.1 Preparation and characterization of chitosan samples

5.1.1 Preparation of chitosan samples

In this project, several types of chitosan samples used. Their physicochemical parameters are presented in *Table 5.1.1*. The chitosan samples prepared in our laboratory by deacetylation of krill chitin are labelled *2K2X*, *2K3X* and *2K2XH*. Deacetylation of chitin samples was performed according to the method described in *Section 4.3.1*. The sample *2K2XH* was prepared from *2K2X* using hydrolyses with concentrated HCl (37%), according to a method developed by Varum *et al.*[169]

Table 5.1.1 Physicochemical parameters of chitosan samples.

Sample	Deacetylation parameters; time (h), temperature (°C), with NaOH, 50% (wt/wt)	Average molecular weight $\bar{M}_V$ by viscosimetry (Lee's Method)	Average molecular weight $\bar{M}_V$ by viscosimetry (Robert's Method)	DD by IR method (%)	DD by ^{1}H-NMR (%)	Moisture Content (wt%)	Ash content (wt%)
2K2X*	1.5h, 1.5h/100^{0}C	270,000	-	80.1	75.2	12.5	1.5
2K3X*	1.5h, 1.5h, 1.5h/100^{0}C	150,000	-	96.2	98.1	10.5	1.1
2K2XH*	Hydrolysed with conc. HCl (37%) for 1h under reflux	150,000	-	78.2	-	9.8	0.1
Chitosan from Crab shells *(Sigma)* Lot no. 91K1265	No deacetylation The sample was purified by regeneration from NaOH	535,000	890,000	78.8	80.6	13.2	1.2
Chitosan from Crab shells *(Sigma)* Lot no. 114F014	No deacetylation The sample was purified by regeneration from NaOH solution	515,000	837,000	-	84.2	10.4	1.8
Chitosan** from Insect cuticles (prepared by Marcin Struszczyk 08.2000)	No deacetylation The sample was purified by regeneration from NaOH solution	396,000	790,000	66.2	68.8	11.8	0.2
Chitosan from Atlantic shrimp (*Primex*, Iceland) Lot no. TM 1238	No deacetylation The sample was used as received	300,000	815,000	-	92	9.1	0.3

**The samples labeled as 2K2X, 2K3X, 2K2XH were prepared from krill chitin flakes delivered by Polymar GmbH Bremerhaven.*
Where: nX- number of deacetylation steps
H-denominate the hydrolysed sample
***This sample was only partially soluble*

The insect chitosan prepared in our laboratory and crab chitosan (*Sigma*) were used after a purification step in which they were regenerated from alkaline media, according to the procedure described in *Section 4.3.2*. The Atlantic shrimp chitosan sample, (*TM 1238*) was used in the experiments as received from (*Primex*, Iceland). The scope was to use different

types of chitosan from different sources as raw materials to prepare *chitosan /HAp* composite samples.

5.1.2 Characterization of chitosan samples

In order to characterize the chitosan two main structural parameters: as the degree of deacetylation, *DD*, expressed in *(%)* and the average molecular weight were determined. Besides them, for some applications, the moisture content and the ash content were also considered.

5.1.2.1 Determination of the average molecular weight

The average molecular weight of chitosan samples was determined by viscometry. The reduced viscosity of different chitosan samples, plotted as a function of concentration, are displayed in *Figure 5.2.1.* Two types of solvent systems, according to Lee[154] and Robert[22] methods, were used.

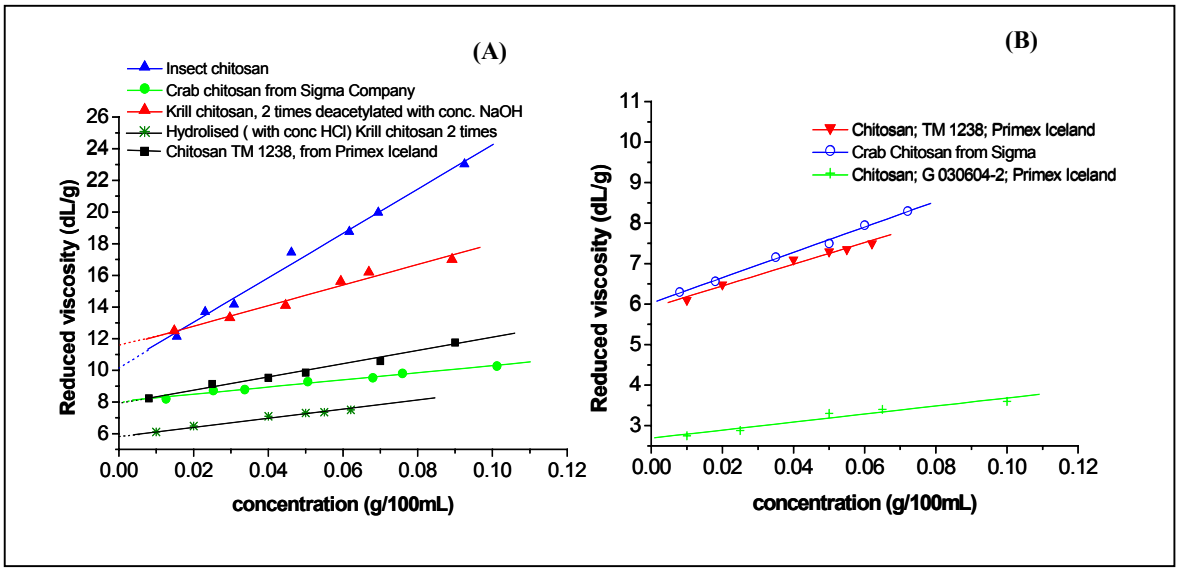

Figure 5.1.1 Reduced viscosity plotted against the concentrations of chitosan samples. A- results obtained by Lee's method [154]; B- results obtained by Robert's method [22]. The all results were fitted using linear functions. The intrinsic viscosity was obtained by extrapolation of curves at C=0. The viscometric average molecular weight of chitosan samples were determined using Equation 4.2.6-5.

The average molecular weight of chitosan (summarized in *Table 5.1.1*) are different, depending on the system of solvents used. Close results should be obtained but unfortunately, could not be experimentally confirmed. These aspects can be explained by association of chitosan chains at supramolecular level, which are strongly dependent on the system of solvents. In Lee's system, which is composed of 4 M urea, 0.2 M acetic acid and 0.1 NaCl, the high urea concentration destroys the hydrogen bonds between chitosan chains. This leads

to lower values of average molecular weight compared to those obtained with Robert's system. The ratios between M_v values obtained by Robert's system and by Lee's system led to scattered values. These values ranged from 2.71 obtained for Atlantic shrimp chitosan (*TM 1238, Primex*) to 1.66 for crab chitosan, (*Lot no. 91K1265, Sigma*). In insect chitosan (*M. Struszczyk, Aug 2000*) the ratio was determined to be ca. 1.99.

The results suggest that beside the chain associations phenomena, some other polymer properties, such as the chain stiffness[170] in different solvent environments and the distribution of molecular weight values (which can be broader or narrower), could explain the obtained results.

5.1.2.2 Determination of the degree of deacetylation *(DD)*

i) Determination of DD (F_A) by ^{1}H -NMR spectroscopy

The determination of *DD* either for chitin or for chitosan is still a big challenge since there is no standardised method. The *DD* values using a ^{1}H-*NMR* spectroscopy method according to Varum *et al.*[44] (see the method description in *Section 4.2.4*) were determined. The chitosan samples with various *DD* exhibit different ^{1}H-*NMR* patterns, as shown in *Figure 5.1.2*. The most affected spectral domain corresponds to that of chemical shift (resonance frequency) of about 2 ppm, where the protons that belong to the $-CH_3$ groups from *GlcNAc* units are found.

ii) Determination of DD (F_A) by IR spectroscopy

The *IR* spectra convey structural information. In order to determine *DD* (F_A) for chitin and chitosan samples several combinations of bands have been tried. In our case, the *DD* (F_A) values were calculated according to Muzzarelli approach[43] [F_A=(A_{1655}/A_{3450}) x1.15] as discussed in *Section 4.2.1*. The results were in a good agreement to those obtained by ^{1}H-*NMR* spectroscopy.

The *DD* values of chitosan samples obtained by *NMR* and *IR* methods are shown in *Table 5.1.1*.

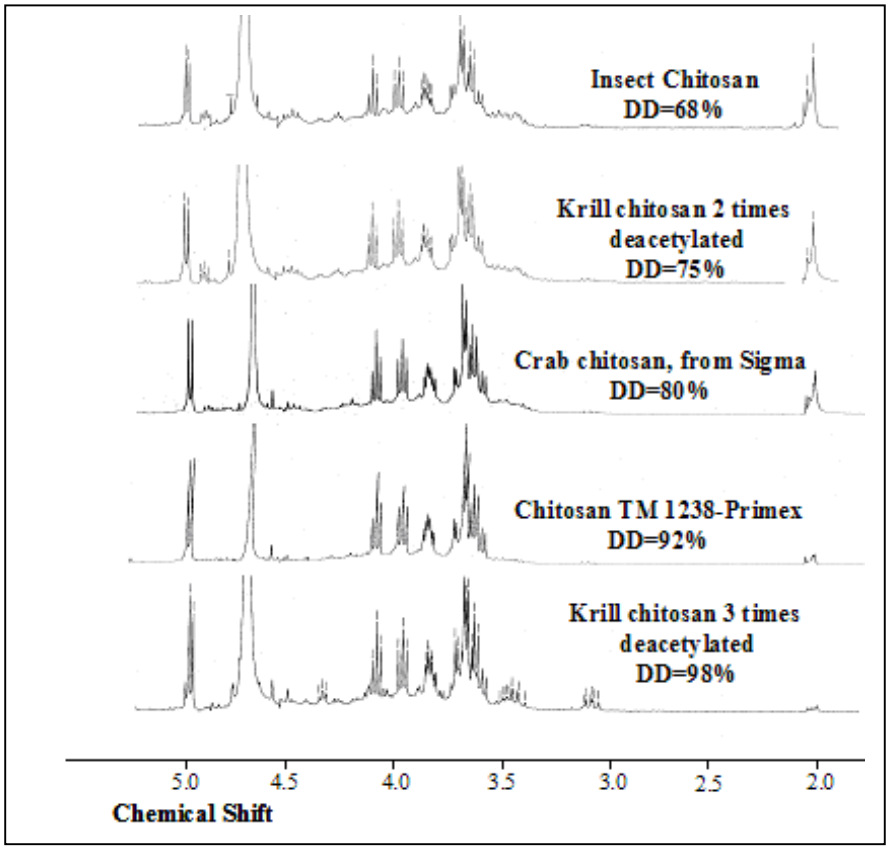

Figure 5.1.2 ^{1}H-NMR spectra of hydrolysed chitosan samples.

5.1.2.3. Evaluation of moisture and ash content

In order to determine the moisture and ash content of chitosan samples, gravimetric methods were used. These are described in *Sections 4.2.12* and *4.2.13.*

The moisture content varies between 9 and 14% whereas the ash content ranged from 0.1 to 3.1%, as presented in *Table 5.1.1*.

5 Experimental Results and Discussions

5.2 Formation of composite hydrogels

Materials

Chitosan samples (presented in *Section 4.1*).
$CaCl_2$, NaH_2PO_4, NaOH, $CuSO_4$, $MnCl_2$ and $Zn(NO_3)_2$ (*Section 4.1*).

Instrumentation

A pH meter (Hanna Instruments) equipped with a measuring glass electrode was used.

5.2.1 Precipitation of composite hydrogel samples

5.2.1.1 Combination ratio between chitosan and *HAp*

The preparation of composite samples, according to the procedure developed in our working group, was carried out. This is presented in *Section 4.3.2*. The work was focused on the preparation of composite samples containing *CPs*, mainly as *HAp* and chitosan. The idea behind this approach was that *HAp* to be synthesized inside the chitosan matrix from soluble salts containing PO_4^{3-} and Ca^{2+} ions (at a molar ratio Ca/P of 1.67, characteristic for *HAp*). $CaCl_2$ and NaH_2PO_4 as soluble precursors of *HAp* in aqueous solution were used.

Hirano *et al.*[171] have mentioned the importance of $CaCl_2$, as precursor in biomimetic processes employed in the mineralization of chitin and chitosan in aqueous systems in the presence of CO_3^{2-} ions. The influence of different acids used to dissolve the chitosan samples on the formation of composites was considered too, and it is discussed in *Section 5.2.2*. By using our stepwise co-precipitation method, different types of composites with respect to the ratio of combination between chitosan and *HAp* were prepared (*Table 5.2.1*).

Table 5.2.1 Preparation of various types of composite samples.

Substance	**Concentration (%) (wt/v)**	**Volume of solutions (mL) mixed to obtain 1 g of *CTS/HAp* composite with respect to its ratio of combination**					
		CTS/HAp 80:20 (wt%)	**CTS/HAp 60:40 (wt%)**	**CTS/HAp 50:50 (wt%)**	**CTS/HAp 40:60 (wt%)**	**CTS/HAp 25:75 (wt%)**	**CTS/HAp 15:85 (wt%)**
$CaCl_2$	11.1	2	4	5	6	7.5	8.5
NaH_2PO_4	13.8	1.2	2.4	3	3.6	4.5	5.1
CTS*	0.2	400	300	250	200	125	75

** CTS is the abbreviation for chitosan. It was dissolved in an aqueous acetic acid solution, 1wt%.*

In order to obtain composites that contain cations, before the co-precipitation of composite, the cations must be complexed to the chitosan. Some cations such as Cu^{2+}, Zn^{2+} and Mn^{2+} with bioactive properties[16, 17, 18], were complexed with chitosan from aqueous solutions[172, 173]. For our purposes, the complex combinations of chitosan were prepared by mixing the $CuSO_4$, $MnCl_2$ and $Zn(NO_3)_2$ as aqueous solutions (50 μg /mL for each cation)

with the chitosan solution. After that, the chitosan solutions containing the complex combinations were used to prepare the composite samples. Various types of composites containing cations with different concentrations ranging from 1ppm (1μg cations /1g of dry composite) up to 250 ppm (250 μg cations/ 1 g of composite) were prepared.

5.2.1.2 Discussions on the composite formation

Since both chitosan and *HAp* are soluble in acidic medium and insoluble in neutral and alkaline medium, a system composed of chitosan, $CaCl_2$, and NaH_2PO_4 and in some cases cations in aqueous solution of 1 wt% acetic acid was neutralized. The co-precipitation of composite sample can be discussed by the variation of pH curve as a function of the added NaOH, as displayed in *Figure 5.2.1*. The curve was obtained for the co-precipitation of 0.5 g of composite prepared from krill chitosan, *2K2X* (at a combination ratio between chitosan and *HAp* of 50:50 wt%). An aqueous solution of 5 wt% NaOH was used to raise the pH in a stepwise fashion during the co-precipitation process. The pH curve (seen in *Figure 5.2.1*), which describes the precipitation of composite, exhibits three distinct zones with the following main features.

i) In the first zone, by increasing the pH, the chitosan chains change their conformations from the extended worm-like to extended random coil and finally it reaches the compact random coil conformations. The screen of the charges along the chitosan chain gives the modification of chain conformation. At a pH of 5.5 about 50% of charges are neutralised while at pH 6.2 all the charges are neutralised. This leads to the modification of the balance between the hydrophilic and hydrophobic interactions and compact chitosan conformations are permitted. The conformational changes are accompanied by the precipitation of $CaHPO_4$ (brushite) at pH 5.5.

ii) The second zone (pH 6.2-6.8) reflects the beginning of the chitosan precipitation, which incorporates a fraction of calcium and phosphate ions (as brushite). The complex environment (pH, ionic strength and the presence of brushite already precipitated) from which chitosan was precipitated, leads to a shift of the chitosan precipitation[128] at a higher pH (6.8) compared to that at which chitosan precipitates normally (6.2-6.4).

iii) The formation of *HAp* occurs in alkaline pH (10.0 – 12.0) which corresponds to the third zone. The pH of composite hydrogel decreased slightly during 24 h (as shown in *Figure 5.2.2*), after that, the product is collected as a hydrogel by filtration.

In the first two zones, some processes that lead to the formation of a defined composite structure take place. As mentioned in the literature, chitosan in aqueous acidic solution exhibits different chain conformations[26] as a function of solution parameters. At low pH of 2-3, it occurs in extended worm-like conformations and then it starts to shrink at more

compact chain conformations as the pH reaches the neutral domain. These conformations depend on the charge density along the chain, which is given by the ionized -NH_2 groups (as -NH_3^+). The electrostatic effects are diminished as the pH increases towards neutral pH, leading to conformations that are more compact. By raising the pH, besides the changes of chitosan conformations, $H_2PO_4^-$ is neutralised in the second step (Ka_2=6.2x10^{-8}) and the result is the formation of brushite, *DCPD,* which is thermodynamically stable in the pH range between 4.5 and 6 (*Section 3.2*). The second zone shows the precipitation of chitosan at pH above 6.4. At this stage, the composite occurs mainly as chitosan/brushite or/and chitosan/*ACPs*. In these types of composites, chitosan adopts compact chain conformations (random coil, more or less expanded)). Some parts of chitosan chains such as segments or loops exhibit a higher degree of freedom (referred to their movement possibility) compared to those from the core of the coil (with a more restricted movement possibility). Thus, the chitosan chain segments with a higher degree of freedom can interact with the brushite crystallites achieving so called 'anchoring domains' by different interactions such as ion-dipole or/and through the complexation of Ca^{2+} to chitosan.

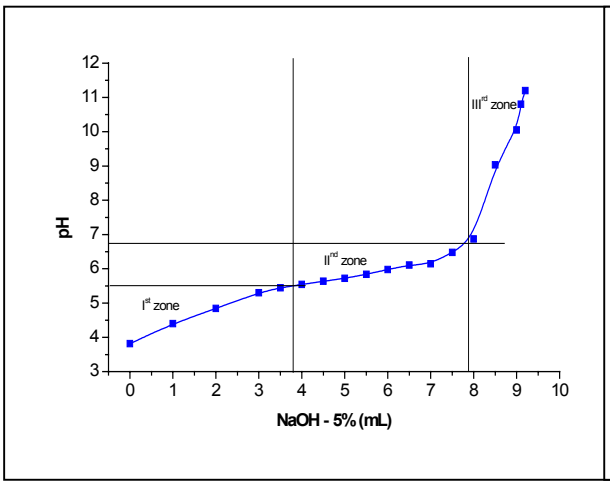

Figure 5.2.1 Variation of pH as a function of the added volume of NaOH solution. The points are simple connected.

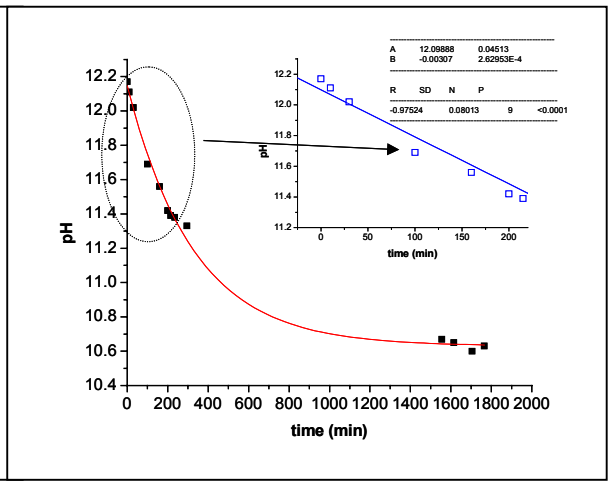

Figure 5.2.2 pH decay during HAp formation in the chitosan matrix. The inset graph (approximated by a linear function) is a zoom in the first period of the HAp formation. The entire data were fitted with a monoexponential function.

At this stage, an interpenetrated hydrogel network containing chitosan, brushite (mainly) and amorphous calcium phosphate *ACPs* (formed besides brushite) is formed.

The third zone is characterised by an abrupt positive slope and consequently the alkaline pH range is reached fast. The formation of *HAp* in aqueous solutions[174] takes place in the alkaline media from different precursors of *CPs*, since the *HAp* is the most stable *CPs* in

the alkaline media, as discussed *in Section 3.2.2.* The pH is an experimental parameter which can monitor the formation of *HAp* in the alkaline media as a function of time. The pH decay is displayed in *Figure 5.2.2.* The curve was fitted with an exponential decay function and it was obtained for a composite 50:50 wt% (prepared from krill chitosan *2K2X*). The composite hydrogel amount was about 1 g dispersed in 220 mL of NaOH aqueous solution. The initial pH value was 12.20. At the end of reaction, (after 24 h) the pH reached 10.62. Since the slope of the curve is more abrupt in first 2-3 h, it can be deduced that the formation *HAp* takes place at a high rate in the first time domain, shown as inset in *Figure 5.2.2.* The pH decay of the system is explained by the formation of *HAp* from the precursors, mainly from brushite and *ACP*, in which the OH^- ions are consumed, according to the below equations.

$10CaHPO_4 + 12OH^- \rightarrow Ca_{10}(PO_4)_6(OH)_2 + 10H_2O + 4\,PO_4^{3-}$ ***(5.2-1)***

$PO_4^{3-} + ACP$ (amorphous Calcium Phosphate) $+ OH^- \rightarrow Ca_{10}(PO_4)_6(OH)_2$ ***(5.2-2)***

5.2.2 Influence of acidic media on formation of composites

In order to see how the acidic medium is influencing the composite formation and its structure, three types of acids such as acetic, malic and citric, were studied. They exhibit different coordination possibilities to the chitosan chains and therefore different composite hydrogels are expected to be formed. The preparation of composite hydrogel (ratio chitosan/*HAp* 50:50 wt%) was conducted such chitosan (*TM 1238*, *Primex*) (0.5 g) was dissolved in 125 ml of an aqueous solution of the acid (1%, 5% and 10% wt/v for acetic, malic and citric acid, respectively). Solutions of 0.149 M sodium dihydrogen phosphate (20 mL) and of 0.249 M calcium chloride (20 mL), calculated for a molar ratio Ca/P 1.67 were added to each chitosan solution. Later, the precipitation procedure followed the same route as described in *Section 4.3.3.* The physical characteristics of composite hydrogels showed that after co-precipitation, the chitosan dissolved in citric acid produced the least amount of composite hydrogel, which was about 30-40% less than for the others two acids (*Table 5.2.2*).

Table 5.2.2 The yield and physical characteristics of composite hydrogels. The ratio of chitosan to HAp was 50:50 wt%. The amount of composite was 1g.

Acids	Yield of Hydrogel (g)	Volume of hydrogel in solution (mL)	Colour of hydrogel
Acetic acid	22.8	100	Semi-transparent
Malic acid	24.4	120	Semi-transparent
Citric acid	15.2	75	Milky white

The yield of hydrogel in malic acid has always been the highest among the three acids used. However, the reason is unclear since repeated trials confirmed that this phenomenon is reproducible.

5.3 Drying and swelling experiments on composites

5.3.1 Introduction

The biopolymer gels differ from the synthetic polymer networks in regard to several aspects. Their structures contain large amounts of water, which is the solvent from which they are formed. Generally, they are obtained by crosslinking in the presence of water. On the other hand, the crosslinks are more often physically than chemically formed whereas in the case of synthetic polymers gel networks chemical crosslinks are achieved. This means that the crosslinking points (covalent bonds) are not only replaced by weaker physical bonds, but they are also ceased to be geometrically small in relation with the rest of the network structure. The contact regions of polymer chains become involved. The most simple example is when two such interacting regions providing the simplest situation, with associations of such segments which form a so called 'junction zone'[164], as shown in *Figure 5.3.1*.

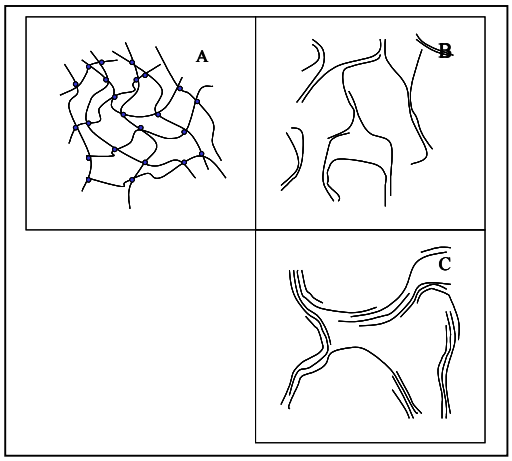

Figure 5.3.1 Schematic representation of gel networks involving A, point (covalent) crosslinks; B, two-chain junction zones; and C, multiple-chain junction zones.

The polysaccharide gels[175-177] obtained from agarose, carrageenan, alginate, chitosan and chitin provide classic examples of this behaviour. The crosslinking is induced either by cooling their solutions, by adding the specific counter-ions or by changing the pH of the system.

5.3.2 Aim of experiments

- To determine the shrinking coefficients expressed as the ratio between the final volume of the specimen (after shrinking, as dried sample) and its initial volume (as composite hydrogel);
- To see how the composition of samples influences the shrinking properties;

- To evaluate the moisture content of composite hydrogel samples related to the transition phenomena from a soft hydrogel state to a physically crosslinked hydrogel;
- To investigate the swelling properties of composite samples;
- To determine the swelling cooperative diffusion coefficients for disk shaped composite samples by means of swelling in water at neutral pH, based on Li-Tanaka's gel model;

5.3.3 Materials and methods

Various types of composite samples prepared with a shrimp chitosan (*TM 1238 Primex*) were used. The composite samples accompanied by the labelling procedure using letters (for the same composition) and digits (for the same diameter of the sample holder), are presented in *Figure 5.3.2*. The samples characteristics are comprised in *Table 5.3.1*.

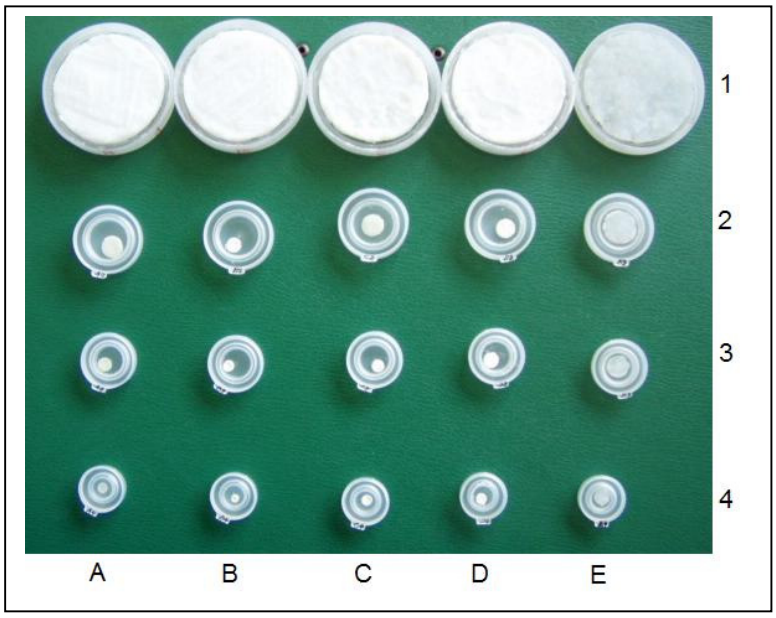

Figure 5.3.2 Five series of composite hydrogel samples, disk shaped, during the drying process at room temperature. The samples labelled with the same letters (A-E) have the same composition. They differ by the disk diameter (1-4). The compositions of samples are presented in Table 5.3.1.

The drying of composite hydrogel samples, using hydrophobic surfaces made of polypropylene, was carried out (see *Figure 5.3.2*). In order to apply the Li–Tanaka's gel model for calculations of diffusion coefficients, the composite samples were disk shaped, having various diameters. The shape is a disk if its thickness is less than 10% of its diameter. The drying experiments under controlled environmental conditions (temperature of 23-25°C and a relative humidity between 45 and 50%) were performed.

5 Experimental Results and Discussions

Table 5.3.1 Characteristics of composite hydrogel samples (composition, initial mass, volume and moisture), disk shaped.

CTS*/HAp 50:50 (wt%) **Moisture content 91.8% (wt%)**		***CTS/HAp 40:60 (wt%)*** **Moisture content 95.1% (wt%)**		***CTS/HAp 60:40 (wt%)*** **Moisture content 92.4% (wt%)**		***CTS/HAp 25:75 (wt%)*** **Moisture content 90.3 (wt%)**		***CTS/HAp 100:0 (wt%)*** **Moisture content 95.7(wt%)**	
Sample code	Initial mass (g) /Initial volume (mL)	Sample code	Initial mass (g) /Initial volume (mL)	Sample code	Initial mass (g) /Initial volume (mL)	Sample code	Initial mass (g) /Initial volume (mL)	Sample code	Initial mass (g) /Initial volume (mL)
A1	17.5346 17.20	B1	16.8596 16.55	C1	14.4650 14.23	D1	16.6475 16.24	E1	15.2248 15.05
A2	1.5539 1.52	B2	1.0267 1.02	C2	1.3851 1.37	D2	1.1990 1.18	E2	1.3634 1.36
A3	0.6004 0.59	B3	0.6156 0.60	C3	0.5861 0.58	D3	0.6678 0.65	E3	0.5559 0.55
A4	0.2055 0.19	B4	0.1884 0.18	C4	0.2883 0.28	D4	0.2815 0.27	E4	0.2007 0.20

CTS is the abbreviation for chitosan.*

The drying und swelling processes under defined experimental conditions were used to evaluate the shrinking and swelling characteristics of samples as well as their swelling diffusions coefficients. The methods were discussed in *Section 4.2.10* and in *Appendix A-IX*. The water release and uptake were monitored as a function of time. The swelling of samples in de-gassed, bidistilled water (pH=7) at 23-25^{o}C was performed.

5.3.4 Results and discussions

The composite hydrogels, were prepared according to the co-precipitation method previously described in *Sections 4.3.2* and *5.2*. In order to remove water freeze-drying (under low pressure) and air-drying methods were employed. The results were different; by freeze-drying, powdered composite were obtained whereas the second route leads to solid ceramic-like composites. The macromorphology of various types of composite samples are presented in *Figure 5.3.3*. They are described below the picture. The dried composites can uptake water and consequently, they swell up to a certain limit which is a function of composition. A general scheme that presents both drying and swelling processes of composite samples is shown in *Figure 5.3.4*. In this sense, three routes can be discussed. The routes (*A*) and (*C*) indicate in the right part the drying processes that take place either at the room temperatures or elevated ones (up to 100^{o}C), in the presence and absence of salt solutions ($CaCl_2$), added in some cases before drying.

Figure 5.3.3 Macromorphology of composites (50:50 wt%) made of Atlantic shrimp chitosan, TM 1238; Primex, Iceland. The sample descriptions are given below the picture.

1- composite hydrogel suspended in alkaline solution as formed after the co-precipitation

2- composite hydrogel collected by filtration

3- freeze-dried composite hydrogel

4- air-dried composite hydrogel (it contains $CaCl_2$ added before drying)

5- air-dried composite hydrogel, salts free

6- swollen air-dried composite in water at pH = 7

7- freeze-dried composite as suspended in water at pH= 7

The drying temperature must not exceed 100^{o}C to avoid the oxidation of chitosan. Both routes labelled as (*A*) and (*C*) lead to solid compact composites, as seen in *Figure 5.3.3* (4,5). They can be re-swollen in water, the processes are shown in the left part of the sketch, but the initial soft hydrogel state cannot be again reached. The maximum amount of water that is absorbed in compact composites was about 65-70%, which is a function of chitosan type and composite composition. The route labelled by (*B*) in the right part describes freeze-drying. By following the route (*B*), a powdered composite is obtained. The re-swelling of the powdered composite in bidistilled water leads to the initial soft hydrogel state of composite, seen in the sketch on the left part as route (*B*). This is a reversible process, being figured out in the sketch with a closed doted circle. Since the rest of processes were irreversible, they

were figured out through open doted circles. The drying routes, labelled as (*A*) and (*C*), exhibits no reversibility. Thus, the transition phenomena from a soft hydrogel state of composite [seen in *Figure 5.3.3* (2)], to a tough and rigid material [seen in *Figure 5.3.3* (5, 6)], take place due to the reorganization of the composite network structure during drying processes.

A simple mode to monitor the drying process is to consider the ratio between the mass of the specimen at a certain drying time, m_t, and its initial mass, m_i, m_t/m_i as a controlling parameter. The drying decay curves were obtained by plotting the m_t/m_i against the drying time.

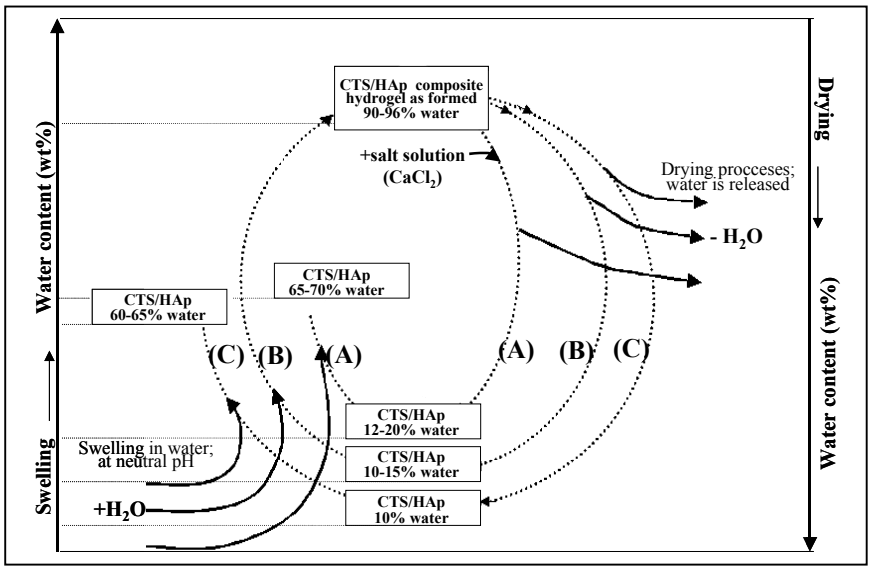

CTS is the abbreviation for chitosan, CTS/HAp is the abbreviation for composite 50:50 wt%.

Figure 5.3.4 Sketch of drying and swelling processes of composite samples. The routes labelled as (A), (B) and (C) are described as follows.
(A) A drying process at either room temperature or at elevates temperatures (50-90^{o}C, in the oven). $CaCl_2$ solution was added and incorporated before drying the composites.
(B) A drying process which takes place by freeze-drying.
(C) A drying process either at the room temperature or at the elevated temperature (50-90^{o}C, in the oven), without adding salt.
The right part of the sketch illustrates the drying processes whereas the left one presents the swelling processes.

The drying decay curve (moisture level decay curve) profiles of composites varying by their composition are displayed in *Figures 5.3.5-5.3.7*- (1). Various types of composite samples lead to different drying patterns (different slopes and different drying times), as seen in *Figures 5.3.5-5.3.7*- (1). Among the series of composite samples, with the same composition, labelled with the same letter, one can observe that different amounts of composite hydrogel lead to different drying slopes. The drying decay curve derivatives are

shown in *Figures 5.3.5-5.3.7*, inset (*2*). Therefore, for the investigated disk samples, the transition period from the soft hydrogel state to the physically stabilized network was estimated. The stabilised network was achieved by increasing the crosslinking density in the network as a result of water release processes. Due to a broad transition, the moisture content associated with the transition, using this method, could not be exactly determined. From these experiments, one could estimate that the irreversible transition takes place at moisture content between 40 and 60 wt%.

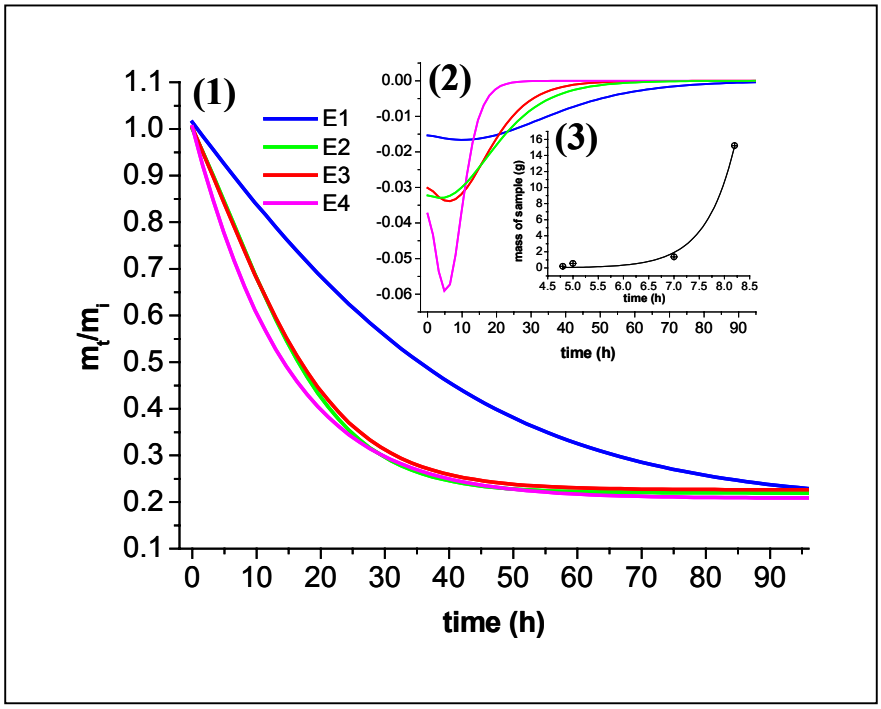

Figure 5.3.5 Chitosan/HAp 100:0 wt% composite samples. The drying decay curves for the samples E_1, E_2, E_3 and E_4 are shown in the main graph. The data were fitted with Sigmoidal functions. The inset (2) displays the derivatives of the drying curves. The inset (3) shows a plot of the initial hydrogel weight against the estimated transition time, evaluated from the minima of derivative curves.

As previously discussed, during drying of composite hydrogels, irreversible structural changes take place. The water release rate is slower at the beginning and at the end of the process and increases in the middle period of drying. The observation is shown by the slope of the graph which changes during drying.

The curves end up with plateaus, where constant weight is reached, as seen in *Figures 5.3.5-5.3.7- (1).*

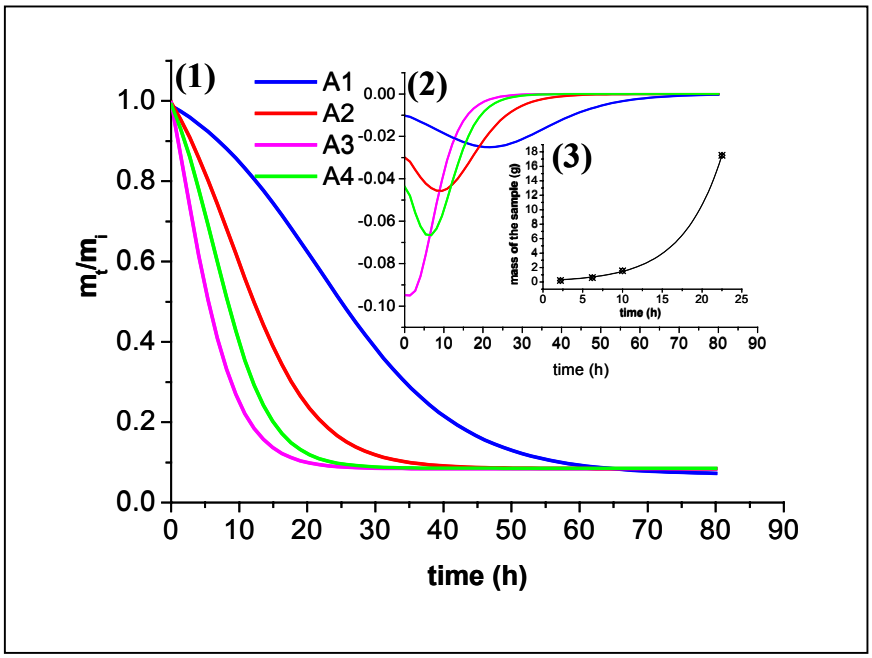

Figure 5.3.6 Chitosan/HAp 50:50 wt% composite samples. The drying decay curves of samples A_1, A_2, A_3 and A_4 are shown in the main graph. The data were fitted with Sigmoidal functions. The inset (2) displays the derivatives of the drying curves. The inset (3) shows a plot of the initial hydrogel weight plotted the estimated transition time, evaluated from the minima of derivative curves.

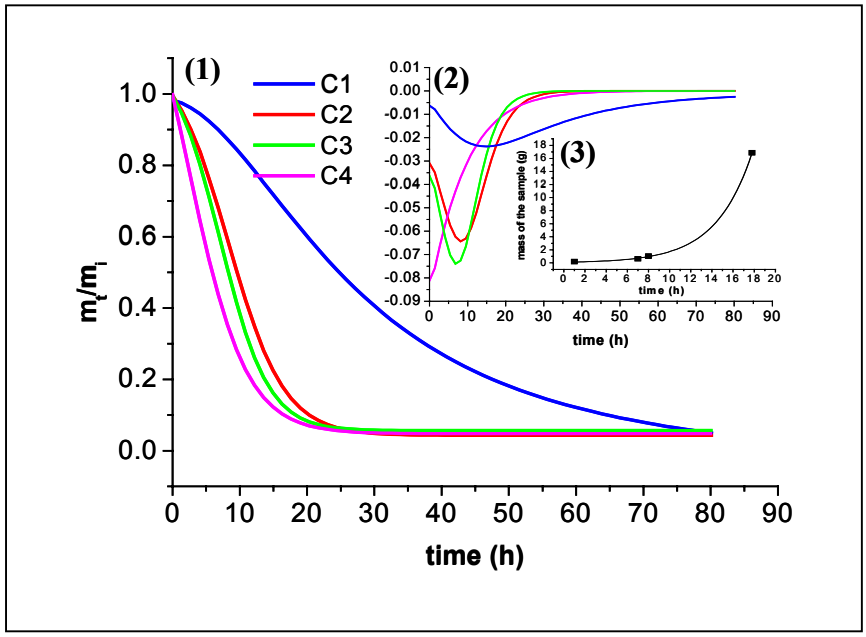

Figure 5.3.7 Chitosan/HAp 40:60 wt% composite samples. The drying decay curves for the samples C_1, C_2, C_3 and C_4 are shown in the main graph. The data were fitted with Sigmoidal functions. The inset (2) displays the derivatives of the drying curves. The inset (3) shows a plot of the initial hydrogel weight against the estimated transition time, evaluated from the minimua of derivative curves.

The first time domain of the drying curves of samples (A_1-E_1) is displayed in *Figure 5.3.8.* As shown in figure, at the beginning, until about 12 h, the curves are approximately overlapped. Later, they evolve according to different kinetics and therefore exhibit different slopes. The water release rate in the case of chitosan was slower as compared to the composite hidrogel samples, since the drying decay curves of composites are lying below the chitosan drying curve.

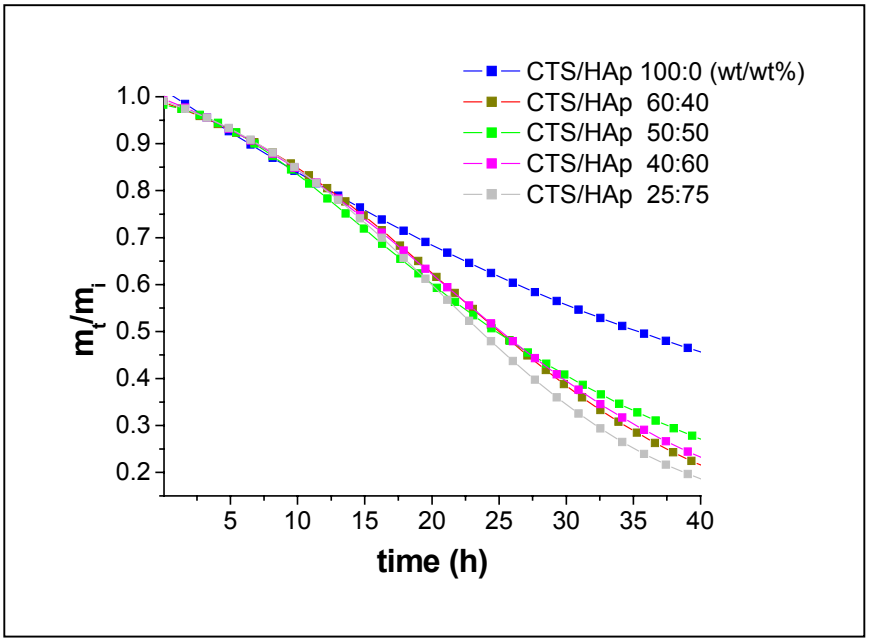

Figure 5.3.8 The first time domain of the drying decay curves of composites labelled by A_1, B_1, C_1, D_1, and E_1, (described in Table 5.3.1). The data were fitted with Sigmoidal functions. CTS is the abbreviation for chitosan.

The water release rate in the middle time domain of drying is a function of composition. The derivatives of drying curves show minima, which are sharper or broader, depending on the initial hydrogel amount, as seen in *Figures 5.3.5- 5.3.7-(2)*. The initial amount of samples plotted against the estimated transition time (given by the valley position of the derivative curves) might lead to a linear dependence as the amount of the sample increases. In spite of using the same disk shaped composite gel samples, this linearity was not observed, as seen in *Figures 5.3.5-5.3.7-(3)*. Deviations from the linearity at the bigger disk samples appeared. The biggest disks behave like a flat cylinder at start. Cylinder shaped gel samples exhibit different drying-swelling kinetics[165] compared to those of disk shaped samples. For our experimental purposes, since the shrinking coefficients of the samples with the same composition show close values, the samples were considered as disks.

5.3.4.1 Evaluation of shrinking coefficients of composites

The ratio between the initial volume of the hydrogel and its final volume (measured for the dried composite), V_i/V_f, defined as the shrinking coefficient, *Sc*, was experimentally determined by using the method described in *Section 4.2.10.1*. They were determined for the disk shaped samples (series A_i-E_i). For the same type of sample, S_c values were averaged. Among the investigated samples, the chitosan sample (seen as *chitosan/HAp 100:0 wt%*) exhibits the smallest shrinking coeficient whereas the composite samples exhibit greater ones. The results are comprised in *Table 5.3.2*.

Table 5.3.2 Shrinking coefficient values of disk shaped composite samples.

***CTS*/HAp 50:50 (wt%)* Moisture content 91.8 wt%**		***CTS/HAp 40:60 (wt%)* Moisture content 95.1 wt%**		***CTS/HAp 60:40 (wt%)* Moisture content 92.4 wt%**		***CTS/HAp 25:75(wt%)* Moisture content 90.3 wt%**		***CTS/HAp 100:0 (wt%)* Moisture content 95.7 wt%**	
Sample code	Shrinking Coefficient. ($V_{initial}$/ V_{final})	Sample code	Shrinking Coefficient. ($V_{initial}$/V_{final})	Sample code	Shrinking Coefficient ($V_{initial}$/ V_{final})	Sample code	Shrinking Coefficient ($V_{initial}$/ V_{final})	Sample code	Initial Shrinking Coefficient ($V_{initial}$/ V_{final})
A1	22.63	B1	25.85	C1	18.95	D1	25.30	E1	17.36
A2	23.28	B2	26.82	C2	18.07	D2	24.60	E2	18.59
A3	21.07	B3	27.22	C3	23.6	D3	25.12	E3	17.12
A4	19.38	B4	23.69	C4	20.82	D4	25.83	E4	17.38
S_c**(A_i) = 21.6±2.15		S_c (B_i) = 25.9±2.05		S_c(C_i) = 20.3±2.50		S_c(D_i) = 25.2±0.80		S_c(E_i) = 17.60±1.0	

** CTS is the abbreviation for chitosan.*

*** Sc values are given as mean ± SD, calculated for four determinations.*

It can be observed that the shrinking coefficient values are depending on the sample composition. The results are within the literature data reported for the physically crosslinked gels networks[178].

5.3.4.2 Determination of the swelling capacity of composites

The sample diameter at different swelling stages was determined using an electronic digital calliper and a magnifying glass (10X-Bima). The normalised diameters, $\Delta d/d_0$, were plotted against the swelling time (*Figure 5.3.9*). Δd describes the growth of sample diameter while d_0 is the initial sample diameter. The plateaux domains[179] from the swelling curves characterize the equilibrium state of the swelling processes, as seen in *Figure 5.3.9*. The

swelling curves are lying with respect to the sample composition. The more the amount of chitosan in composites the higher the level of swelling.

5.3.4.3 Determination of swelling cooperative diffusion coefficients

The composite hydrogel entrap water due to the porous structures and as a result of the presence of hydrophilic components (chitosan and *HAp*). When a dry hydrogel begins to absorb water, the first water molecules entering the network will hydrate the most polar, hydrophilic groups, leading to primary bound water. As the polar groups are hydrated, the gel network swells and consequently the hydrophobic groups are exposed and can interact with water molecules, leading to the hydrophobically bound water, known also as weakly bound water (*see Section 5.8*). After the polar and hydrophobic sites have interacted with water molecules, the gel network will adsorb additional water, due to the osmotic driving force within the interconnected networks of gel microchannels towards 'infinite dilution'. To this additional water adsorption, the physical crosslinks by an elastic retraction force are opposed. Thus, the hydrogel network will reach an equilibrium swelling state (seen as plateaus in the *Figures 5.3.9*). The additional swelling water is called free water or bulk water and it is assumed to fill up the center of the larger pores (micropores).

The incorporation of water changes the internal structure of the composite network and implicitly its mechanical properties. The composites become more flexible compared to the dried ones, which exhibits in some cases a brittle behaviour.

The rate of swelling is a function of swelling cooperative diffusion coefficients and implicitly a function of sample composition. The swelling cooperative diffusion coefficients were determined for disk shaped samples according to a method proposed and developed by Li and Tanaka[165] (*Sections 4.2.10.2*, *4.2.10.3* and *Appendix A-IX*).

At the maximum swelling capacity, their diameters reached the maximum values (d_∞). From the logarithmic plot of $ln\, y = \ln\left(\frac{d_\infty - d_t}{d_\infty - d_0}\right)$ against the swelling time, some structural parameters of the hydrogel network were determined[166] (*Figure 5.3.10*). The fitting parameters as determined, the structural parameters of composite hydrogel network (B_1, τ_1, α, R) as well as the corresponding values of swelling diffusion coefficients are comprised in *Table 5.3.3*. The values of diffusion coefficients are depending on the type and composition of the sample.

5 Experimental Results and Discussions

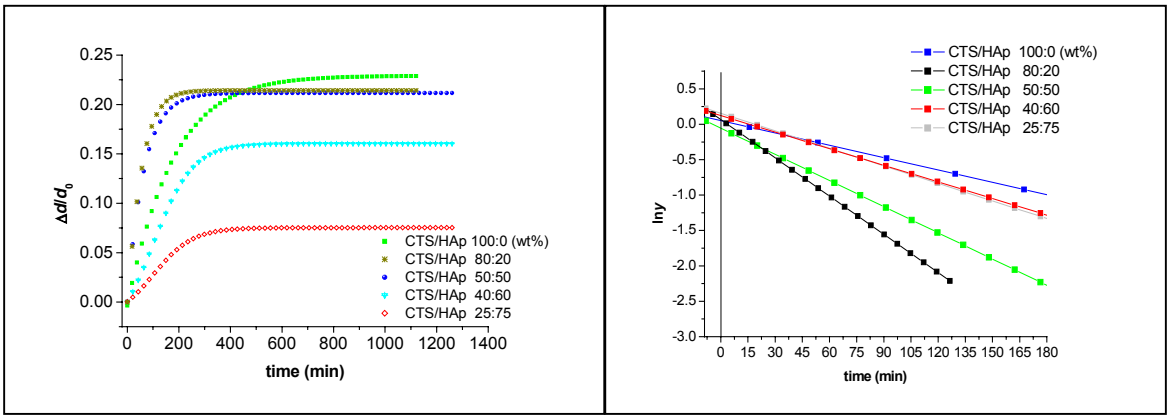

Figure 5.3.9 Swelling curves of composites in bidistilled water.
CTS is the abbreviation for chitosan.

Figure 5.3.10 $\ln y = \ln\left(\frac{d_\infty - d_t}{d_\infty - d_0}\right)$ *plotted versus the swelling time for composites with different ratios between chitosan and HAp.*

Table 5.3.3 Summary of the fitting parameters (obtained from logarithmic plot), the composite gel network parameters (R, α_1, τ_1, B_1) and the cooperative diffusion coefficients (determined from the swelling processes).

Sample	a_∞ (cm)	Fitting parameters (linear fit)	R	α_1	τ_1 (min)	B_1	Cooperative diffusion coefficient* (10^{-6} cm^2/s)
CTS#/HAp 100:0 wt%	0.105	*$r^{2,}$ ****=0.996 A**= 0.05258 B***= -0.00581*	0.60	1.2	19.02	0.994	20.2±3.1
CTS/HAp 80:20 wt%	0.060	*r^2= 0.977 A=0.06755 B= -0.01802*	0.60	1.2	16.60	0.982	8.3±0.9
CTS/HAp 50:50 wt%	0.060	*r^2= 0.992 A= -0.05369 B=-0.01233*	0.60	1.2	18.63	0.987	7.6±1.1
CTS/HAp 40:60 wt%	0.060	*r^2=0.989 A= 0.12398 B= -0.00781*	0.42	1.8	8.07	0.999	6.9±0.8
CTS/HAp 25:75 wt%	0.040	*r^2= 0.977 A= 0.15747 B= -0.00827*	0.18	2.2	6.35	0.991	2.6±0.5

**The values are given as mean ± SD taken for three determinations*
***A is the intercept term (or constant)*
****B is the slope of linear plot*
***** r^2 is the linear regression coefficient*
#CTS is the abbreviation for chitosan

The plot of the swelling diffusion coefficients as a function of chitosan content is shown in *Figure 5.3.11.* The graph displays an increasing trend from *chitosan/HAp* 15:85

wt% to *chitosan/HAp* 100:0 wt% sample. These values are within literature data reported for some other hydrogel networks. Based on Li – Tanaka's gel model, Saiz *et al.* [166] have determined the cooperative swelling diffusion coefficients for various polyacrylamide gel samples. They have determined values between 9 and 11.40x10^{-6} cm^2/s. Zhang *et al.* [180] have used an electrochemical method to determine the diffusion coefficients of polyacrylamide gels. In their case, the swelling diffusion coefficient values ranged between 4.4 and 6.4x10^{-6} cm^2/s. In our case, for the composite samples, the diffusion coefficients were between 2.6 and 8.3x10^{-6} cm^2/s. Chitosan showed the greatest diffusion coefficient among the investigated samples of ca. 20 x10^{-6} cm^2/s.

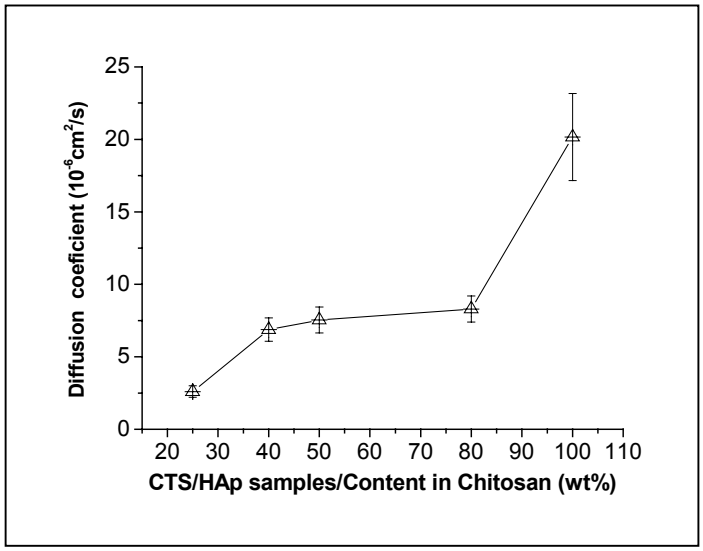

Figure 5.3.11 Cooperative diffusion coefficients of composite samples plotted as a function of chitosan content. The points are simple connected. CTS is the abbreviation for chitosan.

5.3.5 Conclusions

By using the drying experiments, the shrinking coefficients of the disk shaped composite samples were determined.

The drying procceses of composite hydrogel samples is complicated being influenced by many factors such as the shape of the sample, its initial moisture content, the type of chitosan, the enviromental factors, etc.

According to Li –Tanaka's gel model, the swelling diffusion coeficients of different types of composites were determined.

5 Experimental Results and Discussions

5.4 Structure and properties of composite hydrogels

Materials

Composites as hydrogel and powdered freeze-dried samples were analysed.

Methods

i) Analysis of composite morphology (by microscopic techniques).
ii) Analysis of external surface area (by *BET* method).
iii) Monitoring the mass loss of composite hydrogels as a function of temperature, using a *TGA* technique.

Instrumentation

Optical microscope, *OM*; type Olympus AX 70, objective 20X;
Transmission Electron Microscope, *TEM*; type EM 902 (Zeiss);
Scanning electron microscope, *SEM*; type BS 340 (Tesla);
BET surface analyzer; type TriStar 3000 V3; adsorption gas N_2;
Thermogravimetric analyser, *TGA*; type Thermowaage Linseis L 81;
Energy disperse X-ray spectroscopy, *EDS*; as incorporated device in a *SEM* system type Jeol 6310, Oxford Instruments AN 10 000-EDS-XR;

The sample preparation procedures were described in *Section 4.2.3*.

After the preparation of composite samples as hydrogel, we try to answer to those questions concerning their structure.

- *How are the components (chitosan and CPs crystallites) structured in the composite hydrogel?*
- *What is the size range in which the inorganic CPs crystallites lie?*
- *How can be probed the presence of chitosan and of HAp in composites?*
- *Do they have a homogenous or a non-homogenous structure?*
- *How big are the external surface areas of the composite hydrogel networks?*
- *What is the water retention range of the composite hydrogel samples?*

In order to answer to these questions, different experiments using microscopic techniques, *BET* measurements and *TGA* analyses were performed.

5.4.1 Preliminary characterization by microscopic techniques

5.4.1.1 Optical microscopy (*OM*)

One of the simplest ways to investigate the composite hydrogel samples is to use *OM* technique. The images were taken on a composite hydrogel 50:50 wt% as formed after its co-precipitation. The composite hydrogel was prepared using a krill chitosan (*2K2X*) see *Sections 4.1* and *5.1.1*. The composite sample was investigated by *OM* without any additional preparation steps. As shown in *Figure 5.4.1*, the composite hydrogels are composed of small micro-gel domains that are joined in large macro-gel domains (aggregates). Since the samples

are white-semitransparent, it was difficult to obtain high quality optical images due to the multiple reflection of the light on the sample. One could not get a clear-focused *OM* images.

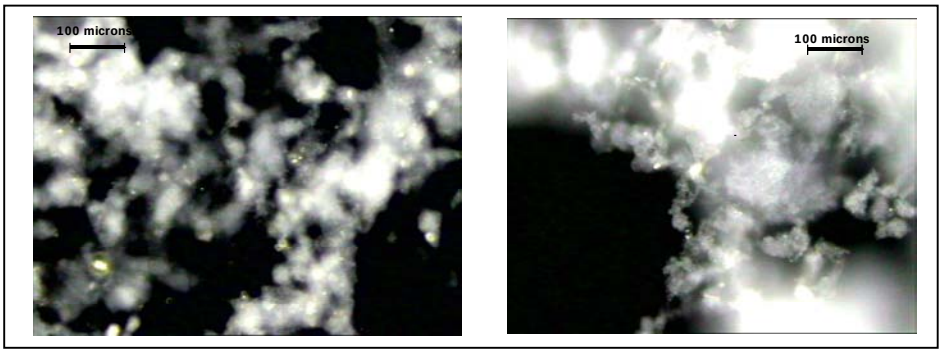

Figure 5.4.1 OM images of the composite hydrogel.

The inorganic crystallites (as *CPs*) cannot be distinguished at this level of magnification. This suggests that the composite hydrogels might have a homogenous structure (most probably structured at the nanolevel scale).

5.4.1.2 Electron microscopic investigations (*TEM* and *SEM*)

In order to obtain information about the network structure of composite hydrogels, *TEM* measurements were performed.

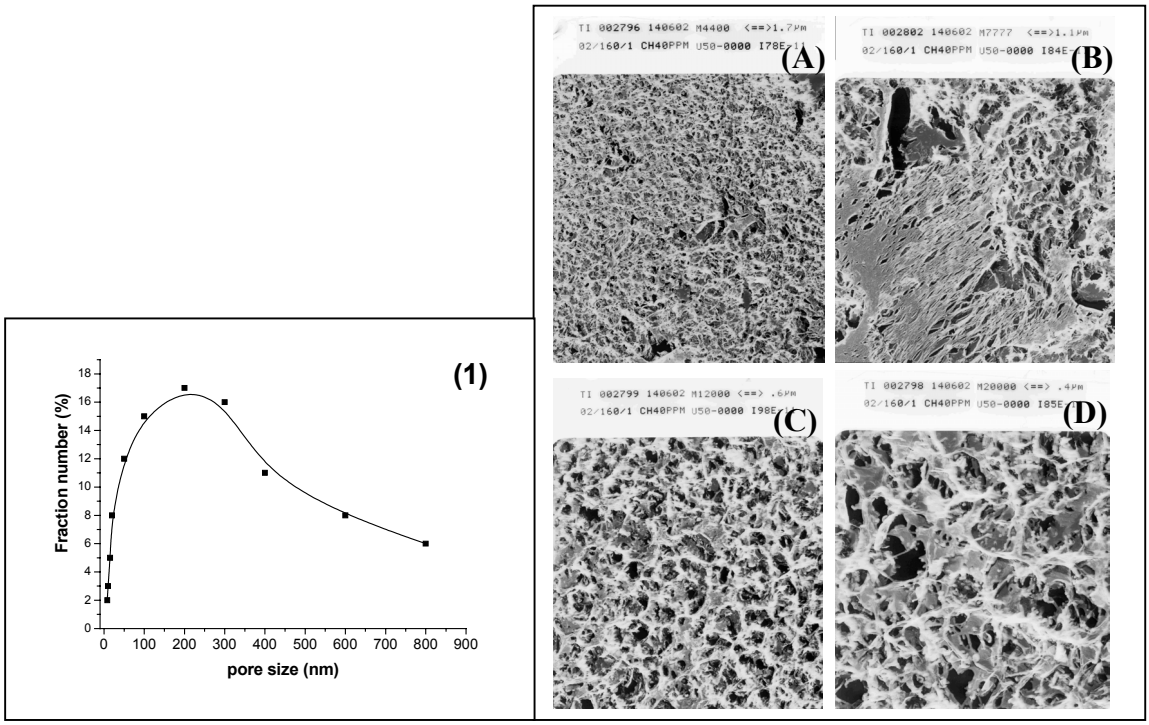

Figure 5.4.2 TEM micrographs of chitosan/HAp 50:50 wt% composite hydrogel at different magnification levels, in an increasing order of magnification from A (scale bar 1.7μm) to D (scale bar 0.4μm). The graph (1) displays the pore size distribution of the hydrogel network.

5 Experimental Results and Discussions

The composite sample used in these experiments was prepared from Atlantic shrimp chitosan (*TM 1238, Primex*).

- *The first scope of these experiments was thought to obtain information about the three-dimensional structure of the hydrogel structure with water entrapped in the network.*
- *The second scope was to see how the freeze-drying process affects the structure of the composite hydrogel.*

The three-dimensional *(3d)* structures of composite hydrogels at different magnification levels are shown in *Figure 5.4.2 (A, B, C, D)*. From the micrographs, it can be deduced that the composite hydrogel presents a porous gel network structure. The network structure is mostly achieved by physical crosslinking through the hydrogen bonds formed between the chitosan chains. The average pore size of the hydrogel network was estimated to be about 200-300 nm, as shown in *Figure 5.4.2, graph (1).*

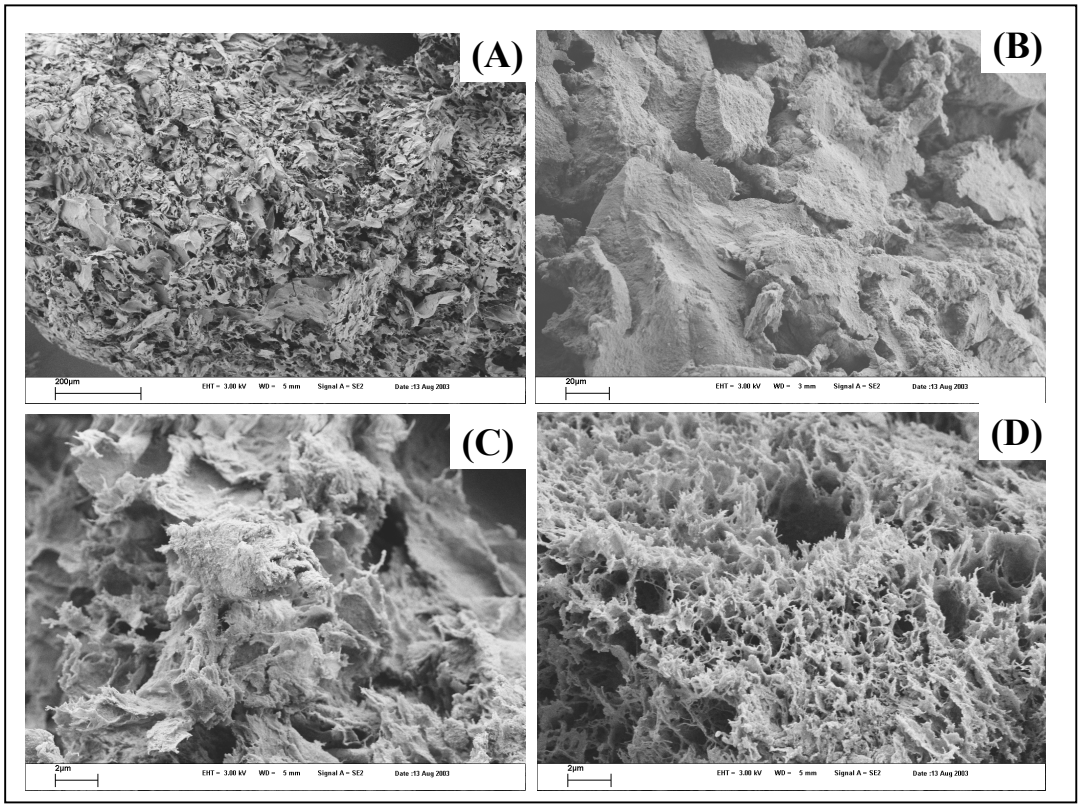

Figure 5.4.3 SEM micrographs of a solid chitosan/HAp 50:50 wt% freeze-dried composite.

In the large pores of composite hydrogels, the free water (known as bulk water) is accommodated while in the small pores the bound water is constrained. The analysis of these types of water, which occur in the composite hydrogel network, is discussed in *Section 5.8.* The pore size ranges from few nanometers up to few hundreds of nanometers. The morphology of the hydrogel network does not reveal the inorganic fillers of *CPs*. Regarding

the second scope, the solid freeze-dried composite hydrogels (as powders), by using *SEM* were analyzed. The morphologies of composites showed interesting structural features.

As seen in the micrographs, both porous and compact structures were identified [*Figure 5.4.3 (A-D)*]. The porous regions exhibit a spongy-like structure, formed due to the presence of chitosan as the polymer matrix[181], as seen in *Figure 5.4.3 (C, D)*. There are also other regions, where compact structures were identified, as seen in *Figure 5.4.3 (B)*. For further morphological investigations, a compact region of the composite was magnified, as seen in *Figure 5.4.4 (A)*. The micrographs revealed the fine structures of composite, as seen in *Figure 5.4.4 (C, D)*. The sphere-like *CPs* particles with diameters between 30 and 70 nm were attributed according to their shape, to be composed of amorphous calcium phosphates phases[62], *ACPs*. These particles are located in some regions from the outer part of the freeze-dried network and occur in composites in small amounts, besides *HAp*.

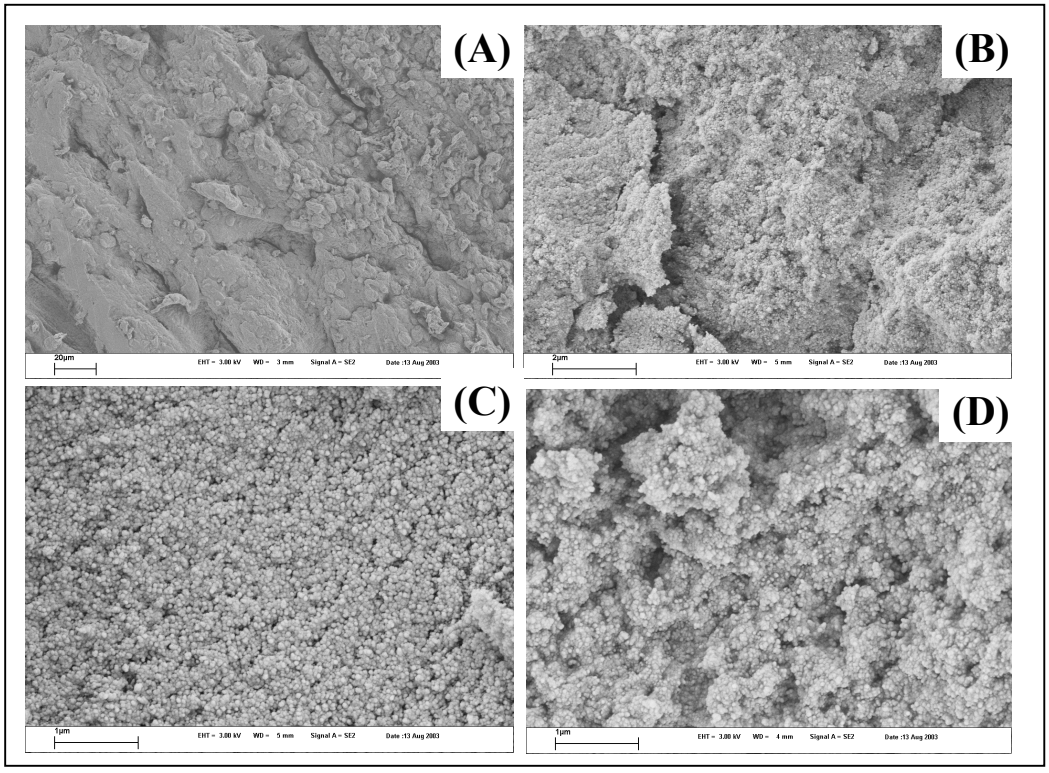

Figure 5.4.4 SEM micrographs of a freeze-dried chitosan /HAp 50:50 wt% composite samples, in a compact area at different magnification levels.

Energy dispersed X-ray spectroscopy, *EDS*, was employed during *SEM* measurements. By using this technique, the emission spectrum of elements, which compose the composite sample, was recorded. The spectra measured for two types of composites with different proportion between chitosan and *HAp* are shown in *Figure 5.4.5*. The characteristic elemental peaks were obtained. The emitted X-ray radiation depends on the type of element.

Elements, such as C, O, P and Ca were identified, and by their presence, probed the qualitative composition of composites. Unfortunately, this technique is only qualitative or semi-quantitative[182].

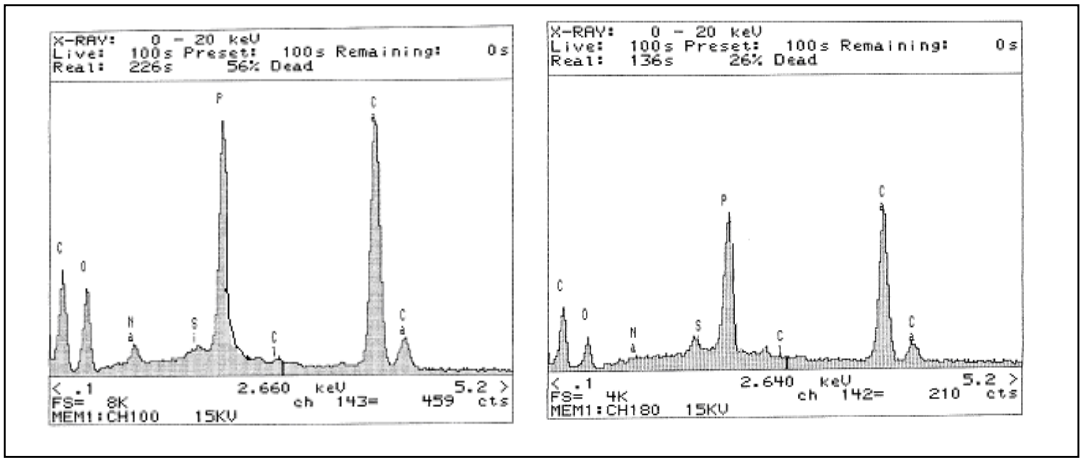

Figure 5.4.5 EDS spectra of composites.

5.4.2 External surface area of freeze-dried composites

The surface area and the particle size (spherical approximation) were measured by liquid N_2 adsorption onto freeze-dried composites. Due to its porous structure and content of nanoparticles, the external surface area of composite is expected to be very large with respect to its mass (expressed in m^2/g). In order to determine the surface area, *BET* measurements were performed. The main goals of these experiments were to establish the range of the external surface area of the powdered freeze-dried composites and implicitly to determine the mean particle size of composites using the spherical approximation, according to *Equation 5.4.2-1*. Another goal was to see how the external surface area of composites is influenced by the composition. Various types of composites, as listed in *Table 5.4.1* were measured. They were prepared using crab chitosan (*Lot. no. 114F-014*, *Sigma*). The external surface area, using *BET* and Langmuir methods (see *Appendix XI*), as well as the mean particle size diameter of composites were determined (*Table 5.4.1*).

Table 5.4.1 Summary of surface area of powdered freeze-dried composites.

Chitosan/HAp composite Content in apatite (wt/wt%)	*BET* surface area (m^2/g)	Langmuir surface area (m^2/g)	True sample density (compact specimen) (g/cm^3)	Particle size diameter (mean value) (spherical approximation) (μm)
20	38.779	53.562	1.25	0.123
50	34.880	48.337	1.50	0.114
70	93.928	127.835	1.70	0.038
85	109.786	151.910	1.90	0.029

The mean particle size diameter can be determined according to the following equation,

$$d = \frac{6}{S_0 \rho} \ (\mu m) \qquad \textit{(5.4.2-1)}$$

where d is the mean particle size diameter, S_o is the *BET* surface area and ρ is the true sample density (determined for compact specimens, air dried). The external surface area ranges from 30.99 m^2/g for the *chitosan/HAp* 80:20 wt% composite sample up to 151.91 m^2/g, value obtained in the case of *chitosan/HAp* 15:85 wt% composite sample.

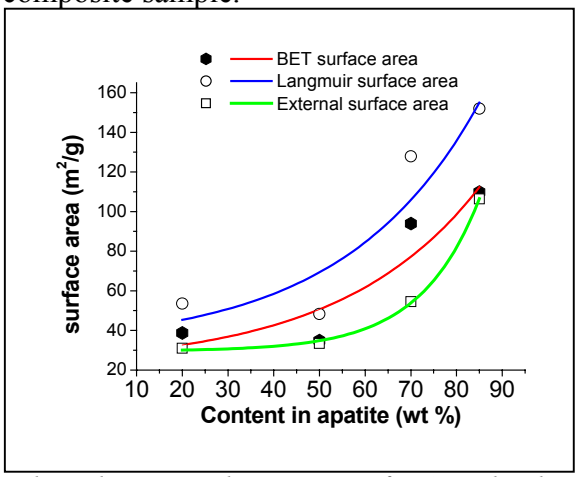

Figure 5.4.6 External surface area of composites plotted against the content of HAp. The data were fitted by using monoexponential functions.

The curves (seen in *Figure 5.4.6*) show an exponential increasing trend as the *HAp* content increases. The mean particle size, obtained by using the spherical approximation, emphasize the presence of nanoparticles in the composites.

5.4.3 Thermogravimetric measurements on composite hydrogels

Materials

Composite hydrogel samples (*chitosan/HAp* 50:50 wt%), in different drying stages, were investigated. They were prepared using a krill chitosan (*2K2X*). The samples are labeled as follows.

S_1 original composite hydrogel as formed after the co-precipitation at pH 7;
S_2 solid composite sample obtained after drying of S_1 for 18 h at 60ºC;
S_3 solid composite sample obtained after drying of S_1 for 24 h at 60ºC;
S_4 solid composite sample obtained after drying of S_1 for 36 h at 60ºC;

Temperature program: The temperature was raised from 25°C up to 500°C at a constant rate of 20°C/min. The measurements were carried out in air (flow rate of 1mL/min). The method is discussed in *Section 4.2.7* and in *Appendix A-VII*. Since all the samples contain chitosan, the thermograms show features of chitosan decomposition[183]. The samples S_2, S_3, and S_4 show three plateaus while S_1 exhibits only two plateaus because of its high moisture content,

see *Figure 5.4.7*. The first order derivatives reveal the temperatures at which the maximum decrease of mass occurs (as seen in *Figure 5.4.8* and *Table 5.4.2*).

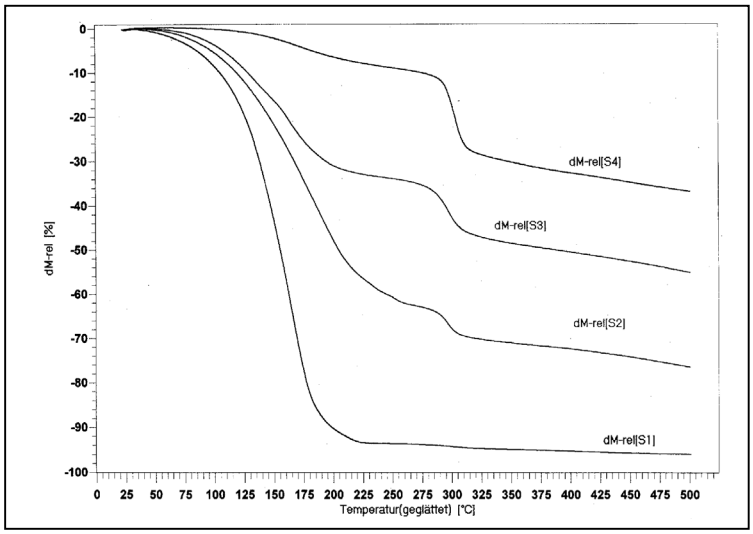

Figure 5.4.7 Thermogram patterns of samples S_1 - S_4.

Table 5.4.2 Summary of thermogravimetry results

Sample code	Initial weight of sample	T1** Δ-M / min * Δ-M (mg /%)	T2** Δ-M / min * Δ-M (%)	Δ-M total (mg / %)
S_1	87.00 mg	165.2 ºC 27.03 mg/min 81.28 mg /93.4%	-	81.28 mg / 93,4 %
S_2	66.50 mg	195.3 ºC 9.04 mg/min 41.72 mg / 63.7 %	223.3 ºC - 8.98 mg	50.82 mg / 76.2 %
S_3	46.20 mg	163.8 ºC 4.8 mg/min 15.63 mg / 33.8 %	297.7 ºC 5.99 mg/min 9.82 mg / 21.3 %	25.49 mg / 55.1 %
S_4	90.20 mg	201.8 ºC 8.79 mg / 9.7 %	305.1 ºC 21.08 mg/min 24.56 mg / 27.2 %	33.44 mg / 37.0 %

**At the maximum reaction rate*

*** Transition temperatures (T1 and T2) between two plateaus domains*

The loss of free water occurs at maximum rate between 165^o and 202ºC (T1) whereas T2 reflects the loss of bound water and the possible decomposition of the chitosan matrix. The moisture content of samples was calculated from the first decomposition step, between the first two plateaux. In the case of the original composite hydrogel, S_1, the moisture content was 93.4% while the drying time increases for the S_2 – S_4 decreased moisture content values were obtained. The moisture values indicated a slow release kinetic of water from the composite hydrogel samples.

5 Experimental Results and Discussions

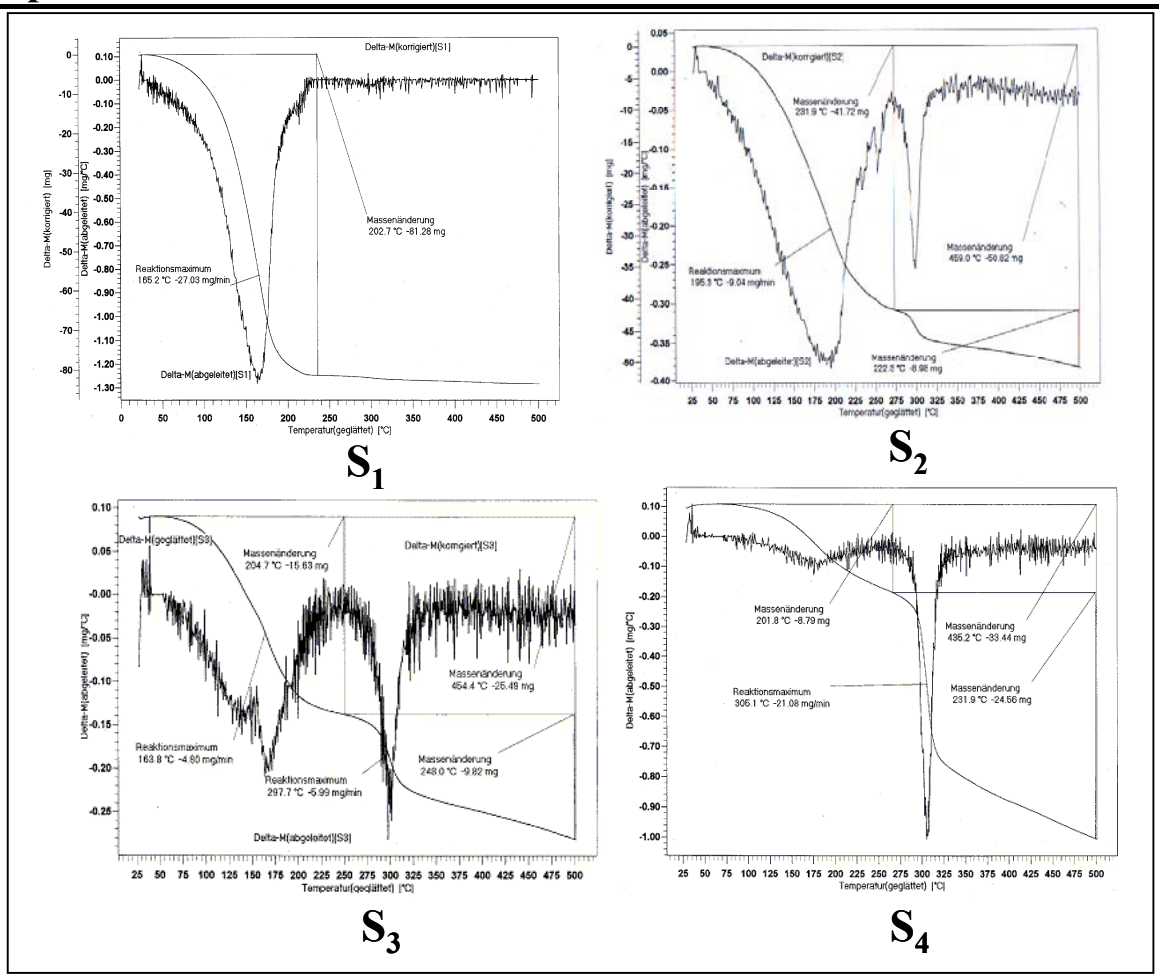

Figure 5.4.8 First order derivatives of thermograms of samples S_1 - S_4.

5.4.4 Conclusions

The composite hydrogel samples exhibit a typical gel network structure as probed by *TEM* measurements. The hydrogel network structure is achieved due to the presence of chitosan as a polymer matrix, which generates the crosslinking domains through the hydrogen bonds between the chains. The calcium phosphate fillers, *CPs*, which reinforce the chitosan matrix, are in the nanosize range, as shown by *SEM* measurements. By using *SEM* coupled with *EDS*, the qualitative presence of both chitosan and *CPs* in the composites (through their elemental characteristic peaks) was identified. *BET* measurements confirmed the presence of *CPs* nanoparticles in the composites. The water holding capacity of composite hydrogels was determined by *TGA* to be about 90-95 wt%. In order to obtain more information regarding the *CPs* type, some other experimental techniques of investigations such as *XRD* and *TEM* on solid composites must be employed. Thus, the type of *CPs* as well as its particle size distribution within the chitosan matrix it is expected to be determined.

5 Experimental Results and Discussions

5.5 Zeta potential and particle size distribution measurements

5.5.1 Evaluation of particle size

The goals of these experiments were on one side to determine the size distribution of both composite micro-gel domains and CPs particles, which reinforce the composite matrix. On the other side, the zeta potential variation during the composite formation was studied and the influence of ionic strength on zeta potential behaviour of composites was investigated, too.

From a composite hydrogel (50:50 wt%) made of krill chitosan (*2K2X*) four types of samples according to the following methods, were prepared.

- A composite hydrogel sample was dispersed by sonication in bi-distilled water for 20 min. Before measurements, the sample was filtered through a cellulose membrane with pore size 0.8μm. The sample is labelled as *S3N* and it contains micro-gel particles.

- For the next set of experiments the chitosan matrix from the composite hydrogel was dissolved in acidic medium. Two procedures using acidic treatments were employed as follows.
  a) By using acetic acid at pH 5-6, the sample is labelled as *S1AcOH*.
  b) By using HCl, 1M at pH 1.5-2, the sample is labelled as *S2HCl*.

- In the last approach, the chitosan matrix from the composite was removed by combustion at about 800°C. The result was also the isolation of *CPs* particles. The sample was labelled as *S4HT*.

The last two set of experiments led to the isolation of *CPs* particles which reinforce the chitosan matrix.

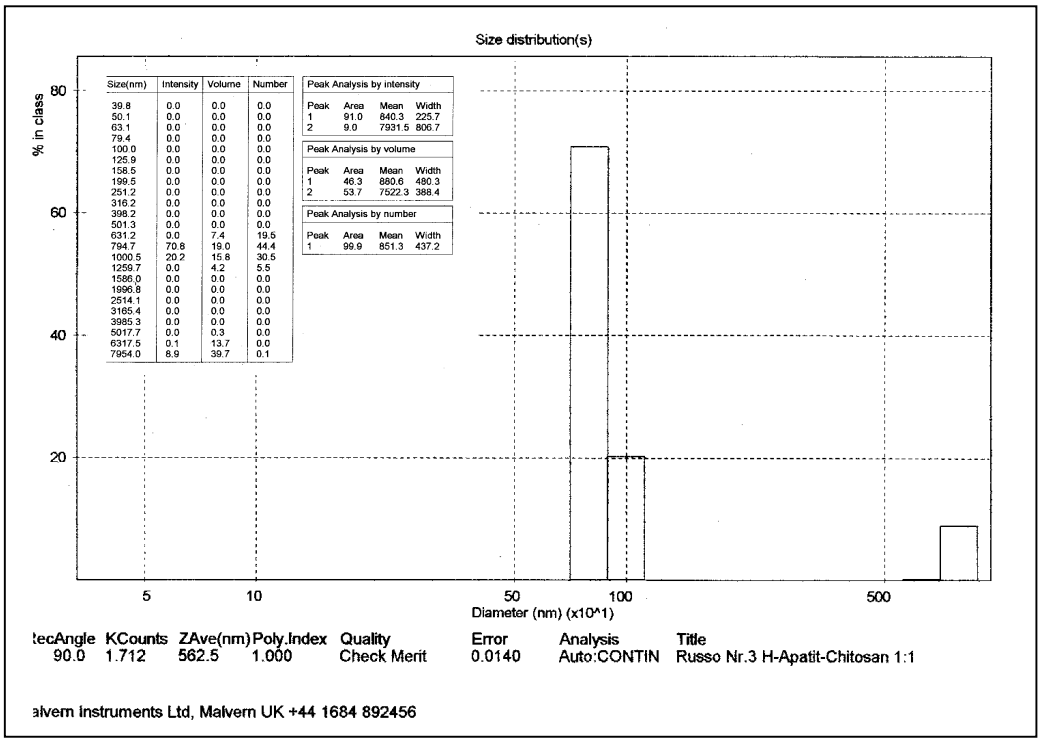

Figure 5.5.1-1 Particles size distribution of sample S3N.

5 Experimental Results and Discussions

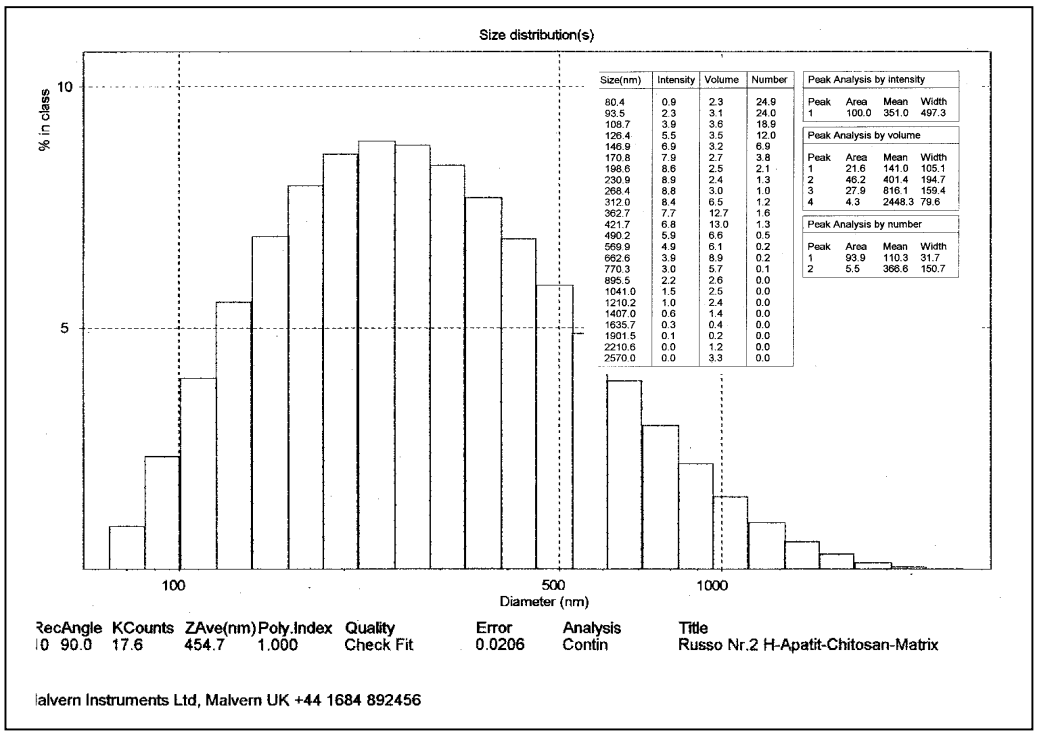

Figure 5.5.1-2 Particles size distribution of sample S1AcOH.

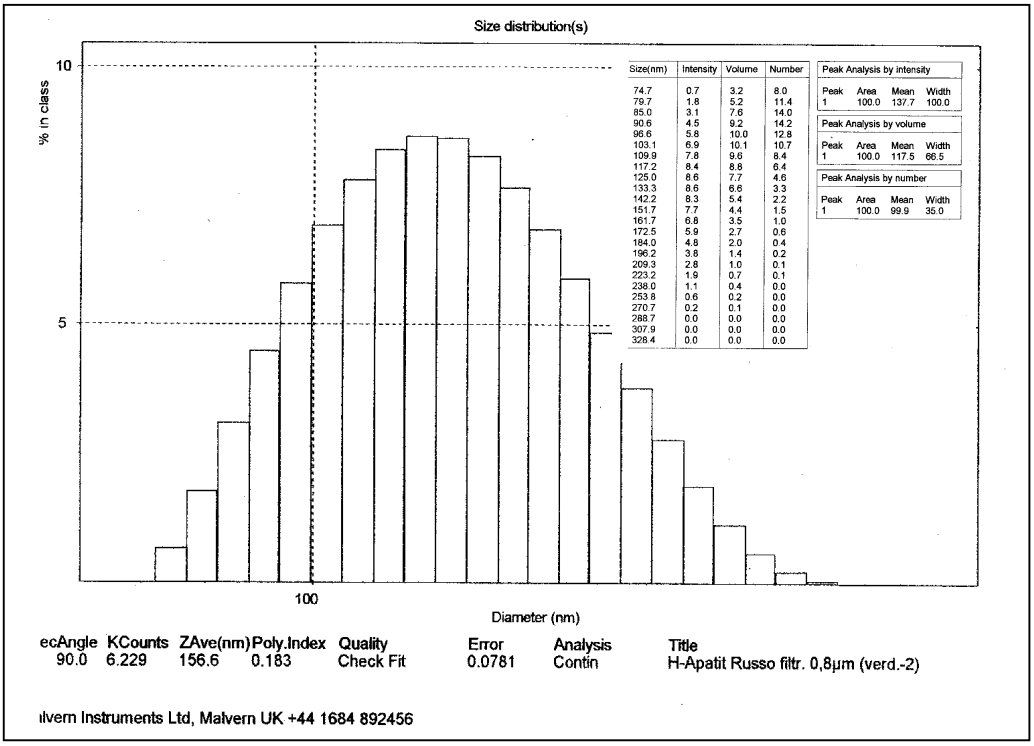

Figure 5.5.1-3 Particles size distribution of sample S2HCl.

In the case of composite hydrogel labelled as *S3N* dispersed in bidistilled water, the smallest micro-gel particles size were evaluated to be about 0.8-1 μm. The sample does not exhibit a Gaussian distribution, as seen in *Figure 5.5.1-1.*

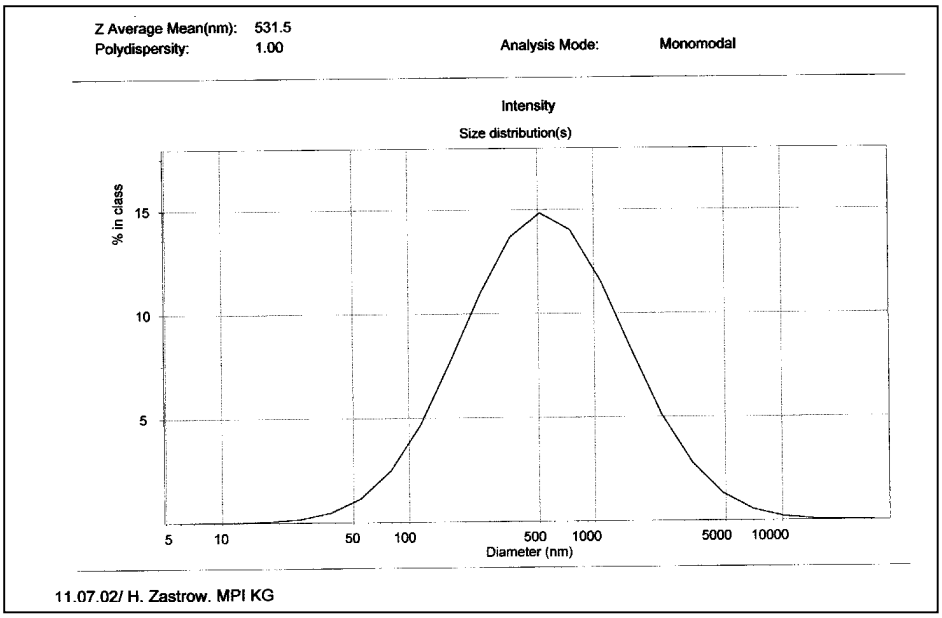

Figure 5.5.1-4 Particles size distribution of sample S4HT.

When the chitosan matrix was removed from the composite sample either by acidic treatments or by combustion, the size distribution curves approached the Gaussian profiles, as seen in *Figures 5.5.1-2 - 5.5.1-4*. Theoretically, by removing the chitosan matrix from the composite structure, the remaining particles should correspond to the *CPs* phases (mainly as *HAp*). The size distribution curves obtained using acetic acid show a broad distribution profile with the maximum value between 200 and 300 nm, as shown in *Figure 5.5.1-2.* Hydrochloric acid produced smaller particles compared to those obtained using acetic acid. The mean size is 120-140 nm as seen in *Figure 5.5.1-3*. When the chitosan matrix was removed by combustion, the size distribution curve showed that larger particles were formed as compared to those produced by the acidic treatments. The mean diameter is 500 nm, as seen in *Figure 5.5.1-4.* The results are explained by the aggregation processes of *CPs* phases, which take place at high temperatures.

5.5.2 Zeta potential measurements

a) Formation of HAp in the chitosan matrix

The formation of *HAp* in the chitosan matrix takes place mainly from brushite, as proved by *XRD* measurements (the results are discussed in *Section 5.6*). The zeta potential measurements of particles of composite hydrogel might give additional information about the

diffusion processes of ions from the bulk solution into the charged surface of composite hydrogel particles in its earlier stage of formation.

Sample preparation

The composite hydrogel sample was obtained using 100 mL of 0.5 wt% chitosan (*TM 1238*, *Primex*) solution in 1 wt% aqueous acetic acid solution at which 5 mL of 11.1 wt% $CaCl_2$ aqueous solution and 3 mL of 13.4 wt% NaH_2PO_4 aqueous solution were added. The pH value was raised from 3.4 to 12 by adding 5 wt% of NaOH aqueous solution. When the pH reached 12, a small portion of about 10 mL of composite hydrogel as aqueous alkaline suspension, was sampled and sonicated for 2 min. The variation of the ζ-potential was followed as a function of time (during formation of *HAp*, for 2.5 h), as shown in *Figure 5.5.2-1*. Every 10-15 min, a fresh portion of about 10 mL of composite hydrogel was collected, sonicated and measured. The ζ-potential values showed a decreasing trend in negative range from about *-5 mV* to about *-30mV*. The ζ-potential decay is abrupt in the first time domain (0-50 min, being defined by the tangent line drawn to the graph) and then, it reached constant values (seen as a plateau in *Figure 5.5.2-1*). The brushite crystallites, initially formed in the chitosan matrix (at pH of 5-5.5) are dissolved in alkaline medium while the *HAp* nanocrystallites are formed. The formation of *HAp* occurrs in alkaline media due to the diffusion of ions into the composite matrix. Ions such as OH^-, Ca^{2+}, PO_4^{3-}, etc, from the bulk solution diffuse towards the charged layer of composite particles down the concentration gradient. The ζ-potential curve suggests that two regimes of diffusion processes of ions might be discussed.

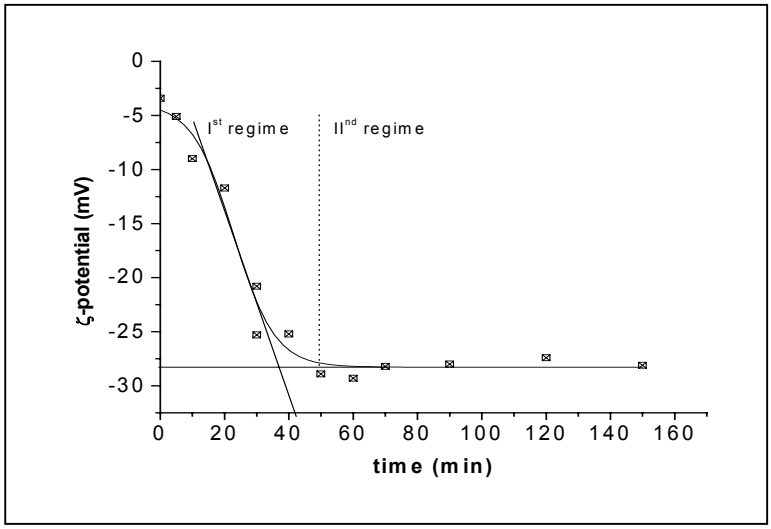

Figure 5.5.2-1 Variation of ζ-potential during the HAp formation inside the chitosan matrix.

The first regime (0-50 min) can be treated as a non-stationary regime with respect to the modification of the ζ-potential of composite hydrogel charged layer. Consequently, the concentration of ions is a function of time. The initial ζ-potential value was about $-5mV$, being given by the presence of brushite in aqueous solutions (as a function of pH and presence of salts[184]). The Fick's second diffusion law describes the processes that take place in this first regime, according to *Equation 5.5.2-2*. In the second regime, see *Figure 5.5.2-1*, the solid/liquid interface reaches an equilibrium state. Therefore, the concentration of ions next to the charged layer of composite particles is not time dependent. This means that the consuming rate of ions due to the *HAp* formation equals the diffusive rate of ions from the bulk solution towards the charged layers. Fick's first diffusion law, as expressed by *Equation 5.5.2-1*, describes this regime.

$$J_{D,i} = -D\frac{dc_i}{dx} \qquad \textbf{(5.5.2-1)}$$

$$\frac{dc_i}{dt} = D\frac{\partial^2 c}{\partial x^2} \qquad \textbf{(5.5.2-2)}$$

$J_{D,i}$ is the ionic flux through unit area of the surface while D is the individual diffusion coefficient.

b) Determination of the isoelectric point of different types of composites

The isoelectric point, *IP*, is defined as the pH value at which the ζ-potential value is zero. For a colloidal system, *IP* is important since coagulation takes place in the range of *IP* values.

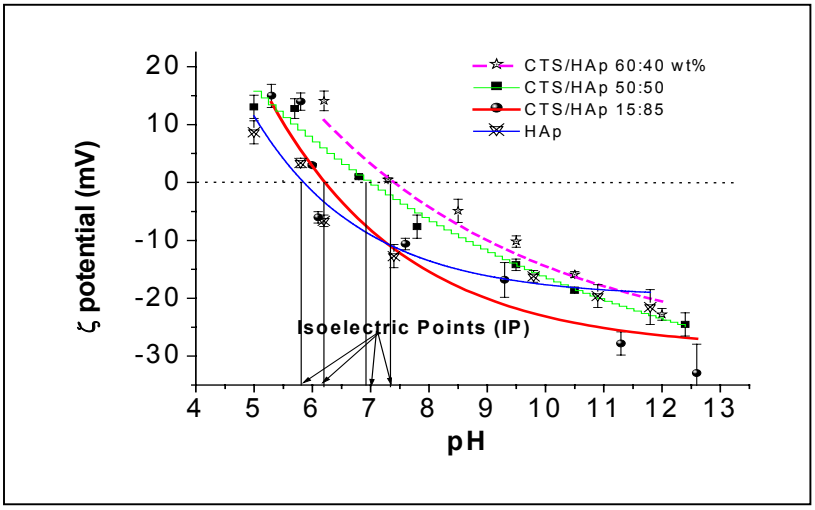

Figure 5.5.2-2 ζ-potential curves of composites (CTS/HAp 50:50 wt%, CTS/HAp 60:40 wt% and CTS/HAp 15:8 wt%) and HAp plotted as a function of pH.*
**CTS is the abbreviation for chitosan.*

The ζ-potential values of various composites with different ratios between chitosan and *HAp* were plotted against the pH, as shown in *Figure 5.5.2-2*. In acidic pH range, the ζ-potential values are positive. Around the neutral range, ζ-potential changes to negative.

The curves show a decrease of the ζ-potential starting from positive values towards negative as the pH increases from acidic to alkaline. The curve of ζ-potential versus pH display similarities to those described in literature for colloidal systems in aqueous media[185]. The *IP* values show that the more the chitosan in the composites the greater the *IP*. The plot of *IP* values as a function of *HAp* content is linear, as seen in *Figure 5.5.2-3*. For *HAp* the *IP* was ca. 5.7 which is in agreement with the results reported in literature[185, 186]. The composites exhibit *IP* values above to *HAp*, being shifted towards neutral pH.

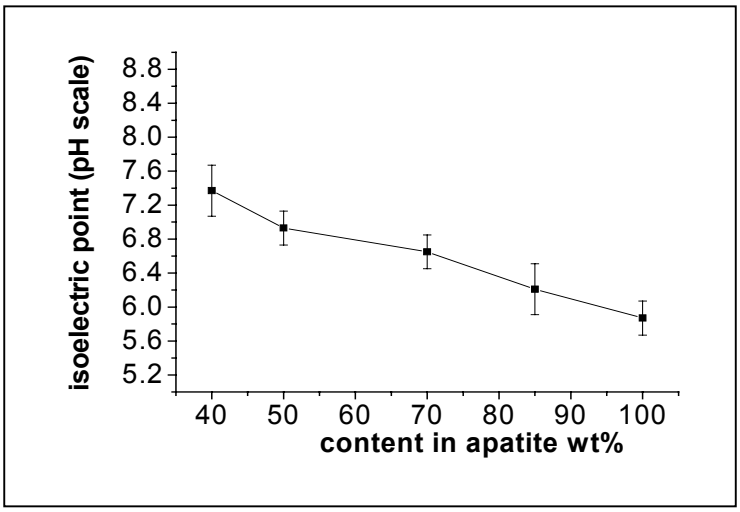

Figure 5.5.2-3 Isoelectric points of composites (CTS/HAp 50:50 wt%, CTS/HAp 60:40 wt%, CTS/HAp 70:30 wt%, CTS/HAp 15:85 wt%) and HAp plotted as a function of HAp content. The points are simple connected.*
**CTS is the abbreviation for chitosan.*

c) Influence of the ionic strength on ζ-potential of composites

The presence of salt modifies the properties of the charged layer of colloidal particles. In practice, the salts are added to the colloidal systems in order either to improve their stability or to get their coagulation[187]. The ζ-potential curves of a *chitosan/HAp* 50:50 wt% composite sample as a function of salt concentration for two types of salts ($CaCl_2$ and NaCl), are presented in *Figure 5.5.2-4*. The ζ-potential values exhibit a decreasing trend to negative values as the salts concentration increases.

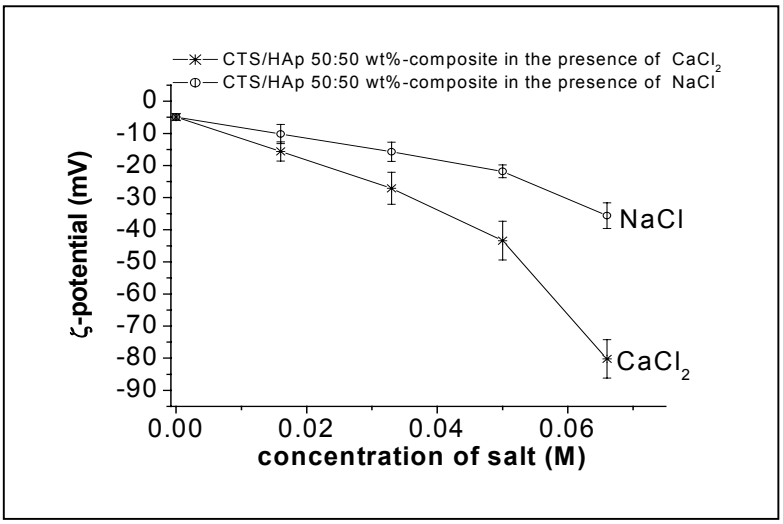

Figure 5.5.2-4 ζ-potentials values of CTS/HAp 50:50 wt% composite samples as a function of ionic strength (in the presence of $CaCl_2$ and NaCl), measured at pH 7.2. The points are simple connected. *CTS is the abbreviation for chitosan.*

The decreasing tendency of ζ-potential of composite samples suspended $CaCl_2$ solutions was more pronounced compared to those in NaCl. The results can be explained by different ionic strengths produced by $CaCl_2$ and NaCl at the same molar concentration. The ionic strength given by $CaCl_2$ is stronger than that of NaCl, since $CaCl_2$ forms three ions on solution whereas NaCl forms only a pair of ions.

5.5.3 Conclusions

The micro-size domains of the composite hydrogels are about 0.8-1 μm.

The size measurements showed that either the sizes of *CPs* particles (mainly as *HAp*) are about of 100-500 nm or their internal structure is composed of even smaller particles, much below 100-500 nm. In order to clarify the hypotheses regarding the size particle domains of *CPs* crystallites, *XRD* and *TEM* measurements must be employed.

ζ-potential measurements, showed that *HAp* formation takes place in two diffusive regimes: a non-stationary regime at the beginning and later a stationary regime. The *IP* of different types of composites were determined by ζ-potential measurements as a function of pH. As compared to *HAp*, the *IP* values were shifted towards neutral pH values with respect to the sample composition. The ζ-potential values of composite hydrogel samples (as dispersed in aqueous solutions) were affected by the ionic strength environments. The composite dispersed in $CaCl_2$ presented higher value of ζ-potential values (in negative range) than that obtained in NaCl.

5 Experimental Results and Discussions

5.6 Nanostructure of composites by *XRD*, *TEM* and *CSLM* techniques

5.6.1 Introduction

Diffraction line broadening is one of the approaches that are used in biological apatites investigations[158]. The evaluation of average crystallite size in bone, dentine and teeth can be performed using X-ray diffraction[188, 189] on powdered samples. The mineral phase of bone is mainly composed of *HAp* which has hexagonal symmetry[189, 190]. The average crystallite size of *HAp* in bone[190] is to have 2-3 nm in thickness and 20-40 nm in length along the ***c*** axis (perpendicular to the basal plane[191]). The properties of bone mineral crystallites were found to vary with age and diseases[192]. The electron microscope techniques[193] such as scanning electron microscopy, *SEM*, transmission electron microscopy, *TEM,* or hybrid systems, scanning transmission electron microscopy, *STEM* are often used to study the local order, structure, morphology and elemental composition of materials by examination of diffracted and transmitted electron beams. In order to obtain structural information about biomaterials, especially composites, both techniques must be employed.

5.6.2 Aim of experiments

- To study the kinetic of *HAp* formation inside the chitosan matrix by *XRD*.
- To see whether the chitosan amounts in the composites influence the average particle size of *HAp* crystallites.
- To evaluate the average particle size of *HAp* crystallites and their crystallinity degrees for different types of composites by *XRD*.
- Structural investigation of composite samples by *TEM* and *CSLM;* Comparison between *TEM* and *XRD* results.

5.6.3 Materials and methods

Materials

Composite samples are described in *Section 4.2.8*. The composite samples were prepared using a shrimp chitosan (*TM 1238*, *Primex*).

Instrumentation

An X-ray diffractometer, *XRD* system, type Siemens D 5005 with Cu, $K\alpha_{1,2}$ X-ray radiation and a scintillation counter with a variable divergence and anti-scatter slits was used. Detection with a secondary graphite monochromator; measurement range from 5 to 60^{o} (2θ); step angle, 0.020 degree. The micrographs were taken using an electron microscope, *SEM-TEM* hybrid system, type Gemini LEO 1550, LEO Oberkochen and a confocal scanning laser microscope, *CSLM*, type Leica TCS NT.

Sampling and data analysis

To 500 mL solution of chitosan 0.2 wt% in 1 wt% aqueous acetic acid solution, 20 mL of $CaCl_2$, 11.1 wt% and 12 mL of NaH_2PO_4, 13.4 wt% with the molar ratio Ca: P of 1.67 (which leads to the formation of *HAp*) were added. Later on, in order to raise the pH of the system, an aqueous 5 wt% NaOH was drop-wise added. At pH 5.5, about 100 mL of composite hydrogel suspension was collected by filtration. After adjusting the pH to 11, samples were collected at 0.3, 1, 2, 4, 8 and 24 h. By using a freeze-drying technique under low pressure, hydrogel composites were obtained as powders and used for *XRD* measurements. Dedicated software such as WinFit for *XRD* data, MicroCall Origin 6.1 and SigmaPlot for mathematical data computation were used.

Determination of crystallites size of HAp

The crystallite size was calculated by Scherrer's equation presented in *Section 4.2.8.*

Evaluation of the crystalinity degree

The crystallinity degree (X_c) corresponds to the fraction of crystalline apatite phase. The calculation of the crystallinity degree was carried out according to the methods described in *Section 4.2.8* and *Appendix A-VIII.*

Evaluation of particle size distribution by TEM

It was performed according to the methods described in *Section 4.2.8.*

CSLM measurements

Samples with thickness of ca. 0.5-1 mm in aqueous environment were investigated. A reflection method (in three dimensional space) in *X-Y* scan mode was chosen as modality to distinguish between the composite domains that have different densities. A *UV* 100x1.4NA - PL APO 1.4-0.7 objective that allows to vary the *Z* position and to scan different sections of the sample (*X-Y* planes) was used.

5.6.4 Results and Discussions

5.6.4.1 XRD measurements

a) Kinetic of HAp formation in the chitosan matrix

As previously reported, *HAp* occurs mainly in needle-like shapes as synthesised in the polymer matrices[194] and grows in the direction of c-axis [195] which corresponds to the (002) reflection peak. The average size of *HAp* crystallites calculated from the (002) reflection peak leads to a description of *HAp* formation in chitosan matrix as a function of time.

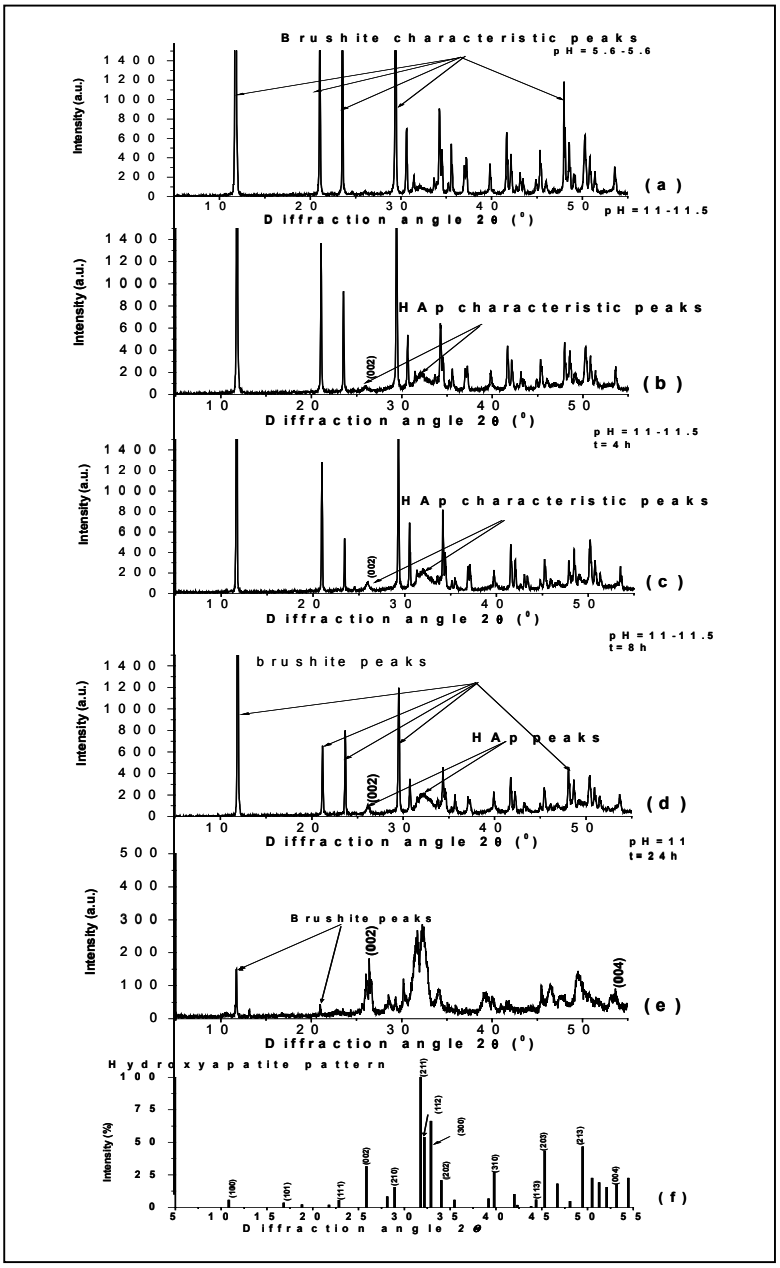

Figure 5.6.1 Transformation of brushite (a) to HAp (e) in aqueous alkaline media. The XRD patters labelled by (b), (c) and (d) describe the intermediary CPs phases (mixtures between brushite and HAp). The graph (f) shows the characteristic XRD lines pattern of HAp.

As shown in *Figure 5.6.1(c, d, e),* two phenomena evolve in opposite directions, the dissolution of brushite and the formation of *HAp.* Two groups of *XRD* reflection lines can be used to monitor the *HAp* formation; one at $2\theta=26°$ and the group of peaks which range from $2\theta=30°$ to $2\theta=34\text{-}36°$. Since the reflection peak (002) at $2\theta=26°$ is well resolved (no interference), for quantitative purposes it is recommended to be used. In the alkaline conditions (pH 11-12), the unstable brushite and the accompanying amorphous calcium

phosphates, *ACP*, phase transform towards a more stabile *HAp*[68, 69], according to *Equations 5.6.1* and *5.6.2*.

$$10CaHPO_4 + 12OH^- \rightarrow Ca_{10}(PO_4)_6(OH)_2 + 10H_2O + 4\,PO_4^{3-} \quad \textbf{(5.6.1)}$$

$$PO_4^{3-} + ACP + OH^- \rightarrow Ca_{10}(PO_4)_6(OH)_2 \quad \textbf{(5.6.2)}$$

After 24 h, the transformation of brushite and *ACP* into *HAp* is nearly complete. Only traces of brushite are still identified according to *XRD* reflection peaks from $2\theta=12°$ and $21°$, respectively. The *HAp* average crystallite size grows up as the reaction time increases (seen in *Figure 5.6.2* and *Table 5.6.1)*. The stability of *HAp* at the pH of 5.5-5.6 is explained on base of the solubility isotherms of *CPs* compounds, as discussed in *Section 3.2.2*. *HAp* is the least soluble phase between pH 4.2 and 12.5. Consequently, its solubility isotherm lies below to the others *CPs* compounds (as seen in *Figure 3.2.1*).

Table 5.6.1 Average crystallite size for HAp formation inside of chitosan matrix.

Time (h)	Line width (002), FWHM** (°)	Crystallinity degree (X_c)	Line width (002), FWHM, (rad)	Average crystallite size, L (nm)	Remarks
0.3	0.6307	0.0551	0.0110	15.80	The peak at 2θ=26.04° is hardly distinguished.
1	0.4585	0.1434	0.0080	21.60	Intensities of *HAp* peaks increase as the reaction time increases.
2	0.4299	0.1739	0.0075	23.30	After 2h, the intensity of the brushite peaks diminished slightly compared to the initial state.
4	0.3783	0.2589	0.0066	28.50	Mid-period in *HAp* formation. Characteristic apatite peaks enhance in time.
8	0.3210	0.4179	0.0056	31.40	8 h after the growth of *HAp* crystallites.
24	0.2866	0.5874	0.0050	34.80	After 24 , *HAp* is fully formed. The brushite peaks vanished.

***FWHM full-width at half maximum of peak height*

The growth rate of *HAp* crystallites at a constant temperature of 22°C is a function of time, as seen in *Figure 5.6.2* (A). In the first 20-30 minutes, the growth rate is about 50 nm/h. After 2 h, it decreases to 4-5 nm/h since the synthesis of *HAp* started. In the middle period, the growth rate decreased to 1.20 nm/h. At the end, after 24 h, a plateau was reached and the growing rate value is about 0.1-0.2 nm/h. The inset labelled as (B) in *Figure 5.6.2* shows the variation of crystallinity degree of *HAp* as a function of time during its formation.

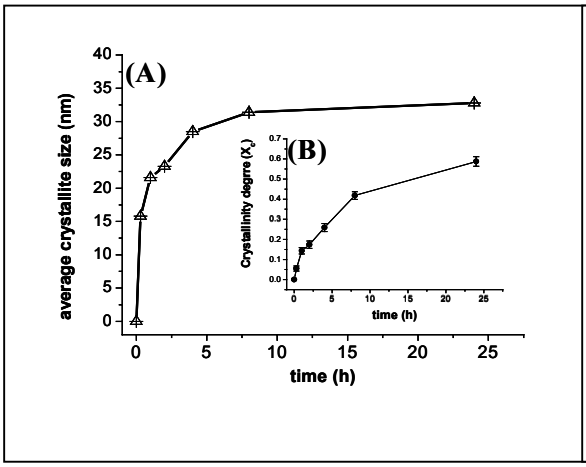

Figure 5.6.2 Size evolution of the HAp nanocrystalltes in aqueous alkaline media as a function of time (A). The inset (B) shows the evolution of HAp crystalinity as a function of time.

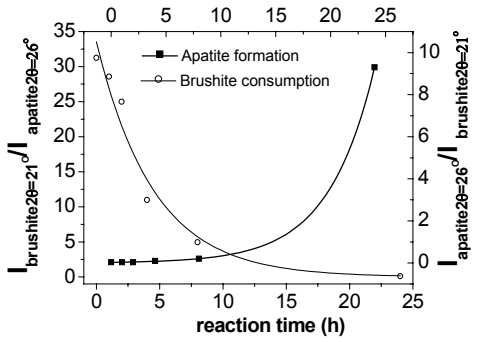

Figure 5.6.3 HAp formation and brushite consumption monitored by the ratio of two XRD reflection peaks as a function of time.

From the graphical representation of *HAp* crystallite size versus the formation time *(Figure 5.6.2)* one can conclude that the reaction of *HAp* formation inside the chitosan matrix is completed after about 8-10 h, which in fact is not true. However, after this period, most probably a pseudo-stationary regime is reached in which the *HAp* crystallites are formed from other calcium phosphate phases and, beside this, the small and irregular *HAp* crystallites are dissolved and re-formed as large and regular *HAp* crystallites. In order to quantify the kinetics of reaction through a parameter which can be related to the concentration, the ratio between two characteristic reflection peaks of brushite and *HAp* was used as controlling parameter and graphically represented against the reaction time, as seen in *Figure 5.6.3*. Since the ratio between the peak intensities of brushite/*HAp* is proportional to concentration[196], it was used to monitor both brushite and *HAp* concentrations as a function of the reaction time. The curves displayed in *Figure 5.6.3* show that the reactions take place according to first order exponential laws, described by the *Equation 5.6.3*,

$$C = C_0 + A_0 e^{\mp t_i / t_0} \qquad \textbf{(5.6.3)}$$

where C is the concentration of either brushite or *HAp*, C_0 is their initial concentrations, and t_i is the reaction time. The signs ″minus″ and ″plus″ describe either the exponential decay or growth. A_0 and t_0 are the offset factors and were determined from the exponential plots as A_0=0.030±0.0015 and t_0=4.191±0.0350. In brushite the initial concentration C_0 (calculated from the ratio $I_{brushite}/I_{apatite}$ at t=0) follows a decay profile whereas the *HAp* concentration increases exponentially starting from the initial concentration C_0=0. Since the state parameters

of the system are defined, its evolution can be easily described by the concentration ratio between *HAp* and brushite by using the *Equation 5.6.3*.

b) Influence of composition on HAp average crystallites size. The bimodal distribution

The investigation of the influence of chitosan content on the average particle size of *HAp* was also studied. A series of samples (*HAp*, composites and chitosan) such as *HAp* (1), *chitosan/HAp* 15:85 wt% (2), *chitosan/HAp* 30:70 wt% (3), *chitosan/HAp* 50:50 wt% (4), *chitosan/HAp* 80:20 wt % (5) and chitosan (6) were investigated by *XRD*.

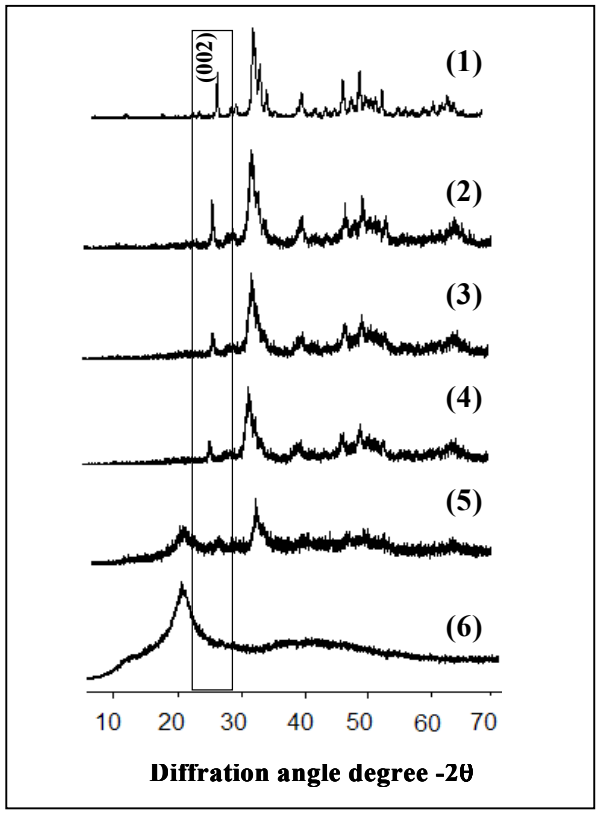

Figure 5.6.4 XRD patterns for HAp (1), composite samples such as chitosan/HAp 15:85wt% (2), chitosan/HAp 30:70 wt% (3), chitosan/HAp 50:50 wt% (4), chitosan/HAp 80:20 wt% (5) and chitosan (6), respectively. The (002) reflection peak domains of HAp from the composite samples are shown.

The *XRD* patterns of samples are presented in *Figure 5.6.4*. These patterns exhibit the structural features of both *HAp* and chitosan with respect to their ratio in composite samples. The average crystallite size and its corresponding crystallinity were calculated, in the first approach, using a Gaussian function to fit the data (WinFit software). The results are summarized in *Table 5.6.2*. They suggest that, the more the chitosan in the composite the smaller the average crystallites size of *HAp*. As such, the average crystallite size of *HAp* is controlled.

Table 5.6.2 Average crystallite size and corresponding crystallinity of HAp from various types of composites.

Specimen	Line width (002), FWHM***, (°)	Crystallinity (X_c) (%)	Line width (002), FWHM, (rad)	Average crystallite size*, L (nm)
CTS/HAp 80:20 wt.%	0.5636	0.0751	0.00983	13.90±1.60
CTS/HAp 50:50 wt.%	0.4538	0.1430	0.00792	17.34±5.50
CTS/HAp 30:70 wt.%	0.3092	0.4408	0.00539	25.42±4.25
CTS/HAp 15:85 wt.%	0.2266	1.1877	0.00395	34.69±6.20
CTS/HAp 0:100 wt.%	0.2168	1.3565	0.00378	36.26±5.10

**Mean ±SD calculated using a WinFit dedicated software.*
*** CTS is the abbreviation for citosan.*
**** FWHM is the full width of the peak at half of its maximum.*

In order to evaluate the crystallinity, as an alternative to the average crystallite size, *Equation 4.2.8-2* was applied. The crystallinity values of composites, comprised in *Table 5.6.2*, show that they have a low degree of crystallinity. The *chitosan/HAp* 0:100 wt% has the highest value (1%) whereas the smallest value was found at *chitosan/HAp* 80:20 wt% (0.075%). For biomedical purposes, samples containing nanoapatites (with low crystallinity) are preferred due to their high *in vivo* resorbability rate[174].

Three *HAp* samples varying by their crystallinity, are overlapped for a close comparison as seen in *Figure 5.6.5.*

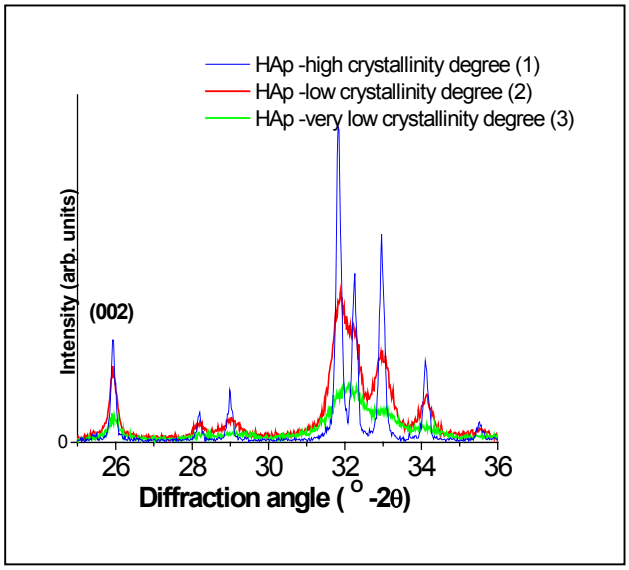

Figure 5.6.5 XRD patterns of three different HAp samples varying by their crystallinity degrees.

5 Experimental Results and Discussions

The *XRD* patterns indicate that the preparation method has a crucial influence on the *HAp* crystallinity. The structural features of *HAp* crystallites from composite samples show similarities to those of natural bone apatites[62].

The *XRD* diffraction patterns of composite samples presented in *Figure 5.6.4* reveal that the (002) reflection peak of *HAp* from 2θ=26^o is a combination of two peaks at the same position. One on the bottom (found as broad, with a low intensity) and the second one, which partially overlap the first one, exhibits higher peak intensity, being much sharper compared to the first one. The peak features suggest a bimodal distribution of *HAp* crystallites in the composite matrix. Therefore, in order to perform a complex analysis of the *HAp* (002) reflection peaks we applied a second approach, i.e. a mathematical function composed of a sum of two Gaussian functions[197], *Equation 5.6.4*. If α_2=0, this constraint will simplify the function at a single Gaussian and $\beta_1 = \beta_m \sqrt{2\ln 2}$, where β_m is the peak width. In this case, a monomodal distribution is obtained, as shown in *Table 5.6.2*. If $\alpha_2 \neq 0$, this reflects the occurrence of two particle size domains with different length sizes. Two contributions given by $\beta_1 = \beta_{m,n} \sqrt{2\ln 2}$ (where $\beta_{m,n}$ is the peak width of the narrow peak which leads to the average particle size in the large size domain) and by $\beta_2 = \beta_{m,b} \sqrt{2\ln 2}$ (where $\beta_{m,b}$ is the peak width of the broad peak which leads to the average particle size in the small size domain) define the *HAp* bimodal distribution inside the chitosan matrix. The (002) reflection peaks of different composites fitted with *Equation 5.6.4* are shown in *Figure 5.6.6.* The values of β were determined by fitting the (002) reflection peaks of *HAp* either with a Gaussian or with a sum of two Gaussian functions, given by *Equation 5.6.4*,

$$I = I_0 + \frac{\alpha_1}{\beta_1 \sqrt{\pi / 4\ln 2}} e^{\frac{-4\ln 2(2\theta - 2\theta_0)^2}{\beta_1^2}} + \frac{\alpha_2}{\beta_2 \sqrt{\pi / 4\ln 2}} e^{\frac{-4\ln 2(2\theta - 2\theta_0)^2}{\beta_2^2}} \qquad \textbf{(5.6.4)}$$

where: I is the peak intensity
I_0 shows the background level
2θ represents the diffraction angle
$2\theta_o$ is the maximum peak position
$\beta_{1,2}$ are the peak widths of the crystallite size domains
$\alpha_{1,2}$ are the intensities of the Gaussian functions.

The crystallite size was calculated according to Scherrer's equation *(4.2.8-1)*. The instrumental broadening contribution on a muscovite monocrystal using various detector slits, with a Ni filter at 2θ=26.8^o, step 0.01^o was determined.

Its contribution was evaluated at β_{inst}=0.062 (degree-2θ). All measured line widths were then corrected with respect to the instrumental broadening contribution using the following equation $\beta^* = \sqrt{\beta^2 - \beta_{inst}^2}$, where β^* represents the crystallite size contribution to the peak broadening while the β_{inst} is the instrumental broadening contribution.

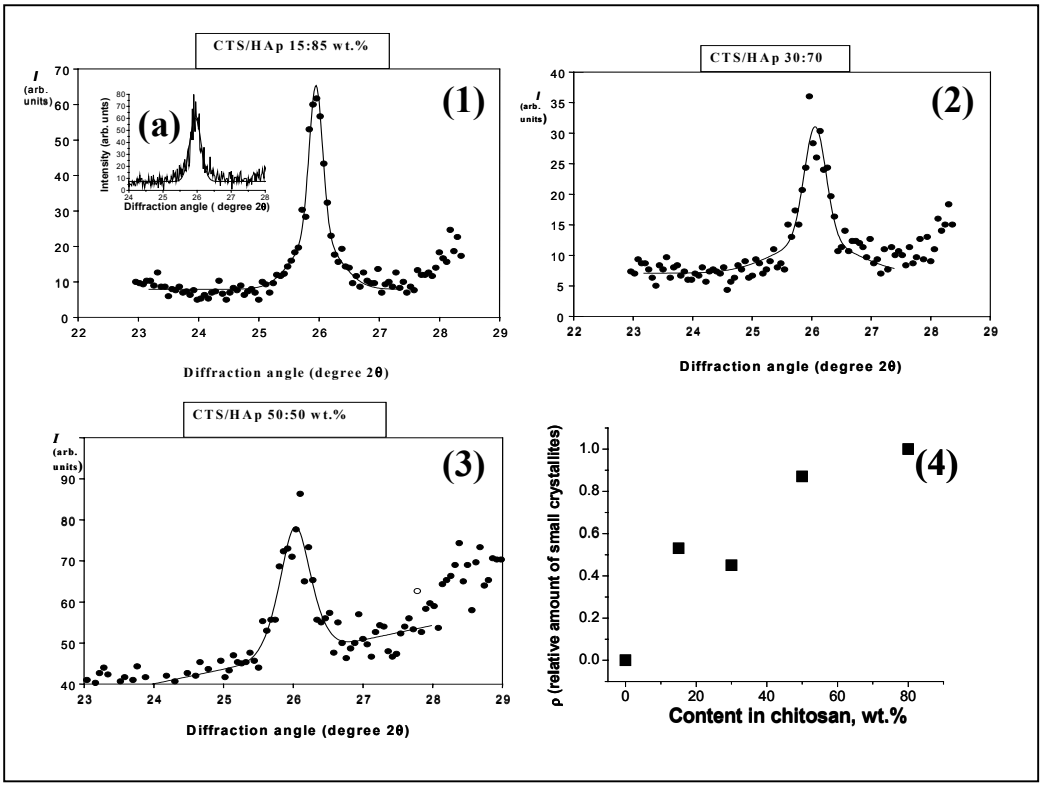

Figure 5.6.6 XRD patterns of (002) reflection peak of HAp fitted as a sum of two Gauss functions, graphs (1-3). For comparison, the inset (a) displays the same peak as (1) but fitted using one Gaussian function. The bimodal distribution of HAp crystallites in the composite samples can be shown as a function of the relative amount of small crystallites plotted versus the percentage of HAp in the composite sample, as seen in graph (4).

The inset (a) shows for a close comparison the (002) reflection peak fitted using a single Gaussian function while the graph (1) shows the same peak fitted by a sum of two Gaussian functions. The fitting parameters lead to quantitative information about the structural features of composites. Besides the peak widths, $\beta_{1,2}$, which lead to the *HAp* average crystallite size from the two size domains, there are other parameters such as $\alpha_{1,2}$ related to the amount of *HAp* crystallites from the size distribution domains, determined according to *Equation 5.6.4*. In order to quantify in relative terms the amount of small *HAp* crystallite size, the normalized relative amount of small crystallites, ρ, defined as

$$\rho = \frac{\alpha_2}{\alpha_1 + \alpha_2} \qquad \textbf{(5.6.5)}$$

was considered. $\alpha_{1,2}$ are the intensities of the narrow and broad Gaussian peaks.

The graph (4) from *Figure 5.6.6* presents the plot of ρ as a function of chitosan content. A linear increase of the relative amount of small particle size in the composite samples as the content of chitosan increases was observed. The values of the average crystallite size of *HAp* according to the bimodal distribution are presented in *Table 5.6.3*.

Table 5.6.3 Summary of the bimodal distribution of HAp crystallite size.

Specimen	α_1 (arb. units)	Line width (002) β^*_1[#] (Degree-2θ)	Average crystallite size, in large size domain, given by β^*_1 (nm)	α_2 (arb. units)	Line width (002) β^*_2 (Degree-2θ)	Average crystallite size, in small size domain, given by β^*_2 (nm)	Relative amount of small crystallite $\rho=\alpha_2/\alpha_1+\alpha_2$
CTS/HAp 0/100 wt.%	83.85±1.10	0.2433	32.32±2.60	-	-	-	0
CTS/HAp 15/85 wt.%	11.86±1.50	0.1762	44.64±3.10	13.8±1.70	0.6400	12.35±1.30	0.53
CTS/HAp 30/70 wt.%	8.62±1.46	0.3038	25.86±3.80	8.7±1.91	1.1573	6.78±3.50	0.45
CTS/HAp 50/50 wt.%	2.85±0.16	0.2371	33.11±5.80	15.0±0.16	0.4356	18.03±3.50	0.87
CTS/HAp 20/80 wt.%	-	-	-	5.0±1.64	0.5081	15.57±6.30	1

[#] *$\beta^*_{1,2}$ are the corresponding corrected $\beta_{1,2}$ line widths from Equation 5.6.4*

In literature, the reported size values of *HAp* nanocrystallites prepared using wet precipitation methods are ranging from 80 to 200 nm in length and 20 to 40 nm in width and thickness[198].

5.6.4.2 Microscopic investigations

a) TEM measurements

In order to confirm the *XRD* results with respect to the bimodal distribution of *HAp* crystallites inside the composite samples, *TEM* measurements were performed. The *HAp* was rod-like as nano-crystallites dispersed in the chitosan matrix. The *TEM* measurements confirmed the bimodal distribution of *HAp* nanocrystallites within composite matrix. The first is the cluster-like domains, where the *HAp* particles are agglomerated and the second mode is the inter-cluster (scattered) domains where the scattered *HAp* crystallites are observed, as seen in *Figure 5.6.7.* Neither in the cluster-like nor in the scattered domains the large crystallites (in the micro range) of *HAp* were identified. The presence of chitosan, which interacts with the *HAp* nanocrystallites might explain the lack of the *HAp* micro-crystallites. The *TEM* micrograph showed that the *Figure 5.6.7* (2) was used to calculate the distribution of both width and length of *HAp* nanocrystallites in the cluster-like and scattered size domains. The diameters of the cluster-like size domains range between 200 nm and 400 nm, as seen in

Figure 5.6.7 (1, 2). Between the two size distribution domains, *HAp* crystallites exhibit different structural features. In the cluster-like domain, the distribution peak is narrow and shows an average crystallite size of 17-18 nm. In the scattered region the distribution peak is broader and the average crystallite size value is greater than in the cluster-like domains, being about 40 nm.

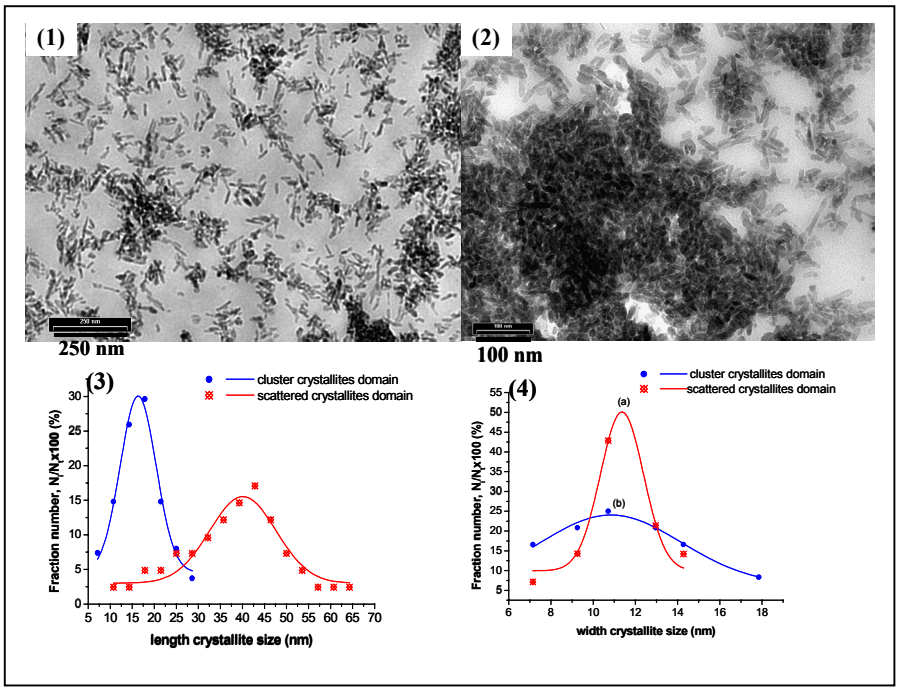

Figure 5.6.7 TEM measurements on a chitosan/HAp 50:50 wt% composite sample. The micrographs (1,2) display the sample at two magnification levels. Below the micrographs, the HAp distribution curves for both length and width crystallite sizes are shown in graphs (3,4).

Since the crystallite shape is mainly needle-like the crystal width show nearly the same average values of about 11 nm in both domains which gives a monomodal distribution with respect to the width distribution, as seen in *Figure 5.6.7*, graph 4.

The *HAp* nanocrystallites adopt a cluster-like organization in the earlier stage of bone mineralization[198-200], known as growth cartilage tissues.

b) CSLM measurements

Since in the cluster-like domains a greater density is found compared to the scattered domains of *HAp*, the *CSLM* measurement on a *Z*-cross-section through the sample at a given *X-Y* section leads to the formation of the reflected image. The image reveals the *HAp* cluster-like domains as blue spots, as seen in *Figure 5.6.8*. The roughness of composites gives information about the diameter of *HAp* cluster-like size domains. The graphical representation of the reflected intensity versus *X-Y* position gives information about the topography of

composites. The diameters of cluster-like size domains range from 180 nm to about 400 nm, which is in good agreement with those obtained by *TEM*.

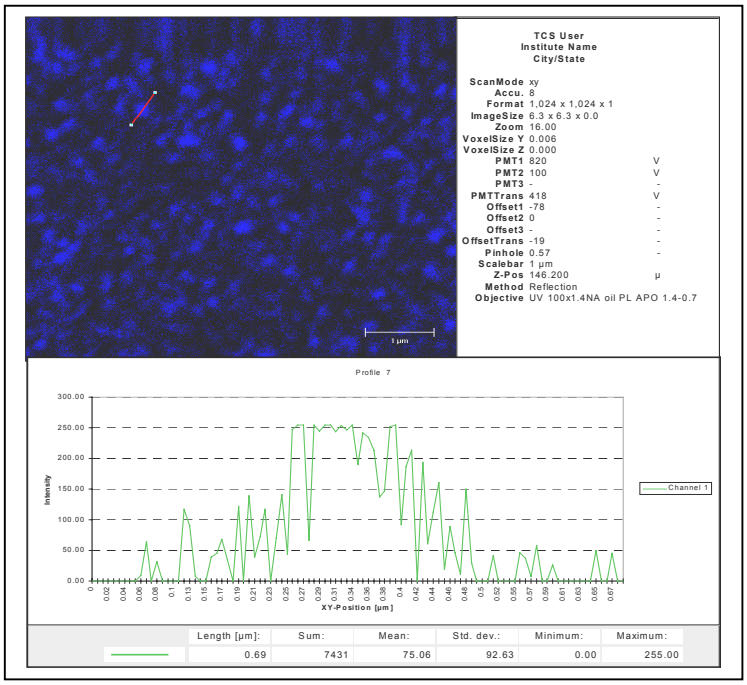

Figure 5.6.8 CSLM image of a chitosan/HAp 50:50 wt% composite. In the above image, the cluster-like structure of HAp crystallites can be observed. Below is presented the roughness measurement, which lead to the HAp cluster-like size domain. The scale bar is 1µm.

5.6.5 Conclusions

The kinetics of *HAp* formation in aqueous media in the presence of chitosan matrix using *XRD* measurements was evaluated. A mathematical function composed of a sum of two Gaussian functions was used to fit the (002) *HAp* reflection peaks. Based on the fitting parameters, the analytical data related to the average particle size distributions were extracted. A bimodal distribution of *HAp* crystallites in the composite samples such as cluster-like domains that form dendritic aggregates and scattered domains was identified. The small *HAp* crystallites were identified in the cluster-like size domains with average size between 7 and 18 nm whereas in the scattered domains larger *HAp* crystallites between 25 and 45 nm occur. The intensities of Gaussian functions are directly related to the particle concentrations which allowed us to conclude that the average of *HAp* crystallite size can be controlled by the chitosan content from the composite samples. The more the amount of chitosan in composite the smaller the average crystallite sizes of *HAp*. The *TEM* measurements confirmed the *XRD* results regarding the *HAp* bimodal distribution in composites. *HAp* from the composite samples is in the range of sizes of biological *HAp*. The sizes of cluster-like *HAp* domains were estimated to be between 200 and 400 nm by *TEM* and *CSLM* techniques.

5 Experimental Results and Discussions

5.7 Structural investigations of composites by *IR* and Raman spectroscopy

5.7.1 Introduction

The Raman and *IR* spectroscopy techniques are successfully applied to analyze the composite materials, either artificial or natural ones[201, 202]. One of the problems in the use of *IR* and Raman methods is the identification of spectral bands[203] in complex sample matrices. The vibrational activity is different in Raman and *IR*, some frequencies are both *IR* and Raman active, but others are active either in Raman or in *IR*. The positions of Raman and *IR* bands are influenced by the chemical composition and structure[204], especially by the symmetry changes such as the space group of crystals and/ or by crystalline or amorphous domains of polymer lattices. One of the interest fields refers to the investigation of composite materials that contain *CPs* phases reinforcing the polymer matrices. Bone and the teeth are examples of natural composite materials that contain *CPs* phases. Conventional Raman spectroscopy analyses on bone apatites are usually difficult due to the fluorescence of complex organic matrices[204]. Biological apatites are normally described either as poorly crystalline or as nanocrystalline materials, as characterized by their *XRD* broad diffraction peaks. The biological apatites do not occur in a pure form[63] as *HAp* with the formula Ca_{10} $(PO_4)_6$ $(OH)_2$. They are found as substituted *HAp*, which means that either cations, anions or vacations can substitute different ions from standard structure of *HAp* resulting modified structures as presented below,

(Ca, Sr, Mg, Na, H_2O, [ ])$_{10}$ (PO_4, HPO_4, CO_3, P_2O_7)$_6$ (OH ,F, Cl, H_2O, O, [ ])$_2$.

On that ground, the study of these biomaterials presents a great interest in the elucidation of composition and structures understanding. Two types of carbonate substitutions have been described in natural apatites related compounds such as type *A* (OH^- substituted by CO_3^{2-}) and type *B* (PO_4^{3-} substituted by CO_3^{2-}). Besides other analytical techniques, Raman and *IR* spectroscopy [204] might bring additional information about the composite samples in regard to their components and to their structural features.

5.7.2 Aim of experiments

- To identify the components of composite samples by their characteristic group bands.
- To study the composites with respect to the inorganic–organic interactions reflected in the chemical shifts of spectral bands either in the position or in the intensity.
- To investigate the changes of the chitosan chain conformations in the composite samples.

5.7.3 Materials and methods

Samples

Composite samples with different proportions between components such as *CTS*/HAp* 100:0 wt% (*CTS*), *CTS/HAp* 80:20 wt%, *CTS/HAp* 50:50 wt%, *CTS/HAp* 30:70 wt%, *CTS/HAp* 15:85 wt% and *CTS/HAp* 0:100 wt % (*HAp)* were measured. They were used in powdered form as freeze-dried and air-dried samples. The composites were prepared from shrimp chitosan (*TM 1238, Primex*).

**CTS* is the abbreviation for chitosan.

Instrumentations

i) A Perkin Elmer *FT-IR* 1720 spectrometer was used in transmission mode, the wavenumber domain was from 4000 cm^{-1} up to 400 cm^{-1}; the samples were analyzed in KBr pellet at a resolution of 2 cm^{-1}.

ii) Raman measurements were performed at room temperature using Confocal Raman Microscopy (CRM200, Witec). The circular polarized laser light (diode pumped Green laser, λ=532nm, CrystaLaser) was focused onto located material area with diffraction limited spot size through a microscope object ($\times$60, NA=0.80 Nikon). The scattering light was collected by an air-cooled CCD (PI-MAX, Princeton Instruments) behind a grating (600 g/mm) spectrograph (Acton) with a high resolution of 6 cm^{-1}.

Sample preparations and data analysis were presented in *Sections 4. 2.1* and *4.2.2*.

5.7.4 Results and discussions

5.7.4.1 Structural investigations by *IR* spectroscopy

A series of composites with different ratios of chitosan and *HAp* were recorded from 4000 cm^{-1} to 400 cm^{-1}. In order to identify the presence of chitosan and *HAp* in composites, the *IR* spectra were analysed for the characteristic group frequencies[135].

The first part of *IR* spectra (3800-2600 cm^{-1}) of composites is displayed in *Figure 5.7.1-1*. Here, one can identify the *-OH* band at 3570 cm^{-1}, (seen as a shoulder) for *HAp* and for *chitosan/HAp* 15:85 wt% composite sample [(*Figure 5.7.1-1* (e) and (d)]. For the other samples, this band is overlapped by the broad water band (3700-3300 cm^{1}). In addition to the water broadening contribution, the *-N-H* stretching vibration band from 3470 cm^{-1} also contributes to the band broadening in the range of 3600-3300 cm^{-1}.

The *–C-H* stretching vibration gives the next band located between 2840 and 2930 cm^{-1}. The band intensity increases as the amount of chitosan in composite increases.

The second spectral domain (2200-400 cm^{-1}) is shown in *Figure 5.7.1-2*.

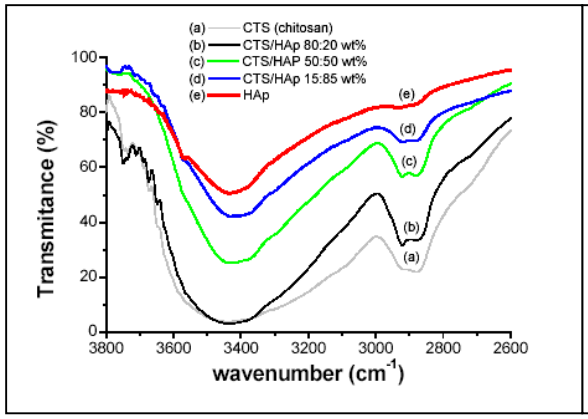

Figure 5.7.1-1 IR spectra of composites in the range of 3800- 2600 cm^{-1}.

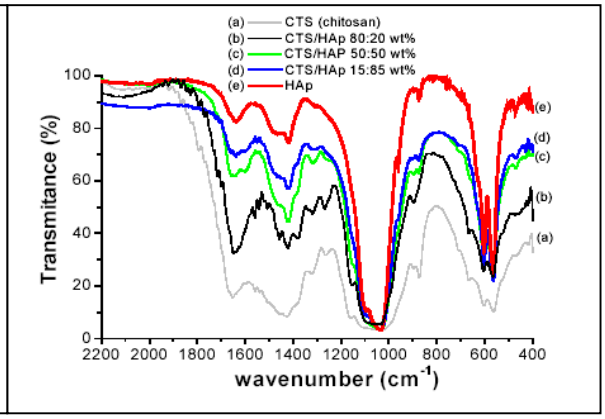

Figure 5.7.1-2 IR spectra of composites in the range of 2200- 400 cm^{-1}.

Here the amide bands, the *-C-O* vibrations modes and the *-P-O* vibrations modes (in stretching and bending modes) are localised. The phosphate stretching vibration bands from *HAp* were indicated at 1036 cm^{-1}, 1091 cm^{-1} and 963 cm^{-1} whereas those from 603 cm^{-1} and 565 cm^{-1} are assigned to the phosphate bending vibrations. A summary of *IR* frequencies, which take into consideration the functional groups found for *HAp* and chitosan sample, is given in *Table 5.7.1-1*. The composite samples characterised by the *IR* absorption bands of their components (chitosan and *HAp*) , exhibit the bands shifted mainly in intensity with respect to the composite composition, as seen in *Figures 5.7.1-1* and *5.7.1- 2 (a)-(e).*

Table 5.7.1-1 Characteristic IR group frequencies for chitosan, HAp and composite samples.

Groups	O-H	N-H	C-H	C=O	C-O	P-O
Wavenumber (cm^{-1})	3450-3480; 630	3470; 1660	2850-2880	1620-1660	1020-1150	1025; 560-602 1091, 1036, 963

The *IR* absorption bands identified at 1662 cm^{-1}, 1590 cm^{-1} and 1545 cm^{-1} are assigned to the amide *I* and amide *II* groups given by the presence of chitosan in composites. The carbonate bands found at 1450 cm^{-1} and 1421 cm^{-1} appear because of the presence of traces of carbonated apatite in the composites.

5.7.4.2 Structural investigation by Raman spectroscopy

Measurements of Raman spectroscopy were performed as complementary to *IR* spectroscopy to investigate the structural features of composites. Two types of composites, both occurring in dry state were measured by Raman spectroscopy. One type was obtained by

freeze-drying the composite hydrogel samples under low pressure while the second type was obtained by air-drying of composite hydrogel sample at room temperature (23-25° C).

The Raman spectra of chitosan, *chitosan/HAp* 50:50 wt% composite and *HAp*, in the ranges of 2000 –4000 cm^{-1} and 200 - 2000 cm^{-1} are shown in *Figures 5.7.2-1* and *5.7.2-2*.

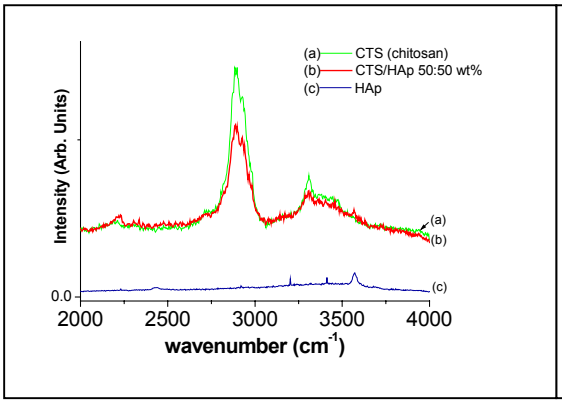

Figure 5.7.2-1 Raman spectra of chitosan, chitosan/HAp 50:50 wt% composite and HAp in the range of 2000-4000 cm^{-1}

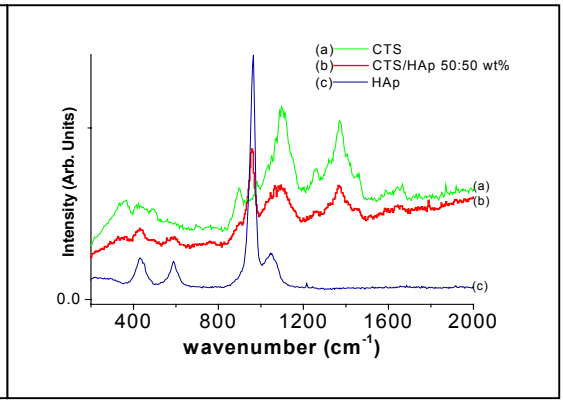

Figure 5.7.2-2 Raman spectra of chitosan, chitosan/HAp 50:50 wt% composite and HAp in the range of 200-2000 cm^{-1}

Based on Raman characteristic bands one can probe the composite components such as chitosan and *HAp*. A summary of Raman bands of chitosan, *HAp* and composite samples as compared to bone, dentine and enamel is given in *Appendix A-X, Table A-X-1*. *HAp* shows a strong and narrow adsorption band at 962-964 cm^{-1} (*Figure 5.7.2-2*). This band appears also in *IR* since it is given by the *-P-O* stretching bond. For the biological apatites or for synthetic ones this band is more or less shifted to higher or lower wavenumbers[201], respectively.

The Raman spectra of composites present a shift of bands mainly in intensity with respect to the amount of components, as seen in *Figures 5.7.2-3* and *5.7.2-4*.

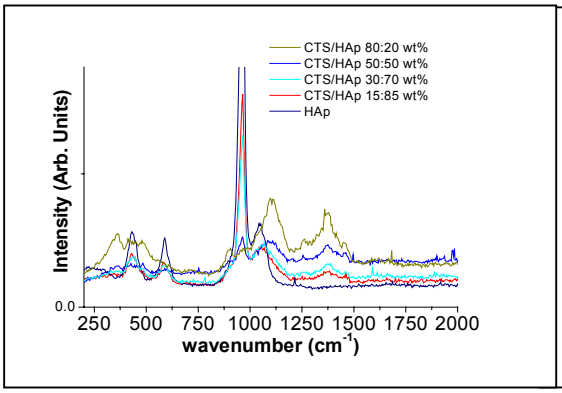

Figure 5.7.2-3 Raman spectra for a series of chitosan/HAp composites in the range of 200-2000 cm^{-1}.

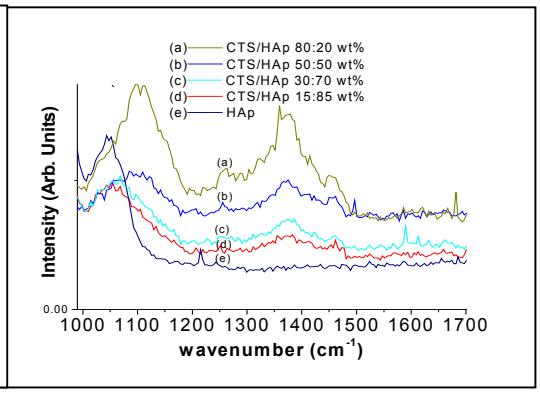

Figure 5.7.2-4 Zoom of the spectral bands in the range 1000-2000 cm^{-1}.

Additionally, the chemical shift is used for various purposes such as a criterion to evaluate the formation of new apatite phases[205], in kinetic investigations[206], to study the structural conformational changes[207], etc.

Structural changes of chitosan chain conformations probed by Raman spectroscopy

The chitosan behaviour in acidic aqueous solution plays an important role in the formation of composite hydrogel samples, as previously discussed in *Section 5.2.1.2*.

By co-precipitation of composite sample in its earlier stage of formation, an interconnected hydrogel porous network structure is formed. It was assumed that by freeze-drying the initial expanded hydrogel network structure can be maintained while by drying at room temperature or at elevated temperatures (below 100°C), the initial expanded hydrogel network structure is affected. Due to water release from the hydrogel network, accompanied by shrinking, some structural reorganization of the network take place. In this sense, one possibility to distinguish the structural changes of network structure is to employ Raman spectroscopy as an analytical investigation tool. By comparing the spectra of composite samples obtained by freeze-drying to those by air-drying, one can expect evidence of network structural changes. This might occur due to the reorientation and conformational changes of chitosan chains from the composite network, which might be reflected as chemical shifts in the Raman spectra. Taking into account amide bands *I* and *III*, it was possible to distinguish between different polymer conformations with respect to their chemical shifts[207], as seen in *Figures 5.7.2-5* and *5.7.2-6*.

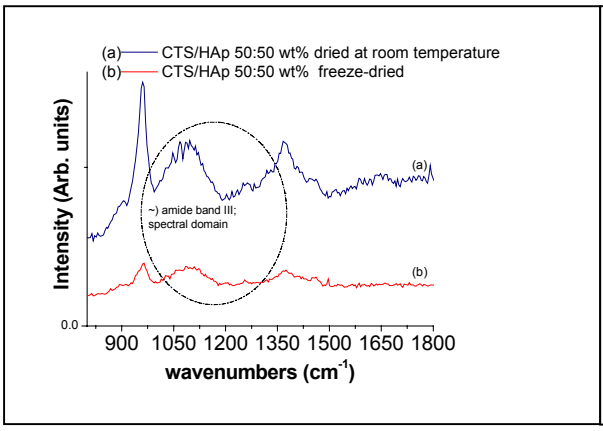

Figure 5.7.2-5 The amide bands I and III domains for two types of chitosan/HAp composite samples obtained by air-drying and freeze-drying processes.

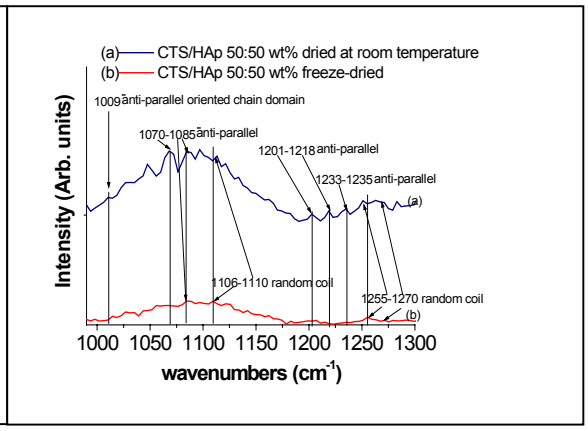

Figure 5.7.2-6 Zoom in the Raman spectra of amide III domain. The assignments of bands to the random coil or/ and the anti-parallel conformations are displayed.

In order to make distinction between the chitosan chain conformations the hyperfine structure of the Raman bands characteristics was analysed. During drying at elevated

temperatures (below 100^{o} C), the hydrogel network structure of the composite is irreversibly changed, since from a soft composite hydrogel material a tough dried ceramic-like material is obtained. The physical crosslinking achieved through intermolecular hydrogen bonding between the chitosan chains stabilize the composite hydrogel network. The formation of hydrogen bonds between chitosan chain segments which have a higher degree of freedom facilitates their relocation and lead to an increase of the local order by ″stretching″ some parts of chitosan chain segments in parallel orientation. The result is the increase of the crosslinking density given by the parallel orientation domains. The summary of the specific bands, as assigned to the random coil and parallel conformation domains in the case of chitosan (which is the polymer matrix of composites), is shown in *Table 5.7.2-1*.

Table 5.7.2-1 Raman shift assigned for chitosan chain conformations taking into account two amide band domains (I and III).

Raman Shift (cm^{-1}) (found bands, cm^{-1})					
*CTS**	*CTS/HAp 80:20 (wt%)*	*CTS/HAp 50:50 (wt%)*	*CTS/HAp 30:70 (wt%)*	*CTS/HAp 15:85 (wt%)*	*Assigned Conformations*[207]
-	1006	1008	1008	1009	1000-1009 Anti-Parallel
1073-1087	1076, 1093	1085	1089	1082	1070-1085 Anti-Parallel
-	1110	1109	-	-	1106 Random coil
1223-1228	1237	1235	1230	1233	1233 Anti-Parallel
1259	1258	1255	1251	1251	1252 Random coil
-	1276	1272	1270	1262	1270 Random Coil
1667	1666	1666	1662	1658	1660 Random Coil
1680	1681	1691	1685	1671	1678 Anti-Parallel

*CTS is the abbreviation for chitosan.

Chen *et al*.[207] have studied the conformational changes of a silk fibroin-chitosan composite using Raman spectroscopy. It was proved that chitosan could stretch the silk fibers by inter-chain interactions given by the hydrogen bonding that induce conformational changes. As shown in *Figure 5.7.2-6*, the freeze-dried composite is characterized by a ″higher density″ of random coil conformations for chitosan, seen in *Figure 5.7.2.6, b* while the air-dried composite by a ″higher density″ of anti-parallel conformations. Neither the freeze-dried nor the air-dried composites exhibit just one type of conformation for chitosan chains, since both of them were identified. A sketch that illustrates the structural re-organization of the

composite hydrogel network during air-drying processes at room temperature is shown in *Figure 5.7.2-7*. The irreversible transition between these structures results of the increase from crosslinking density in the composite network. Some other aspects of these transition phenomena with respect to the water release rate and to the moisture content of composites were discussed in *Section 5.3*.

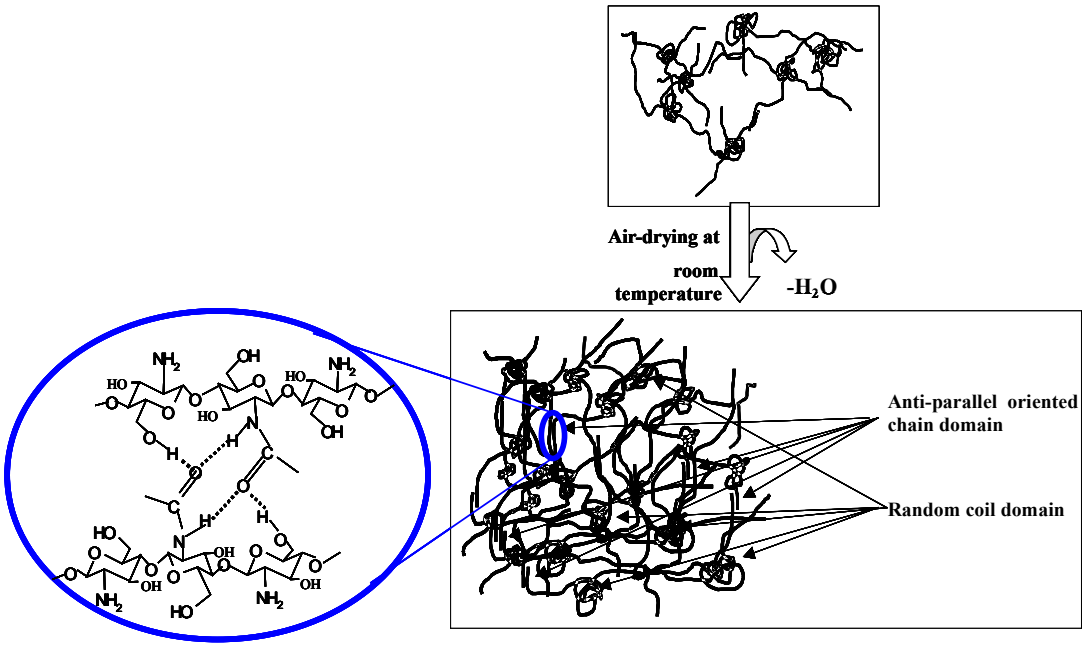

Figure 5.7.2-7 Sketch of the shrinking process of the composite hydrogel network as a result of air-drying at room temperature. The density of anti-parallel chain domains, assimilated as crosslinking regions increases due to the shrinking process. Over a certain value, the crosslinking density achieves a stabilized network structure upon the water swelling process. A parallel oriented chains domain is zoomed in. Here, one can see that the amide bonds from N-acetylamine groups exhibit a limited movement possibility since they are employed in multiple hydrogen bonds.

5.7.5 Conclusions

IR and Raman spectroscopy helped to identify the components of composite samples by their characteristic bands given by the functional groups. Raman and *IR* were found to be very complex comparable to those from natural composites such as bone and dentine. The Raman and *IR* bands shift mainly in intensities with respect to the sample composition. Taking into account the amide bands *I* and *III* from the Raman spectra, the structural reorganization and the conformational changes of the composite hydrogel network structure were probed.

5 Experimental Results and Discussions

5.8 Water states in the composite hydrogels probed by ^{2}H-*NMR* relaxation experiments

5.8.1 Introduction

Water might influence or change the biopolymer organization at a supramolecular level through intermolecular hydrogen bonding. Water can influence the mechanical and rheological properties of materials. Water can exist in free and bound states as evidenced by different techniques such as *TGA*, *DSC*, *NMR*, etc. Three types of water such as non-freezing or strongly bound water, freezing or interfacial weakly bound water and free (bulk) water[208], which interact differently with the polymer gel network, were identified. Among these techniques, *NMR* spectroscopy is a powerful tool to investigate water states and its dynamics in the hydrogel network.

5.8.2 Aim of experiments

- To study the water dynamics in the composite hydrogel network at different ionic strengths by ^{2}H-*NMR* relaxation experiments.
- To estimate the amount of bound water in the composite hydrogel network.

Assumptions

It is assumed that water occurs in the composite hydrogel network in at least two occurrence states. One is so called bound water which interacts strongly with the composite matter being immobilised in the network meshes. Another state is constituted by the free water which freely rotates in the hydrogel network. We assumed that by changing the ionic strength in the composite hydrogel network, the water binding sites would be affected. The induced water dynamics might yield information about the bound water in the hydrogel network.

5.8.3 Materials and methods

Materials, methods and NMR pulse sequences

For *NMR* relaxation experiments, the composite hydrogel samples in different ionic strength environments were measured, as discussed in *Section 4.2.4*.

i) T_1 was determined by inversion recovery method using the following pulse sequence: d_1-(180^0-τ-90^0-)$_n$.

ii) T_2 was determined using the Carr-Purcell-Meiboom-Gill (*CPMG*) pulse sequence[145], described as d_1-$90°_x$-(d_2-$180°_{x'}$)$_n$. The 90° pulse length was 16 μs, the delay time d_2 was 10 ms. The *NMR* measurements were performed at 25.0± 0.3°C in a liquid probehead.

The basic concepts of the *NMR* relaxation methods were discussed in *Section 4.2.4.2* and *Appendix A-V*.

Instrumentation

A Bruker 400 MHz Advance *NMR* spectrometer was used.

5.8.4 Results and discussions

The relaxation times T_1 and T_2 of composite hydrogels at different ionic strength were measured. Spin-lattice relaxation time, T_1, was determined by fitting the longitudinal magnetization recovery, I_z, according to the following equation,

$$I_z(t) = I + P * \exp(-t / T_1) \qquad \textbf{(5.8.4-1)}$$

where I and P are constants and t is the measuring time.

Spin-spin relaxation time, T_2, was determined by fitting the echo amplitude decay using the following equation,

$$I_z = P * \exp(-t / T_2) \qquad \textbf{(5.8.4-2)}$$

The magnetization decay functions can be treated either using a mono-exponential or a bi-exponential approach. Both of them in the present section are discussed. In order to determine the solvent contribution to the composite hydrogel network, two types of normalisation were performed. By normalisation of relaxation rates R_i (i=1,2), obtained from $T_{1,2}$ (according to *Equation 4.2.4-2*) either to the *NMR* solvent (10% D_2O in water) or to the $CaCl_2$ solutions (by using *Equation 4.2.4-5*) the specific relaxation rates were calculated (see *Section 4.2.4*). The specific relaxation rates monitor the relative changes of the relaxation rates due to either the variation of amount of water in the hydrogel network or as a result of water-hydrogel network interactions.

5.8.4.1 Qualitative description by a mono-exponential approximation

In order to evaluate the dynamics of water in the composite hydrogel[209] network, the relaxation times T_1, T_2, and hence the relaxation rates R_1, R_2 were calculated. The specific relaxation rates, either normalised to the salt free solvent or to the salt containing solvent were compared to those obtained for the $CaCl_2$ solutions.

In $CaCl_2$ solutions (measured in the absence of the composite hydrogel), the relaxation rates, R_{2sp}, linearly increases with the concentration of $CaCl_2$ (*Figure 5.8.4-1)*. This behaviour occurs since the salt scales linearly with water molecules from its hydration shell.

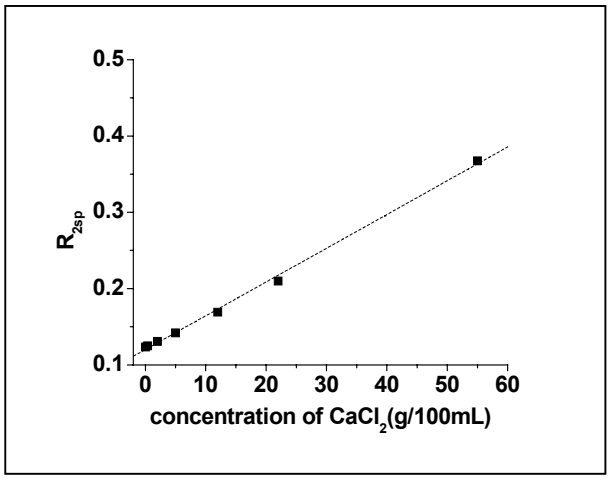

Figure 5.8.4-1 R_{2sp} of $CaCl_2$ solutions (in the absence of composites) versus salt concentration. R_{2sp} values were obtained from normalization of R_2 values of the $CaCl_2$ solutions to R_2^o of 10% D_2O in water.

The specific relaxation rates give information regarding the water dynamics in the presence or the absence of salt with respect to the relative fraction of bound water. The experimental data obtained from a mono-exponential approach are summarized in *Table 5.8.4-1*.

Table 5.8.4-1 NMR parameters determined from the mono-exponential approach.

Conc. of $CaCl_2$ g/100mL	T_1 mono-exponential (s)	R_1 mono-exponential (1/s)	T_2 mono-exponential (s)	R_2 mono-exponential (1/s)	R_{2sp} normalised to the solvent (10% D_2O in water)	R_{2sp} normalised to the $CaCl_2$solutions in (10% D_2O in water)
0	0.392	2.5510	0.2102	4.7569	1.3720	1.1116
0.4	0.404	2.4752	0.1965	5.0875	1.5369	1.2559
2	0.399	2.5062	0.1887	5.2988	1.6422	1.3369
5	0.381	2.6246	0.1666	5.9959	1.9898	1.6210
12	0.358	2.7932	0.1288	7.7615	2.8703	2.3119
22	0.337	2.9673	0.1226	8.1566	3.0673	2.3619
55	0.268	3.7313	0.1041	9.6079	3.7910	2.5029

By varying the ionic strength, both T_1 and T_2 decrease with the amount of ions. The variation of specific relaxation rates at different salt concentrations obtained by normalization of R_2 on 10% D_2O in water and on $CaCl_2$ solutions are displayed in *Figure 5.8.4.2(a)* and *(b),* respectively. Both curves exhibit a rapid increase of R_{2sp} up to about 12g of $CaCl_2$ /100 mL. Above this value, a slow increase of R_{2sp} was observed for the case (*a*) whereby for the case (*b*) R_{2sp} reaches a plateau.

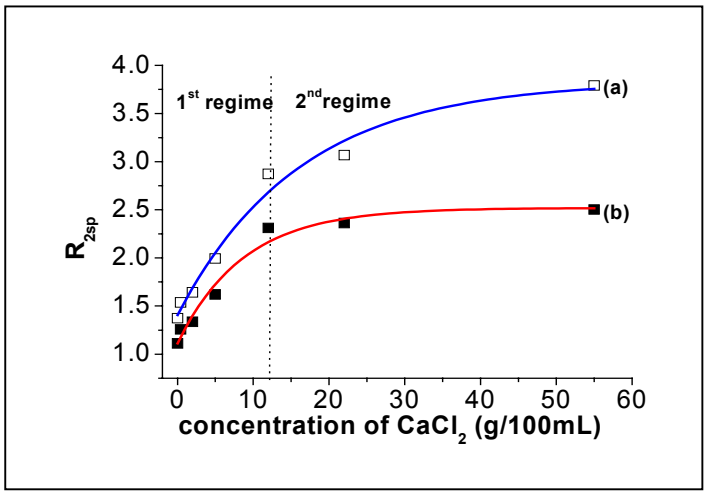

Figure 5.8.4-2 Variation of specific relaxation rates of composite hydrogel samples at different concentrations of $CaCl_2$. (a): R_2 normalised on R_2^o of 10% D_2O in water;(b): R_2 normalised on R_2^{CaCl2} of $CaCl_2$ solutions;

The results suggest that water dynamics within the composite hydrogel network can be discussed with respect to two regimes. In the first regime, the rapid enhancement of specific relaxation rates might be explained either by a decrease of water mobility constrained in the hydrogel network or by an increase of the fraction of water molecules as the ionic strength increases. Since the Ca^{2+} ions bring their hydration shell into the network meshes of composite hydrogel, the fraction of bound water is altered. Once Ca^{2+} ions get into these meshes, they can replace a certain fraction of water from bound sites. However, water from hydration shell contributes to the increase of fraction of bound water. On the other side, the presence of Ca^{2+} ions in the network might lead to a stronger immobilization of bound water and hence R_{2sp} can be enhanced as a consequence of the increase of the residence time of Ca^{2+} ions in the binding sites. In the second regime, the difference between the evolution of R_{2sp} (curves a and b) accounts clearly only the contribution of Ca^{2+} ions with its hydration shell to the water dynamics in the hydrogel network.

Since the relaxation rates are additive, the influence of salt on the composite hydrogel, is also given by ΔR_{2sp} which is obtained from the mathematical subtraction between different relaxations rates. The elucidation of the increase of R_{2sp} with salt concentration might be given by $\Delta R_{2sp.}$ Since the relaxation rates are additive the R_{2sp} normalized on $CaCl_2$ is subtracted from R_{2sp} normalized on D_2O and is graphically represented versus salt concentration *(Figure 5.8.4-3).*

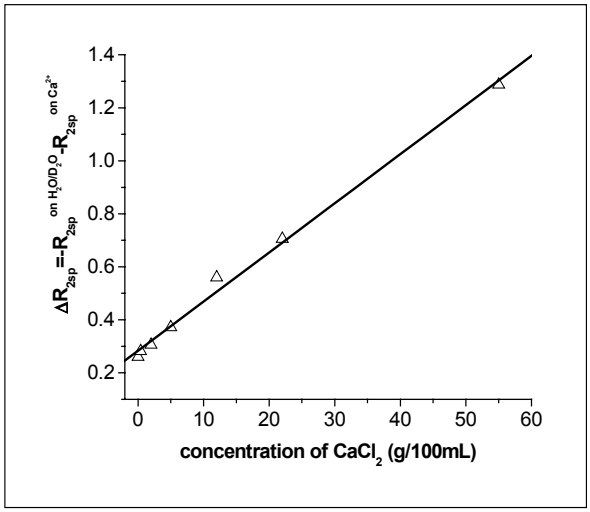

Figure 5.8.4-3 ΔR_{2sp} of composite hydrogels plotted against the concentration of $CaCl_2$.

R_{2sp} is linearly increasing with salt contents. The positive slope might account the contribution which arises from a long residence time of water in the bound sites since it is $\Delta R_{2sp} = R_{2sp}^{D_2O} - R_{2sp}^{CaCl_2} > 0$.

5.8.4.2 Quantitative evaluation of fraction of bound water given by bi-exponential approximation

In this section, the magnetization decay of deuterons was fitted using a bi-exponential function. As an example, the fit of the magnetization decay with a mono- and a bi-exponential functions are presented in *Figure 5.8.4.4- (1)* and *(2),* respectively. A better fit is obtained in the case of the bi-exponential fitting. This can also be visualised from the residual plot (insets *(a)* and *(b)*. In the mono-exponential case, the values scattered around zero whereas in the bi-exponential case the values approach zero.

For quantitative evaluations, T_2 is obtained from the bi-exponential fit and a *"Two sites model"*[146] is considered. This model assumes that, there is a fast exchange process between water molecules, which exist in free and bound sites. Here, T_{21} (R_{21}) is chosen to describe the slow motion process (given by immobilised water) and T_{22} (R_{22}) for the fast motion (free water). The *NMR* parameter values are summarized in *Table 5.8.4-2.*

Since there is an exchange between the two molecular sites, the fraction of water molecules can be determined as follows[210],

$$\frac{1}{T_2} = \frac{\eta}{T_{21}} + \frac{1-\eta}{T_{22}} \qquad \textbf{(5.8.4-3)}$$

where i=1,2, T_{22} is the short relaxation time in the binding sites and T_{21} is the long relaxation time in the free sites. The fraction of bound water, η, (expressed as g /g bound water per dry material) is ranging from 0.16 to about 0.47 for the composite hydrogel samples. The range of η scales with the ionic strength and indicates that the lower value corresponds to the no-added salt composite hydrogel sample. The fraction of bound water can also be expressed as the percentage of the bound water per corresponding amount of dry composite.

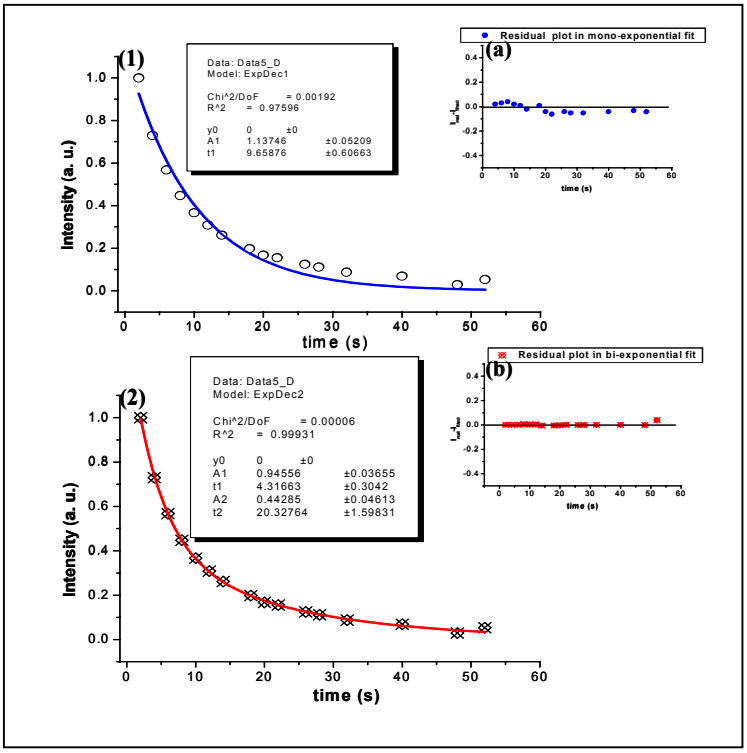

Figure 5.8.4-4 Two comparative fits of the magnetization decay of deuterons, in the case of a composite hydrogel sample with 2% $CaCl_2$. Curve (1): mono-exponential decay plot. Curve (2): bi-exponential decay plot. Insets (a) and (b) display the residuals of the mono and bi-exponential plots, respectively.

Table 5.8.4-2 Summary of NMR parameters obtained with the bi- exponential function.

Concentration of $CaCl_2$ in g/100mL	T_{21} bi-exponential (s)	R_{21} bi-exponential (1/s)	T_{22} bi-exponential (s)	R_{22} bi-exponential (1/s)
0	0.50804	1.9683	0.0876	11.4149
0.4	0.38961	2.5667	0.07997	12.5046
2	0.31193	3.2058	0.06393	15.6422
5	0.26821	3.7285	0.05121	19.5274
12	0.24794	4.0332	0.0577	17.3314
22	0.24301	4.1150	0.06152	16.2560
55	0.18819	5.3138	0.06927	14.4359

In this case, the bound water in the composite hydrogel network ranges from 13.88% to about 40% as a function of ionic strength. Since the fraction of bound water depends on the ionic strength, the bound water from hydration shell of Ca^{2+} and Cl^- ions was considered for calculations. The amount of bound water brought by ions in the composite hydrogel network is comprised in *Table 5.8.4-3.*

Table 5.8.4-3 Fraction of bound water brought in the composite hydrogel network as an increase of $CaCl_2$ concentration.

Conc. of $CaCl_2$ (g%, wt/v)	Conc.of $CaCl_2$ mol/L	Amount of $CaCl_2$ (mmol) in the NMR tube (270µL)	Amount of water in 1st shell of hydration for Ca^{2+} (1 Ca x 7.5 H_20)	Amount of water in 1st shell of hydration for Cl^- $1Cl^-x1H_2O$	Amount of bound water brought by $CaCl_2$ (mg)	Bound water amount brought by $CaCl_2$ / composite (mg/g)
0.4	0.0360	0.0097	0.0729	0.0194	1.6614	76.9166
2.0	0.1801	0.0486	0.3645	0.0972	8.3106	384.7500
5.0	0.4500	0.1215	0.9112	0.3037	21.8682	1012.4166
12.0	1.0800	0.2916	2.1870	0.5832	49.8636	2308.5000
22.0	1.9800	0.5346	4.0009	1.0692	91.2618	4225.0833
55.0	4.9500	1.3365	10.0237	2.6730	228.5400	10580.5555

It is assumed that in aqueous solutions, Ca^{2+} is surrounded by 7-7.5 molecules of water[211] in the first hydration shell. In the case of Cl^-, each ion carries between 1 and 6 water molecules in the first hydration shell. The capacity of anions to bind water is not as strong as that of cations. For Cl^-, one water molecule can be considered as strongly bound to the anion[212]. Based on these considerations, one can plot R_{21} and R_{22} as a function of the bound water brought in the composite hydrogel network by the ions *(Figure 5.8.4-6).*

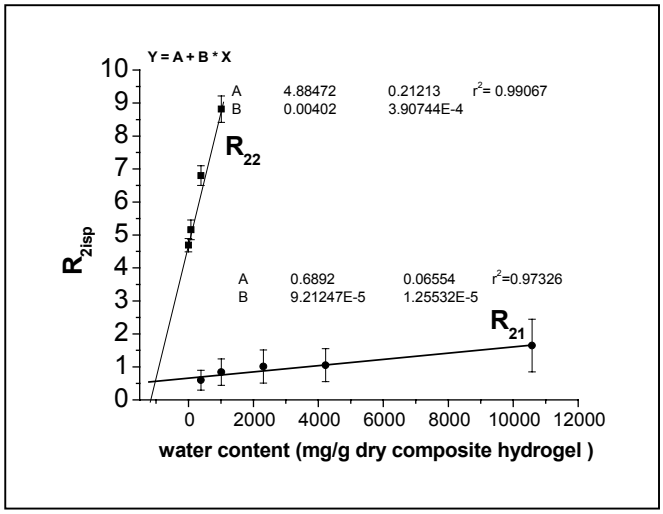

Figure 5.8.4-6 R_{2isp}; (i=1,2) plotted against the amount of the bound water brought by the $CaCl_2$ in the hydrogel network.

Both components, such as the slow, R_{21}, and the fast, R_{22}, exhibit a linear dependence as the fraction of bound water in the composite hydrogel network increases. From the linear dependence, the weakly and strongly bound water was determined according to *Equations*[204] *5.8.4-4* and *5.8.4-5;*

$$R_{21}=0.69+9.21x10^{-5}\ W_{\text{weakly bound}} \qquad \textbf{(5.8.4-4)}$$

$$R_{22}=4.88+4.02x10^{-3}\ W_{\text{strongly bound}} \qquad \textbf{(5.8.4-5)}$$

The weakly bound water was determined from the projection of R_{21} to *OX* axis. The extrapolation of R_{22} to the *OX* axis gives the sum of weakly and strongly bound water, which is about 1150 mg per 1g of dry composite. The difference between the summed contributions of weakly and strongly bound water and the weakly bound water gives the values of the strongly bound water in the composite hydrogel network. This was evaluated to be about 10 - 15 mg/g dry composite that is in agreement to the value determined by using the first approach based on *Equation 5.8.4-3.*

5.8.5 Conclusions

The dynamics of water molecules in the composite hydrogel samples in both weak and strong bound molecular sites were studied using ^{2}H-*NMR* relaxation experiments. The dynamics of water in composite hydrogel samples induced by the presence of different ionic strength environments were probed. The relaxation rates linearly increase with the salt content up to 10-12% of $CaCl_2$. Once this concentration's exceeded, some reorganization of composite hydrogel network was observed. Due to the heterogeneities of the pores in composite hydrogel network, the small pores might strongly entrap water whereas in the large pores the water molecules might exhibit a large mobility interval. By using a bi-exponential approach, the ^{2}H relaxation experiments allowed evaluation of the amount of strongly bound water in the composite hydrogel network. The amount of strongly bound water is about 10-15mg/g of dry composite. Baumgartner *et al.*[209] have determined the fraction of bound water in different cellulose hydrogels by ^{1} H-*NMR* relaxation measurements. This ranged between 13.8 –15.2 mg/ g of dry material. Le Botlan *et al.*[213] have evaluated the bound water of different types of wheat starches by time domain *NMR* spectroscopy. The fraction of bound water was determined to be about 12 - 17 mg/g of dry material. Our value, determined for the bound water of composites containing chitosan, cross the literature data for the systems containing naturally related polysaccharides.

5.9 Mechanical tests on composites

5.9.1 Introduction

J. D. Currey[161] has reported the factors that determine the bending strength of compact bone, together with some possible explanations. The bending strength of wide variety of bone type specimens is proportional to the Young's modulus of elasticity.

The mechanical parameters of bone are taken as criteria for design and fabrication of new bone substitute materials.

The aim of these experiments was to evaluate the mechanical properties of different types of composite samples measured in dry and wet states.

5.9.2 Materials and methods

The sample description is given in the following table.

Table 5.9.1 Summary of the description of composite samples used for mechanical tests.

No.	Specimen code	Density of specimen (g/cm^3)	Content in *HAp* (wt%)	Remarks on sample preparation
1	VR-030617-01	1.40	*0*	*CTS** (*TM 1238*, *Primex*) regenerated from alkaline media, dried at room temperature for 5 days and then 4h in the oven at 70°C. The samples were dried in cylinder holders of hydrophobic plastic.
2	VR-030617-02	1.50	50	Composite made of *CTS* (*TM 1238*, *Primex*) *CTS/HAp* 50:50% dried at room temperature for 5 days then for 4h at 70°C in the oven.
3	VR-030617-03	1.57	50	Composite made of *CTS* TM 1238, *CTS/HAp* 50:50% (1mL of $CaCl_2$, 10% was added to 20 g of gel composite) dried at room temperature (22°C) for 5 days. $CaCl_2$ was washed with distilled water and the sample was dried for 4h at 70° C in the oven.
4	VR-030617-04	0.85	50	The same as 3, followed by swelling in distilled water and then the sample was freeze dried in order to get porous structure.
5	VR-030617-05	1.29	50	Idem 3, without washing the $CaCl_2$ from the composite network.
6	VR-030617-06	0.80	0	The same as 1, but swollen in distilled water and freeze-dried. A porous chitosan specimen was obtained.
7	VR-030619-01	1.68	70	Composite *CTS/HAp* 30:70% made of *CTS* (*TM 1238*, *Primex*), dried at room temperature for 5 days then for 4h at 70°C in the oven.
8	VR-030619-02	1.43	30	Composite *CTS/HAp* 70:30% made of *CTS* (*TM 1238*, *Primex*), dried at room temperature for 5 days and then for 4h at 70°C in the oven.
9	VR-030626-01	1.55	50.5	Composite *CTS/HAp* 50:50% made of *CTS* (*TM 1238*, *Primex*), reinforced by *HAp* particles with particles size less than 80 μm; at 30g composite hydrogel 0.0140 g *HAp* was added then dried at room temperature until a completely dried specimen was obtained.
10	VR-030626-02	1.60	52	The same as 9, but at 30 g composite hydrogel 0.0500 g *HAp* was added.
11	VR-030626-03	1.64	60	The same as 9, but at 30 g *CTS* hydrogel 0.2 g of *HAp* was added.

*CTS** is the abbreviation for chitosan

Instrumentation and the set up of experiments

Instrument: Instron M4202
Software: Instron Series IX version 8.06.00

Test Type: Flexural (three point bending) and compressive tests
Load cell: 1 KN
Span of holder: 17.52 mm
Geometry of specimen: Rectangular (2÷4 mm x 2÷4mm x 30mm)
Number of specimens: 3-5
First crosshead speed: 1 mm/min for flexural tests and 2 mm/min for compressive tests
Temperature: 22°C
Relative humidity: 50 %

Methods

The densities of samples by using a liquid displacement method[214] with degassed isopropanol as a displacement solvent were determined. The mechanical experiments in flexural mode (three point bending test) and in compressive mode were performed, as presented in *Section 4.2.9*. In the flexural mode the samples were measured as dried, whereas in the compressive mode, both dry and wet samples were measured. In order to diminish the *SD* values, the mechanical tests were performed on at least three specimens of the same sample. The results were analysed using the *MicroCall Origin 6.1* software in statistic mode.

5.9.3 Results and discussions

The mechanical parameters such as the Young's modulus, the maximum yield at stress and the ultimate stress can be determined either by three point bending (flexural) or by compressive tests. For our purposes, both methods were considered.

The results of the three point bending tests obtained on dry composite samples are shown in *Tables 5.9.2* and *5.9.3*. The maximum yield at stress is defined as the maximum value to which the specimen can be loaded before it breaks.

Table 5.9.2 Maximum yield at stress values of composite samples in a flexural mode.

Sample code	*no. exp.*	*Mean (Yld. Str.) (MPa)*	*S.D. (Yld. Str. Er±) (MPa)*	*Min (Yld. Str.) (MPa)*	*Max (Yld. Str.) (MPa)*	*Sum (Yld. Str.) (MPa)*
VR 030617 01	**[1:5]**	**56.76**	**8.13**	**43.86**	**65.89**	**283.81**
VR 030617 02	**[1:3]**	**30.63**	**4.84**	**25.06**	**33.80**	**91.91**
VR 030617 03	**[1:4]**	**42.24**	**1.76**	**40.06**	**44.35**	**168.98**
VR 030617 04	**[1:3]**	**3.51**	**0.05**	**3.47**	**3.58**	**10.54**
VR 030617 05	**[1:3]**	**21.38**	**5.67**	**15.87**	**27.21**	**64.14**
VR 030617 06	**[1:3]**	**3.34**	**1.19**	**2.20**	**4.58**	**10.02**
VR 030619 01	**[1:3]**	**12.63**	**6.28**	**8.36**	**19.85**	**37.90**
VR 030617 01	**[1:4]**	**10.09**	**1.71**	**7.59**	**11.37**	**40.36**
VR 030626 01	**[1:4]**	**10.08**	**1.71**	**7.59**	**11.36**	**40.35**
VR 030626 02	**[1:3]**	**6.07**	**0.38**	**5.66**	**6.43**	**18.23**
VR 030626 03	**[1:4]**	**22.58**	**3.72**	**20.20**	**28.07**	**90.32**

5 Experimental Results and Discussions

The experimental data regarding the yield at stress lead to the following observations. Chitosan yields at 56.76 MPa (sample code VR 030617 01) followed by the composite samples VR 030617 03 and VR 030617 02, which yields from 30.63 MPa up to 42. 24 MPa. The porous specimens (either the composite or chitosan samples) are the smallest weakest of all. They yield at one order of magnitude lower than the rest of specimens. Thus, 3.51 MPa was the yield stress of sample VR 030617 04 (porous composite) and 3.34 MPa for sample VR 030617 06 (porous chitosan). The Young's modulus calculated from the linear region of the stress-strain curves *(Equation 4.2.9-2)* are summarized in *Table 5.9.3*.

Table 5.9.3 Young's modulus data of composite samples in flexural mode.

Sample code	*no. exp.*	*Mean (Mod.) (MPa)*	*S.D. (Mod. Er±) (MPa)*	*Min (Mod.) (MPa)*	*Max (Mod.) (MPa)*	*Sum (Mod.) (MPa)*
VR 030617 01	**[1:5]**	**2739.20**	**370.77**	**2343.00**	**3183.00**	**13696.1**
VR 030617 02	**[1:3]**	**3361.11**	**386.24**	**3138.00**	**3807.00**	**10083.2**
VR 030617 03	**[1:4]**	**2423.25**	**263.74**	**2094.00**	**2692.00**	**9693.11**
VR 030617 04	**[1:3]**	**122.370**	**38.25**	**87.21**	**163.10**	**367.45**
VR 030617 05	**[1:3]**	**389.46**	**191.48**	**172.60**	**535.20**	**1168.23**
VR 030617 06	**[1:3]**	**84.196**	**13.11**	**74.37**	**99.09**	**252.12**
VR 030619 01	**[1:3]**	**2992.00**	**1337.32**	**1968.00**	**4505.00**	**8976.68**
VR 030617 01	**[1:4]**	**440.32**	**49.63**	**390.80**	**480.10**	**1760.10**
VR 030626 01	**[1:4]**	**265.40**	**102.63**	**132.80**	**381.10**	**1061.95**
VR 030626 02	**[1:3]**	**189.76**	**50.745**	**143.60**	**244.10**	**569.13**
VR 030626 03	**[1:4]**	**2374.75**	**642.82**	**1691.00**	**3219.00**	**9499.17**

The Young's modulus values range from 100 MPa (porous chitosan specimens) up 3.36 GPa , the greatest value measured (for the composite sample VR 030617 02). The smallest values were from porous samples. The Young's modulus of the reinforced composite such as VR 030626 01 and VR 030626 02 was of ca. 200 MPa which is one order of magnitude lower than that of the non-reinforced composite (2.5-3 GPa) specimens. Sample VR 030626 03 was stiffer than the first two reinforced samples. These data suggest that by reinforcing the composite with *HAp* particles up to a certain value, the yield stress and the Young's modulus decreased with increasing the amount of *HAp*. Once this limit is exceeded, the mechanical performances increase as the amount of *HAp* increases. It is hard to explain this behaviour. However, most probably the interface interactions between the composite matrix and the *HAp* fillers might be responsible.

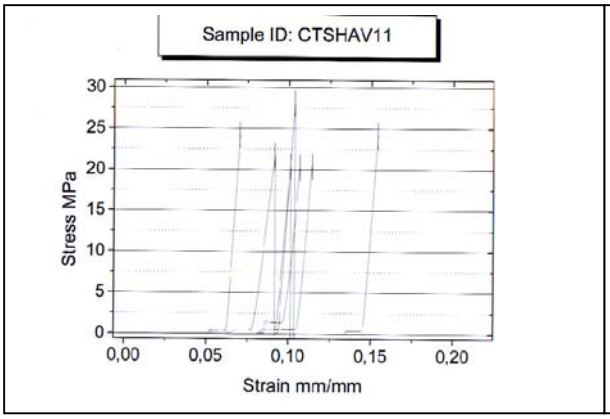

Figure 5.9.1 Stress - strain curves in flexural mode of composite sample reinforced by HAp, sample code VR 030626 03.

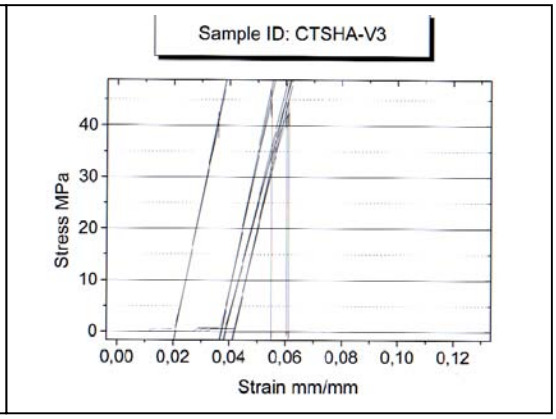

Figure 5.9.2 Stress - strain curves in flexural mode of a composite sample code VR 030617 03.

The stress - strain curves obtained for different types of composites are displayed in *Figures 5.9.1-5.9.4*. From the profile of stress - strain curves, the toughness and brittleness characteristics of the sample can be evaluated. The toughness is linked to the area below the curves and the brittleness is mainly connected to the form of the breaking line. It can be observed that the specimens exhibit different profiles of breaking lines. Samples labelled as VR 030617 01, (*Figure 5.9.1*) and VR 030619 01 (*Figure 5.9.4*) do not show a secondary loading region after the first linear loading region. These types of the loading curves are typical for the brittle ceramic materials[162]. The second loading region is a characteristic feature for the plastic materials and it is also found for the composite samples containing $CaCl_2$, as seen in *Figure 5.9.3*.

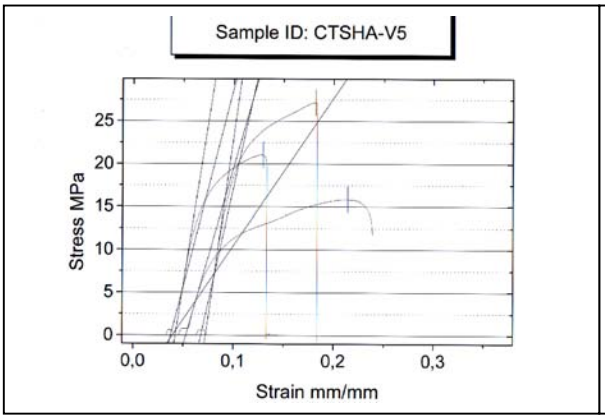

Figure 5.9.3 Stress - strain curves in flexural mode of CTS/HAp 50:50 wt% composite containing $CaCl_2$; sample code VR 030617 05.

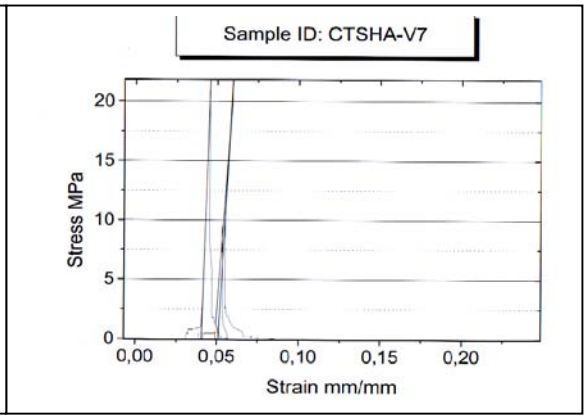

Figure 5.9.4 Stress against strain curves in flexural mode of CTS/HAp 30:70 wt%; sample code VR 030619 01.

This profile of the stress-strain loading curve can be explained by the fact that the samples containing $CaCl_2$ retain more water in their structure compared to the specimens with no content of salt. The presence of water in different states of occurrence in the composite matrix can influence and even change the mechanical properties of the composite specimens.

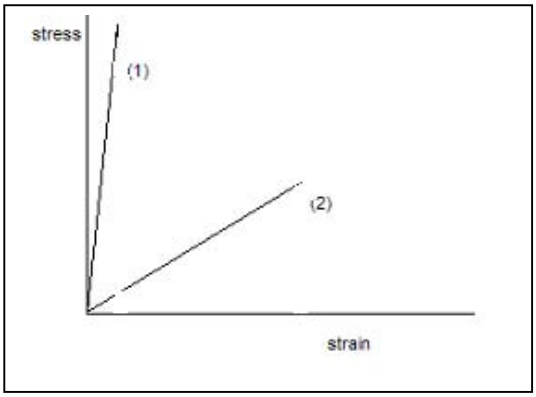

Figure 5.9.5 Stress-strain curves for two specimens (1) and (2), respectively. The stiffer material, specimen 1, is less tough compared to specimen 2 since it takes less energy to break it (area below the graphs). Hence, specimen 1 is stronger than specimen 2 because it reaches a higher yield at stress[162].

The stiffness and the toughness of materials are determined from the stress-strain curve profiles *(Figure 5.9.5)*.

Besides the three points bending test, mechanical tests in compressive mode, in both dry and wet states on composite specimens were performed. The data obtained from compression experiments are summarized in *Table 5.9.4*.

Table 5.9.4 Mechanical data in compressive tests as measured on dry and wet samples.

Sample code	Dry compression test; Compressive Young's modulus (MPa)	Dry compression test; Ultimate stress value (MPa)	Dry/wet Compressive Young's modulus	Wet compression test; Compressive Young's modulus (MPa)	Wet compression test; Ultimate stress value (MPa)	Dry/wet Ultimate stress value
VR 030617 01	526.12±85.23	28.15±2.12	43.83	12.48±2.09	0.62±0.04	45.48
VR 030617 02	703.52±125.12	35.18±4.04	26.92	26.14±5.21	2.10±0.25	16.67
VR 030617 03	730.09±113.49	29.78±5.10	24.06	30.01±3.40	2.11±0.40	14.50
VR 030617 04	128.00±23.15	3.50±0.25	16.09	7.89±4.05	0.55±0.13	6.36
VR 030617 05	175.67±20.08	5.32±0.48	10.29	17.11±3.04	0.70±0.15	7.62
VR 030617 06	66.78±15.11	3.73±0.53	12.00	5.58±0.80	0.69±0.07	5.40
VR 030619 01	1847.09±353.76	23.12±2.38	123.13	15.08±2.03	0.77±0.05	29.88
VR 030617 01	126.98±15	12.46±1.33	17.32	7.33±1.62	1.25±0.08	9.96
VR 030626 01	144.33±10.67	14.33±4.60	13.85	10.42±1.89	1.65±0.07	8.64
VR 030626 02	276.32±23.34	17.02±2.12	23.29	11.86±1.87	1.85±0.09	9.20
VR 030626 03	1160.67±191.34	29.67±5.34	82.73	14.02±1.52	1.30±0.05	22.83

5 Experimental Results and Discussions

The ultimate yield at stress and the compressive Young's modulus were calculated. By using the ratio between dry/wet values obtained for the ultimate stress values and for the compressive Young's modulus values, the data analysis gives evidences on mechanical properties of dry/wet composite specimens. The results show that the mechanical properties in the wet state are at least one order of magnitude lower than those obtained in dry state for the same type of sample *(Table 5.9.4)*. The Young's modulus measured for the wet samples range between 5 and 30 MPa while in some cases for the dry state it exceeds 1 GPa. In order to determine the influence of the *HAp* content and hence the sample density on mechanical properties, different samples with various compositions were compared with each other.

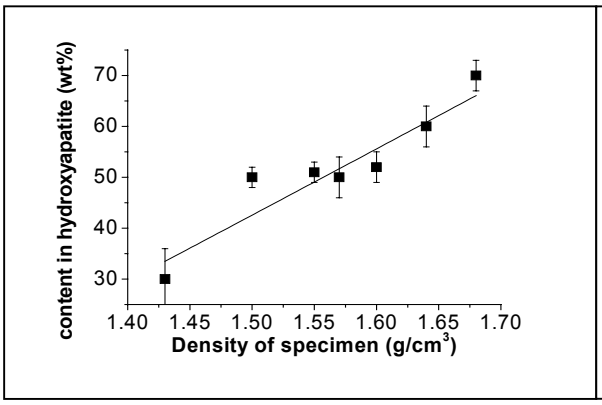

Figure 5.9.6 Content of HAp (wt %) in composite samples as a function of sample density.

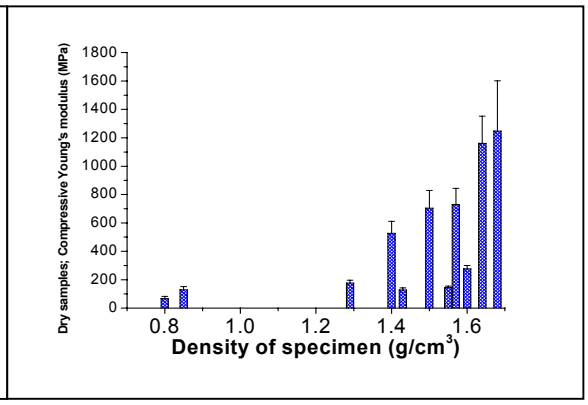

Figure5.9.7 Compressive Young's modulus in dry state for a series of sample containing chitosan/HAp 50:50 wt% as a function of sample density.

A linear increase of the specimen density as the content of *HAp* in the composite samples increases was obtained *(Figure 5.9.6)*.

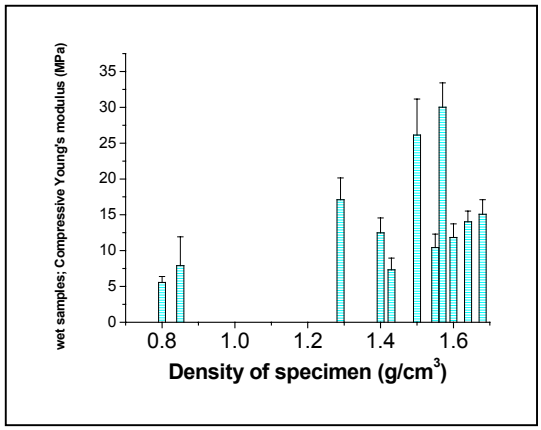

Figure 5.9.8 Compressive Young's modulus in wet state for a series of composites (chitosan/HAp 50:50 wt%), as a function of sample density.

For the compressive Young's modulus, a general increasing trend of values was observed as the sample density increases *(Figures 5.9.7* and *5.9.8)*. For the composite samples in dry state, the compressive Young's modulus ranges from 126 MPa for porous *chitosan/HAp* composite up to about 1.8 GPa for *chitosan/HAp* 30:70 wt% composite. In the case of Young's modulus, the same increasing trend was found, as the sample density increases. For the reinforced composite specimens, one can expect better mechanical performance compared to the non-reinforced composites.

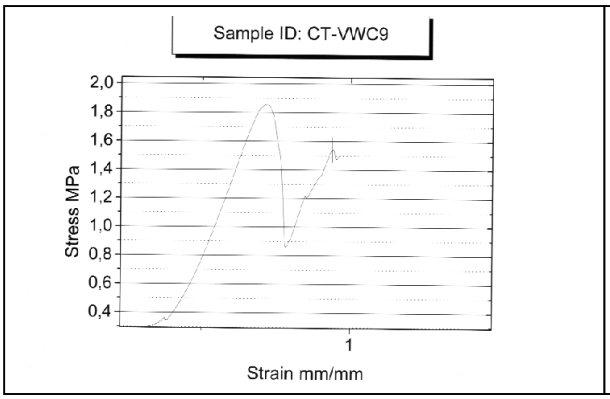

Figure 5.9.9 Stress –strain curve in wet compression experiments for a composite reinforced by HAp, sample code VR 030626 01.

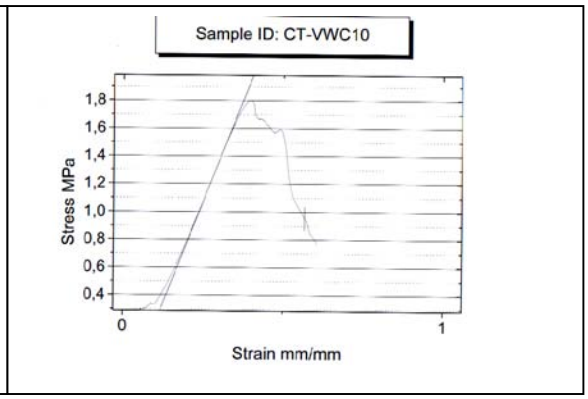

Figure 5.9.10 Stress-strain curve measured in wet compression experiments for a composite reinforced by HAp, sample code VR 030626 02.

The results are contrary to our expectations. They suggest that the interactions between the composite matrix and the *HAp* fillers make the composites less brittle compared to those without fillers. This is in accord to the breaking line shapes identified in the stress - strain loading curves. The reinforced samples became less brittle due to the enlargement of the cracking surface area compared to the non-reinforced composite samples. Thus, it was found that the samples corresponding to the codes VR-030617 02 and VR-030617 03 have the greatest values for ultimate yield at stress and for compressive Young's modulus. In order to show the stress-strain curve profiles, two samples in wet compressive experiments are shown in *Figures 5.9.9* and *5.9.10*. The compressive Young's modulus of composites in dry and wet states represented as a function of *HAp* content are shown in *Figures 5.9.11* and *5.9.12*. They exhibit the same trend as found in the case of bone samples as a function of *HAp* content[161]. Their mechanical performances are enhanced as the content of *HAp* increases.

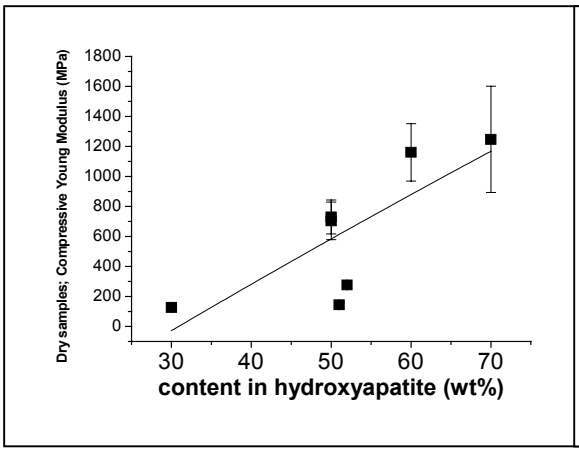

Figure 5.9.11 Compressive Young's modulus of dried samples as a function of HAp content.

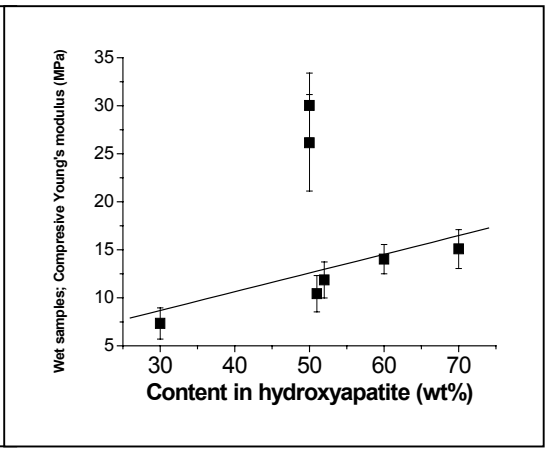

Figure 5.9.12 Compressive Young's modulus of wet samples as a function of HAp content.

5.9.4 Conclusions

The mechanical tests carried out on composite samples allowed us to evaluate some of the mechanical parameters such as the bending Young's modulus, the yield at stress in three point bending tests as well as the compressive Young's modulus and the ultimate stress in dry and wet conditions.

The mechanical parameters were found to vary between certain limits as presented below.

i) *Yield at strain* (flexural mode) is ranging from 6 up to about 42 MPa;
ii) *Bending Young's modulus* is ranging from 84 MPa to about 3.4 GPa (for compact bone this parameter is ranging from 7 up to 20 GPa);
iii) *Compressive modulus* is ranging from 127 up to ca. 1.8 GPa for dry specimens while in the case of wet specimens is ranging from 7 up to ca. 30 MPa;

Our data are within the literature reported data for this family of composites. For *chitosan /HAp* nanocomposites, obtained by a one step co-precipitation method, Yamaguchi *et al.*[13] have determined for the bending Young's modulus values ranging from 50 to 300 MPa. In the case of *chitosan / HAp* nanocomposites, obtained by in situ hybridization, Hu *et al.*[215] have bending Young's modulus up to ca. 3.9 GPa. The mechanical performance of composites is one order of magnitude less than those determined for compact bone (11-20 GPa for bending Young's modulus and between 124-174 for the Yield at strain) but they are comparable to those of cancelous (spongy) bone[75-77, 79] (0.05- 1GPa for the bending Young's modulus).

5 Experimental Results and Discussions

5.10 Partial enzymatic degradation of composite samples

5.10.1 Introduction

From the viewpoint of biodegradability, the biomaterials can be classified in biodegradable and bioinert ones. In the case of biodegradable implantable materials, an important issue is to evaluate their enzymatic behaviour *in vitro*. From the degradation curve profiles, the enzymatic degradation rate can be determined. The enzyme must be chosen in order to degrade the organic matrix of composite materials. Artificial biomaterials containing chitosan as a polymer matrix are usually degraded by lysozyme. This enzyme is wide spread in nature in animals and plants. Lysozyme occurs in egg white and in body fluids of mammals. The function of lysozyme is to hydrolyse the *ß (1-4)* glycosidic bond between residues of *N*-acetylmuramic acid (*NAcM*) and between *N*-acetylglucosamine (*GlcNAc*) from polysaccharides[216]. According to the sub-site nomenclature proposed by Davies *et al.*[217], the binding sub-sites can be written as (-4)(-3)(-2)(-1)(+1)(+2). The amino acid residues participating to the binding substrate[218] are *Asn59*, *Trp62*, *Trp63* and *Ala107* at sub-site (-2), *Trp62* at sub-site (-3) and *Asp101* at sub-sites (-3) and (-4). At the sub-sites (+1) and (+2), the *Arg114* and *Phe34* are considered as binding contact sites. The binding energy of these seven binding sub-sites determined for two types of lysozymes are comprised in *Table 5.10.1*.

Table 5.10.1 Binding energy of individual sub-sites of lysozime enzymes [216, 217]

Type of lysozyme	**Sub-sites (according to Davies) Binding energy (Kcal/mol)**						
	(-4)	**(-3)**	**(-2)**	**(-1)**	**(+1)**	**(+2)**	**(+3)**
Hen egg white lysozyme	-2.0	-3.0	-5.0	+4.5	-2.5	-1.5	*)
Goose egg white lysozyme	*)	-0.5	-2.2	+4.2	-1.5	-2.6	-2.8

*) not determined

5.10.2 Aim of experiments

- To obtain the enzymatic degradation curves of different types of composite samples.
- To see how the chitosan type influences the enzymatic degradation profile.
- To evaluate the degradation rates with respect to the composite composition.
- To see whether the pH changes during the degradation period.
- To identify the degradation products such as chitosan oligomers by *MALDI-TOF* mass spectroscopy.
- To study the samples morphologies before and after the enzymatic degradation by using *TEM*.

5.10.3 Materials and methods

Materials

i) Lysozyme from hen egg white (*Merck*), 100,000 U/mg.

ii) Two series of composite samples as described below, were analysed.

- ♦ Composite samples containing different types of chitosan, varying by their *DD*.
- ♦ Composite samples *50:50* wt% prepared from Krill chitosan, *DD* =75% and containing different amounts of cations (Cu^{2+}, Mn^{2+} and Zn^{2+}).
  A summary of composites description is given in *Table 5.10.3-1*.

Table 5.10.3-1 Composite samples used in the enzymatic degradation experiments

Sample code	Sample description
VR 03 0402 02	(*CTS*/HAp* 50:50 wt% made of insect chitosan (*M. Struszczyk, Aug 2000*), *DD*= 67
VR 02 0612 01	(*CTS/HAp* 50:50 made of krill chitosan (*2K2X*), *DD* =75%)
VR 03 0402 01	(*CTS/HAp* 50:50 made of crab chitosan (*Lot no. 91K1265*, *Sigma*), *DD* =80%
VR 03 0327 06	(*CTS/HAp* 50:50 made of shrimp chitosan (*TM 1238*, *Primex*), *DD* = 92%
VR 02 0612 02	(*CTS/HAp* 50:50 made of krill chitosan (*2K2X*), *DD* =75%, Cu^{2+}, Mn^{2+}, Zn^{2+}, 30 ppm)
VR 02 0612 04	(*CTS/HAp* 50:50 made of krill chitosan (*2K2X*), *DD* = 75%, Cu^{2+}, Mn^{2+}, Zn^{2+}, 120 ppm)
VR 02 0612 05	(*CTS/HAp* 50:50 made of krill chitosan (*2K2X*), *DD* = 75%, Cu^{2+}, Mn^{2+}, Zn^{2+}, 150 ppm)

**CTS* is the abbreviation for chitosan. Where 1 ppm is expressed as 1μg cations /1g of dry composite.

iii) Simulated body fluids[219], *SBF*, a saline solution with a complex chemical composition as enzymatic medium was used. Its composition is given in *Table 5.10.3-2*.

Table 5.10.3-2 Composition of SBF solution in bidistiled water[219, 220]

Type of ion	Na^+	K^+	Mg^{2+}	Ca^{2+}	Cl^-	HCO_3^-	HPO_4^{2-}	SO_4^{2-}
Concentration of ion (mM)	***141.2***	***5***	***1.5***	***2.5***	***147***	***4.2***	***1.0***	***0.5***
Type of salt - Concentration (mM)	NaCl 136 $NaHCO_3$ 4.2 Na_2HPO4 1	KCl 5	$MgCl_2$ 1 $MgSO_4$ 0.5	$CaCl_2$ 2.5	NaCl 136 KCl 5 $MgCl_2$ 1 $CaCl_2$ 2.5	$NaHCO_3$ 4.2	Na_2HPO4 1	$MgSO_4$ 0.5

Instrumentation

Thermostatic water bath; type Veb mlw; W1

MALDI-TOF-Spectrometer; type Bruker Reflex II

Scanning electron microscope, *SEM*; type BS 340 Tesla

Methods

Since lysozyme activity is a function of pH and temperature, being sensitive to the experimental conditions[167], the working parameters must be well controlled. In order to mimic the conditions of the living body *(in vivo),* the experiments were carried out in simulated body fluids, *SBF*, at 37^{o} C. The pH of *SBF* solution is ca. 7.04. The enzymatic degradation experiments were performed according to the method described in the *Section 4.2.11*. In order to mimic the lysozyme concentration in the human body fluids[221], the lysozyme concentration used was 1 mg/mL. As control samples (reference), composite samples in *SBF* solutions with no enzyme were incubated. During the degradation period of 50 days at 37^{o} C, by using a Macherey-Nagel pH paper, the pH of the supernatant was determined. The identification of chitosan oligomers from supernatants of degraded composites (after the degradation period) were performed by *MALDI-TOF* mass spectroscopy[222]. The basic principles of *MALDI-TOF* mass spectroscopy are given in *Appendix A-XII*. The sample preparation for *MALDI-TOF* analysis is briefly described here. About 2 mL of the supernatant sample containing chitosan oligomers without any preliminary purification was freeze-dried. Between 1.5 and 3 mg of freeze-dried supernatant samples, was dispersed in 50μL water / methanol mixture (1:1 v/v). The mass spectra were analysed for the *m/z* characteristic cluster lines of chitosan oligomers.

5.10.4 Results and discussions

5.10.4.1 Yield of the enzymatic degradation

In order to monitor degradation the yield of the enzymatic degradation, *YD* as a controlling parameter was used (calculated according to *Equation 4.2.11-1*). The *YD* plotted against the degradation time leads to the enzymatic degradation curve. The enzymatic curves probed that the degradation process takes place while for the control composite samples no degradation was observed. In composite samples prepared with different types of chitosan, as described in *Table 5.10.3-1*, the enzymatic degradation rates show that they are a function of the chitosan type. Due to the specificity of lysozyme to hydrolyze the glycosidic bond only between two *GlcNAc* linked residues, greater degradation rates were obtained for the composite samples which contain chitosan with lower values of *DD*[168].

The degradation curves are lying with respect to the *DD* of chitosan sample, as shown in *Figure 5.10.4-1*. Since the composite samples labeled as VR 03 04 02 02 and VR 02 06 12 01 have the lowest *DD* values, they exhibit the highest degradation rate. After 50 days of

enzymatic degradation, the maximum degradation yields reached 9% and 6.2% for the samples VR 03 04 02 02 and VR 02 06 12 01, respectively.

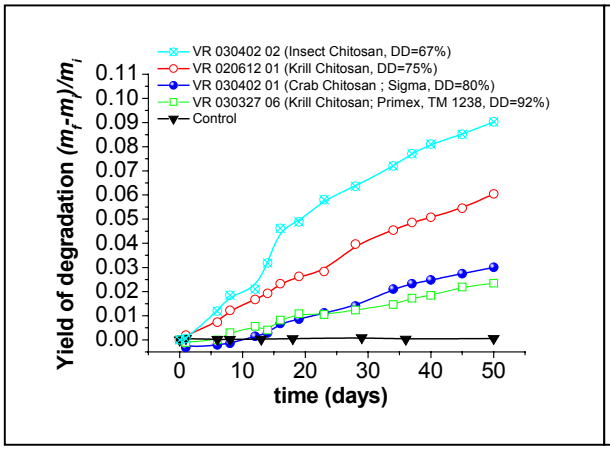

Figure 5.10.4-1 Enzymatic degradation curves of composite samples, made of different types of chitosan samples.

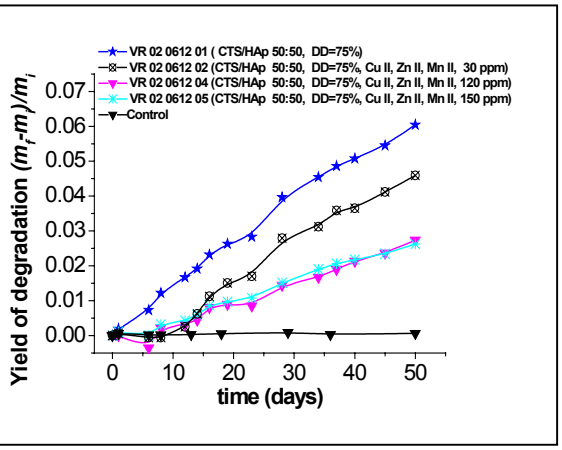

Figure 5.10.4-2 Enzymatic degradation curves for a series of composite samples, made of krill chitosan containing cations.

Table 5.10.4-1 Degradation rates determined by a linear fitting approach.

Sample	**Parameters of the linear fitting ($Y = A + B*X$)**	**Maximum yield of degradation (loss of mass , wt%)**	**Rate of degradation (loss of mass per day, wt%)**
VR 030402 02 (It contains insect chitosan, *DD*=67%)	*R=0.9791* A=0.00475 *B=0.00191*	9.0	1.20×10^{-3}
VR 020612 01 (It contains krill chitosan, *DD*=75%)	*R=0.9956* *A=0.00177* *B=0.00123*	6.2	1.20×10^{-3}
VR 0304 02 01 (It contains crab chitosan; Sigma, *DD*=80%)	*R=0.98647* *A=-0.00492* *B=0.00071*	3.1	0.70×10^{-3}
VR 030327 06 (It contains shrimp chitosan; Primex TM 1238, *DD*=92%)	*R=0.98951* *A=-0.00104* *B=0.00049*	2.5	0.49×10^{-3}

The samples labelled as VR 03 04 02 01 and VR 03 03 27 06 exhibit lower yields of enzymatic degradation among the investigated samples. After 50 days of incubation, they were degraded between 2.5% and 3.1% with respect to their initial mass.

Since the enzymatic degradation patterns exhibit quite a linear dependence in time, the degradation rates can be determined from the slope of the linear plot. They show values ranging from 0.49 x 10^{-3} to 1.20 x 10^{-3} % loss of mass a day. The results are comprised in *Table 5.10.4-1*. The composite samples that contain cations, such as Cu^{2+}, $Mn^{2+}$and Zn^{2+} ranging from 30 to 150 μg/g composite, exhibit lower values of enzymatic degradation yield compared to the composite sample, which does not contain cations, labeled as VR 020612 01.

Consequently, the degradation curves of composite samples containing cations are lying below to the composite sample that contains no cations, as seen in *Figure 5.10.4-2*. It is difficult to draw some conclusions about the inhibition of the enzymatic activity of lysozyme due to the presence of cations. However, their presence could influence the binding sites of enzyme either by a competitive complexation with enzyme or by influencing the chitosan binding capacity to the hydrolytic sub-sites of enzyme. Both possibilities might occur.

5.10.4.2 pH during the degradation period

The scope of controlling the pH during the degradation period is argued from the necessity to know whether the pH as environmental parameter is maintained between certain limits. The pH values were found between 6.8 and 7.4 during the period of degradation. This probes the pH stability in the systems during the enzymatic degradation period.

5.10.4.3 Identification of chitosan oligomers

In order to analyze the supernatants of composite samples after 50 days of enzymatic degradation, *MALDI-TOF* mass spectroscopy measurements were performed. The obtained results revel the following structural features.

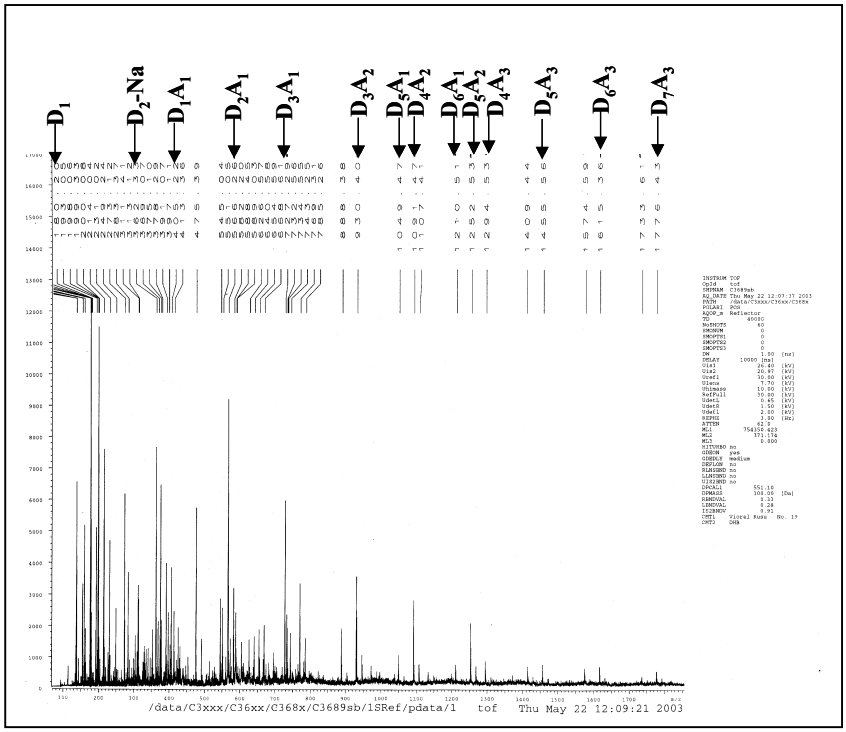

Figure 5.4.10-3 MALDI-TOF spectra of a composite sample (50:50wt%) prepared from insect chitosan (M. Struszczyk, Aug 2000).

♦ As shown in *Figures 5.10.4-3 - 5.10.4-6*, the patterns of mass spectra are displayed as a function of the chitosan type from which the composite samples are prepared.

The chitosan oligomers identified are labelled in the upper part of each mass spectra pattern. The labelling procedure implies the following considerations. The symbol *"D"* refers to the deacetylated residues as *GlcN* whereas *"A"* refers to the acetylated residues, *GlcNAc* that compose the structure of chitosan oligomers. The accompanying indices gives the number of residues. The maximum degree of polymerisation, *DP*, which could be identified for the chitosan oligomer samples, is 10 (D_7A_3), as seen in *Figure 5.4.10-3.*

♦ The small chitosan oligomers, such as those corresponding to $DP_1 \div DP_7$, in all samples were identified. The mass spectra exhibit very complex mass line patterns. They have many *m/z* cluster lines due to the complex ionic environment of *SBF*, from which the oligomers were analysed.

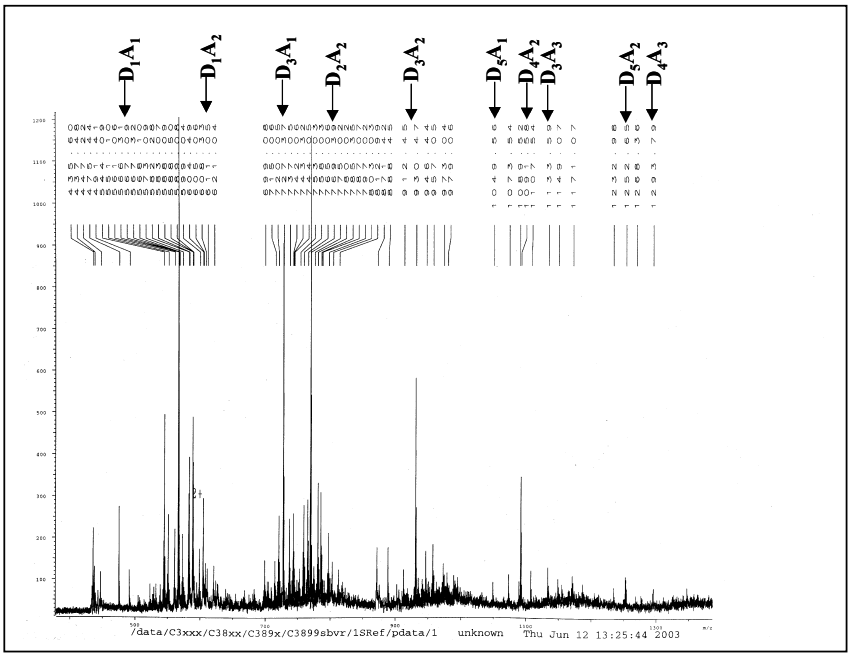

Figure 5.4.10-4 MALDI-TOF spectra of a composite sample (50:50wt%) prepared from Atlantic shrimp chitosan, (TM-1238, Primex).

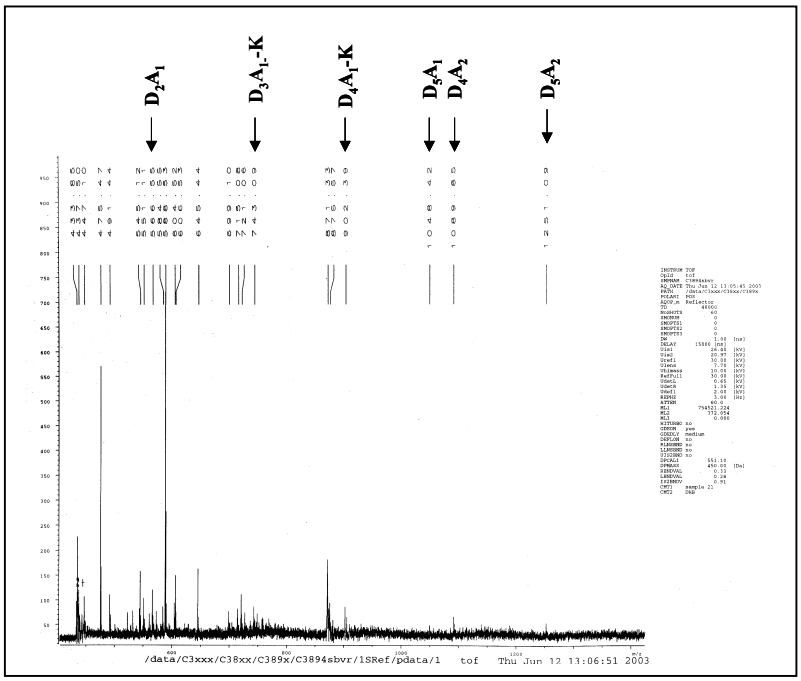

Figure 5.4.10-5 MALDI-TOF spectra of a composite sample (50:50wt%) prepared from crab chitosan (Lot no.91K1265, Sigma).

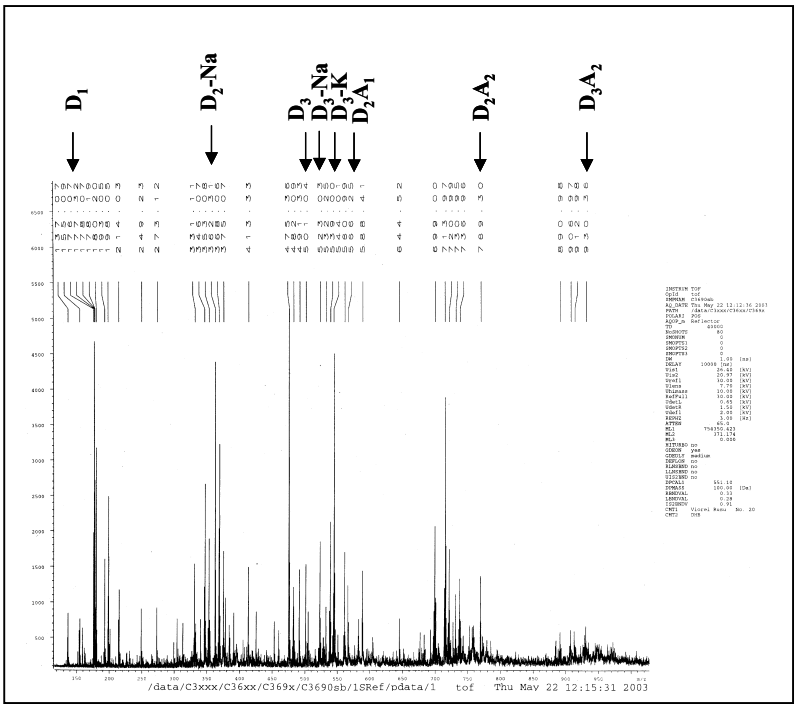

Figure 5.4.10-6 MALDI-TOF spectra of a composite sample (50:50wt%) prepared from krill chitosan; two times deacetylated (2K2X).

5.10.4.4 Analyses of surface morphology of composites

The goal of these experiments was to analyze the changes of the surface morphology of composites as a result of the enzymatic degradation process. The surface morphology,

before and after enzymatic degradation, was examined by *SEM.* Since the enzyme action was mainly concentrated at the sample surface, surface erosion can be observed, as seen in *Figure 5.10.4-7.* In some cases, after the enzymatic degradation, in the degraded surface regions a fiber-like network and some crystallites attached to these fibers were observed, as seen in *Figure 5.10.4-7 (D).*

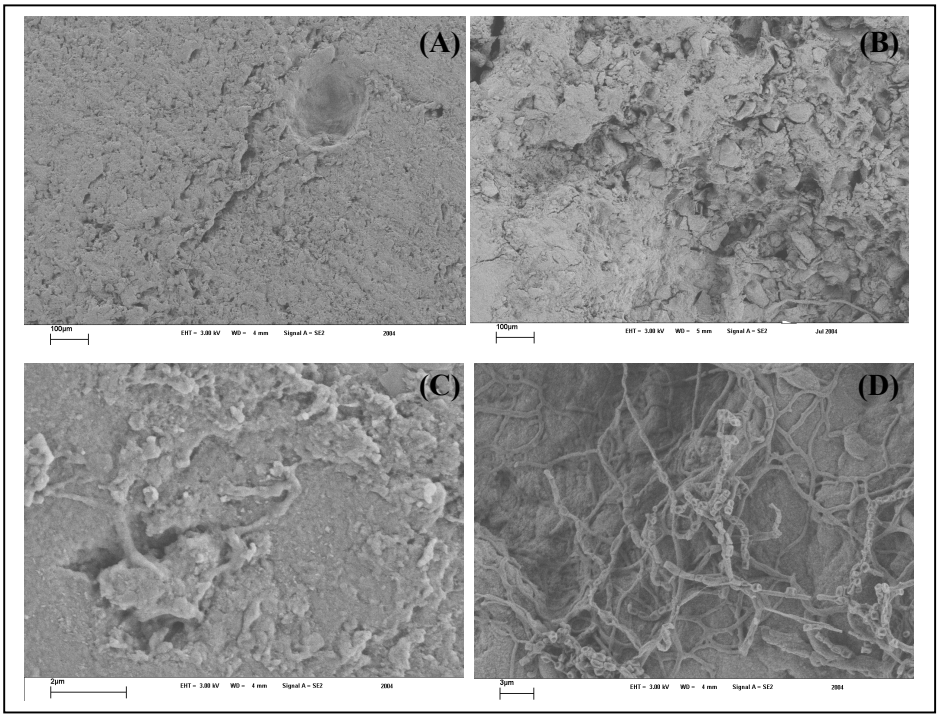

Figure 5.10.4-7 SEM micrographs of a composite sample (VR 030327 06, prepared from Atlantic shrimp chitosan, TM-1238, Primex, Iceland) before (A) and (C) and after the enzymatic degradation (B) and (D).

5.10.5 Conclusions

The degradation curve profiles show a linear dependence of *YD* as a function of degradation period (50 days). The highest degradation rate and hence the highest *YD,* were observed for the sample VR 030402 02 made of insect chitosan *(DD* 67%). The curves of enzymatic degradations lie with respect to the *DD* of chitosan used in the preparation of the composite samples. During enzymatic degradation, the pH slightly varied in the range of neutral values (6.8-7.4). The chitosan oligomers were identified by *MALDI-TOF* mass spectroscopy. They are in the small range, as characterized by their *DP,* which does not exceed 10. *SEM* measurements probed the erosion phenomena of composite surfaces as a result of enzymatic degradation.

6 Summary and Outlook

Summary

There has been an increased interest in developing new strategies of obtaining composite materials with desired properties for biomedical applications. The use of biomaterials as drug delivery systems or as synthetic implants (for example bone replace materials) in medical applications justifies the interest of developing and expanding the field of biomaterials.

The main goals of the project were to develop a co-precipitation approach in order to obtain composite materials containing chitosan and nanosize hydroxyapatite as well as to characterize them using various analytical techniques. The composite materials were characterized with respect to their macro and micro-morphologies, structures, zeta-size properties, enzymatic degradation and mechanical properties.

For the purposes of this project, chitosan was used as a natural polymer matrix for several reasons, such as natural origin; it is biocompatible, biodegradable and bioactive. Additionally, chitosan is obtained from chitin, which is an abundant natural biopolymer. Chitosan in aqueous solutions is the only one natural polycation which exhibits gel-forming properties. These features make it a suitable candidate for the fabrication of new generation of biomaterials.

Taking into account the literature statement of art, we have developed a new stepwise co-precipitation method. In the approaches described in literature hydroxyapatite in aqueous solutions are mainly prepared through the reaction between $Ca(OH)_2$ and H_3PO_4. In contrast to these, our preparations have been performed using salts such as NaH_2PO_4 and $CaCl_2$, as hydroxyapatite precursors in the presence of chitosan solutions. Briefly, at a diluted aqueous acidic solution of chitosan, the apatite precursors as soluble salts, were added. By raising the pH in a stepwise fashion adding a diluted alkaline solution, the co-precipitation of chitosan and calcium phosphates phases was achieved. Then, the pH was adjusted to the alkaline range of 10-12 allowing the formation of hydroxyapatite in the aqueous media. This process takes place in time for about 24 h. In this approach, the pH of the system varied from 3 to 12. The low acidic and high alkaline pH values were avoided. The co-precipitation experiments were performed at room temperature (20-25^{o}C). This approach allowed the modification of chitosan matrix with cations such as Cu II, Zn II and Mn II, which led to complex

combinations. Consequently, composites containing chitosan derivatives and nanosize hydroxyapatite were prepared.

In earlier stage of its formation, the composite occurs as hydrogel, due to the presence chitosan. The composite hydrogel reveals a high porous structure probed by structural investigations using *SEM*. The pore size ranged from few nanometers up to 500-600 nm. Due to their porous structure, they exhibit a high capacity to retain water. The composite hydrogels absorb 90-98 wt% water. The release of water from the composite hydrogels can be achieved using either freeze-drying or air-drying techniques. Drying takes time (it is time consuming process). Air-drying can be performed at either room temperature or at elevated temperatures (up to 90^{o}C). By using freeze-drying, powdered composites are obtained while in the case of air-drying method solid, ceramic-like materials are obtained. The water-releasing rate is a function of hydrogel composition indicating that the more the chitosan in the composite the slower the water release rate. According to their swelling behavior in water, the solid composites lead to different results. The powdered composites (obtained by freeze-drying technique) show reversibility which means that by swelling in water they can be brought to the initial soft hydrogel form whereas the air-dried composites show no reversibility. The initial form of soft composite hydrogel cannot be reached. This observation suggests that during water release the composite hydrogel structure modifies involving physical crosslinking of polymer chains by hydrogen bonds, via irreversible processes. By using Li-Tanaka's gel model, the water co-operative swelling diffusion coefficients were determined. The results show that the swelling properties are a function of composite composition. The more the chitosan in composite the greater the values of swelling diffusion coefficients. The co-operative swelling diffusion coefficients are in the range of 2.6 - 8.3 x 10^{-6} cm^2/s, which are within literature data reported for polyacrylamide hydrogels (between 4.4 and 11.4 x 10^{-6} cm^2/s).

The composite samples were investigated with respect to their structure and properties. The micro-gel domains that join into macro-gel domains (as large gel aggregates) were probed by size measurements. The composite hydrogels are soft and hence they can easily deform under a low load. Since the micro-domains of composite hydrogel are formed by charged colloids, the ionic environments affect their properties. Zeta potential measurements show that the composite hydrogels exhibit the isoelectric point values ranging from 5.5 to 7.5, as a function

of composite composition. Thus, the more the chitosan in composite hydrogel the higher the shift of the isoelectric point towards neutral pH. The isoelectric point of hydroxyapatite was about 5.7, which is comparable to the values reported in the literature (5.5).

In order to study the composite structure regarding the inorganic phases, techniques such as *XRD*, *TEM, SEM, EDS* and *CSLM* were employed. By *XRD* experiments was demonstrated that the hydroxyapatite formation in the chitosan matrix starts from brushite in alkaline media. Based on Scherrer's equation, the average crystallite size of the hydroxyapatite was calculated. Its kinetics of formation inside the chitosan matrix by *XRD* measurements was established. The *XRD* and *TEM* measurements allowed the evaluation of crystallite sizes, which ranged from 10 to 45 nm. A bimodal distribution of nanosized hydroxyapatite in composites with respect to its length was identified. The *TEM* and *CSLM* measurements confirmed the cluster-like domain organization, with the size domain between 200 and 500 nm.

In composite hydrogel, water can occupy different molecular sites such as free and bound sites. The water states in the composite hydrogels were probed by ^{2}H-*NMR* relaxation measurements. The amount of bound water in the composite hydrogel ranged between 10 and 15 mg/g of dry composite. These results cross the literature values obtained in the case of starch and cellulose, naturally related polysaccharides. In the later cases, the bound water was evaluated to be between 15 and 30 mg/g of dry material.

The composition of composites was determined by evaluating the characteristic spectral peak, using *EDS*, *IR* and Raman spectroscopic techniques. Thus, the presence of chitosan and hydroxyapatite were revealed. The structural changes during drying were evidenced by Raman spectroscopy. Two types of composites obtained by freeze drying and air-drying were compared to each other. The amide *I* and *III* bands domains were assigned according to literature data and it was proved the modification of structural conformation of chitosan in the composite samples due to drying. The increase of the ″amount″ of parallel orientation domains in the composite hydrogel lead to enough physical crosslinking density, which offers stability of composite hydrogel network upon water swelling. Since the complete water re-swelling of air-dried composites does not reach the initial soft hydrogel form, some irreversible structural phenomena were assumed to be responsible.

6 Summary and Outlook

Further features of composite materials which need to be overcome, are their mechanical properties. By using mechanical measurements performed in three point bending and in compressive tests, the mechanical properties of various types of composites were evaluated. The compressive measurements in the case of both dry and wet states were performed. The yield stress (in flexural mode) ranges from 6 to about 42 MPa. The bending Young's modulus shows values between 0.84 and 3.4 GPa. In compact bone this parameter ranges from 7 to ca. 20 MPa. The compressive modulus varies between 127 and 1.8 GPa for dry specimens while for wet specimens this parameter ranges from 7 to 30 MPa. In a wet state, the mechanical properties are one order of magnitude lower than those evaluated in a dry state.

A prerequisite of understanding the behavior of composites as synthetic implants is to achieve information about their *in vitro* enzymatic degradation behavior. An enzymatic method using lysozyme was designed to evaluate the enzymatic degradation rates of composite samples. The degradation curves are lying with respect to the chitosan type contained by the composite samples. The maximum degradation yield led to 9% loss of mass after 50 days of lysozme treatment. Then, the chitosan oligomers were identified by *MALDI-TOF* mass spectroscopy. The surface topography of composites was examined before and after the enzymatic degradation. The erosion of the composite surface takes place as a result of enzymatic degradation.

Since the composite materials were found biocompatible by the *in vivo* tests, the simple mode of their fabrication and their properties recommend them as potential candidates for the non-load bearing bone substitute materials.

Outlook

In order to improve the mechanical properties of composites in the wet state, either crosslinking or reinforcing processes might be employed.
The enzymatic degradation rates must also be given by the *in vivo* experiments.

References

1 E. Dujardin, S. Mann. Bio-Inspired Materials Chemistry *Adv. Mater.* **2002**, *14*, 775-88

2 B. L. Zhou. Bio-inspired study of structural materials *Mater. Sci. Eng., C* **2000**, *11*, 13–18

3 L. L. Hench. Biomaterials: a forecast for the future *Biomaterials* **1998**, *19*, 1419–23

4 H. Shin, S. Jo, A. G. Mikos. Biomimetic materials for tissue engineering *Biomaterials* **2003,** *24,* 4356-64

5 Z. Ahmad, J. E. Mark. Biomimetic materials: recent developments in organic-inorganic hybrids *Mater. Sci. Eng., C* **1998**, *6*, 183-96

6 J. J. Grodzinski. Biomedical applications of functional polymers *React. Function. Polym.* **1999**, *39*, 99-138

7 K. J. L. Burg, S. Porter, J. F. Kellam. Biomaterial developments for bone tissue engineering *Biomaterials* **2000**, *21*, 2347-59

8 D.W. Hutmacher. Scaffolds in tissue engineering bone and cartilage *Biomaterials* **2000**, *21*, 2529-43

9 A. M. A. Ambrosio, J. S. Sabota, Y. Khan, C.T. Laurencin. A novel amorphous calcium phosphate polymer ceramic for bone repair: I. Synthesis and characterization *J. Biomed. Mater. Res. (Appl. Biomater.)* **2001**, *58*, 295-301

10 I. Manjubala, M. Sivakumar, V. Sureshkumar, T. P. Sastry. Bioactivity and osseointegration study of calcium phosphate ceramic of different chemical composition *J. Biomed. Mater. Res. (Appl Biomater)*, **2002**, *63*, 200-08

11 R. H. Chen, M. L. Tsaih. Effect of temperature on the intrinsic viscosity and conformation of chitosan in dilute HCl solution *Int. J. Biol. Macromol*. **1998**, *23*, 135-41

12 M. Beppu, C.C. Santana. In vitro Biomineralization of Chitosan *Key Eng. Mater*. **2001**, *192-195*, 31-4

13 I. Yamaguchi, K.Tokuchi, H. Fukuzaky, Y. Koyama, K. Takakuda, H. Momna, J. Tanaka. Preparation and Mechanical Properties of Chitosan/Hydroxyapatite Nanocomposites *Key Eng. Mater*. **2001**, *192-195*, 673-76

14 K. Schwarz, M. Epple. Biomimetic Crystallisation of Apatite in a Porous Polymer Matrix *Chem. Eur. J.* **1998**, *4,* 1898-903

15 D. Tian, P. H. Dubois, R. Jerome. Biodegradable and Biocompatible Inorganic-Organic Hybrid Materials I. Synthesis and characterisation *J. Polym. Sci.* **1997**, *A35,* 2295-309

16 Mineral Tolerance of Domestic Animals, Board on Agriculture and Renewable Resources, National Academy of Science, Washington D.C., **1980**

17 Dietary Reference Intakes for vitamin A, K, Arsenic, Boron, Chromium, Copper, Iodine, Iron, Manganese, Molybdenum, Nickel, Silicon, Vanadium and Zinc, Food and Nutrition Board, Institute of Medicine, National Academy Press, Washington D.C., **2001**

18 P. D Saltman, L.G Strause. The role of trace minerals in osteoporosis *J. Am. Coll. Nutr.* **1993**, *12*, 384-89

19 L. Srause, P. Saltman. Spinalbone loss in postmenopausal women supplemented with calcium and trace minerals *J. Nutr*. **1994**, *124*, 1060-64

20 E. J. Vandamme, S. de Baets, A. Steinb, Biopolymers, Wiley, **2002,** 23-38

21 C. D. Nenitescu. Organic Chemistry, Ed. Didactica si Pedagogica, Bucharest, (in Romanian) **1980**, 870-911

22 G. A. F. Roberts. Chitin Chemistry, Houndmills, MacMillan Press Ltd., **1992,** 102-15

23 R. A. A. Muzzarelli, Chitin, Pegamon Press, Oxford, **1977,** 12-67

24 C. J. Brine, P. A. Sandford, J. P. Zikakis. Advances in Chitin and Chitosan, Elsevier Applied Science, **1989,** 13-98

25 K. Kurita, S. Ishii, K. Tomita, S. I. Nishimura, K. Shimoda. Reactivity Characteristics of Squid β-Chitin as Compared with those of Shrimp Chitin : High Potentials of Squid Chitin as a Starting Material for Facile Chemical Modifications *J. Polym. Sci., A Polym. Chem.* **1994**, *32,* 1027-32

26 H. Cölfen, G. Berth, H. Dautzenberg. Hydrodynamic Studies on Chitosans in Aqueous Solution *Carbohydr. Polym*. **2001**, *45*, 373-83

27 K. Mazeau, S. Perez, M. Rinaudo. Predicted influence of N-acetyl group content on the conformational extension of chitin and chitosan chains *J. Carbohydr. Chem*. **2000**, *19,* 1269-84

28 K. Okuyama, K. Noguchi, M. Kanenari, T. Egawa, K. Osawa, K. Ogawa. Structural diversity of chitosan and its complexes *Carbohydr. Polym.* **2000**, *41*, 237-47

29 A. Percot, C. Viton, A. Domard. Optimization of Chitin Extraction from Shrimp Shells *Biomacromolecules* **2003**, *4*, 12-8

30 K. Kurita, K. Tomita, T. Tada, S. Ishii, S.I. Nishimura, K. Shimoda. Squid Chitin as a Potential Alternative Chitin Source: Deacetylation Behaviour and Characteristic Properties *J. Polym. Sci., A Polym. Chem.* **1993**, *31,* 485-91

References

31 K. Kurita, K. Tomita, T. Tada, S. I. Nishimura, S. Ishii. Reactivity characteristics of a new form of chitosan *Polym. Bull.* **1993**, *30*, 429-33

32 B. Nystroem, A. Kjoniksen, C. Iversen. Characterization of association phenomena in aqueos systems of chitosan of different hydrophobicity *Adv. Colloid Interface Sci*. **1999**, *79*, 81-103

33 G. Lang, G. Maresch, S. Birkel. Hydroxyalkyl chitosans in: R.A.A. Muzzarelli, M.G. Peter (Eds.), *Chitin Handbook*, Atec, **1997**, 61-6

34 G. Lang, H. Wendel, S. Birkel. Quaternary chitosan salts in: R.A.A. Muzzarelli, M.G. Peter (Eds.), *Chitin Handbook*, Atec, **1997**, 67-70

35 S. Hirano. N-Acyl-, N-arylidene- and N-alkylidene chitosans, and their hydrogels in: R.A.A. Muzzarelli, M. G. Peter (Eds.), *Chitin Handbook*, Atec, **1997**, 71-6

36 P. R. Rege, L. H. Block. Chitosan processing: influence of process parameters during acidic and alkaline hydrolysis and effect of the processing sequence on the resultant chitosan's properties *Carbohydr. Res.* **1999**, *321*, 235–45

37 G. M. Hall, C. L. Reid, Z. Zakaria. Fermentation of prawn waste by lactic acid bacteria in Chitin Word, edited by Z. S. Karnicki, A.W. Pajak, M. M. Brzeski and P. J. Bykowski, Wirtschaftsverlag NW, Verlag für neue Wissenschaft GmbH, **1994,** 30-7

38 K. Kurita, Y. Kaji and Y. Nishiyama. Enzymatic degradation of β-Chitin: Susceptibility and the Influence of Deacetylation *Carbohydr. Polym*. **2000**, *42,* 19-21

39 A. Tolaimate, J. Desbrières, M. Rhazi, A. Alagui, M. Vincendon, P. Vottero. On the Influence of Deacetylation Process on the Physicochemical Characteristics of Chitosan from Squid Chitin *Polymer* **2000**, *41*, 2463-69

40 K. Kurita. Chemistry and application of chitin and chitosan *Polym. Degrad. Stab.* **1998**, *59*, 117-20

41 G. Berth, H. Dautzenberg, M. G. Peter. Physico-chemical Characterization of Chitosans Varying in Degree of Acetylation *Carbohydr. Polym*. **1998**, *36*, 205-16.

42 M. L. Tsaih, R.H. Chen. Molecular weight determination of 83% degree of deacetylation chitosan with non-gausian and wide range distribution by high performance size exclusion chromatography and capillary viscometry *J. Appl. Polym. Sci*. **1999**, *71*, 1905-13

43 R. A. A. Muzzarelli, R. Rocchetti, V. Stanic, M. Weckx. Methods for the determination of the degree of acetylation of chitin and chitosan in: R. A. A. Muzzarelli, M.G. Peter (Eds.), *Chitin Handbook*, Atec, **1997**, 109-20

44 K. Vårum; M. W. Anthonsen, H. Grasdalen, O. Smidsrød. Determination of the Degree of N-Acetyl Groups in Partially N-Deacetylated Chitins (Chitosans) by High-Field NMR Spectroscopy *Carbohydr. Res*. **1991**, *211*, 17-23

45 Y. Inoue. NMR Determination of the degree of acetylation in: R. A. A. Muzzarelli, M. G. Peter (Eds.), *Chitin Handbook*, Atec, **1997**, 133-36

46 J. Brugnerotto, J. Lizardi, F. M. Goycoolea, W. Argüelles-Monal, J. Desbrieres, M. Rinaudo. An infrared investigation in relation with chitin and chitosan characterization *Polymer* **2001**, *42,* 3569-80

47 F. W. Billmeyer. Textbook of polymer science, 3rd ed. John Wiley&Sons, New York, **1984**, 12-98

48 M. G. Peter. Applications and environmental aspects of chitin and chitosan *J. Macromol. Sci., Pure Appl. Chem.***1995**, A-32, 629-40

49 G. McKay, H.S. Blair, J. R. Gardner. Adsorption of dyes on chitin I. Equilibrium studies *J. Appl. Polym. Sci.* **1989**, *27*, 30-43

50 M. R. Kumar. Chitin and Chitosan fibres *Bull. Mater. Sci*. **1999**, *22*, 905-09

51 R. A. A. Muzzarelli, C. Muzzarelli, M.Terbojevich. Chitin Chemistry upgrading a renewable resource *Carbohydr. Eur.* **1997**, 19-21

52 R. A. A. Muzzarelli, M. Mattioli-Belmonte, A. Pugnaloni, G. Bigini, Biochemistry, histology and clinical uses of chitins in wound healing, Birkhauser, Basel, **1999,** 43-98

53 I. Knorr. Recovery and utilization of chitin and chitosan in food processing waste management *Food Technol. Jap*. **1991**, 114-16

54 R. L. Reis, A. M. Cunha. Characterisation of two biodegradable polymers of potential applications within the biomaterial field *J. Mater. Sci.: Mater. Med.* **1995**, *6*, 786-88

55 K. E. Uhrich, S. N. Canizzaro, R. S. Langer. Polymeric systems for controlled drug release *Chem. Rev*. **1999***, 99*, 3181-89

56 S. Miyazaki, K. Ishii, T. Nadai. The use of chitin and chitosan as drug carriers *Chem. Pharm. Bull*. **1981**, *29*, 3067-69

57 K. D. Yao, Y. J. Yin, M. X. Xu, F. Wang. Investigations of pH sensitive drug delivery system of chitosan/gelatin hybrid polymer network *Polym. Int*. **1995**, *38*, 77-80

References

58 R. A. A. Muzzarelli, M. Mattioli-Belmonte, R. Bigini, G. Ferioli, N. A. Brunelli, M. Fini, R. Giardino, P. Ilari, G. Bigini. Stimulatory effect on bone formation exerded by a modified chitosan *Biomaterials* **1994**, *15,* 1075-81

59 R. A. A. Muzzarelli, V. Ramos, V. Stanic, B. Dubini, M. Mattioli-Belmonte, G. Tosi, R Giardino. Osteogenesis promoted by calcium phosphate-N, N-dicarboxymethylchitosan *Carbohydr. Polym*. **1998**, *36*, 267-76

60 M. Mattioli-Belmonte, N.Vicoli-Aldini, A. De Benedittis, G. Sgarbi, S. Amati, M. Fini, G. Bigini R. A. A Muzzarelli. Morphological study of bone regeneration in the presence of 6-oxychitin *Carbohydr. Polym*. **1999**, *40*, 23-27

61 P. R. Klokkevold, L.Vandemark, E. B. Kenney, G.W. Bernard. Osteogenesis enhanced by chitosan in vitro *J. Periodontol.* **1996**, *67*, 1170-75

62 S. V. Dorozhkin, M. Epple. Biological and Medical Significance of Calcium Phosphates *Angew. Chem. Int. Ed.* **2002**, *41*, 3130-46

63 S. Mann. Biomineralization, Oxford University Press, Oxford, **2001**, 11-156

64 E. C. Victoria, F. D. Gnanam. Synthesis and Characterization of biphasic calcium phosphate *Trends Biomater. Artif. Organs*. **2002**, *16,* 12-14

65 K. de Groot . Bioceramics of calcium phosphate, CRC Press, Boca Raton, FL, **1983**, 87-134

66 F. C. M. Driessens, R. M. H. Verbeeck. Biominerals, CRC Press, Boca Raton, FL, **1990**, 45-165

67 L. C. Chow and S. Tagagi. A natural Bone Cement-A Laboratory Novelty Led to the Development of Revolutionary New Biomaterials *J. Nat. Inst. Stand. Technol*. **2001**, *106,* 1029-33

68 E. Fernandez, F. J. Gill, M. P. Ginebra, F. C. M. Driessens, J. A. Planell, S. M. Best. Calcium phosphate bone cements for clinical applications *J. Mater. Sci. Mater. Med*. **1999***, 10*, 169-76

69 S. Koutsopoulos. Synthesis and characterization of hydroxyapatite crystals: A review study on the analytical methods *J. Biomed. Mater. Res*. **2002**, *62*, 600-12

70 O. E. Petrov, E. Dyulgerova, L. Petrov, R. Popova. Charactrization of calcium phospate phases obtained during the preparation of sintered Ca-P ceramics *Mater. Lett.* **2001**, *48*, 162-67

71 R. S. Lakes. Materials with structural hierarchy *Nature* **1993**, *361*, 511-15

72 S. L. Gunderson and R. S. Schiavone. International Encyclopaedia of Composites*,* edited by S. M. Lee, VCH Publisher, Inc., New York, Vol. 5, **1991**, 12-234

73 J. L. Russell, J. E. Block. Clinical utility of demineralised bone matrix for osseous defects, arthrodesis, and reconstruction: impact of processing techniques and study methodology *Orthopedics* **1999**, *22*, 524-33

74 W. J. Landis, J. J. Librizzi, M. G. Dunn, F. H. Silver. A study of the relationship between mineral content and mechanical properties of turkey tendon *J. Bone Miner. Res*. **1995**, *10*, 859-63

75 J. D. Currey. Handbook of Composites, edited by A. Kelley and S. T. MileiKo, Elsevier Science Publishers, Vol. 4, **1983**, 18-123

76 Y. C. Fung. Biomechanics, Mechanical Properties of living tissue, Springer Verlag Inc., New York, **1993**, 23-189

77 J. B. Park. Biomaterials Science and Engineering, Plenum Press, New York, **1987**, 14-89

78 K. A. Athanasiou, C. F. Zhu, D. R. Lanctot, C.M. Agrawal, X. Wang. Fundamentals of biomechanics in tissue engineering of bone *Tissue Eng.* **2000***, 6*, 361-81

79 S. Weiner and H. D. Wagner. The material bone: Structure-Mechanical Function Relations *Annu. Rev. Mat. Sci.* **1998**, *28*, 271-98

80 M. J. Yaszemski R. G. Payne, W. C Hayes, R. Langer, A. G. Mikos. Evolution of bone transplantation: molecular, cellular, and tissue strategies to engineer human bone *Biomaterials* **1996**, *17*, 175-85

81 T. W. Bauer and G. F. Muschler. Bone graft materials *Clin. Ortop*. **2000**, *371*, 10-27

82 S. D. Boden. Bioactive factors for bone tissue engineering *Clin. Orthop*. **1999**, *367*, 84-94

83 T. P. Gross, R. H. Jinnhah, H. J. Clarke, Q. G. Cox. The biology of bone grafting *Orthopedics* **1991**, *14*, 563-68

84 P. Aspenberg, J. Astrand. Bone allografts pretreated with a bisphosphonate are not resorbed *Acta Orthop. Scand.* **2002,** *73,* 20-3

85 J. E. Block, J. Poser. Does Xenogenic demineralised bone matrix have clinical utility as a bone graft substitute? *Medical Hypotheses* **1995***, 45*, 27-32

86 G. A. Helm, H. Dayoub, J. A. Jane. Bone graft substitutes for promotion of spinal arthrodesis *Neurosurg. Focus* **2001**, *10*, 1-5

87 Trends & Dynamics in Global Orthopedics: US and European Spinal Implants *Datamonitor*-London in Reports

88 United States- Bone Graft Substitutes, *Datamonitor*-London in Reports

References

89 A. S. Greenwald , T. W. Bauer, M. D. Ries. New Polys for Old: Contribution or Caveat? *J. Bone Joint Surg.* Am. 83 (Suppl. 2, Part 1) **2001***,* 27-31.

90 W. Suchanek, M. Yoshimura. Hydroxyapatite based biomaterials for use as hard tissue replacement *J. Mater. Res*. **1998**, *13*, 94-117

91 S. Kannan, A. Balamurugan, S. Rajeswari. Bio-Composites: A review of Literature *Trends Biomater. Artif. Organs* **2001**, *14,* 30-6

92 M. Wang. Developing bioactive composite materials for tissue replacement *Biomaterials* **2003**, *24*, 2133–51

93 M. M. Schwartz. Composite materials handbook 2nd ed. New York: McGraw-Hill, **1992**, 12-134

94 V. I. Sevastianov. Biocompatible materials: Current Status and Future Perspectives *Trends Biomater. Artif. Organs* **2002**, *15,* 20-30

95 S. Kannan, A Balamurugan, S. Rajeswari. Bio-composites: A review of literature *Trend. Biomater. Artif. Organs* **2001**, *14,* 30-36

96 J. C. Knowles, S. Talal, J. D. Santos. Sintering effects in a glass reinforced hydroxyapatite *Biomaterials* **1996**, *17*, 1427-32

97 Y. Okada, M. Kobayashi, M. Neo, T. Kokubo, T. Nakamura. Ultrastructure of the interface between bioactive composite and bone: Comparison of apatite and wollastonite containing glass-ceramic filler with hydroxyapatite and **β**-tricalcium phosphate fillers *J. Biomed. Mater. Res*. **2001**, *57,* 101-07

98 W. Q. Yan, T. Nakamura, K. Kawanabe, S. Nishigochi, M. Oka, T. Kokubo. Apatite Layer-Coated Titanium for Use as Bone Bonding Implants *Biomaterials* **1997**, *18*, 1185-90

99 B. E. Tucker, C. M. Cottell, R.C.Y.Auyeung, M. Spector , G.H. Nancollas. Pre-conditioning and dual constant composition dissolution kinetics of pulsed laser deposed hydroxyapatite thin films on silicon substrates *Biomaterials* **1996**, *17*, 631-37

100 C. Doyle. Bioactive composites in Orthopedics, in Handbook of bioactive ceramics, editors. T. Yamamuro, L. L. Hench, J. Wilson, CRC Press, Inc., **1990**, 162-87

101 C. Klein, A. A. Driesen, K. de Groot, van den Hooff. Biodegradation behavior of various calcium phospates materials in bone tissues *J. Biomed. Mater. Res*. **1983**, 17, 769-74

102 W. Bonfield, M. D. Grynpas, A. E. Tully, J. Bowman, J. Abram. Hydroxyapatite reinforced polyethylene—a mechanically compatible implant material for bone replacement *Biomaterials* **1981**, *2*, 185–86.

103 M. Wang, R. Joseph, W. Bonfield. Hydroxyapatite- polyethylene composites for bone substitution *Biomaterials* **1998**, *19*, 2357-66

104 C. P. M. Verheyen, J. R. de Wijn, C. A. van Blitterswijik, K de Groot. Evaluation of hydroxylapatite/poly-(L-lactide) composites: Mechanical behavoiour *J. Biomed. Mater. Res*. **1992**, *26*, 1277-82

105 L. Rodriguez- Lorentzo, A. Salinas, M. Vallet-Regi, J. San-Roman. Composite biomaterials based on ceramic polymers. I. Reinforced systems based on Al_2O_3/PMMA/PLLA *J. Biomed. Mater. Res.***1996**, *30*, 515-22

106 N. Ignjetovic, S. Tomic, M. Dakic, M. Miljkovic, M. Dlevsic, M. Uskokovic. Synteses and properties of hydroxyapatite/Poly L-lactide composite biomaterials *Biomaterials* **1999**, *20*, 809-16

107 A. A. Ignatius L. E. Claes. In vivo biocompatibility of of bioresorbable poly (L, L,D-Lactide) and poly (L-Lactide –co-glycolide) *Biomaterals* **1996**, *17*, 831-35

108 K. Schwarz*,* M. Epple. Hierarchically structural polyglycolide- a biomaterial mimicking natural bone *Macromol. Rapid Commun.* **1998***, 19*, *613–17*

109 M. Wang, C.Y. Yue, B. Chua L. C. Kan. Hydroxyapatite reinforced polysulfone as a new biomaterial for tissue replacement *Bioceramics* **1999**, *12*, 401–04

110 M. Wang, C.Y. Yue, B. Chua. Production and evaluation of hydroxyapatite reinforced polysulfone for tissue replacement *J. Mater. Sci. Mater. Med*. **2001**, *12*, 821–26.

111 H. Ohmae, J. Takahashi, H. Himura, M. Sakuda. Insolubilized properties of UV-irradiated $C0_3$ apatite-collagen composites *Biomaterials* **1990**, *11*, 568-72

112 S. Itoh, M. Kikuchi, K. Takakuda, Y. Koyama, H. N. Matsumoto, S. Ichinose, J. Tanaka, T. Kawauchi, K. Shinomiya. The biocompatibility and osteoconductive activity of a novel hydroxyapatite/collagen composite biomaterial, and its function as a carrier of rhBMP-2 *J. Biomed. Mater. Res.* **2001** *5,* 445-53

113 Y. Doi, Horiguchi, Y. Moriwaki, H. Kitago, T. Kajimoto, Y. Iwayama. Formation of apatite-collagen complexes *J. Biomed. Mater. Res*. **1996**, *31,* 43-49

114 C. Du, F. Z. Cui, W. Zhang, Q. L. Feng, X. D. Zhu, K. DeGroot. Formation of calcium phosphate collagen composites through mineralization of collagen matrix *J. Biomed. Mater. Res.* **2000**, *50,* 518-27

115 M. Okazaki, H. Ohmae, J. Takahashi, H. Kimura, M. Sakuda. Insolubilized properties of UV irradiated CO_3 apatite- collagen composites *Biomaterials* **1990**, *11*, 568-73

References

116 M. Kikuchi, S. Itoh, S. Ichinose, K. Shinomiya, J. Tanaka. Self organization mechanism in a bone like hydroxyapatite/collagen nanocomposite syntesized in vitro and its biological reaction in vivo *Biomaterials* **2001**, *22*, 1705-11

117 M. B. Yaylaoglu, P. Korkusuz, U. Ors, F. Kurkusuz, V. Hasirci. Development of a calcium phospate – gelatin composite as a bone substitute and its use in drug release *Biomaterials* **1999**, *20*, 711–19

118 Z. Gea, S. Baguenard, L. Yong Lima, A. Weec, E. Khorb. Hydroxyapatite–chitin materials as potential tissue engineered bone substitutes *Biomaterials* **2004**, *25*, 1049–58

119 E. Khor, A. C. A. Wan, W. Hastings. Method of preparing filler containing forms of chitin *US Patent 5, 821,285,* **1998**

120 A. C. A. Wan, E. Khor, G.W. Hastings. Hydroxyapatite modified chitin as potential hard tissue substitute material *J. Biomed. Mater. Res., Appl. Biomater.* **1997**, *38*, 235–41

121 Y. Zhang, M. Zhang. Three dimensional macroporous calcium phosphate bioceramics with nested chitosan sponges for load bearing bone implants *J. Biomed. Mater. Res.* **2002**, *61*, 1–8

122 M. Ito, Y. Hidaka. A chitosan –bonded hydroxyapatite bone filing material, in: R. A. A. Muzzarelli, M. G. Peter (Eds.), *Chitin Handbook*, Atec, **1997**, 373–82

123 Y. Zhang, M. Zhang. Synthesis and characterization of macroporous chitosan/calciumphosphate composite scaffolds for tissue engineering *J. Biomed. Mater. Res*. **2001**, *55*, 304–12

124 I. Yamaguchi, K. Tokuchi, H. Fukuzaki, Y. Koyama, K. Takakuda, H. Monma , J. Tanaka. Preparation and microstructure analysis of chitosan/hydroxyapatite nanocomposites *J. Biomed. Mater. Res*. **2001**, *55*, 20–7

125 M. Ito, Y. Hidaka, M. Nakajima, H. Yagasaki, A.H. Kafrawy. Effect of hydroxyapatite content on physical properties and connective tissue reactions to a chitosan–hydroxyapatite composite membrane *J. Biomed. Mater. Res.* **1999***, 45*, 204–08

126 M. C. Sunny, P. Ramesh and H. K. Varma. Microstructured microspheres of hydroxyapatite ceramic *J. Mater. Sci. Mater. Med*. **2002**, *13* 623–32

127 Y. M. Lee, Y. J. Park, S. J. Lee, Y. Ku, S. B. Han, S. M. Choi, P. R. Klokkevold, C. P.Chung. Tissue Engineered Bone Formation Using Chitosan/Tricalcium Phosphates Sponges *J. Periodontol.* **2000**, *71*, 410-17

128 S. Viala, M. Freche, J. L. Lacout. Effect of chitosan on octacalcium phosphate crystal growth *Carbohydr. Polym*. **1996**, *29*, 197-201

129 S. Viala, M. Freche, J. L. Lacout. Preparation of new organic-mineral composite: chitosan-hydroxyapatite *Ann. Chim. Sci. Mat*. **1998**, *23* , 69-72

130 C. Muzarelli and R. A. A. Muzarell. Natural and artificial chitosan- inorganic composites *J. Inorg. Biochem.* **2002**, *92*, 89-94

131 R. G. Bray, J. P. Sibilia. Molecular spectroscopy-Infrared spectroscopy in A guide to Materials Characterization and Chemical Analysis edited by John P. Sibilia, VCH Publishers, Inc., Second Edition, **1996**, 17-26

132 T. A. Khan, K. K. Peh, H. S. Chung. Reporting degree of deacetylation values of chitosan: the influence of analytical methods *J. Pharm. Pharmaceut. Sci*. **2002***, 5,* 205-12

133 J. R. Ferraro. Introductory Raman Spectroscopy, Second Edition, Elsevier, Academic Press, San Diego, **1994**, 15-98

134 R. G. Bray, J. P. Sibilia. Molecular spectroscopy-Raman spectroscopy in A guide to Materials Characterization and Chemical Analysis edited by John P. Sibilia, VCH Publishers, Inc., Second Edition, **1996**, 27-32

135 G. Socrates, Infrared and Raman Characteristic Group Frequencies: Tables and Charts, 3rd Edition, Wiley, **2001,** 12-175

136 M. Handkea, M. Sitarz, M. Rokita, E. Galuskin. Vibrational spectra of phosphate–silicate biomaterials *J. Mol. Struct.* **2003**, *651–653*, 39–54

137 I. Nothinger, A. R. Boccaccini, J. Jones, V. Maquet, L. L. Hench. Application of Raman microspectroscopy to the characterization of bioactive materials *Mater. Characteriz.* **2003**, *49*, 255-60

138 I. R. Lewis, H. G. M. Edwards. Handbook of Raman Spectroscopy, Marcel Dekker Inc. New York, **2001**, 12-67

139 D. B. Murphy. Fundamentals of light microscopy and electron imaging, Wiley-Liss Inc, **2001**, 12-118

140 M. P. C. Vaz, S. P. Herrmann, S. Crestana. Thickness and size distribution of clay-sized soil particles measured through atomic force microscopy *Powder Technol.* **2002**, 126, 51– 8

141 O. Elizalde, G. P. Leal, J. R. Leiza. Particles size distribution measurements of polymeric dispersions: A comparative study *Part. Syst. Charact*. **2000**, *17*, 236-43

References

142 I. Catelas, J. D. Bobyn, J. B. Medley, J. J. Krygier, D. J. Zukor, O. L. Huk. Size, shape, and composition of wear particles from metal–metal hip simulator testing: Effects of alloy and number of loading cycles *J. Biomed. Mater. Res*. **2003**, *67A*, 312–27

143 R. R. Ernst, W. A. Anderson. Application of Fourier Transform Spectroscopy to Magnetic Resonance *Rev. Sci. Instrum.* **1966**, *37*, 93-5

144 R. R. Ernst. Kernresonanz-Fourier-Transformations Spektroscopie *Angew. Chem.* **1992**, *104*, 817-18.

145 Y. H. Carr, E. M. Purcell. Effects of diffusion on free precession in nuclear magnetic resonance experiments *Phys. Rev.* **1954**, *94*, 630-33

146 F. Hanus, P. Gillis. Relaxation of water adsorbed on the surface of silica powder *J. Magn. Reson*. **1984**, *59*, 437-45

147 G. P. van der Beek, M. A. Cohen Stuart, T. Cosgrove. Polymer adsorption and desorption studies via proton NMR relaxation of the solvent *Langmuir* **1991**, *7*, 327-34

148 P. P. Sibil. Physical Chemistry Source Book, McGraw Hill Inc., **1998**,12-124

149 D. F. Evans, H. Wennerstram. The Colloidal Domain, Where Physics, Chemistry Biology and Technology Meet, VCH Publisher Inc., **1994**, 18-87

150 T. M. Riddick. Control of Colloid Stability through Zeta Potential, Published for *Zeta–Meter, Inc*. by Livingston Publishing Company, Wynnewood, Pennsylvania, **1968**, 12-14

151 R. H. Müller. Zetapotential und Partikelladung in der Laborpraxis, Wissenschaftliche Verlagsgesellschaft GmbH, Stuttgart , **1996**, 18-240

152 R. J. Hunter. Zeta potential in colloid science, Academic Press, Oxford, **1988**, 4-46

153 Y. P. Khanna, M. E. McDonnell, P. K. Han. Rheology and Molecular Weight of Polymers in A guide to Materials Characterization and Chemical Analysis edited by John P. Sibilia, VCH Publishers, Inc., Second Edition, **1996**, 287-304

154 V. F. Lee. PhD thesis in University microfilms, **1974**, 74/29446

155 Y. P. Khanna. Thermal Characterization of Materials in A guide to Materials Characterization and Chemical Analysis edited by John P. Sibilia, VCH Publishers, Inc., Second Edition, **1996**, 261-80

156 N. Nanjeeva, F. Reidinger. X-Ray Analysis in A guide to Materials Characterization and Chemical Analysis edited by John P. Sibilia, VCH Publishers, Inc., Second Edition, **1996**, 143-49

157 S. N. Danilchenko, O.G. Kukharenko, C. Moseke, I. Yu. Protsenko, L. F. Sukhodub, B. Sulkio-Cleff. Determination of the Bone Mineral Crystallite Size and Lattice Strain from Diffraction Line Broadening *Cryst. Res. Technol*. **2002**, *37*, 1234-40

158 H. P. Klug, L. E. Alexander. X-ray diffraction procedures for polycrystallite and amorphous materials John Wiley and Sons, Second Edition, New York, **1974,** 17-98

159 C. S. Barrett, J. B. Cohen, J. Jr. Faber, R. Jenkins, D. E. Leyden, J. C. Russ, P.K. Predecki. Advances in X-ray Analysis, *Vol. 29*, Plenum Press, New York, **1986,** 6-57

160 E. Landi, A. Tampieri , G. Celotti, S. Sprio. Densification behavior and mechanisms of synthetic hydroxyapatites *J. Eur. Ceram. Soc.* **2000**, *20*, 2377-87

161 J. D. Currey. What determines the bending strength of compact bone? *J. Exp. Biol.* **1999**, *202*, 2495–503

162 J. E. V. Vincent. Structural Biomaterials, Princeton University Press, **1990,** 40-223

163 M. T. Sheu, J. C. Huang, G. C. Yeh, H. Ho. Characterization of collagen gel solutions and collagen matrices for cell culture *Biomaterials,* **2001**, *22*, 1713-19

164 A. H. Clark, S. B. Ross-Murphy, K. Nishinari, M. Watase. Sher Modulus- Concentration Relationships for Biopolymer Gels. Comparison of Independent and Cooperative Crosslink Descriptions in Physical Networks edited by W Burchard and S. B. Ross- Murphy, Elsevier Applied Science, London, New York, **1990,** 58-139

165 Y. Li, T. Tanaka. Kinetics of swelling and shrinking gels *J. Chem. Phys*. **1990**, *92,* 1365-71

166 J. M. Gonzalez-Saiz, M. A. Fernandez-Torroba, C. Pizarro. Study by response surface methodology of the swelling kinetic of weakly basic polyacrylamide gels in water *Eur. Polym. J.* **1999**, *35*, 509-16

167 S. K. Banerjee, J. A. Rupley. Temperature and pH Dependence of the Binding of Oligosaccharides to Lysozyme *J. Biol. Chem.* **1973**, *248,* 2117-24

168 A. Kristiansen, K. M. Varum, H. Grasdalen. Quantitative studies of the non-productive binding of lysozyme to partially N-acetylated chitosans *Biochim. Biophys. Acta* **1998**, *14,* 137-50

169 K. M. Varum, M. H. Otto, O. Smidsrod. Acid hydrolysis of chitosans *Carbohydr. Polym.* **2001**, *46*, 89-98

170 K. Mazeau, S. Perez, M. Rinaudo. Predicted influence of N-Acetyl group content on the conformational extension of chitin and chitosan chains *J. Carbohydr. Chem.* **2000**, *19,* 1269-84

References

171 S. Hirano, K. Yamamoto, H. Inui. Calcium Chloride as a biomimetic intermediate for the mineralization of carbonate ions of water as calcium carbonate in gelatinous matrices of chitosan and chitin *Energy Convers. Mgmt.* **1997**, *38,* 517-21

172 A.V. Kucherov, N.V. Kramareva, E. D. Finashina, A. E. Koklin, L. M. Kustov. Heterogenized redox catalysts on the basis of the chitosan matrix 1. Copper complexes *J. Mol. Catal. A: Chem.* **2003**, *198*, 377–89

173 F. C. Wu, R. L. Tseng, R. S. Juang. Kinetic modeling of Liquid-phase adsorption of reactive dyes and metal ions on chitosan *Wat. Res*. **2001**, *35,* 613-18

174 A. Ebrahimpour, M. Jonsson, C. F. Richardson, G. H. Nancollas. The characterization of Hydroxyapatite Preparations *J. Coll. Interf. Sci,* **1993**, *159*, 558-63

175 B. Amsden, N. Turner. Diffusion Characteristics of Calcium Alginate Gels *Biotechnol. Bioeng.* **1999**, *65*, 605–10

176 L. Vachoud, N. Zydowicz, A. Domard. Physicochemical behavior of chitin gels *Carbohydr. Res.* **2000**, *326*, 295–304

177 Y. L. Cuan, L. Shao, K. de Yaoz. A study on correlation between water state and swelling kinetics of chitosan-based hydrogels *J. Appl. Polym. Sci.***1996**, *61*, 2325-35

178 F. M. Goycoolea, A. Heras, I. Aranaz, G. Galed, M. E. F. Valle, V. A. Monal. Effect of chemical crosslinking on the swelling and shrinking properties of thermal and pH responsive chitosan hydrogels *Macromol. Biosci*. **2003**, *3*, 612-19

179 Y. K. Bhardwaj, Virendra Kumar, S. Sabharwal. Swelling behavior of radiation-polymerized polyampholytic two-component gels: dynamic and equilibrium swelling kinetics *J. Appl. Polym. Sci.* **2003**, *88*, 730-42

180 W. Zhang, I. Gaberman, M. Ciszkowska. Effect of the volume phase transition on diffusion and concentration of molecular species in temperature-responsive gels: electroanalytical studies *Electroanal.* **2003***, 15,* 409-13

181 S. V. Madihally, H. W.T. Matthew. Porous chitosan scaffolds for tissue engineering *Biomaterials* **1999**, *20*, 1133-42

182 M. V. Regi, A. M. Romero, C. V. Ragel, R. Z. LeGeros. XRD, SEM-EDS, and FTIR studies of in vitro growth of an apatite like layer on sol-gel glasses *J. Biomed. Mater. Res.* **1999**, *44*, 416-21

183 F. A. A. Tirkistani. Thermal analysis of chitosan Schiff bases *Polym. Degrad. Stab.* **1998**, *60,* 67-70

184 U. Gbureck , J. Probst, R. Thull. Surface properties of calcium phosphate particles for self setting bone cements *Biomol. Engineer.* **2002***, 19*, 51-5

185 G. Michael Lloyd Jr., Gordon D. Nifong, David J. Robertson, Hassan El Shall, Robert S. Akins. Separation of Dolomite from South Florida Phosphate Rock, Vol. III, University of Florida, **1988**, 4-22

186 P. X. Zhu, Y. Masuda K. Koumoto. Site selective adhesion of hydroxyapatite microparticles on charged surfaces in a supersaturated solution *J. Coll. Interf. Sci*. **2001**, *243*, 31-6

187 J. C. Knowles, S. Callcut, G. Georgiou. Characterization of the rheological properties and zeta potential of a range of hydroxyapatite powders *Biomaterials* **2000**, *21*, 1387-1392

188 S. N. Danilchenko, C. Moseke, L. F. Sukhodub, B. Sulkio-Cleff. X-ray diffraction studies of bone apatite under acid demineralization *Cryst. Res. Technol.* **2004,** *39,*71 – 7

189 P. Fratzl, S. Schreiber, A. Boyde. Characterization of Bone Mineral Crystals in Horse Radius by Small- of a range of hydroxyapatite powders *Biomaterials* **2000**, *21*, 1387-92

190 N. Sasaki, Y. Sudoh. X-ray Pole Figure Analysis of Apatite Crystals and Collagen Molecules in Bone *Calcif. Tissue Int.* **1997**, *60*, 1807-12

191 X. Su, K. Sun, F. Z. Cui, W. J. Landis. Organization of apatite crystals in human woven bone *Bone* **2003**, *32,*150–62

192 A. L. Boskey. Variations in bone mineral properties with age and disease *J. Musculoskel. Neuron Interact.* **2002**, *2,* 532-34

193 H. M. Kim C. Rey, M. J. Glimcher. X-Ray diffraction, Electron Microscopy, and Fourier Transform Infrared Spectroscopy of apatite crystals isolated from chicken and calcified cartilage *Calcif. Tissue Int*. **1996**, *59*, 58-63

194 Q. Liu, J. R. Wijn, C. A. van de Blitterswijk. Nano-apatite/polymer composites: mechanical and physicochemical characteristics *Biomaterials* **1997**, *18*, 1263-70

195 J. D. Hartgerink, E. Beniash, S. I. Stupp. Self-Assembly and Mineralization of Peptide- Amphiphile Nanofibers *Science* **2001**, *294*, 1684-87

196 J. M. Toth, W. M. Hirthe, W. G. Hubard, W. A. Brantley, K. L. Lynch. Determination of the ratio of Hap/TCP mixtures by X-ray-diffraction *J. Appl. Biomater.* **1991**, *2*, 37-40

197 L. J. Kescskes, R. H. Woodman, S. F. Trevino, B. R. Klotz, S. G. Hirsch, B. L. Gersten. Characterization of a Nanosized Iron Powder by Comparative Methods *Kona* **2003,** *21*,143-49

References

198 Y. X. Pang, X. Bao. Influence of temperature, ripening time and calcinations on the morphology and crystallinity of hydroxyapatite nanoparticles *J. Eur. Ceram. Soc.* **2003**, *23*, 1697-704

199 I. Zizak, P. Roschger, B. M. Misof, A. Berlanovich, S. Bernstorff, H. Amenitsch, K. Klaushofer, P Fratzl. Characteristic of mineral particles in the human /bone cartilage. *J. Struct. Biol.* **2003**, *141*, 208-17

200 J. M. Fernandez-Pradas, G. Sardin, J. L. Morentza. Inhomogenity of calcium phosphate coatings deposited by laser ablation at high deposition rate *Appl. Phys. A* **2003**, *76*, 251-56

201 P. Meuer, A. Wolf, R. Hansch, M. Okrusch, J. Popp, U. Posset, W. Kiefer. FT-Raman- Spectroscopic Study on the Luminescence of Synthetic and Mineral Apatites *Mikrochem. Acta* **2000**, *133*, 203-7

202 A. R. Boccacini, J. Jones, V. Maquet, L. L. Hench. Aplication of Raman microspectroscopy to the characterization of bioactive materials *Mater. Characteriz*. **2003**, *49*, 255-60

203 G. Penel, G. Leroy, C. Rey, E. Bres. MicroRaman Spectral Studies of the PO_4 and CO_3 Vibrational Modes in Synthetic and Biological Apatites *Calcif. Tissue Int.* **1998**, *63*, 475-81

204 G. L. Darimont, B. Gilbert, R. Cloots. Non-destructive evaluation of crystallinity and chemical composition by Raman spectroscopy in hydroxyaptyte-coated implants *Mater. Lett.* **2003**, *34,* 57-61

205 L. Yang, Y. Leng, L.-T. Weng. Characterization of chemical inhomogeneity in plasma-sprayed hydroxyapatite coatings *Biomaterials* **2003**, *24*, 2585-92

206 G. Penel, G. Leroy, E. F. Bres. Bone microraman investigation : a new method for sample preparation *Appl. Spectrosc.,* **1998**, 52, 312-13

207 X. Chen, W. Li, T. Yu. Conformational Transition of Silk Fibroin Induced by Blending Chitosan *J. Polym. Sci. B: Polym. Phys*. **1997**, *35*, 2293-96

208 J. Wolfe1, G. Bryant, K. L. Koster. What is 'unfreezable- water', How unfreezable is it and how much is there? *CryoLetters* **2002**, *23*, 157-66

209 S. Baumgartner, G. Lahajnar, A. Sepe, J. Kristl. Investigation of the state and dynamics of water in hydrogels of Cellulose Ethers by ^{1}H NMR spectroscopy *Pharma. Sci. Tech.* **2002**, *3,* 1-8

210 V. Blinc, I. Rutar, A. Zapancic, G. Zidansek, J. Lahajnar. Proton NMR relaxation of absorbed water in gelatin and collagen *Appl. Magn. Reson*. **1995**, *9,* 193-97

211 A. Stace. Cluster Solutions *Science* **2001**, *294*, 1292-93

212 J. H. Choi, K. T. Kuwata, Y. B. Cao, M. Okumura. Vibrational spectroscopy of the $Cl^-(H_2O)$ anionic clusters *J. Phys. Chem*. **1998**, *102*, 503-05

213 D. L. Botlan, Y. Rugraff, C. Martin, P. Colonna. Quantitative determination of bound water in wheat starch by time domain NMR spectroscopy *Carbohydr. Res.* **1998**, *308*, 29-36

214 S. V. Gupta. Practical Density Measurement and Hydrometry, IOP Publishing Ltd, London **2002**, 2-18

215 Q. Hu, B. Li, M. Wang, J. Shen. Preparation and characterization of biodegradable chitosan/hydroxyapatite nanocomposite rods via in siti hybridization: a potential material as internal fixation of bone fracture *Biomaterials* **2004**, *25*, 779-85

216 T. Fukamizo. Chitinolytic enzymes: catalysis, substrate binding, and their application *Curr. Protein Pept. Sci*. **2000**, *1,* 105-24

217 G. D. Davies, K. S. Wilson, B. Henrissat. Nomenclature for sugar binding subsites in glycosyl hydrolases *Biochem. J*. **1997**, *321*, 557-59

218 T. Fukamizo, K. Hayashi, S. Goto. The role of binding subsite A in reactions catalyzed by hen egg white lysozyme *Eur. J. Biochem.* **1986**, *158*, 463-67

219 T. Kokubo, H. Kushita, S. Sakka, T. Kitsugi, T. Yamamuro. Solutions able to reproduce in vivo surface-structure changes in bioactive glass-ceramic A-W *J. Biomed. Mater. Res*. **1990**, *24*, 721-34

220 F. Miyaji, Y. Morita, T. Kokubo, T. Nakamura. Surface structural change of bioactive inorganic filler-resin composite cement in simulated body fluid: Effect of resin *J. Biomed. Mater. Res*. **1998**, *42,* 604–10

221 P. Velos, P. M. Cherry and D. Miller. An improved method for measuring human tear lysozyme concentration *Arch. Ophthalmol.* **1985**, *122*, 151-56

222 D. J. Havey. Matrix-Assisted Laser Desorption/Ionization Mass Spectrometry of Carbohydrates *Mass Spectrom. Rev.* **1999**, *18*, 349-51

223 G. Attard, C. Barnes. Surfaces, Oxford University Press, Oxford, **1998,** 3-36

224 F. Hillenkamp, M. Karas, R. C. Beavis, B. T. Chait. Matrix Assisted Laser Desorption / Ionization Mass Spectrometry of Biopolymers *Anal. Chem.* **1991**, *63*, 1193-202

225 H. Pasch, W. Schrepp. MALDI-TOF Mass spectrometry of Synthetic Polymers, Springer -Verlag, **2003**, 12-49

Appendix

Appendix

A-I *Table A-I-1 Solubility constants, density and pH stability range in aqueous solution for some relevant calcium phosphate compounds;*

Ca/P ratio	Compound name and abbreviation	Chemical formula	Density	Solubility at 25°C ($-\log K_{ps}$)	Solubility* at 37°C ($-\log K_{ps}$)	pH stability range in aqueous solutions at 25°C
0.5	Monocalcium phosphate monohydrate, (*MCPM*),	$Ca(H_2PO_4)_2\ H_2O$	2.23	1.14	no data	0.0-2.0
0.5	Monocalcium phosphate anhydrous, (*MCP*),	$Ca(H_2PO_4)_2$	2.58	1.14	no data	not stable in solution; stable above 100°C
1	Dicalcium phosphate dihydrate or brushite, (*DCPD*),	$CaHPO_4{\cdot}2H_2O$	2.32	6.59	6.63	2.0-6.0
1	Dicalcium phosphate anhydrous or monetite, (*DCPA*),	$CaHPO_4$	2.89	6.90	7.02	not stable in solution; stable above 100°C
1.2-2.2	Amorphous calcium phosphate, (*ACP*)	$Ca_x(PO_4)_y\ nH_2O$	variable	cannot be measured	cannot be measured	metastable
1.33	Octacalcium phosphate, (*OCP*)	$Ca_8H_2(PO_4)_6{\cdot}5H_2O$,	2.61	96.6	95.9	5.5-7
1.5	α-Tricalcium phosphate, (*α-TCP*),	$Ca_3(PO_4)_2$	2.86	25.5	25.5	It cannot be precipitated from aqueous solution
1.5	β-Tricalcium phosphate, (*β-TCP*)	$Ca_3(PO_4)_2$	3.07	28.9	29.5	It cannot be precipitated from aqueous solution
1.67	Hydroxyapatite, (*HAp*)	$Ca_{10}(PO_4)_6(OH)_2$	3.16	58.4	58.6	4.2-12
2.0	Tetracalcium phosphate , (*TTCP*)	$Ca_4(PO_4)_2O$	3.05	38-44	42.4	It cannot be precipitated from aqueous solution

*The solubility constant is expressed as the logarithm of ion product constant. The concentration is in mol L^{-1}

A-II *FT-IR* spectroscopy

An *IR* spectrometer consists of three principal parts: a source, a monochromator and a detector. In infrared spectroscopy, the source emission is continuous and it covers the range of interest while in Raman spectroscopy the source emission is monochromatic. There are two types of IR spectrometers; one is disperse, where the wavelength is gradually varied using a prism and slit set-up while the second type is based on Michelson interferometer.

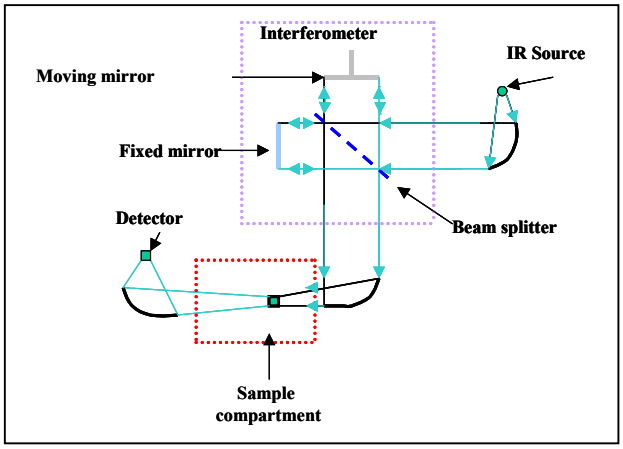

Figure A- II-1 Sketch of a FTIR spectrometer

In a Michelson interferometer[131], the radiation from the source is splitted using a beam splitter in a way that half the radiation is reflected on a fixed mirror and the other half is reflected on a moving mirror, as shown in *Figure A-II-1*. The reflected radiation from the two mirrors then interferes constructively or destructively depending on the wavelength and the position of the moving mirror. When the mirror is moving with a constant speed, the frequency of the resulting sinusoidal response for each spectral element depends only on the wavelength. The spectra are obtained by computing the Fourier transform of the interferogram.

A-III Raman spectroscopy

As shown in *Figure A-III-1*, a Raman confocal spectrometer has four main parts such as the radiation source (laser), a sample compartment with a holographic laser filter, a monocromator chamber, and the detector parts [photomultiplier and charge-coupled device (CCD)].When an intense beam of monochromatic light from a laser source impinges onto a material, scattering can occurs in all directions. As depending on the scattered frequencies can be Rayleigh scattering and Raman scattering[133]. In the case of Raleigh scattering the frequency of the scattered light is the same as original light υ_0. Raman scattered frequencies show both higher and lower values compared to υ_0.

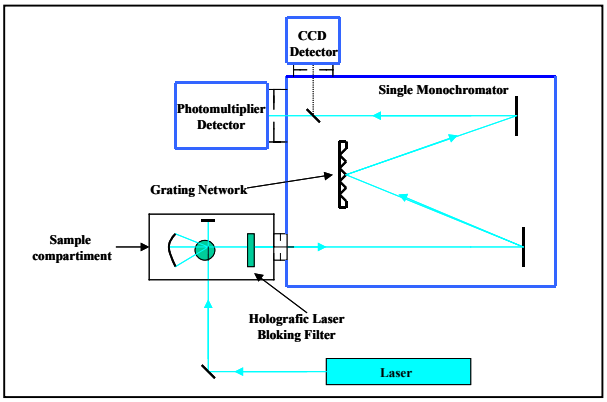

Figure A-III-1 Sketch of a Raman confocal spectrometer

The intensities of these frequencies are considerably diminished. The differences, $\Delta\upsilon$, between the incident and scattered frequencies are equal to the vibrational frequencies of the sample. Therefore, Raman spectroscopy like *IR* spectroscopy provides characteristic frequencies of functional groups that are present into the sample. Sometimes the *IR* and Raman frequencies correspond but it is not a rule since they are governed by different selections rules[134]. Raman and *IR* are complementary analytical techniques and serve to structural investigations.

A-IV Microscopic techniques

Microscopy techniques are used for the examination and characterization of materials at enhanced magnification[138, 139]. As radiation source either visible light as in *OM* and *CSLM* or an electron beam as in *TEM* and *SEM* are used. The resolution, Δa, is the minimum distance between two point that can be distinguished and is calculated according to *Equation A-IV-1*.

$$\Delta a = \frac{\lambda}{n_L \sin k} \qquad \textbf{(A-IV-1)}$$

where: λ is the wavelength
n_L is the refractive index
k is the aperture of the microscope

In *OM* the image is obtained from the visible light, transmitted through or reflected from the sample. The range of magnification extends from *10X* to about *1500X* with a limit of resolution of about 0.2 μm.

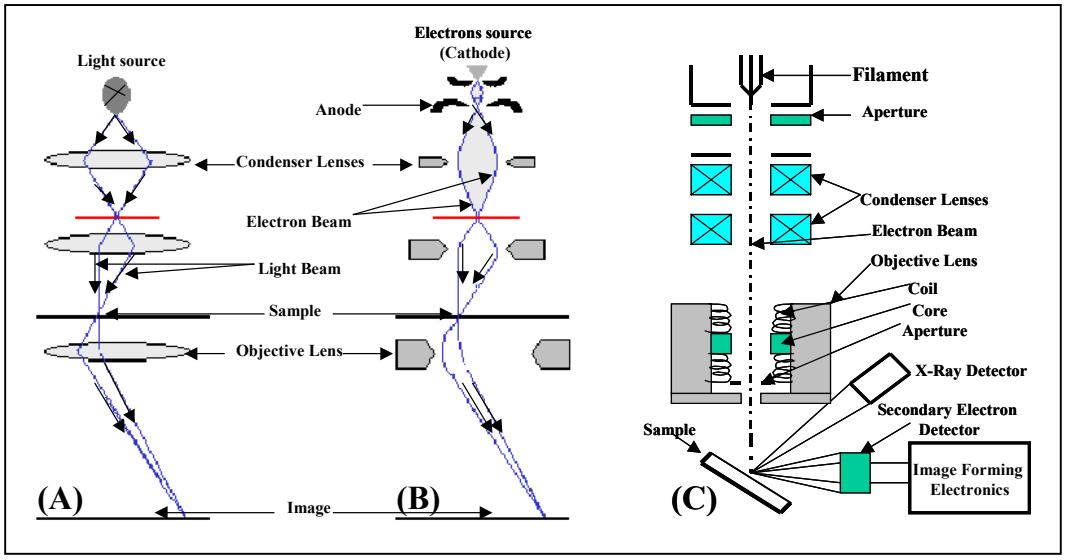

Figure A-IV-1 Sketch of OM (A), TEM (B) and SEM (C) microscopic systems

The practical resolution that can be reached for *TEM* and *SEM* systems is between 1.5-3 nm. *Figure A-IV-1* shows the following microscopy techniques such *OM* (A), *TEM* (B), and *SEM* (C). The geometries of these systems are different due to the position of sample plane and the construction principle as seen in *Figure A-IV-1*. Both *TEM* and *SEM* systems can be equipped with the energy disperse *X*-ray detector. Additionally, qualitative information about the material composition can be obtained by energy disperse spectroscopy (*EDS*).

A-V *NMR* spectrometry

A magnetic field, *Bo*, and a radio frequency coil are the main components of a *NMR* spectrometer. As shown in *Figure A-V-1*, the sample tube is placed in magnet field, which is surrounded by a super-conducting solenoid. The direction *z* of the magnetic field, B_0, is along the axis of the sample tube. The precessing magnetic moments pick out the appropriate rotating components of B_1, according to *Equation A-V-1*,

$$\nu_L = \left|\frac{\gamma}{2\pi}\right| B_0 \quad \text{or} \quad \omega_0 = \gamma \cdot B_0, \qquad \textbf{(A-V-1)}$$

where ν_L is the Larmor frequency an γ is the gyromagnetic ratio.
As the magnetization vector, M_{xy}, rotates in the *x-y* plane, in the *RF* coil is induced a current whose frequency is ω_0. Its amplitude is proportional to the magnitude of M_{xy}.

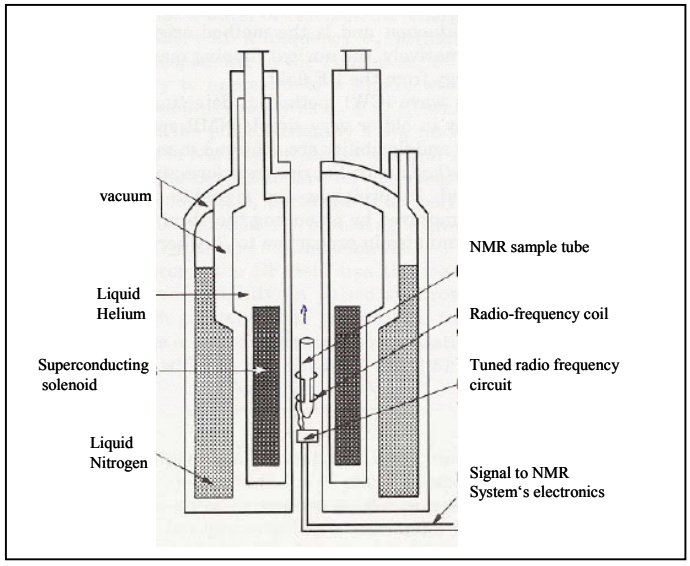

Figure A-V-1 Sketch of a cross section of superconducting magnet for NMR spectroscopy

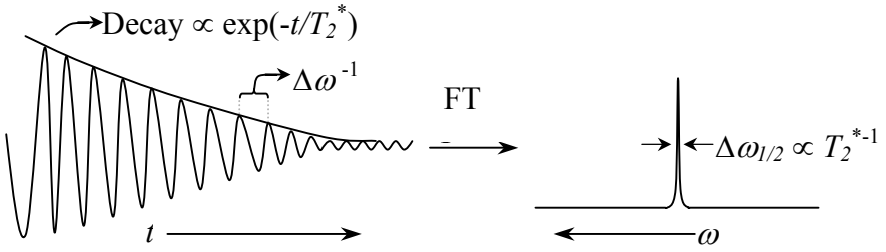

Figure A-V-2 The NMR spectrum in time domain (FID) and its Fourier transformation in a frequency domain for a molecule with chemically equivalent protons.

When all *NMR* signals are received simultaneously, the input into the computer is a voltage that is varying with time.The voltage is converted into an analog-to-digital converter. The function, *f(x),* stored in the computer is called the free induction decay[142], *FID*. The *FID* is an interferogram with an exponential decay envelope. The exponential decay can be represented by $v(t) = exp\ (t/T^*_2)$. The *FID* (time domain spectrum) is Fourier transformed function that appears as a frequency domain spectrum *Figure A-V-2*.

Ernst and Anderson [143, 144] have invented the Pulse-Fourier- Transform- procedure. Time and frequency are inversely related.

f(ω) is the frequency domain spectrum while *f(t)* is the time domain spectrum (*Figure A-V-2)*;

A-VI Electrokinetic phenomena

Electrokinetic phenomena[148, 149] are described as events associated with the movement of the charged particles through a continuous medium or with the movement of the continuous medium over a charged particle. There are four electrokinetic phenomena such as electrophoresis, electroosmosis, streaming potential and sedimentation potential. All these phenomena are related through the zeta-potential (ζ) of the electrical double layer that exits at the charged particle and solution interface. To describe these interactions at the interface, two main models have been proposed as shown in *Figure A-VI-1*(A). The interface can be described as a plane capacitor with the distance between charged planes, *d*.

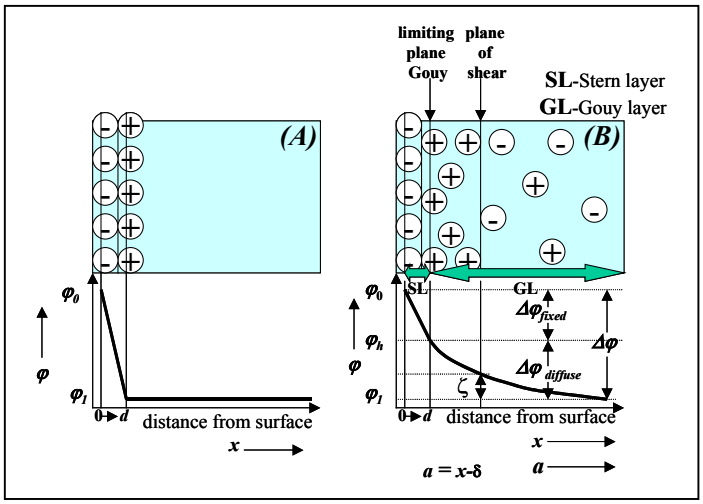

Figure A-VI-1 Two models of charged double layer together with the potential curves as a function of distance from the surface. (A): Helmholtz model (double layer model), (B): Stern model with one fixed layer (Stern layer) and one diffuse layer (Gouy layer).

According to *Equation A-VI-1,* the capacity is a function of the total charges, *Q*, the potential difference between electrodes, $\Delta\varphi$, and the permitivity of the medium, (ε), $\varepsilon=\varepsilon_o\varepsilon_r$, where ε_o is the vacuum permitivity, and ε_r is relative permitivity of the medium to the vacuum.

$$C = \frac{Q}{U} = \frac{\varepsilon_0 \varepsilon_r \cdot A}{d} \qquad \textbf{(A-VI-1)}$$

According to the Stern model, as displayed in *Figure A-4.2.5-1 (B)*, two alternative layers of ions are considered. The fixed layer is located adjacent to the charged surface and is called Stern layer. The second layer is named Gouy layer being a diffuse layer. The Gouy layer *(a=x-δ),* shows an exponential decrease from φ_h to φ_l that represents the potential in the bulk solution. The share plane is located in diffuse Gouy layer and its potential is ζ. The displacement of the charged layers occurs at the shear plane between the charged surface and its ionic atmosphere. The potential at the share plane represents the ζ-potential. The electrostatic potential, φ, is determined from the charge distribution, $\rho(a)$, as described by the Poisson equation, shown as *A-VI-2*, where *a* is the position of an ion in the Gouy layer.

$$\frac{d^2\phi}{da^2} = -\frac{\rho(a)}{\varepsilon_0 \varepsilon_r} \qquad \textbf{(A-VI-2)}$$

The Smoluchowski relation, shown as *Equation A-VI-3,* can be deduced from the Poisson equation taking into account the boundary conditions

$$\zeta = \frac{\eta \cdot u}{\varepsilon_o \cdot \varepsilon_r \cdot E} \qquad \textbf{(A-VI-3)}$$

where, η is the solution viscosity, E is the electrical field and u is the mobility of ions under experimentally conditions. The relationship between the transport rate, v_e and the ζ-potential that is valid for all four electrokinetic phenomena is expressed in *Equation A-VI-4.*

$$v_e = \frac{\varepsilon_0 \varepsilon_r \zeta E}{4\pi\eta} \qquad \textbf{(A-VI-4)}$$

The conditions for the validity of *Equation VI-4* imply that the thickness of the double layer to be smaller compared to the curvature radius of particles.

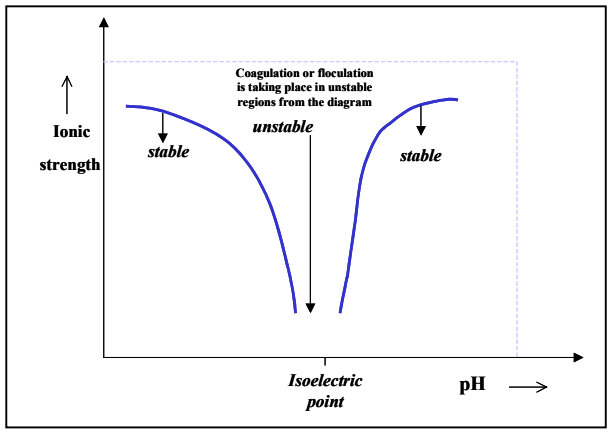

Figure A-VI-2 Stability diagram of a colloidal system with one IP as function of ionic strength and pH.

The isoelectric point, *IP*, is defined as the pH value at which the ζ-potential becomes zero. A stability map-diagram of a colloidal system with one *IP* shown as a function of pH and ionic strength is displayed in *Figure A-VI-2*. In practice, this parameter is an important issue which refers to the flocculation and coagulation processes of charged colloids.

A-VII Thermogravimetric analysis (*TGA*)

TGA is a technique that deals with a continuous monitor of sample weight as a function of temperature and/or as a function of time at a desired temperature[155]. The main parts of a thermogravimetric analyzer are presented in the sketch from *Figure A-VII-1*. The sample is placed in a furnace under a controlled atmosphere, either in an oxidative (air) or in an inert (nitrogen, argon) one. The temperature in the furnace is varied and controlled by sensors and any changes in the sample weight are recorded by a recording balance. One way of recording the weight variation is based on the fact that the sample is heated up from the room temperature, up to 1500-1700^o C with a rate between 5 and 10^o C. The second mode of working is to heat up the sample up to a desired temperature and then to follow the evolution of the sample weight as a function of time.

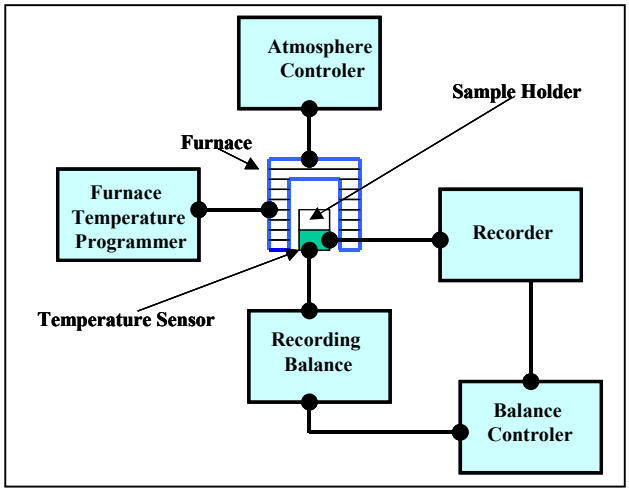

Figure A-VII-1 Sketch of a thermogravimetric analyzer

A-VIII X-Ray powder diffraction

The sketch of an X-Ray diffractometer with the description of the main components[156] is given in the *Figure A-VIII-1*. The basic principle consists of the interaction of the X-ray radiation with the matter. If a monochromatic X-ray radiation is directed onto a crystalline material, reflection or diffraction of the X-rays at various angles with respect of the primary beam are obtained. The Bragg law links the wavelength of the X-ray beam, λ, the angle of diffraction, 2θ, and the distance between each set of atomic planes of the crystal lattice, d, as presented as *Equation A-VIII-1*.

$$n\lambda = 2d\sin\theta \qquad \textbf{(A-VIII-1)}$$

The parameter, n, represents the order of diffraction. This equation can be used for the calculation of the interplanar distances of either crystalline or semi-crystalline materials.
The only restriction to get *XRD* pattern is that the analysed material might be crystalline or semi-crystalline.

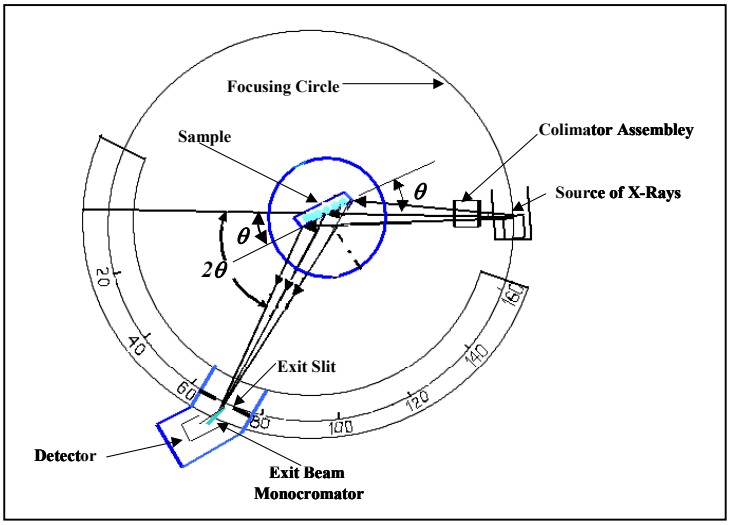

Figure A-VIII -1 Sketch of an X-Ray diffractometer.

Determination of the crystallite size;

XRD is sensitive to the crystallite size[157] according to Scherrer equation *(Equation A-VIII-2)*. The average crystallite size, L, is determined as following,

$$L = \frac{K\lambda}{\beta_m \cos\theta} \qquad \textbf{(A-VIII-2)}$$

where: L average crystallite size
β_m band width at half of the maximum intensity
K constant referred to the crystallite shape and is approximately equal to unity
λ X-ray wavelength

However, the data obtained by X-ray diffraction technique must need further refinement since not only the crystal shape and size but also the lattice strain is influencing the peak broadening. The strain of lattice is measured as a change in the *3d*-spacing positions in a strained sample after the X-ray bombardment compared to the same lattice unstrained. If is considered that β_n is the broadening peak contribution given by the lattice strain, it can be calculated according to *Equation A-VIII-3,*

$$\varepsilon = \frac{\beta_n}{4tg\theta} \qquad \textbf{(A-VIII-3)}$$

where ε is the lattice strain and β_n is the lattice strain contribution to the width of peak.
In a real measurement, the profile of the observed diffraction peak, *h (x),* is a convolution of three functions as described by f_m *(x)* is the contribution given by average crystallite size, f_n *(x)* given by the lattice strain contribution and g *(x)* is given by the measuring instrument profile[158, 159]. The convolution is mathematically described as following,

$$h(x) = g(x) + f_m(x) + f_n(x) = \int_{-\infty}^{+\infty}\int_{-\infty}^{+\infty} g(y) f_n(\xi) f_m[1-(y+\xi)]dyd\xi \qquad \textbf{(A-VIII-4)}$$

where ξ and y are dependent variables. Evaluation of L and ε can be obtained after the separation in components corresponding to the mentioned sources of broadening.

Evaluation of the crystalinity degree;

The crystallinity degree noted as X_c, was introduced[160] in order to make distinction between different apatite samples. It is defined as corresponding to the fraction of crystalline apatite phase in the investigated volume of powdered sample. The relation that can be used to calculate the crystallinity degree is presented below

$$X_C \approx 1-(V_{112/300}/I_{300}) \qquad \textbf{(A-VIII-5)}$$

where X_c is crystallinity degree;
I_{300} is the intensity of *(003)* reflection;
$V_{112/300}$ is the intensity of the hollow between *(112)* and *(300)* reflections.

A-IX Drying and swelling of composite samples under controlled conditions

Noncooperative Junction Zone Model; It is assumed that a polymer chain has *s* segments available to participate in the formation of associating network. Each of these segments has the potential to make contact with *m* nearest neighbour chains. The functionality of the chain is expressed according to *Equation A-IX-1*.

$$f = ms \qquad \textbf{(A-IX-1)}$$

Structural studies on biogels (agar gels) have showed that the maximum value for '*m*' is 7. In many theoretical calculation it is preferred to use the average estimated value of *m*=5.
In this model the shear modulus *G* is expressed as follows,

$$G = Ne^{(\alpha, f)} a\ RT \qquad \textbf{(A-IX-2)}$$

where: *Ne* is the number of counts elastically chains per unit of volume;
α is the degree of crosslinking, it is taking values between 0 and 1;

a is a structural parameter. In the case of polysaccharide gels, the value is 10;
R is the universal gases constant;
T is the absolute temperature (K).

The term aRT refers to the free energy of the system. It involves the enthalpy and as well as the entropic contributions.

The Cooperative Junction Model; It is considered that the polymer chain have s segments for the junction zone formation, but now the specific number n of these segments (supplied by different chains) combine one-another to form each junction zone. The functionality of the chain changes as compared to the previous model and becomes;

$$f = (s-1)\,(n-1)+1 \qquad \textbf{(A-IX-3)}$$

For this model the mass action relationship that give the degree of crosslinking is written as:

$$\alpha = \left\{ n^{1/(n-1)} K^{1/(n-1)} s\, C/M \right\}^{n-1} (1-\alpha)^n \qquad \textbf{(A-IX-4)}$$

Each cooperative junction model is defined in terms of fixed s and n. The degree of crosslinking makes the phase transition between glass and rubbery state in the case when this parameter increases as a function of an environmental parameter such as temperature, composition, pressure, etc. In some other practical examples, the degree of crosslinking remains relative constant but the composition changing drives the glass- rubbery phase transition.

***Li - Tanaka's Gel Model*;** The general equation for swelling and shrinking of a gel disk shaped sample is expressed according to Li - Tanaka's gel model[165] as:

$$\frac{u(r,t)}{u(r,0)} = \sum_n B_n \exp\left[-t/\tau_n\right] \qquad \textbf{(A-IX-5)}$$

where: t denotes the time of either swelling or shrinking process;
$u(r,t)$ is the displacement vector of a point in the gel network.

When the gel is fully swollen indicating the final equilibrium location, it is u=0. The displacement vector of a point from the gel network can be described as an infinite sum of an exponential decay with the characteristic times τ_n. B_n is a structural parameter that depends only on the geometry of the gel and as well as on R. The ratio between the sheer modulus G, and the longitudinal osmotic modulus M_{os}, is R, and it is expressed in *Equation A-IX-6*.

$$R = \frac{G}{M_{os}} \qquad \textbf{(A-IX-6)}$$

At the last swelling stage, the first term of the series, given by *Equation A-IX-5,* becomes much more greater than the others and hence it is dominant and rest can be neglected. Therefore, the swelling kinetic experiments allow the determination of B_1 and τ_1. Taking $r=a$, where a is the diameter of the disk, *Equation A-IX-5* becomes in a logarithmic form as *Equation A-IX-7,*

$$\ln\frac{u(a,t)}{u(a,0)} = \ln\left(\frac{d_\infty - d_t}{d_\infty - d_0}\right) = \ln B_1 - \frac{t}{\tau_1} \qquad \textbf{(A-IX-7)}$$

where d_t, d_0, and d_∞ refer to the diameters of disk shaped samples at a given time (d_t), at initial time (d_0) and at the maximum diameter (d_∞) resulted from the swelling process. τ_1 represents the relaxation time. Both B_1 and τ_1 are experimentally determined by plotting the second term of the *Equation A-IX-7* as a function of time. From the swelling measurements, the effective cooperative diffusion coefficients of hydrogels[166], Dc, for the disk shaped samples can be calculated according to *Equation A-IX-8*,

$$D_c = \frac{3a_\infty^2}{\tau_1 \alpha_1^2} \qquad \textbf{(A-IX-8)}$$

where: a_∞ is half the thickness of the disk at the maximum swelling;
α_1 is a function of R and hence on B_1 and can be evaluated as was described by the Tanaka's gel model for the disk shaped samples.

So far, a dependency between the degree of crosslinking (α) and diffusion cooperative coefficients (D_c) is established as described by *Equation A-IX-8*. It is important to see how these parameters are influencing each other. α_1 can be evaluated from Tanaka diagrams of the disk shaped gels samples, as shown in *Figure A-IX-1*. In order to evaluate the swelling diffusion coefficients, $\ln\left(\frac{d_\infty - d_t}{d_\infty - d_0}\right)$, is plotted versus the swelling time according to *Equation A-IX-7*.

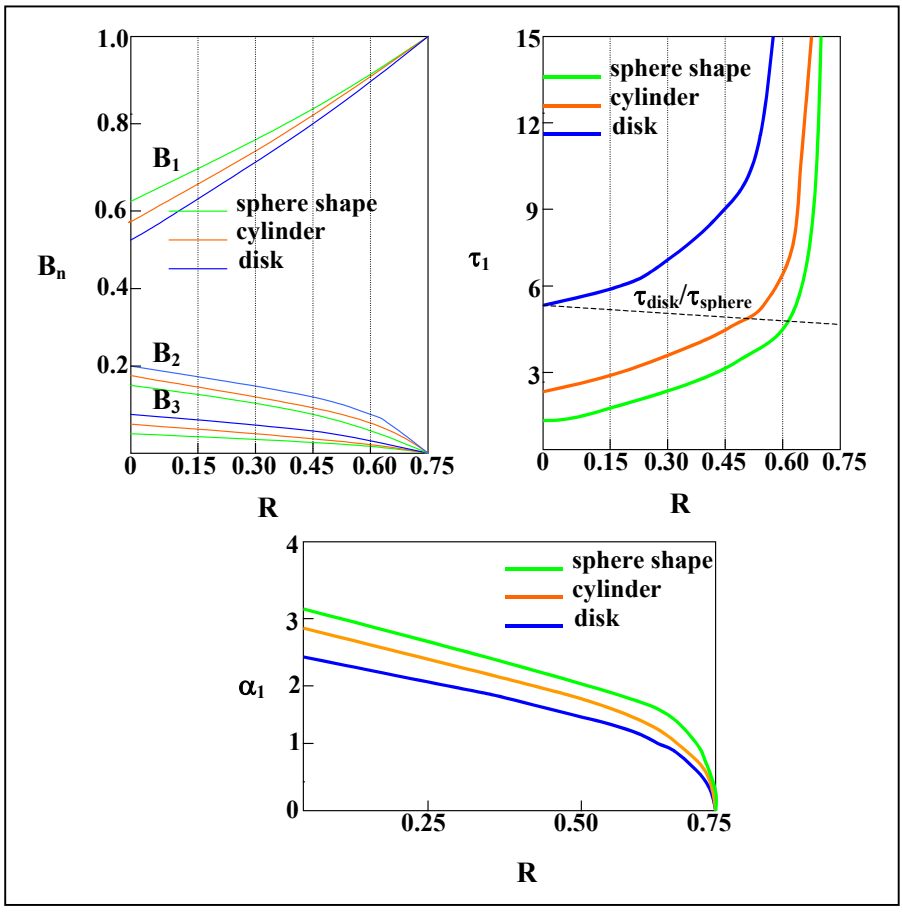

Figure A-IX-1 Dependence of some structural parameters (B_n, τ_1, α_1) of the gel network as a function of R (the ratio of shear modulus to longitudinal modulus). R can vary from 0 to ¾, according to the Tanaka- Lee's gel model [165].

From the logarithmic plot analyses, B_1 is determined by extrapolation to *OY* axis as the limiting *ln* B_1 value and τ_1 represents the slopes of graphs. α_1 can be evaluated according to Tanaka-Lee's gel model, as seen in *Figure A-IX-1*.

A-X Table A-5.7.2-2 Raman bands of composites compared to some natural bio-composite containing biological apatite phases such as bone, dentine and enamel[201-206].

Assigned bands (cm^{-1})	*Chitosan* *Raman bands*	*CTS/HAp composite* *Raman bands*	*Hydroxy-apatite (HAp)* *Raman bands*	*Enamel* *Raman bands*	*Dentine* *Raman bands*	*Bone* *Raman bands*
**) 3350 free OH^- stretching*			3561	3573		
**) 3200-3450 $-NH_2$ deformation symmetric and asymmetric stretching*				3513		
	3433	3433				
	3311	3311				
**) 2500-3500 -OH stretching; hydrogen bonded or/and solid sample*					2988	2986
	2920; shoulder	2920			2923	-
					2948	2946
**) 2880-2990 -CH stretching*	2891	2891			2881	2882
**) 1660-1670 amide I band*	1662	1655-65			1660	1662
**) 1550-1590 amide II band*	1588	1588				
**) 1350-1480 amide III band *) 1415-1450 $-CH_2O-$ def. *) 1440-1470 $-CH_3$ asymmetric bending deformation*	1457	1446			1450	1449
**) 1320-1390 -OH deformation from member ring sample*	1375	1363				
**) 1210-1330 amide III band $-CONHCH_3$ deformation*	1255	1258			1260	1262
**) 1080-1100 -CO- stretching*	1093	1091				
**) 940-1077 P=O stretching*			1048		1102	1103
			962;		1069	1071
		956	shoulder		1046	1044
**) 1100-1103 amide III band*		1106-10			1031	1032
				1002	1003	1005
**) 1100-1107 CO_3^{2-} stretching*				959	959	961
**) 800-1000 ring vibration-deformation*	980	956		959	959	961
	900	900			920	924
**) 870-875 P-OH stretching*					873	873
**) 400-530 $-CH_2$ OH deformation*	493	435		450	450	452
	416	344		433	432	432
	357					
**) 420-680 P-Element; PO_4^{3-} stretching*		583	590	608	610	611
		435	436	588	590	590
				579	580	584
				450	450	452
				432	432	432

A-XI Surface area determination

The gas adsorption technique[223] can be used to determine the specific surface area powdered or solid materials. As well as the pore size distribution can be evaluated.The dry sample is usually evacuated of all gas and cooled to a temperature of 77K, the temperature of liquid nitrogen. At this temperature, inert gases (nitrogen, argon and krypton) are physically adsorbed on the surface of the sample. This adsorption process can be considered to be a reversible condensation or layering of molecules on the sample surface during which heat is evolved.

Determination of the specific surface area

a) Langmuir approach

Assumptions; The adsorbed molecules do not interact and the surface is progressively covered by a monolayer. The adsorption rate is proportional to the free surface of sample and to the gas pressure. Moreover, the desorption rate is proportional to the covered surface. At equilibrium, *Equation A- XI-1*, describes the process,

$$(1-\theta)p = b\theta \qquad \textbf{(A-XI-1)}$$

where θ is the part of the surface covered with adsorbed molecules, p is the equilibrium pressure, a and b are constants. If V is the adsorbed volume and V_m the volume of a monolayer covering all the surface, we have $\theta=V/V_m$ which leads to *Equation A-XI-2* :

$$\frac{P}{V} = \frac{P}{V_m} + \frac{b}{V_m} \qquad \textbf{(A-XI-2)}$$

The slope of P/V as a function of p gives V_m, allowing the determination of the specific surface area on condition that the surface occupied by a single adsorbed molecule is known, in the case of N_2 it is 16.27 $Å^2$.

b) Brunauer, Emmet, Teller (BET surface area) approach

It is based on generalization of the Langmuir theory to multilayers adsorption, with the following assumptions:The evaporation rate of adsorbed molecules in a layer is equal to the condensation rate on the layer under it. At saturation, the number of layers is considered as infinite. The resulting equation is *Equation A-XI-3*:

$$\frac{P}{n(P_0 - P)} = \frac{1}{n_m c} + \frac{(c-1)}{n_m c}\frac{P}{P_0} \qquad \textbf{(A-XI-3)}$$

P is the equilibrium pressure, P_0 is the saturation pressure, n is the adsorbed gas quantity (for example in volume units), n_m is the monolayer gas quantity, c is the *BET* constant. Nitrogen is used most often to measure *BET* surface, but if the surface area is very low, argon or krypton may be used as both give a more sensitive measurement, because of their lower saturation vapor pressures at liquid nitrogen temperature.
From the adsorption isotherms the specific surface area and the parameter c can be deduced by plotting $P/(n(P_0-P)) = f(P/P_0)$.

A-XII *MALDI-TOF* mass spectroscopy

MALDI-TOF mass spectroscopy is a technique which deals well with thermolabile, non-volatile organic compounds especially those of high molecular weight and is used successfully in biochemical areas for the analysis of proteins, peptides, glycoproteins, oligosaccharides, and oligonucleotides[224]. The mass accuracy depends on the type and performance of the analyser of the mass spectrometer, but most modern instruments should be capable of measuring masses to within 0.01% of the molecular weight of the sample, at least up to about 40,000 Dalton. The matrix and polymer are mixed at a molecular level in an appropriate solvent with a large excess of the matrix. The sample to be analysed[225] is dissolved in an appropriate volatile solvent, at a concentration of about 10 pmol/µL and then, mixed with an equal volume of a solution containing a large excess of a matrix. The solvent prevents aggregation of the polymer. The sample/matrix mixture is placed onto a sample probe tip. Under vacuum conditions, the solvent is removed, leaving co-crystallized polymer molecules homogeneously dispersed within matrix molecules. The matrix transforms the laser energy into excitation energy for the sample, which leads to sputtering of analyte and matrix ions from the surface of the mixture [see *Figure A-XII-1* (A)]. The time-of-flight analyser separates ions according to their mass (m)-to-charge (z) (*m/z*) ratios by measuring the time it takes for ions to travel through a field free region known as the flight, or drift, tube.

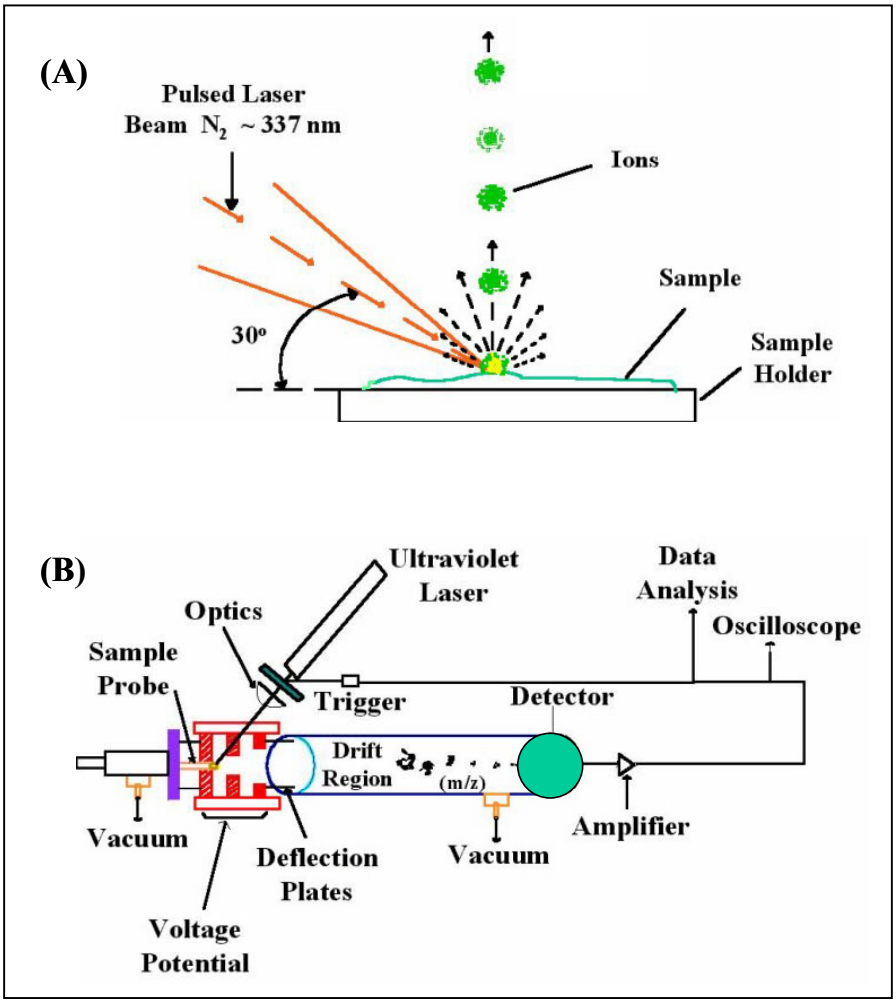

Figure A XII-1 MALDI-TOF mass spectroscopy technique. (A) Sample ionisation, (B) Sketch of a MALDI-TOF mass spectrometer.

The heavier ions are slower than the lighter ones.

The *m/z* scale of the mass spectrometer is calibrated with a known sample that can either be analysed independently (external calibration) or pre-mixed with the sample and matrix (internal calibration). The *TOF* mass spectrum is a recording of the detector signal as a function of time. The time of flight for a molecule of mass m and charge z to travel this distance is proportional to (m/z)1/2. This relationship, t ~ (m/z)1/2, can be used to calculate the ions mass. Through calculation of the ions mass, conversion of the *TOF* mass spectrum to a conventional mass spectrum of mass-to-charge axis can be achieved.

A general sketch of a *MALDI-TOF* spectrometer is presented in *Figure A XII-1* (B). The component main parts of the machine are illustrated.

MALDI is a soft ionisation method and so results predominantly in the generation of singly charged molecular-related ions regardless of the molecular weight, hence the spectra are relatively easy to interpret.

In positive ionisation mode the protonated molecular ions ($M+H^+$) are usually the dominant species, although they can be accompanied by salt adducts, a trace of the doubly charged molecular ion at approximately half the m/z value, and/or a trace of a dimeric species at approximately twice the m/z value. Positive ionisation is used in general for protein and peptide analyses.

In negative ionisation mode the deprotonated molecular ions ($M-H^-$) are usually the most abundant species, accompanied by some salt adducts and possibly traces of dimeric or doubly charged materials. Negative ionisation can be used for the analysis of oligonucleotides and oligosaccharides.

Acknowledgements

First, I would like to thank Professor Martin G. Peter for giving me the opportunity to work in his research group. Prof. Peter has supervised my PhD work and gave me many professional advices.

I would like to thank my wife, my parents, my relatives and my friends for their help, and their generous support during my PhD period.

I also acknowledge my colleagues Chuen-How Ng, Sven Barhke, Derek Lightner, Ljubisha Jovanovic, Jean Fotie, Zenko Zanev, Alexander Jantz, Andre Gessner, Attila Böhme, Dirk Peikow, Frau Matern, Frau Patzl, Daniel Goltz, Frau Rotmann, Fanny Lebouc, Telma Franco and Michael Sefkow, for a pleasant working atmosphere as well as for their contributions in achieving this project. Some of my colleagues must be particularly acknowledged;
Dr. Ng for assistance, correction the drafts, for his advice and for his material contribution to the project with the mechanical tests on composite samples, performed in England;
Derek for the fruitful discussions, for friendship meetings with Coke and Twix in American style as well as for the correcting the drafts;
Sven for assistance and for the analysing the chitosan oligomers by *MALDI-TOF* mass spectroscopy;
Dr. Michael Sefkow for fruitful and efficient discussions;

Dr. Max Wilke, Geology Department, for helping me with the *XRD* measurements;

Dr. Fridrich , Inorganic Chemistry Department, for helping me with the *TGA* measurements;

Frau Nachtigal, Analytical Department, for performing the *IR* spectra on composite samples;

Prof. Joachim Koetz and his co-workers Frau Dr. Kosmella, Frau Dr. Tiersch, Daniela Robertson and Jennifer Baumann, Colloidal Chemistry Department which helped me with their support and fruitful discussions. My grateful thanks goes to them for helping me to get the *TEM* and *SEM* micrographs of composites, for the measuring the microgel size domains as well as for the *DSC* measurements;

Acknowledgements

Mihaela Rusu and Prof. Monika Schonhoff, MPI Golm, for the *NMR* relaxation measurements and for their professional support for the interpretation of *NMR* data;

Paul Lazar, MPI Golm, for performing the *OM* measurements;

Wen-Fei Dong, MPI Golm, for this nice guy I should say something more. Besides his wish to collaborate, he is always prepared to help you either with advice or with Raman, *SEM*, *BET* measurements;

Frau Praast and Frau Zastrow, MPI Golm, for performing zeta size measurements;

Dr. Alexei Antipov, MPI Golm, for making the *CSLM* measurements;

Silvia Nita, MPI Golm, for helping me with her advices about the enzymatic experiments, for reading the PhD draft as well as for her useful suggestions.

Prof. Julian Vincent and Dr. Hugh Perrott, Center for Biomimetics, University of Bath, England, for allowing us to perform the analysis of mechanical properties of composites (Prof. Julien Vincent) and for the *SEM* and *EDS* measurements (Dr. Hugh Perrott);

Prof. Peter Fratzl is specially acknowledged for his contribution to the *XRD* data interpretation (for the brilliant idea as well as for the mathematical computation).

Special thanks are going to Dr. Angelo Valeriani, the Coordinator of IMPRS Potsdam-Golm, for his support and advise throughout my PhD period;

I acknowledge my former leader, Dr. Viorica Tamas (Biotehnos SA, Romania) that oriented me towards a research career into the frame of Natural Sciences.

I would also like to thank Prof. R. Lipowsky the Speaker of IMPRS Potsdam-Golm, for the financial support during my PhD period.

MARIN VIOREL RUSU

21 Aug 1968	I was born in Bistrita/Romania
1974-1978	Primary School (Bistrita/Romania)
1978-1982	Secondary School (Bistrita/Romania)
1982-1986	High School (Bistrita/Romania)
1987-1992	Faculty of Chemistry, University of Bucharest/Romania
Jun 1992	Dipl. Chem. Project: Obtaining of new complex combinations in a mixed system La II-Cu II, using ligands containing carboxyl groups Supervisor: Prof. Dr. Elena Cristurean
Sept 1992-Mar 1993	Military Service
1 Sept 1993	Employed as chemist at the SC Biotehnos SA Bucharest (a small private pharmaceutical and cosmetic company), in Analytical Department (after passing an examination)
Sept 1993-Dec 2000	SC Biothehnos SA Bucharest/Romania
Since Jan 1995	Responsibilities in leading and managing research projects on natural compounds such as lipids, steroids and vitamins with respect to their separations (from natural sources) and to their physicochemical characterization.
Mar 1996	Chromatographic separation techniques of natural compounds- Course (one month) at the Institute of Genetics- Kisinev, Republic of Moldavia, Coordinator Prof. Dr. Pavel Chintea
Since Jun 1996	I have been appointed Head of the Laboratory of Chromatography in Analytical Department-Biotehnos SA.
Sept 1996-Jul 1998	Auxiliary Assistant Professor for laboratory lectures at the Faculty of Chemistry, University of Bucharest (Inorganic Chemistry Department- supervisor Prof. Dr. Tudor Rosu) (part time job)
Aug 1997	The NMR applications in medicine and other fields; Course (two weeks) at Neptun, Romania, Coordinator Prof. Dr. Gheorghe D. Mateescu – (University Cleveland, Ohio, USA).
Jan 1998 - Dec 2000	Consultant specialist on analytical laboratory instrumentations (GC, GC-MS, Spectrophotometers, etc) at the Labim SRL and Addis International SRL (part time job)
Jan 2001 - Dec 2003	PhD student in the frame of Biomimetic Systems at the International Max Plank Research School Potsdam –Golm Project: Composite materials made of chitosan and nanosized apatite; Preparation and physicochemical characterization Supervisor: Prof. Dr. Martin G. Peter
Jan 2004-Dec 2004	Researcher at the Institute of Chemistry, University of Potsdam/ on a European Project: Bone Glue

Papers and Communications

Chueng-How Ng , V. Rusu and Martin G. Peter
Formation of chitosan hydroxyapatite composites in the presence of different organic acids, Poster Presentation
Glykane und Glykomimetika in Medizin und Pharmazie
Symposium, Berlin-Dahlem, 14 Oct **2003**

V. Rusu and M. G. Peter
Developing of new bone substitute materials containing chitosan and/or chitosan derivative and hydroxyapatite -oral communication- IMPRS
Symposium, Potsdam-Golm 14-15 Oct **2002**

V. Tamas, C. Barcutean, V. Rusu, N. Dociu, S. Jipa, T. Setnescu, I. Mihalcea
The study of some lipidic extracts by chemiluminescence and other complementary techniques, Poster presentation
XIIth National Conference on Analytical Chemistry – Craiova **1998**;

C. Doneanu, V. Radulescu, D.M. Efstatiade, V. Rusu, A. Covaci, Capillary GC/MS characterization of fatty acids from indigenous silkworm oil
J. Microcolumn. Sep. 9, 37-41, **1996**

V. Tamas, V.Ionita Manzatu, V. Rusu, M. Ilie, M. Dumitrascu,
Gas-Chromatography Pattern Recognition studies of some lipid extract for pharmaceutic and cosmetic use, Poster presentation,
Euroanalysis IX-Bologna, **1996**

E.Chirila, V. Magearu, M. Draghici, V.Rusu, A. Bleotu
Analytical characterisation of petrochemical effluent by GC-MS
Analele Universitatii "Ovidius" Constanta, Inginerie, Vol. VI Chimie, **1995**

List of publications resulted from the PhD Project

Viorel M. Rusu, Chuen-How Ng, Martin G. Peter
Micro- and macro-morphology of chitosan/hydroxyapatite nanocomposites; Structures and mechanical properties
(In preparation)

Viorel M. Rusu, Chuen-How Ng, Martin G. Peter
Studies on the degradation behaviour of chitosan/hydroxyapatite nanocomposites in the presence of lysozyme
(In preparation)

Viorel M. Rusu, Chuen-How Ng, Mihaela Rusu, Wen-Fei Dong, Martin G. Peter
Water state characterization, swelling kinetics and diffusion characteristics of hydrogel networks of chitosan / hydroxyapatite nanocomposite
Submitted to *Biomacromolecules* (Sept 2004)

Viorel M. Rusu, Chuen-How Ng, Max Wilke, Brigitte Tiersch, Peter Fratzl, Martin G. Peter
Size-controlled hydroxyapatite nanoparticles as self-organized organic-inorganic composite materials
Biomaterials (2005-in press)

Chuen-How Ng, Viorel M. Rusu and Martin G. Peter
Formation of chitosan hydroxyapatite composites in the presence of different organic acids
Advances in Chitin Science, Vol. 7 (in press)